SAPIENZA
UNIVERSITÀ DI ROMA

Faculty of Mathematical, Physical and Natural Sciences

Ph.D. in Earth Science

(XXXI course)

Integrated geophysical investigation to detect buried structures: examples in the south-eastern part of Rome and its surroundings (Latium, central Italy)

Tutor:
Prof.ssa Francesca Bozzano
Co-Tutor:
Prof. Salvatore Piro (ITABC-CNR)

Ph.D. candidate
Francesco Smriglio
(ID. 1196938)
Francesco.Smriglio@Uniroma1.it

Referee:

Prof. Nikos Papadopoulos (IMS, Greece)

Prof. Michele Di Filippo (IGAG-CNR, Italy)

Ph.D. Coordinator:

Prof. Giovanni Battista Andreozzi

Academic year 2017-2018

INDEX

Riassunto .....

Abstract .....

Chapter I- Introduction 1

1.1 Background 1

1.2 Objectives and thesis organization 5

Chapter II-Theory of Geophysical data integration 7

2.1 General concepts 7

2.2 Interpretative approach 7

2.3 Graphical integration 8

2.4 Mathematical transformation 9

2.5 Statistical methods 11

2.5.1 Principal Component Analysis (PCA) 11

2.5.2 Cluster Analysis (CA) 13

2.5.3 Bayesian Maximum Entropy (BME) 15

Chapter III- Theory of Geophysical methods 18

3.1 The magnetic method 18

3.1.1 Introduction 18

3.1.2 Magnetic behaviors of materials 20

3.1.3 The earth magnetic field (e.m.f.) 22

3.2 Ground Penetrating Radar (GPR) 24

3.2.1 Introduction 24

3.2.2 Electromagnetic propriety of subsoil 26

3.2.3 GPR fundamentals 27

3.3 Electrical Resistivity Tomography (ERT) 31

3.3.1 Introduction 31

3.3.2 Potential of homogenous subsoil 33

3.3.3 Type of arrays 34

Chapter IV-Parco della Caffarella test site 37

4.1 Geological setting of Parco della Caffarella 37

4.2 Information about cavity network 41

4.3 Data Collection 43

4.4 Data processing 46

4.4.1 ERT Data Processing 46

4.4.2 GPR Data Processing 48
4.5 Data Interpretation 49
4.5.1 ERT data Interpretation 49
4.5.2 GPR Data Interpretation 52
4.5.2.1 GPR 70 MHz Time-Slice 52
4.5.2.2 GPR 400 MHz Time-Slice 52
4.6 Results of data integration 54
4.6.1 Graphical integration 54
4.6.2 Mathematical integration 55
4.6.3 Statistical integration 58
4.7 Concluding remarks 61
Chapter V- Magliano Sabina Test site 62
5.1 Geological and archeological setting 62
5.2 Data Collection 65
5.3 Data processing 68
5.3.1 GPR data processing 68
5.3.2 Magnetic data processing 68
5.4 Data interpretation 70
5.4.1 GPR data interpretation 70
5.4.2 Magnetic data interpretation 71
5.5 Results of Data integration 73
5.5.1 Graphical integration 73
5.5.2 Mathematical integration 74
5.5.3 Statistical integration 78
5.6 Concluding remarks 82
Chapter VI - Final remarks and conclusions 83
References 84
Acknowledgement 94
Appendix A - Parco della Caffarella 95
Appendix B - Magliano Sabina 138

Riassunto

Nell'ambito dell'*engineering geology*, il problema delle cavità antropiche che interessano centri abitati è particolarmente sentito, infatti, stando a modelli geologici recentemente sviluppati, esse possono migrare verso la superfice mettendo così a repentaglio la presenza di edifici, strade e l'incolumità degli stessi abitanti. Inoltre, i metodi d'investigazione diretti (quali sondaggi geognostici e indagini dirette del reticolo caveale) risultano essere piuttosto costosi e necessitano di numerose persone oltre di una certa quantità di tempo per essere realizzate. Al contrario i metodi indiretti (geofisici), oggetto del presente lavoro, consentono di indagare cavità di dimensioni anche ridotte in maniera estensiva oltre che generalmente rapida. Ciò premesso, nell'ambito del presente Dottorato, sono stati usati diversi metodi geofisici di *near surface*, integrandoli fra loro, allo scopo di caratterizzare le cavità presenti in due diversi *test sites* in ambito urbano ed extraurbano. La prima area test, indagata con il metodo GPR e il metodo ERT, è quella del Parco della Caffarella, in cui si ha una conoscenza solamente parziale di un esteso reticolo caveale scavato nelle pozzolane rosse dal quale si estraevano, in epoca etrusca e romana, materiali per l'edilizia. L'area indagata ha dimensioni 48 m x 30 m e la zona di sovrapposizione fra il metodo ERT e il GPR risulta essere di 48m x 14 m. Più in dettaglio, sono state eseguiti 14 profili ERT (modello *Syscal Junior-Iris Instrument*),aventi lunghezza 47 m con i 48 elettrodi posti ogni metro. L'*array* scelto è stato il doppio-dipolo poiché assicura una buona risoluzione sia in termini di variazioni verticali che orizzontali delle resistività, come ampiamente noto in letteratura. L'area in oggetto è stata indagata con il GPR (Modello SIR-3000, GSSI) usando dapprima un'antenna bistatica, ad offset costante, ad alta frequenza (400 MHz) e successivamente un'antenna monostatica a bassa frequenza (70 MHz). Nel primo caso i profili sono stati acquisiti con un'interdistanza pari a 0.5 m mentre nel secondo con un'interdistanza pari a 1 m. I dati sono stati elaborati con *software* specifici per estrarre delle sezioni tempo-profondità (time-slice) dell'area indagata con i dati GPR e delle sezione profondità bidimensionali (*depth-slice*) con i dati ERT. La seconda area è sita nel territorio di Magliano Sabina-Loc. Madonna del Giglio (Rieti), nella quale, da numerose fonti archeologiche è nota la presenza di strutture funerarie a fossa (VII-VI sec. a.C.), parzialmente collassate. L'area di dimensioni 80 m x 30 m è stata indagata, dapprima con il GPR (Modello SIR-3000,GSSI) usando un'antenna bistatica ad offset costante ad alta frequenza (400 MHz) acquisendo i profili ogni 0.5 m e successivamente con il magnetometro differenziale *fluxgate* (FM256-Geoscan Research), suddividendo l'area in 7 quadrati di 10 m di lato, con i profili paralleli acquisiti ogni metro e le misure lungo il profilo ogni 0.5 m. La zona di sovrapposizione fra i due metodi è stata di 70 m x 10 m. Anche in questo caso dai dati GPR sono state ricavate le *time-slices* mentre i dati magnetici sono stati elaborati con la crosscorrelazione normalizzata bidimesionale allo scopo di far emergere le anomalie da un contesto geologico altrimenti piuttosto rumoroso. Dopo le suddette operazioni, per entrambi i siti sono stati testati diversi metodi di integrazione sia di tipo qualitativo (*Contour map overlay*, *RGB Colour Composite*) che di tipo quantitativo (*data sum*, *data product*, *binary representation*) oltre di tipo statistico (*Principal Component Analysis*, *K-mean Cluster analysis*, *Bayesian Maximum Entropy*). I risultati, incoraggianti, mostrano come alcuni dei metodi summenzionati siano fin da ora spendibili in un contesto applicativo, mentre altri si trovino ad un livello di ricerca.

Abstract

In the frame of engineering geology, the problem of anthropogenic cavity that affects inhabited centers is very complex. In fact, according to geological models developed in the last years, cavities can migrate upward toward the surface, jeopardizing the presence of buildings, roads and safety of people. Moreover, direct investigation methods (like boreholes or direct exploration) are quite expensive and they need a large amount of time to be done. On the other hand, geophysical methods allow investigating cavities extensively and quickly. Having said that, we used different integrated geophysical methods in order to characterize cavities in two different test sites. The first test area, investigated with the GPR and ERT method, is the so called "*Parco della Caffarella*", in which an extended cavity network, quarried by Etruscan and Romans in the *pozzolane rosse* formation, is only partially known. The total surveyed area was 30 m x 48 m in size. The whole area has been investigated with the GPR method and partially with ERT method in the winter 2017. GPR measurements have been collected, along parallel profiles, employing the SIR3000 (GSSI) system, equipped with a 400 MHz bistatic antenna with constant offset and a 70 MHz monostatic antenna. The horizontal spacing between parallel profiles at the site was 0.50 m and 1 m respectively for the two antennas. The ERT measurements have been acquired in an area with dimension 14m x 48m partially overlapping the area surveyed with GPR. 14 parallel profiles, with a length of 48 m, have been acquired using an Iris Syscal Junior Switch-72. The Double Dipole configuration has been chosen and the 48 electrodes were arranged with a spacing of 1 m for all profiles. The collected data were processed using specific software in order to extract time-slices from GPR data and depth-slice to ERT data. The second area is located in the territory of *Magliano Sabina-Madonna del Giglio* (*Rieti*), in which, by numerous archaeological sources is attested the presence of ditch tombs (VII-VI century a.C.) partially collapsed. The selected area was 30 m x 80 m in size. The whole area has been investigated with the GPR method and partially with the fluxgate gradiometer in the spring 2017. GPR measurements have been collected, along parallel profiles, employing the SIR3000 (GSSI) system, equipped with a 400 MHz bistatic antenna. The horizontal spacing between parallel profiles at the site was 0.50 m. The Fluxgate Gradiometer measurements have been acquired in an area with dimension 10 m x 70 m, overlapping the same area investigated with GPR. In particular, the area was divided into 10 squares 10 m x 10 m where the vertical gradient of total magnetic field has been measured using a fluxgate gradiometer FM256 (Geoscan Research, UK) along parallel profiles with horizontal spacing 1 m and with a sampling interval of 0.5 m. Also in this case, from the GPR data the time-slices were obtained while using the magnetic data the bidimensional normalized crosscorrelation was applied in order to gain dipolar anomalies in a so noisy geological framework. After the aforementioned operations, for both test sites, we tested several integration methods: qualitative type (contour map overlay, RGB Color Composite), quantitative type (date sum, date product, binary representation) and statistical type (Principal Component Analysis, K-means Cluster analysis and Bayesian Maximum Entropy). The results show how some of the aforementioned methods are useful in the frame of engineering geology, while other are at research state level.

Chapter I- Introduction

In the present work we try to make a contribution referred to the identification of buried cavities in urban and suburban environments. The term "cavity" is used to indicate disruptions of the so-called “anthropogenic sinkholes”, as underground quarries, reservoirs, tanks, hydraulic tunnels and in archaeological sense, funerary structures. These collapses can be extremely hazardous for the urban centers, because they can occur suddenly as in the well-known cases of *Via Giosafat* (Santoro & Federici, 1999) and *Via Borsa* (Lanzini,1999), both occurred in Rome, in which there was a degradation of cavity network due to soil weathering. Having said that, in the present Ph.D. thesis an experimental investigation into two different test sites having as core subject the integration of different geophysical methods for the identification of buried cavities is presented; in addition we also try to make a hypothesis about the conservation status of cavity network. The diversity of the selected test sites is related to different factor like the location (the former is located in an urban area while the second is in an uninhabited center) and the stratigraphy, because the first is located in a volcanic area while the second area is characterized by clayey formations. The first site, located in the *Parco della Caffarella* (portion of the well-known *Parco dell’Appia Antica)*, in Rome, has a particular interest for both archaeological and geological reason because in the area the presence of an intricate cavity network quarried by Etruscan and Roman is already known. The second site, located close to the small town *Magliano Sabina* (Rieti) is known to have close to it a series of necropolis composed by ditch tombs. In the area of the *Parco della Caffarella*, Ground Penetrating Radar (GPR) and Electrical Resistivity Tomography (ERT) has been used whereas in *Magliano Sabina* area we employed Magnetometer Fluxgate Differential (MFD) and the GPR. Then, we tested several integration methods (graphical, mathematical and statistical) in order to identify the buried cavities.

1.1 Background

Geophysical methods are frequently used for engineering (e.g. Jongmans & Garmabois, 2007) or archeological studies (e.g. Piro *et al*., 2007; Barone *et al*, 2015; Piro *et al*.,2016). Among them, identification of cavities is very important both for engineering study as for archeological research (e.g. Piro *et al*., 2001). In fact cavities, as reported by Bianchi Fasani *et al*., (2012), can be extremely hazardous in urban framework because they can migrate upward until to reach the subsurface. The methods for cavity identification are generally divided in two main categories: invasive and noninvasive.

They are listed below and briefly described:

- **Boreholes**: They provide detailed punctual-type information; the high cost of this type of surveys and the limits the perforation depth, making thus impossible to characterize large areas with only their use.
- **Guided Boreholes** (television survey in the hole and speleological survey): They provide direct information on the shape and volume of the voids but an extended cavity network are needed in order to allow the access to a camera or an operator.

- **Noninvasive methods are surveys with geophysical methods**: They are less expensive, may also provide information with a high degree of detail, enabling the reconstruction of the substrate no longer in punctual form like occurs using boreholes but in an extended way.

Depending on the physical measured parameter they are divided as follow:

- *Gravimetric methods*: It is definitely among the most used investigation method for cavity identification (e.g. Di Filippo & Toro,1999; Balia *et al*.,2003; Di Filippo *et al*.,2004; Styles *et al*.,2006; Martinez-Moreno et *al*.,2014; Heath *et al*.,2017). In many cases, it involves small anomalies that are measurable only through long operations for data acquisition and processing. In addition, to locate cavities at limited depth, an instrument with good sensitivity and great precision in corrections (e.g. topographic) is needed.

- *Electrical Resistivity Tomography (ERT)*: This method is very often applied in cavity detection surveys (e.g. Van Schoor., 2002; Gibson *et al*., 2004; Dobecki & Upchurch, 2006; Cardarelli *et al*.,2006; 2010; Metwaly & AlFouzan, 2013; Bianchi Fasani *et al*.,2013, Ungureanu *et al*., 2017). Also it is useful for identification of structural discontinuities (e.g. Zhu *et al*., 2017) and in to the detection of groundwater contamination (e.g. Moghaddam *et al*., 2017).

- *Ground Penetrating Radar (GPR)*: In recent years the GPR has become one of the most used for the identification of cavity network, both in karst environment or on the soil environments (Davis & Annan, 1989; Benson, 1995; McMechan *et al*., 1997; Young & Sun, 1998; Witten and Calvert, 1999; Batayneh *et al*., 2002; Boubaki *et al*., 2011; Orlando, 2013, Garcia-Garcia, 2017; Rubio-Melendi *et al*., 2018). The resolution and investigation depth which is possible to obtain performing a GPR survey are influenced by soil characteristics of surveyed area, and, mainly in a negative sense, by clay content and water. The ability to make continuous sections in real time of the subsoil, the non-invasively of method and the high cost/benefits ratio and the rapidity in the acquisition of the high resolution data makes it a method of wide applicability.

- *Seismic methods*: These methods are quite used for the investigation of cavities (e.g. Laparoux *et al*.,1999; Cardarelli *et al*.,2010; Bitri *et al*., 2016) even if, up to now, they were certainly less employed in this field of research if compare to the aforementioned methods. Basically, they consist in generating seismic waves in a point of the soil and in detecting the arrival, by means of suitable sensors (geophones). In most cases, elastic waves are generated on the surface with the use of flying masses or though explosions, for this reason they are hard to use, because it can produce, especially in these particular areas, the damage and sudden collapses of the cavities.

- *Magnetic method*: It is very used for cavity detection both in geological and archeological framework (e.g. Mochales *et al*., 2008; Balkaya *et al*., 2012); it is hard to use in very urbanized framework (like city center) because they contain a large amount of background noise caused, for example, by extended buried pipes or electric cables. Anyway, where possible to use it, this method is very useful to survey large area in a short time and, in addition, the data processing is very fast using specific softwares (e.g. Geoplot 3.0).

The choice of which method to use depends on several factors. Basically there is based on (Brizzolari *et al*., 1992):

- The contrasts between the physical properties of the subsoil and the target.
- The target of the geophysical survey.
- Economic and logistics factors.

A preliminary study about the geological framework of the area subject of survey is therefore very important for an appropriate choice of the method to be employed (e.g. Scotto di Santolo *et al*., 2015). Generally, for the identification of buried target different methods are employed and integrated (Brizzolari *et al*, 1992; Cammarano *et al*., 1997; Piro *et al*., 2000, 2017); in this way will it be possible to reduce the uncertainty typical of each indirect prospecting and increase the information provided by the research. Listed below are presented some case studies in which different geophysical methods are integrated in a framework similar to those presented in this work.

- **Cardarelli *et al*., 2008** (Montelibretti, Rome, Italy)

The aim of this work was to detect buried structured in an unexplored area (total dimension 20 m x 20 m) of Sabine Necropolis, inside the research area of National Research Council, close to the location of the Institute for Technologies Applied to Cultural Heritage, Montelibretti (Rome). In these surveys the authors used three different geophysical methods: MDF, ERT and GPR. The results of magnetic investigation show that the area is characterized by many dipolar anomalies in a range of -40 to +35 nT/m, spatially organized in circular shape anomalies. All the ERT pseudosections show an horizontal band with a higher resistivity value (respect to the background), and the presence of anomalies reaching, in some case, resistivity values of 120-140 Ω ·m. GPR time-slices shows that the individual reflections, probably due to the heterogeneities of the tuff layer, they are not located in the same position of the magnetic anomalies. This occurrence can be ascribed either to the lack of a voided cavity or to a cavity having a very poor conservation state. The authors, plotted the three map obtained by the employed methods on a common topographic map; following the boundaries of the negative anomalies a probable shape of the buried structure was drawn in the magnetic map; In the ERT map the low resistivity anomalies (40-50 Ω·m) correspond probably to collapsed structures that has similar shape to those detected by magnetic map. The results of GPR time-slices confirm the aforementioned situation because there are no sharp variations in terms of dielectric proprieties of the

material. Direct archaeological excavation, made successively to the geophysical survey during the summer of 2005 confirmed the results and the interpretation.

- **El-Qadi *et al*., 2005** (Cairo, Egypt)

In the eastern part of Greater Cairo, a new housing development namely Al-Amal Town is planned; The area is on the main limestone plateau that contains many intercalations of marl and clay, which are considered hazardous for housing developments. The main objective of this work is to apply ERT and GPR to investigate the structure of a cave and to delineate any unknown caverns that might hinder future public development at Al-Amal. The survey was conducted above an exposed cave with unknown extensions (total area surveyed with GPR was about 1000 m^2 while 3 ERT were collected close to the known cave). The results of resistivity pseudosections show a relatively moderate resistivity background (19–40 Ω·m). This can be referred to the lithologic intercalation of marl (calcareous shale) with limestone; in some area high resistivity values (about 800 Ω·m) were detected. GPR time-slices shows a hyperbolic radar signal due to a cave at a depth of about 2 m, with a width of about 4 m, which is in good agreement with the known cave system in the study area. Moreover, some anomalous zones are delineated and are believed to reflect extensions of the cave system and other small karstic features. It should be stressed that also in this case different geophysical datasets were not probably merged together in order to study the cavity network but they were compared visually.

- **Bianchi Fasani *et al*., 2013** (Rome, Italy)

In this paper a multidisciplinary – geophysical and geological – method oriented to cavity location was described, tested and validated. The authors coupled ERT surveys with borehole drilling; firstly both methods were tester in an area in which a cavity network in known and the it was applied in an second test site in which the orientation of cavity network was still unknown. The authors conclude that the physical reconstruction offered by ERT, when supported by a detailed geological model, was considered very useful in defining the geometry of the subsoil and consequently increasing up to 86% the percentage of success in cavity location when compared to the one obtained by drilling combined with only geological information.

- **Boubaki *et al*.,2011 (Dourdan, France)**

The authors tested ERT and GPR complementarity over an existing cave at the Abbaye de l'Ouye, close to the small town of Dourdan (France); a single ERT profile was collected and in was overlapped by a single GPR profile. For the ERT profile, they used the Wenner configuration using 48 electrodes with 0.5 m spacing. The GPR mono-offset profile was acquired using 250 MHz antennas with a RAMAC Mala system. Traces were collected every centimeter. It consisted of 1024 samples for a time window of 80 *n*s. From hyperbolas fitting and the multi-offset profile analysis, they determined a velocity of 0.08 m/ns for the

electromagnetic wave propagating in the soil. Then they use the radargram to define the limits of the cavity using arrival time-picking of the top reflection after migration of the data and assuming a flat floor for the cave. The aforementioned information was introduced in two different ways: firstly they impose arbitrarily a high resistivity of 10000 Ω·m inside the limits determined by the GPR and secondly they introduced the GPR information as sharp boundaries allowing the model to take any electrical resistivity distribution: the RMS in both cases was less than 1% but the shape of cavity was less accurate in the former then in the latter. The authors conclude that introducing GPR information such as depth of top and a shape for the cavity that drops out from the migration process, help to create an electrical resistivity model that well fits the reality.

Thus, as reported before, some paper are about the integration of different geophysical methods addressed to solve an engineering problem; it is less common anyway to find work in which geophysical datasets are fuse together in order to obtain a map containing all the anomaly detected by the employed methods. Geophysical integration methods are divided into main categories: qualitative (e.g. Kvamme, 2007; Ogden *et al.*,2009), and quantitative (e.g. Piro *et al*.,2000;2009). The qualitative integration (graphical) allows combining information of acquired data within different ways in order to obtain a representation of the subsoil containing various levels of information easy to interpret. It is difficult however to effectively represent maps composed of more than two or three sets of data because it can generate confusing images. It is also necessary to stress that this type of integration in purely qualitative, which returns as a result only images and not new sets of data that could allow further analysis. Performing the quantitative integration (e.g. Piro *et al*., 2000) which is carried out by means of mathematical processes and statistical purposes, it is possible to obtain more detailed overview of the subsoil because this type of integration is based on a numerical comparison between the anomalies detected by different geophysical methods.

In Chapter II the different types of integration methods are presented and discussed in details.

1.2 Objectives and thesis organization

The aim of the present work is to verify if different integration methods of geophysical datasets may be helpful into the location of the cavity in suburban environments and if these methods may also be applicable in the field of engineering geology.

In addition, we can identify some open questions that addressed the present work, they are listed below:

1. How we could provide a “quick way” to identify cavities merging different geophysical methods?
2. Different integration methods can be applied in terms of engineering geology?
3. Could we make a hypothesis about the conservation state of cavities?
4. It is possible to understand which are the “best” integration methods?

The thesis is organized as follow:

- ✓ In the *Chapter I* introduction, background and thesis objectives are presented.
- ✓ In the *Chapter II* theory about integration of geophysical methods is reported.
- ✓ In the *Chapter III* theory about the geophysical methods employed in this work are reported briefly.
- ✓ In the *Chapter IV* geological setting, data collecting, processing and interpretation about the first test site (*Parco della Caffarella*, Rome, Italy) are reported; then the results of data integration methods are presented and discussed.
- ✓ In the *Chapter V* geological setting, data collecting, processing and interpretation about the second test site (*Magliano Sabina*, Rieti, Italy) are reported; then the results of data integration methods are presented and discussed.
- ✓ In the *Chapter VI* concluding remarks are reported.

Chapter II-Theory of Geophysical data integration

2.1 General concepts

During a geophysical survey, because of a small contrast of physical properties between the buried targets and the subsoil, geophysical methods may not be enough accurate to detect buried targets (e.g. Piro, 1998; Zheng *et al*., 2013). Thus, to perform a geophysical survey as accurate as possible, it is necessary to increase the signal/noise ratio (e.g. Cammarano *et al*., 1997). It is possible to solve these kinds of problems using different acquisition techniques and integrate different geophysical methods for the same survey (e.g. Piro, 1996). So, the integration and comparison between different geophysical methods could help to determine the position, the extension and the depth of a body located in the subsoil (Piro *et al*., 2000). Indeed, as reported, for example, by Brizzolari *et al*., (1992), each geophysical method measures variations of a single physical parameter of the subsoil, therefore if the various methods are used individually, they may not allow an adequate characterization of anomalous bodies. Thus, in the past decades, a lot of attempts have been made to produce a quantitative method for the integration of two or more geophysical datasets collected using near-surface geophysical techniques. Geophysical data sets have included GPR, ERT, Magnetic Gradiometer, and Electromagnetic (EM) methods (e.g. Neubauer & Eder-Hinterleitner 1997, Doneus & Neubauer, 1998, Hargrave, *et al*., 2006, Kvamme, 2007, Keay *et al*.,2009; Piro & Gabrielli, 2009; Ernenwein,2009; Kalayci,2013; Piro *et al*., 2016; Küçükdemirci *et al*.,2018). The quantitative integration of two or more geophysical data sets has been explored by K.L. Kvamme (2007). His research outlines some of the advances in the management, portrayal, and interpretation of subsurface data through the use of geophysical instruments and the computer methods utilized in the display of those data sets. Furthermore, Kvamme (2007) explains the versatility that geophysics brings in the realm of archaeological surveys and incorporates the idea of data fusion based on the opinion that combined information (or use of more than one data set) will lead to more insight than simply using only one type of data to interpret subsurface features. More in details, Kvamme (2007) summarizes four possible data fusion methods that are reported below

- ✓ Interpretative approach
- ✓ Graphical integration
- ✓ Mathematical Transformation
- ✓ Statistical

2.2 Interpretative approach

Referring to the first area of work, a successful interpretation of geophysical data depends by the careful and experienced eye of the interpreter. In addition, knowledge of the surveyed area in the geological context is essential, as well as knowing how anomalies will appear in the data for any given type of geophysical technique (Kvamme, 2007). When combining several data sets, that knowledge becomes even more important as variables are added to the total data available because each type of technique responds uniquely to characteristics of the subsurface; for example, magnetometry to soil magnetic susceptibility changes,

electrical resistivity and electromagnetic (EM) induction to conductivity changes, and ground penetrating radar (GPR) to changes in dielectric permittivity contrasts. The aforementioned approach at integrating data is perhaps the simplest and most widely utilized method, as it does not require much technological effort beyond the data pre-processing stage. Geophysical findings within this phase of interpretation are traditionally subjective and incorporate deductive reasoning in order to draw conclusions about the subsurface features and locations of buried targets. Another advantage of the above mentioned method includes the ability of the interpreter to incorporate an *isolation technique* to visualize and interpret data. The so called isolation technique is defined as "*the determination of a set of parameters that will separate an event from its surroundings"* (Sheffield *et al*., 2000). The isolation technique allows important situation to become visible, particularly it occurs when significant anomalies are underlined; if the anomalies are matched together in the same local, the researcher can then assume that location holds an important feature, worth investigating further. Additionally, each geophysical technique can be integrated separately as a different layer within the GIS program, as well as layers depicting geology and topography (Hill, 2008) to complement the geophysical data and interpretation of the subsurface. There are, however, disadvantages to this method, the most important is that a qualitative interpreting approach may lead to various levels of error depending on the individual conducting the interpretation. To sum up, the interpretive approach is still extremely subjective and dependent on the experience of the interpreter, which is its biggest disadvantage.

2.3 Graphical integration

The computer graphic (**CG**) method of integrating geophysical data has been used with increasing frequency in the last three decades (e.g. Raper, 1989; Sayar *et al*., 2005; Campana & Piro, 2008). Two-dimensional overlays are created using specific software (GIS etc); in cases where several geophysical techniques are utilized in the same area, it is relatively easy to have one data set displayed as a gray-scale image, another with isolines contours, another with shaded relief mapping, etc.; this will enable each type of data to be displayed separately while at the same time exhibiting the relationships between each different data set when they are overlain. The negative aspect of the method, however, is that there can be a huge volume of data from different geophysical techniques for a surveyed area and all of which can become hopelessly merged unless an interpreter comes prepared with a well-conceived data management scheme for the project (Conolly & Lake, 2006). Translucent overlays of varying opacity are another version of the CG method, but again, there is a need to be careful in the format of display to minimize misinterpretation of the primary features within the subsurface.

Red-Green-Blue (RGB) color composite is a standard for displaying satellite imagery for decades (e.g., Schowengerdt 1997)—have been adopted by the geophysical community to aid in delineating various features within the subsurface based on parameters set in place to classify anomalies. The power of the RGB method blends as an intuitive visualization tool whereby the richness of structure and relative ease by which

objects can be visually separated is very compelling. A key tool of RGB method is that color-based co-rendering techniques work well when the individual data sources are naturally correlated to some degree, as is the case with multispectral satellite imagery or Magnetic Resonance Imaging (MRI) data in medical imaging (e.g. Viola *et al*., 2015). However, the technique defines a linear mapping function and the user must choose whether to scale all three inputs equally or whether to utilize the maximum available dynamic range of each individual component. This linear mapping can lead to changes in the appearance of the generated RGB image; It should be taken into account when interpreting RGB representation and it should be supported by others integration methods.

2.4 Mathematical transformation

Mathematical transformations involve a less qualitative approach compared to the interpretive and computer graphic methods for integrating geophysical data sets. The two divisions of this method are those that utilize binary data (discretized data) and those that employ continuous measurements, both of which require pre-processing of the data to perform optimally (Kvamme, 2007). One advantage in the use of binary data is that the presence of an anomaly is classified as a "1" and the absence of an anomaly is classified as a "0." This is helpful when mapping a large data set and trying to determine trends in the area. However, because this is a black and white case of anomaly detection, characteristics of the anomaly (e.g. intensity) are not differentiated. The second type of mathematical transformation for data integration involves operations on Continuous Data (CD) sets. These transformations effectively convert data into a form that can be statistically manipulated, thus facilitating subsequent data analysis. These CD operations must also take into account the various measurement scales, different data ranges, and the even distributional forms that exist with each geophysical method (Kvamme, 2007). Normalization of the data sets must take place prior to any integration method, or else resulting values will present a false representation of the combined data set and lead to possible misidentification of anomaly locations (e.g. Patro & Sahu, 2015). Among CD operation the Data Sum and Data product (Piro *et al*., 2000; Küçükdemirci *et al*., 2015; Piro *et al*.,2016;2017) are briefly presented.

In order to perform a quantitative integration of the results obtained by different methods is necessary to make their results numerically comparable (Piro *et al*., 2000). To achieve this condition, it is necessary to give some assumptions. Thus, we can employ *M* different methods to perform a geophysical survey and indicate with $\mathbf{m}i$ the generic survey (with i=1,….,M).

The results obtained with the method $\mathbf{m}_i$ can represent through the function $f\mathbf{m}_i(\mathbf{r})$, where **r** is a vector located in a three-dimensional Cartesian reference system, with the x-y plane placed on the surface of the soil and the z axis directed downwards. The values that this function takes will be characterized by a unit of measure dependent on the specific parameter detected with the method $\mathbf{m}_i$.

Thus, it is possible to define the function as $f\mathbf{m}_i(\mathbf{r})$ an indicator of the presence anomaly source detected with a specific method $\mathbf{m}_i$. Moreover, if we indicate with z_m the depth of investigation, the $f\mathbf{m}_i(\mathbf{x,y})$ represent the trend of as $f\mathbf{m}_i(\mathbf{r})$ in the plane $z = z_m$. Then, in order to obtain the integration of the data of a quantitative values of the individual functions $f\mathbf{m}_i(\mathbf{x,y})$ obtained for each geophysical method which represent the trend of the parameters defined by the experimental measures, they must be numerically comparable (Piro *et al*.,2000).

For the aforementioned reason, it is defined the function f_{mi} is the undisturbed value of $f\mathbf{m}_i(\mathbf{r})$: the response of m-*I* method if any anomalous body was below the ground.

The function $fm_i(x,y)$ - *fmi* will indicate the trend of physical parameter investigated with the generic method m_i to the depth z_m with respect to its "undisturbed" value. The module of this function $|fm_i(x,y) - i|$ will have the maximum value in the points in which the anomaly has its maximum intensity.

Normalizing this function respect to its maximum value it is possible to define a new function expressed by eq. 2.1

(2.1) $$f_{mi}\,(x,y) = \frac{f_{mi} - \widetilde{fmi}}{Max\, f_{mi}\,(x,y) - \widetilde{fmi}}$$

it is dimensionless and therefore it is independent to the original unit of measure of the different methods

$f_{mi}\,(x,y)$ satisfy the following condition (eq.2.2):

(2.2) $$0 < f_{mi}\,(x,y) < 1$$

Because $f_{mi}\,(x,y)$ is dimensionless, it will be equal to 1 at the points of maximum discontinuity where it represents the Indicator of Source Occurrence (ISO) for anomaly caused by the presence of anomalous bodies in the subsoil independently from the adopted geophysical method.

Because all the employed geophysical methods **M** are potentially able to detect the properties of the same target, it is possible to combine them through the following operation:

- Sum of ISO functions

It is described by the eq.2.3:

$$\overline{F\ (x,y)} = \frac{1}{M}\sum_{M_i}^{M} F_{m_i}\ (x,y) \quad \textbf{(2.3)}$$

It is the indicator of the distribution of anomaly source detected by at least one of the methods used. I.e. the function is equal to 1 only at those points in which the employed methods detected the maximum anomaly while it will be equal to 0 at those points in which no one method has highlighted anomaly.

- Product of ISO function

It is described by the eq. 2.4:

$$F^{*}(x,y) = \prod_{m_i}^{M} F_{m_i}(x,y) \quad \textbf{(2.4)}$$

It represents the indicator of the distribution of anomaly source detected by all the methods used. I.e. the function is equal to 1 only at the points in which all methods recorded the maximum anomaly while it will be equal to 0 at those points when even only one method revealed no anomaly.

2.5 Statistical methods

2.5.1 Principal Component Analysis (PCA)

The PCA method can account for determining amounts of variance between data sets (Kvamme,2007; Jolliffe *et al*., 2016); when data is standardized, each variable within the statistical method contributes a variance of unity (Davis, 2000). The PCA is "*designed to reduce redundancy in multispectral data*" (Lillesand *et al*., 2008, p.527). In essence, the variables that describe the data are transformed into new variables, which are called "Principal Components (PC)". These new variables are linear combinations of the original variables, also they are mutually orthogonal (Todeschini, 1998). From a mathematical point of view, **t**he PCA method consists of a rotation process of the original data which are defined by a matrix "**X**" (dimension of *n x p*); these rotation effected in the way that the first new axis is oriented in the direction of maximum data variance, the second axes is perpendicular to the first and it is in the direction of the following maximum data variance: this occurs for all the *p* new axes (Wold *et al*., 1987). Fig. 2.1 is referred to a two data example: the first Principal Component (PC1) is oriented in the direction of maximum variance of data and its origin is perpendicular to the PC2 and it represents the residual variance of data; Each of the two components is a linear combination of the two original variables (Wold *et al*.,1987; Todeschini,1998).

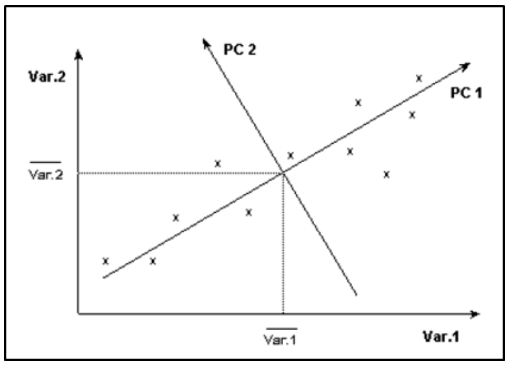

Fig. 2.1 Example of PCA referred to two data (Todeschini, 1998)

To perform the PCA the following steps should be employed (Smith, 2002):

a) Get the complete datasets; for example it could be composed by two variables.
b) Subtract the mean from each of the data dimensions. The mean subtracted is the average across each dimension.
c) Calculate the Covariance matrix (CM)
d) Calculate the eigenvectors and eigenvalues of the covariance matrix. It is important to notice that these eigenvectors are both unit eigenvectors and their lengths are both 1. This aforementioned process, can be considered as the key process of PCA because, it characterizes the extracted data.
e) Choose components and form a feature vector. In this passage, the reduction of data dimensions came out. In fact, it turns out that the eigenvector with the highest eigenvalue is the Principal Component (PC) of the dataset. From a general, point of view, once eigenvectors are found from the covariance matrix, the next step is to order them by eigenvalue, from highest to lowest. This process strings the components in order of significance. For these reasons, if the eigenvalues are small only a small amount of information will be lost. To sum up, if the dataset is composed by *n* dimensions, *n* eigenvalue and eigenvector could be calculate, and then only the first *p* eigenvectors will be chosen; in this way the final data set has only *p* dimensions.
f) Form the Row Feature Vector (RFV). It is composed by the eigenvector already taken and it forms a matrix with these eigenvector in the columns.
g) Derive the final data. In order to obtain the final data, the transpose of the matrix must be calculated and it must be multiplied for the original data set. This can be summarized by the eq. 2.5:

(2.5)

Where:

$$\mathbf{FD} = RFV * RDA$$

RFV= It is the matrix with the eigenvectors in the columns *transposed* so that the eigenvectors are now in the rows; the most significant eigenvector at the top.

RDA=it is the mean-adjusted *transposed* data.

FD= it is the final data set, with data items in columns and their dimensions along rows.

Performing this process, the data are now expressed in terms of the chosen vectors; using the aforementioned approach it is possible to understand the correlation between data and the percentage of information given by each dataset (Jolliffe *et al*., 2016). All of the aforesaid steps can be done quickly using a GIS based software (ArcGIS, QGIS).

2.5.2 Cluster Analysis (CA)

CA is known as an unsupervised classification, which covers all classification techniques relying only on input data and not biased by the desired output (Coleou *et al*., 2003). Its simplicity of implementation often makes it selected for multivariate statistical analysis. The object of CA is to identify subclouds within the N-dimensional crossplot (Cormack, 1971). Davis (2000,p.487) describes the CA as follows: "*Cluster analysis includes a series of advanced algorithms that define natural groupings in bodies of multivariate data such that each one is more or less homogeneous and distinct from others*". It has been applied in different frames: from analysis of Quasar spectra (Marss *et al*., 2017) to biomarkers analysis applied to chronical rhinosinusitis (Tommasen *et al*., 2016). The description of cluster analysis principles can start from the query if there are any groups as shown by the fig. 2.2.

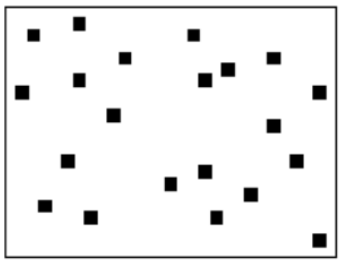

Fig.2.2 There are any clusters here? (Modified from Todeschini, 1998)

The basic principle is the search of not casual structures present in the data; In the CA classes are not known *a priori*: on the contrary, the main goal is to find the presence of groups (Todeschini, 1998). If at the end of CA process is possible to give a meaning to the identified groups, they could be described as classes (Gazley *et al*., 2015). The most common methods of CA use the Distance Matrix (DM). The DM (symmetric) is defined as the matrix of size n x n (where n is the number of objects), wherein in each row (an object) there are all the distances of the other objects from that considered (the diagonal elements of this matrix are equal to zero, i.e. the distance of each object from itself is nothing). Then, the algorithm used by a particular method may request the conversion of DM in a similarity matrix (SM). The SM is a symmetric square matrix, whose diagonal elements are equal to one. Each cluster is characterized by its position in the p-dimensions space and by the so called centroids which can be described as the mean vector calculated for

each object assigned to the cluster. In addition, each cluster is characterized by the number of objects that contains, by the compactness of the objects around the centroid (defined by the standard deviation referred to the centroid) and by its form in the space p-dimensional. Fig. 2.3 shows three different types of cluster, spherical cluster, oblique cluster, sparse objects cluster.

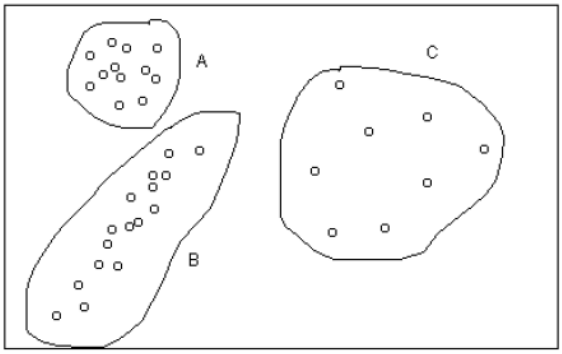

Fig. 2.3 (A) Spherical cluster, (B) oblique cluster, (C) sparse object cluster (Modified from Todeschini, 1998)

The first step to perform a CA is to choose the appropriate type of distance (for example, the Euclidean distance), then calculate the matrix of the distances. After that, applying the clustering algorithm, it is possible to obtain the partitioning of object in clusters (Jain, 2010). The interpretation of each cluster leads to identification of classes. This process is reported in fig.2.4.

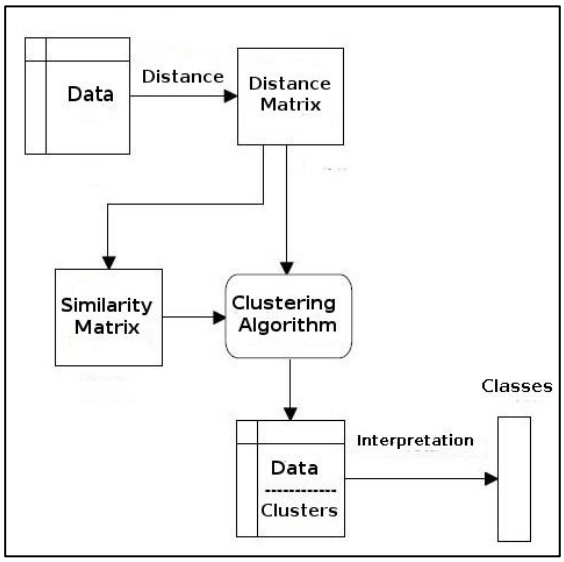

Fig. 2.4 CA Flowchart (Modified from Todeschini, 1998)

One of the most known CA methods is so called k-means (MacQueen, 1967); it is based on an algorithm that compare the difference of each object respect to the geometric center (called centroid) of each cluster. In this type of CA the number of clusters is decided above by the statistician. More in details the algorithm follows these steps (Kvamme, 2007):

a) It places arbitrarily the objects inside a determined number of clusters.
b) It calculates the centroid of each cluster.

c) It measures the distance between each object and each centroid.
d) It assigns each object to the nearest cluster; in this way the Sum of Square Error (SSE) is minimized.
e) If at least one object is moved to a different cluster the point b will be repeated and the process restart until all object are assigned to nearest new cluster.

2.5.3 Bayesian Maximum Entropy (BME)

The Bayesian Maximum Entropy (BME) approach was introduced in 1990 by George Christakos in a work entitled "*A Bayesian/maximum-entropy view to the spatial estimation problem"* BME has the ability to combine data from various sources and of varying quality for spatiotemporal prediction (Christakos, 1990). In other words, BME has the power to incorporate soft data in a spatial analysis. This methodology has been applied to a number of real-world environmental health studies (e.g. Douaik *et al*.,2005; Choi *et al*., 2006; Law *et al.*, 2006; Yu *et al*., 2009; Jat & Serre, 2016; Chen *et al*.,2018). According to Serre (1999), "*The double epistemological goal of BME is informativeness (prior information maximization given general knowledge) and cogency (posterior probability maximization given specificatory knowledge*". The main principle of BME is that the Knowledge (**K**) of a surveyed area is the union of General Knowledge base (*G*) and the Site Specific Knowledge (*S*). Thus, **K**= G *U* S. The General Knowledge (G) can be describe as results obtained from physical known laws, scientific theories, summary statistics etc (Christakos, 2000). "G" can be also divided in two main categories:

- Analytic knowledge which involves logical relation (like "soil permeability values are nonnegative")
- Synthetic knowledge which involves statements of fact and physical law (like F=m·a)

The site-specific knowledge "S" (also called "case-specific knowledge") is related to the specific situation (e.g. samples of rocks collect in the field). The bulk of Site-specific knowledge consists in a datasets representing natural variables. In the frame of geostatistics, the data regarding the site-specific knowledge can be divided in two categories (Christakos, 2000):

- *Hard data* which are can be described as data obtained with the help of instrument which are considered accurate. In the real world, these means that the error during the acquisition process can be controlled (e.g. Bevington & Robison, 1992).
- *Soft data* which represent data expressed in terms of intervals of values, probability statements, empirical correlations (e.g. D'Or *et al*., 2001).

The epistemic approach on which the BME is based upon concerns three major stages of integration that are summarized below. In the first stage, called prior stage, the basic assumptions are given and the form of a prior probability density function is derived such that its entropy is maximized subject to the general knowledge available (Serre, 1999; Bogaert & D'Or, 2002). The second stage, called the meta-prior or pre-

posterior stage, considers the specificatory knowledge composed of both the hard and soft data (Serre, 1999). The third and final stage is the integration or posterior stage (Serre, 1999). Both knowledge bases are considered in this stage, and the goal is to maximize the posterior probability given both the general knowledge and the specificatory knowledge (Serre & Christakos, 1999). Using Bayesian conditionalization to update the prior probability distribution function with respect to the specific data collected, the posterior probability density function is derived. This posterior distribution provides the BME prediction (Christakos, 2000; Christakos *et al*., 2001).

Now we would to better investigate the stages above cited.

1) *The Prior Stage*. In this stage the probability function considered is relative to the general knowledge ***G***. These can be expressed by eq.2.6

   (2.6) $$\text{Prob}_G[\boldsymbol{\chi}_{\mathbf{map}}] = p \in [0,1]$$

   which means " the probability of the map $\boldsymbol{\chi}_{\mathbf{map}}=(\chi_{\text{data}},\chi_k)$ given the general knowledge base G is *p*, where 0 means minimum probability and 1 means maximum probability". Another way of expressing the meaning of the aforementioned equation is by saying that probability about $\boldsymbol{\chi}_{\mathbf{map}}$ are relative to knowledge ***G*** (Christakos, 2000 p.92).
2) *The meta-prior stage*. In this stage, we collect and organize the site Specific knowledge S that can be easily incorporated to the BME process. S includes site-specific evidence or empirical statement that in the following stage will be fused with the general knowledge.
3) *The integration or posterior stage*. In this stage the new probability function is related to the total knowledge K expressed by eq.2.7:

   (2.7) $$\text{Prob}_K[\boldsymbol{\chi}_{\mathbf{k}}] = p' \in [0,1].$$

This equation means that the probability of a map $\boldsymbol{\chi}_{\mathbf{k}}$ given the total knowledge base **K**=G *U* S is *p'* in which 0 means minimum probability whereas 1 means maximum probability. The probability function assumes a connection between mapping probability and the available knowledge. Thus, as reported by Christakos, 2000 p.95 "*the probability is epistemic, supported by empirical data and related to the inductive evidence*". It should be stressed that while at the prior stage the probability (eq.2.6) refers to the whole domain (including data and estimation points) e.g. $\mathbf{P}_{\mathbf{map}}=(\mathbf{P}_{\mathbf{map}},\mathbf{P}_{\mathbf{k}})$, the probability of the posterior stage includes only estimation points $\mathbf{P}_{\mathbf{k}}$.

The BME approach is summarized in fig.2.5

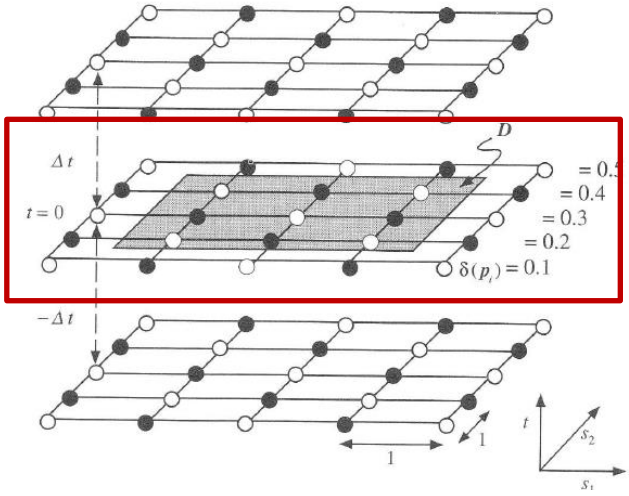

Fig.2.5 Visual approach to BME, black points represents hard data, white points soft data (Christakos, 2000)

Solid circles represents hard data obtained at space/ time point p=(s1,s2,t), white circles represents soft data in form of observation interval. Estimates are sought at points within region D. It should be stressed that in our work we use static data, thus t=0 (red square in fig.2.5).

Chapter III- Theory of Geophysical methods

3.1 The magnetic method

3.1.1 Introduction

The magnetic method is classified as passive geophysical method because it just measures the Earth Magnetic Field as Potential Field (Norinelli, 1999). The aim of a magnetic prospection is to study the buried structures based on magnetic differences between the buried targets and the surrounding soil (Witten, 2006).

If we consider a magnet bar (fig.3.1), the Coulomb's law describes the pole strength as described by eq.3.1:

$$\mathbf{F} = \mathrm{C}\frac{p_1\ p_2}{r^2} \quad (3.1)$$

where p_1,p_2 are the poles strengths

C is a constant of Coulomb which value is $9{\cdot}10^9$ Nm^2/C^2.

r is the distance between poles.

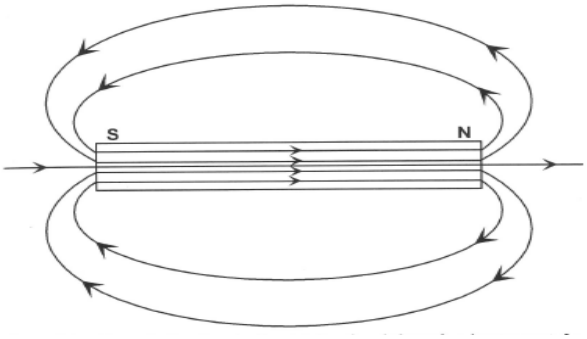

Fig.3.1 Magnetic field lines in magnet bar (Aspinal *et al*., 2009)

More often, we refer to magnetic flux density (**B**) which is a vector having magnitude and direction usually oriented in the direction of pole N.

B is expressed by the eq. 3.2

$$\mathbf{B} = \mathrm{C}\frac{p}{r^2} \quad (3.2)$$

Any magnet has two poles of straight which are equal and opposite, thus the B can be calculate using a vector sum (eq.3.3).

$$\boldsymbol{B_1} = +\mathrm{C}\frac{p}{r_1^2} \quad (3.3)$$

and

$$\boldsymbol{B_2} = -\mathrm{C}\frac{p}{r_2^2} \quad (3.4)$$

The fig.3.2 shows a magnetic field **H** created by a loop of radius r and electric intensity I.

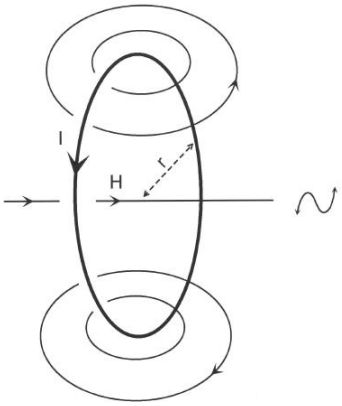

Fig. 3.2 Magnetic field H created by a loop of radius r and intensity I (Aspinal *et al.*, 2009)

The magnitude of magnetic field will be (eq.3.5):

(3.5) $$\mathbf{H} = \frac{I}{2r}$$

where:

H= Magnitude of magnetic field

I = intensity of power

r = radius of loop

Comparing the figure 3.1 and 3.2, it is possible to describe (eq. 3.6) the magnetic moment (***m***)

(3.6) $$\boldsymbol{m = I * A}$$

Where

I = Intensity of power

A=Area of the loop

In air **H** and B can be considered as equal unless a proportional factor ($\mu_0 = 4\pi * 10^{-7}$ TmA^{-1}), thus:

(3.7) $$\mathbf{B} = \mu_0 * \mathbf{H}$$

If a medium is present the eq.3.7 became (eq.3.8):

(3.8) $$\mathbf{B} = \mu_R \mu_0 * \mathbf{H}$$

where

μ_R= magnetic permeability of the medium

The intensity of magnetization M created in the medium by H can be expressed by eq.3.9:

(3.9) $$\mathbf{M} = \frac{\mathrm{m}}{\mathrm{l}} * \mathrm{A}$$

where

m=induced magnetic moment

l= specimen length

A=area of the pole face

Clearly, the magnitude of **M** is dependent by **H**, thus is possible to write the eq.3.10:

(3.10) $$\mathbf{M} = k * \mathbf{H}$$

where *k* is magnetic susceptibility and it can be described as the propriety to a material to be attracted to a magnetic field.

The table 3.1 shows the *k* values for some minerals (e.g. Aspinal, 2009; Leucci, 2015)

Mineral	***k* (10^3)**	**Mineral**	**k(10^3)**
Graphite	0.1	Calcite	-0.0001/-0.1
Limonite	2.5	Ilmenite	300-3500
Quartz	-0.01	Pyrite	0.05-5
Hematite	0.5-35	Magnetite	1200-19200
Pyrrhotite	1-6000	Sphalerite	0.7

Table 3.1 *k* values for most common minerals (modified from Leucci, 2015)

Minerals have different values of *k*; it is due to magnetic field behavior formed by electrons. These magnetic fields can overlap or oppose to the external magnetic field (Witten, 2006).

3.1.2 Magnetic behaviors of materials

Referring on their different behaviors (fig. 3.3), materials can be classified into four groups (Witten, 2006):

Diamagnetic materials: They create an induced magnetic field opposite to an external applied magnetic field. Their susceptibility values are low and often negative (fig.3.3a).

Paramagnetic materials: They create an induced magnetic field overlapping an external applied magnetic field. Their *k* values are positive but low (fig.3.3b).

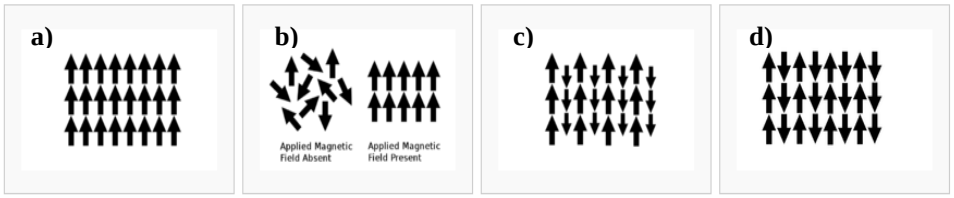

Fig. 3.3 Orientations of magnetic moments in materials. a) ferromagnetic b)Paramagnetic c)Ferrimagnetic d) Antiferrimagnetic (Modified from Aspinal *et al.*,2009)

Ferromagnetic materials: they have a strong spontaneous magnetization and for this reason, they have higher k value. The magnetization degree of ferromagnetic material decreases when temperature increases; at Curie temperature (Tc) it became similar to paramagnetic material (fig.3.3c).

Antiferromagnetic materials: They, (e.g. Hematite), don't produce an induced magnetic field even if they are inside an external magnetic field (fig.3.3d).

Magnetization of materials could happen by different methods (Aspinal *et al*.,2009):

- *Induced Magnetization*

The IM occurs when there is a difference between a specific material and the soil around it, It will show induced magnetization in the direction of earth field (eq. 3.11).

$$\boldsymbol{\Delta k} = \mathrm{k}_{\mathrm{feature}} - \mathrm{k}_{\mathrm{soil}} \quad \textbf{(3.11)}$$

- *Thermal Remanent Magnetization (TRM*)

This type of magnetization occurs when igneous rock starts cooling and the temperature is above the Curie temperature (T<Tc). The materials lose magnetic order and they become paramagnetic, so that their magnetic moments can readily align with the ambient magnetic flux density. Once the material has cooled below Tc, the magnetic order appears again.

- *Chemical Remanent Magnetization (CRM)*

This magnetization occurs when grains precipitate from a solution or they are formed during chemical reactions and the grains record the direction of the magnetic field at the time of mineral formation.

- *Depositional remanent magnetization (DRM)*

DRM is formed in clastic sediments when fine particles are deposited on the bottom of a water column. The Earth Magnetic Field aligns the grains, yielding a preferred direction of magnetization. In the frame of an archeological prospection, buried structures like foundations, streets or floorings can generate magnetic anomalies which are influenced by magnetic characteristics between materials and surrounding soil. Weston (2002) shows that topsoil influenced by anthropic factor has high concentration of iron oxides that can modify magnetic susceptibility. The most relevant iron oxides for archeological prospection are hematite (α–Fe_2O_3), magnetite (Fe_3O_4) and maghemite (γ–Fe_2O_3).

In table 3.2, *k* values for the major class of rocks are shown (Reynolds, 2011)

Rock	**k (10^3)**
Dolomite	0-0.9
Limestone	0-3
Sandstone	0-20

Amphibolite	0.7
Shale	0.3-3
Gneiss	0.1-25
Quartzite	4
Granite	0-50
Rhyolite	0.2-35
Syenite	30-40
Basalt	0.2-175
Diorite	0.6-120
Andesite	160
Gabbro	1-90

Table 3.2 *k* values for the most common rocks (Reynolds, 2011)

Table 3.2 shows that igneous rocks have higher values of *k* than sedimentary or metamorphic rocks; this is caused by high percentage of magnetite (Aspinal *et al*., 2009). The presence of magnetite is strictly dependent on acid/basic ratio of the rocks (Reynolds, 2011). Very often foundations and dugouts can generate anomalies caused by filling material which are very rich with ferromagnetic minerals. Sometimes, if an organic matter is present, bacterial activity could also generate magnetite or maghemite (Aspinal *et al*., 2009).

Table 3.3 reports some *k* values for the most common archeological materials (Aspinal *et al*.,2009)

Archeologic material	**k (10^{-5})**
Limestone walls	0-20
Lateritic walls	80-210
Fragment of amphora	700-1200
Subsoil	25-60
Soil	15-45

Table 3.3 k values for the most common archeological materials (Aspinal *et al*., 2009)

3.1.3 The Earth Magnetic Field (e. m. f.)

To a first approximation, the general trend of E.M.F. can be considered quite similar to a magnetic dipole located in the earth core (fig. 3.4).

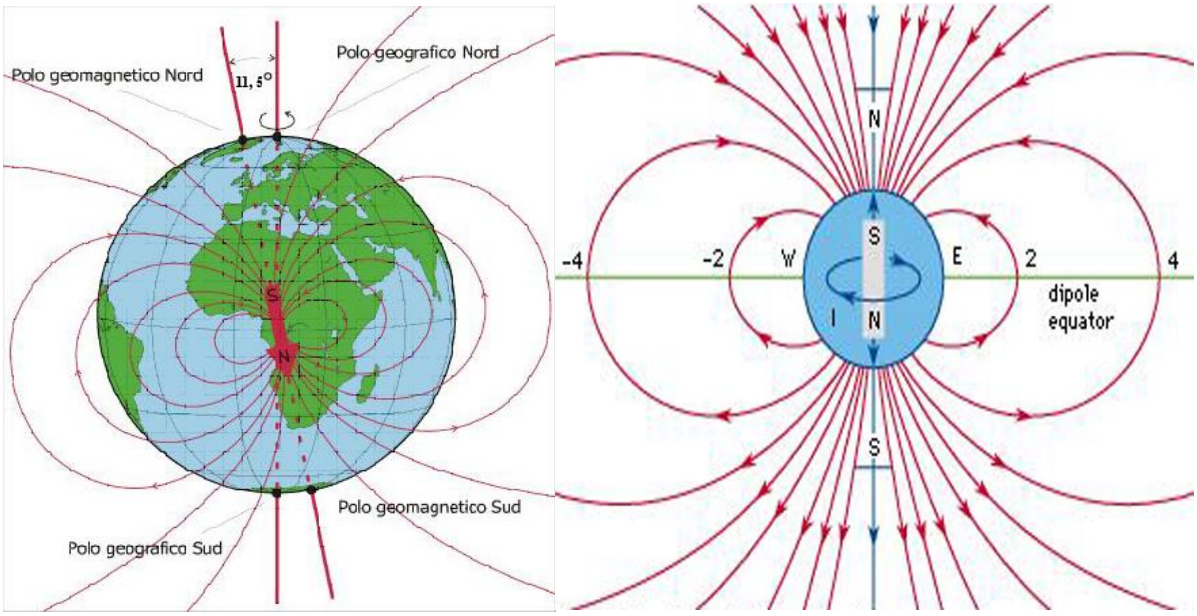

Fig. 3.4 Earth magnetic field (Modified from Piro, 2012)

Actually the 94% of earth magnetic field is dipolar; the other 6% is non-polar and it is related to three different sources, reported below (McElhinny *et al*., 1998):

- The earth crust; it takes origin from magnetized rocks
- Electric power which are present in ionosphere and magnetosphere; they take origin from interaction between solar wind and E.M.F.
- Electromagnetic induction phenomena which takes origin from the shallow mantle.

The dipole source has the following characteristics:

M=8-10^{22}Am^2 and inclination of 11 degree respect to earth rotation axis. The dipole axis intersects the earth surface in two points which are known as a "geomagnetic poles". Furthermore, the magnetic poles don't match with the dipole poles and the magnetic equator doesn't match with terrestrial equator (fig.3.4) (Kearey *et al*., 2013).

The geomagnetic field is formed by the coordinates X, Y, Z, the magnitude F, the horizontal component H, the inclination I and the declination D.

These parameters are linked each other by eq.3.12:

(3.12) $$\mathbf{F} = \sqrt{(x^2 + y^2 + z^2)} = \sqrt{H^2 + Z^2}$$

and

(3.13) $$\tan I = \frac{Z}{H}; X = H\cos D; Y = H\sin D; Z = F\sin I$$

thus

(3.14) $$\tan I = 2\tan\varphi$$

where φ is the geocentric latitude.

To measure the e.m.f. and their components, four types of magnetometers exist (see Kearey *et al*., 2013) which are: Fluxgate magnetometer, proton magnetometer, Optically Pumped Potassium Magnetometers and magnetic gradiometers. In this section only the fluxgate magnetometer will be briefly described because it has been used during the survey. This type of magnetometers have been developed in the frame of II World War in the detection of submarines from the air (Kearey *et al*., 2013). It uses the inverse of the magnetic dipole induced in a ferromagnetic rod by an electrical current flowing thought a wire would around the rod. When a ferromagnetic rod is exposed to an external magnetic field a dipole moment is induced inside the rod. The magnetic field produced by this induced magnetized rods, induces an electrical current in a coil of wire that is coiled around the rod. This induced current can be measured and it is proportional to the strength of the component of the external magnetic induction along the direction parallel to the axis of the rod (fig.3.5). The fluxgate magnetometer measures the vector of magnetic field along the axis of the magnetometer rods, thus they can be considered as a vector instruments.

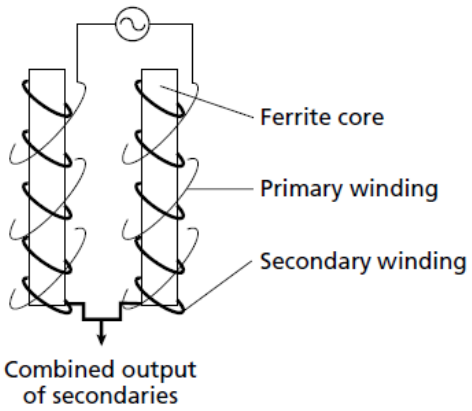

Fig.3.5 Scheme of a Fluxgate magnetometer (modified from Kearey *et al*., 2013)

3.2 Ground Penetrating Radar (GPR)

3.2.1 Introduction

In the frame of near surface geophysical methods, one of the best tools in term of spatial resolution, fast acquisition time, extension of the investigated area and repeatability of the measurements is the Ground Penetrating Radar (GPR) (e.g. Conyers & Goodman, 1997; Goodman & Piro, 2013). A GPR transmitter emits electromagnetic (EM) energy into the ground; when the EM waves encounter a buried target or a boundary between materials with different dielectric proprieties, it is reflected back to the surface. A receiving antenna can then record the variations in the return signal (Conyers & Goodman, 1997, Jol, 2008- fig.3.6).

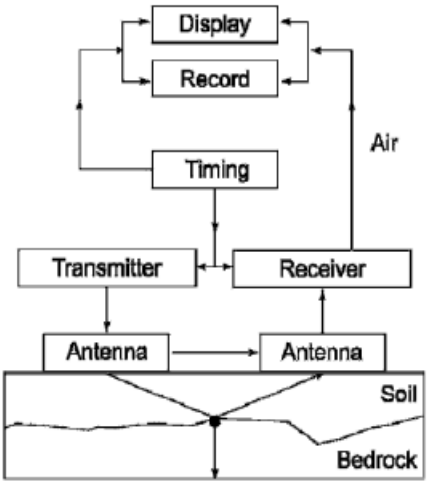

Fig.3.6 Foundation of GPR (Jol, 2008)

The foundations of GPR is related to EM theory described by Maxwell's equations (Annan, 2005). Thus we have:

(3.15) $$\nabla \mathbf{x} \mathbf{E} = -\frac{\partial b}{\partial t}$$

(3.16) $$\nabla \mathbf{x} \mathbf{H} = \mathbf{j} + \frac{\partial D}{\partial t}$$

(3.17) $$\nabla \cdot \mathbf{D} = \boldsymbol{\rho}$$

(3.18) $$\nabla \cdot \mathbf{B} = \mathbf{0}$$

where:

E and ***H*** are the electric and magnetic fields intensity,

B is the magnetic flux density vector,

D is the electric displacement vector,

J is the electric current density vector,

ρ is the electric charge density,

t is the time.

These fields interact with the surrounding media; where this interaction is macroscopically it is described by the following equations (Annan, 2005):

(3.19) $$\mathbf{J} = \boldsymbol{\sigma} \mathbf{E}$$

(3.20) $$\mathbf{D} = \boldsymbol{\varepsilon} \mathbf{E}$$

(3.21) $$\mathbf{B} = \boldsymbol{\mu} \mathbf{H}$$

(3.21bis) $$\mathbf{M} = \mathbf{kH}$$

From a general point of view, the equations above describe the response of subsoil to electromagnetic input. Two of them describe the relationship between the electric field *E* and the conductive current *J*, the electric displacement *D*. The other two describe the relationship between the magnetic field *H*, the magnetic induction *B* and the magnetic polarization *M*. The dielectric permittivity ε, the electric conductivity σ, the magnetic permeability μ and the magnetic susceptibility k are the four constitutive parameters that describe the electromagnetic properties of a material (Daniels, 2004).

3.2.2 Electromagnetic propriety of subsoil

Referring to the previous paragraph, we can affirm that EM wave propagation is controlled by the electromagnetic proprieties of the ground (Annan, 2005). The complex dielectric permeability is presented by the following equation:

(3.22) $$\boldsymbol{\varepsilon} = \boldsymbol{\varepsilon}' - \boldsymbol{i}\boldsymbol{\varepsilon}''$$

The relative complex magnetic permeability:

(3.23) $$\boldsymbol{\mu} = \boldsymbol{\mu}' + \boldsymbol{i}\boldsymbol{\mu}''$$

And the relative complex conductivity:

(3.24) $$\boldsymbol{\sigma} = \boldsymbol{\sigma}' + \boldsymbol{i}\boldsymbol{\sigma}''$$

The real electric permittivity ε and the real magnetic permeability μ are written as follow:

(3.25) $$\boldsymbol{\varepsilon} = \boldsymbol{\varepsilon_0}\boldsymbol{\varepsilon_r} \text{ and } \boldsymbol{\mu} = \boldsymbol{\mu_0}\boldsymbol{\mu_r}$$

with ε_0 and μ_0 defined respectively as the dielectric permittivity and magnetic permeability in free space; r is the relative permeability and relative permittivity.

The key parameters of EM wave propagation are velocity of the wave in the soil (**v**), attenuation (**α**), and electromagnetic impedance (**Z**). The **v** (in a homogenous material) is descripted by eq. 3.26 (Jol, 2008):

(3.26) $$\mathbf{v} = \frac{\sqrt{2}}{\left(\sqrt{\mu'^2 + \mu''^2}\sqrt{\varepsilon'^2 + \varepsilon''^2} + \varepsilon'\mu' - \varepsilon''\mu''\right)^{\frac{1}{2}}}$$

In a low loss soil the equation became (Conyers, 2009; Leucci, 2015)

(3.27) $$\mathbf{v} = \frac{C}{\sqrt{\varepsilon_r \mu_r}}$$

In which **c** is EM the velocity in free space;

The attenuation factor (**α**) is given by:

(3.28)

$$\boldsymbol{\alpha} = \frac{\sigma}{2}\sqrt{\frac{\mu}{\varepsilon}}$$

where **σ** is the conductivity.

When an EM wave travels in the subsoil, it is reflected by changes in impedance (**Z**) described by eq.3.29

(3.29)

$$\mathbf{Z} = \sqrt{\frac{\mu}{\varepsilon}}$$

The reflection coefficient between the adjacent layers characterized by Z_1 and Z_2 is:

(3.30)

$$\mathbf{R} = \frac{Z_2 - Z_1}{Z_2 + Z_1}$$

where R is the reflection coefficient for normal incidence on a planar surface.

The eq.3.30 became (eq. 3.31)

(3.31)

$$\mathbf{R} = \frac{\sqrt{\varepsilon_2} - \sqrt{\varepsilon_1}}{\sqrt{\varepsilon_2} + \sqrt{\varepsilon_1}}$$

If we assume the magnetic permittivity μ equal in value to its value on the free space ($\mu_0 = 4 \times 10^{-7}$ H/m) as often occur in near surface applications (Annan,2005).

3.2.3 GPR fundamentals

As described briefly before, GPR uses EM waves emitted from a source in order to detect buried structures as well their position (Conyers & Goodman, 1997). A buried target, in order to be detected, must re-emit some of the waves energy received (Annan & Cosway, 1994; Leucci, 2015). This process requires a strong contrast in electrical proprieties between the target and the surrounding material (Conyers & Goodman, 1997). Changing in electrical permittivity and electrical conductivity provoke scattering of EM energy, thus detecting this scattered energy is possible to detect and find the position of the source of this scattered energy (Annan & Cosway, 1994). The dielectric permittivity ε_r of a soil describes its ability to polarize in presence of an EM field (Von Hippel, 1954). The value of ε_r can vary a lot between materials as shown by table 3.4.

Table 3.1. Typical Relative Dielectric Permittivities (RDPs) of Common Geological Materials

Material	*RDP*
Air	1
Dry sand	3–5
Dry silt	3–30
Ice	3–4
Asphalt	3–5
Volcanic ash/pumice	4–7
Limestone	4–8
Granite	4–6
Permafrost	4–5
Coal	4–5
Shale	5–15
Clay	5–40
Concrete	6
Saturated silt	10–40
Dry sandy coastal land	10
Average organic-rich surface soil	12
Marsh or forested land	12
Organic-rich agricultural land	15
Saturated sand	20–30
Fresh water	80
Sea water	81–88

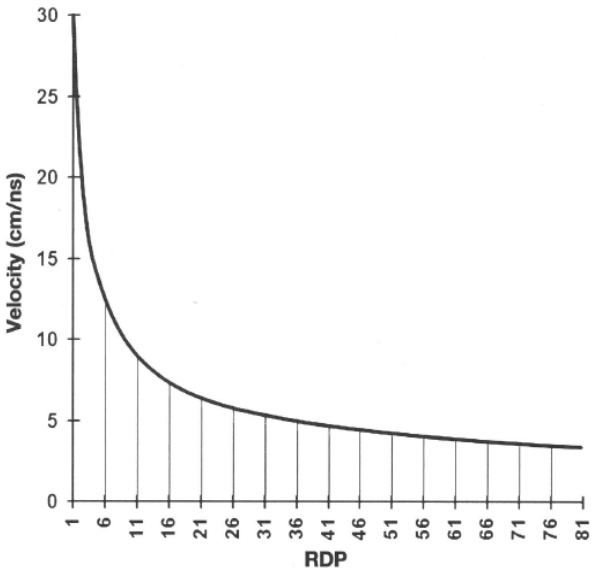

Table 3.4 ε values from the most common subsoil; fig. 3.7. Relationship between radar travel velocity and ε (Conyers & Goodman, 1997)

It is also known that the ε is inversely related to the radar travel velocity (Conyers & Goodman, 1997-fig. 3.7). The EM energy doesn't penetrate in steel; in fact a steel item reflects the 100% of EM energy (Conyers & Goodman, 1997).The main physical behavior is the delay between the time for the source to emit the wave signal and the time for the detector to receive the signal echoes back; the travel time of a EM waves through the subsoil and the return back to the receiving antenna is in order of a few tens to several thousand nanoseconds (Reynolds, 2011).

This time delay (**t**) is expressed by the eq. 3.32 (Conyers & Goodman, 1997; Leucci, 2015):

(3.32) $$\mathbf{t} = \frac{2d}{v}$$

Where **d** is the distance from the target and **v** is the speed of waves in the host medium (Conyers & Goodman, 1997; Leucci, 2015). Basically, assuming uniform velocity conditions, larger is the time delay, greater will be the distance to the target, (Conyers & Goodman, 1997, Daniels, 2004).

For most GPR survey the velocity is expressed by eq.3.33.

(3.33) $$\mathbf{v} = \frac{2C}{\sqrt{\varepsilon_r}}$$

where C is the speed of light

When, during a GPR survey, a target is encountered, a reflection hyperbola caused by the different dielectric proprieties between the target itself and the surrounding media, is formed. More in details, the hyperbolas are formed because radar energy is reflected by buried structured that are not located directly below the transmitting antenna. As the transmitter antenna moves closer to the buried target, the receiver antenna continues to record reflection from the point source before to arrive directly on the top and it will continue to record also when the item has been overcame (Conyers & Goodman, 1997-fig.3.8).

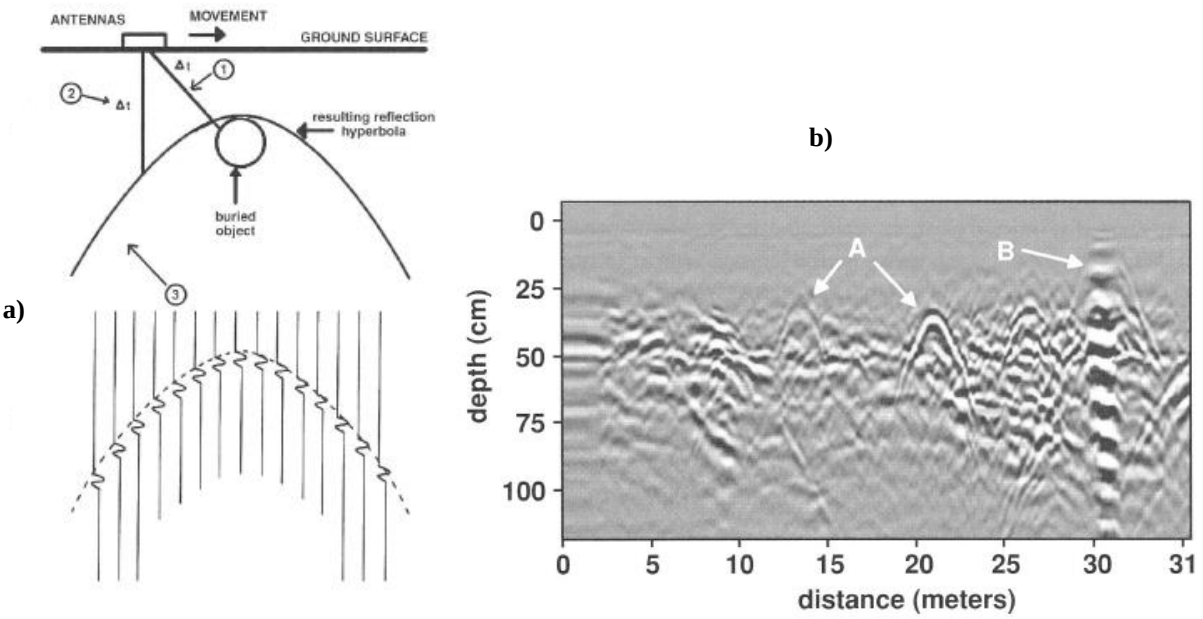

Fig. 3.8 a) Generation of a reflection hyperbola ; b) A radargram in which two hyperbolas (A and B) are shown (Coyners & Goodman,1997)

When a GPR survey has to be done, two main parameters must be considered:

- The amount of attenuation (α)
- The depth of investigation vs resolution

The attenuation is proportional to the electrical conductivity; thus the higher the electrical conductivity is, the higher the attenuation will be. σ increases with the presence of water, soluble salt, and clay contents as reported by McNeill (1980).

In soils, the most important energy losses related to conduction-based, are due to ionic charge transport in the soil solution and electrochemical processes associated with cations on clay minerals (Neal, 2004).

Morey (1974) gives a mathematical equation for the α (eq.3.34)

(3.34)

$$\alpha = 12.836 * 10^{-8} f \sqrt{\varepsilon_r} \sqrt{\left(\sqrt{\tan \delta^2} + 1\right)} - 1$$

where *f* is the frequency of the GPR wave and tan(δ) is the dissipation angle.

δ can be expressed by eq. 3.35:

(3.35)

$$\delta = \frac{\sigma}{2\pi f \varepsilon_0 \varepsilon_r}$$

As a second step, it is necessary to consider the relationship between the investigation depth and the resolution which can be defined as "*the ability to distinguish between two closely spaced features (signals)*

from each other" (Conyers & Goodman,1997). The resolution is function of the frequency (*f*), the wavelength (λ) and v:

(3.36)
$$\lambda = \frac{v}{f}$$

Thus, an increase in *f* (decrease in λ) enhances the resolution, but decreases the investigation depth and vice versa (e.g. Conyers & Goodman, 1997; Leucci, 2015). The resolution is divided by vertical and horizontal resolution (e.g. Daniels, 2004). The vertical resolution is the ability to the system to see the top and the bottom of reflection surfaces located at different depth (Coyners & Goodman, 1997). Sheriff & Geldart, (1982) report that, from a theoretical point of view, in order to detect two reflection surfaces located at different depth, the distance between them should be more than 1/4 λ. If two reflections occur at an distance less than 1/4λ, destructive interference will be formed; on the other hand, if the distant is more than 1/4λ, two different reflection will be formed and the target will be completely seen (Coyners & Goodman, 1997-fig.3.9)

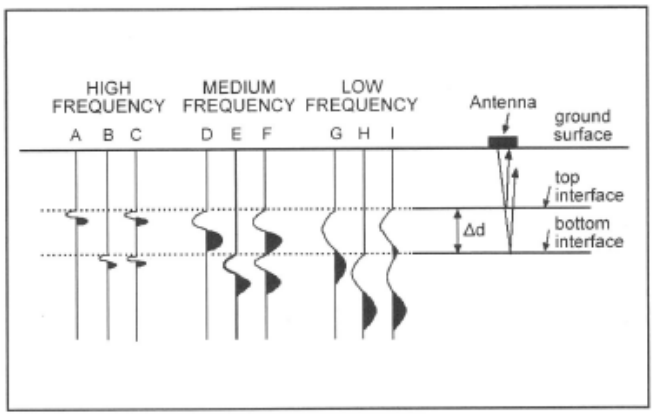

Fig. 3.9 Resolution of the top and bottom of an interface to different frequencies. At high frequencies the waves define both the top (A) that the bottom (B) of the interface. The resultant wave from these reflections can resolve both interface because the distance between the two is larger than the wavelength. The wave of average wavelength (D) resolve both the top and the bottom of interface (E), the resultant wave (F) can solve the two interfaces just because its wavelength is similar to Δd. The low *f* wave solve the top of the interfaces (G) just because Δd is smaller than λ (H) and the resultant wave (I) can solve only the top of the interfaces (Coyners & Goodman, 1997; Leucci, 2015)

The horizontal resolution (Δx) can be defined as the ability to the system to detect two different targets located at the same depth (Conyers &Goodman, 1997; Annan, 2005). Δx is related to different parameters like the *f* of antenna, the type of target and GPR velocity of on the field; it can be expressed by the eq.3.37 (Roberts & Daniels, 1996):

(3.37)
$$\Delta x = 4d\sqrt{\frac{ln2}{2+ad}}$$

where d is the depth of the target and α is amount of the attenuation.

About the horizontal resolution, it is also related to the area illuminated by the GPR antennas (called antenna *footprint*).

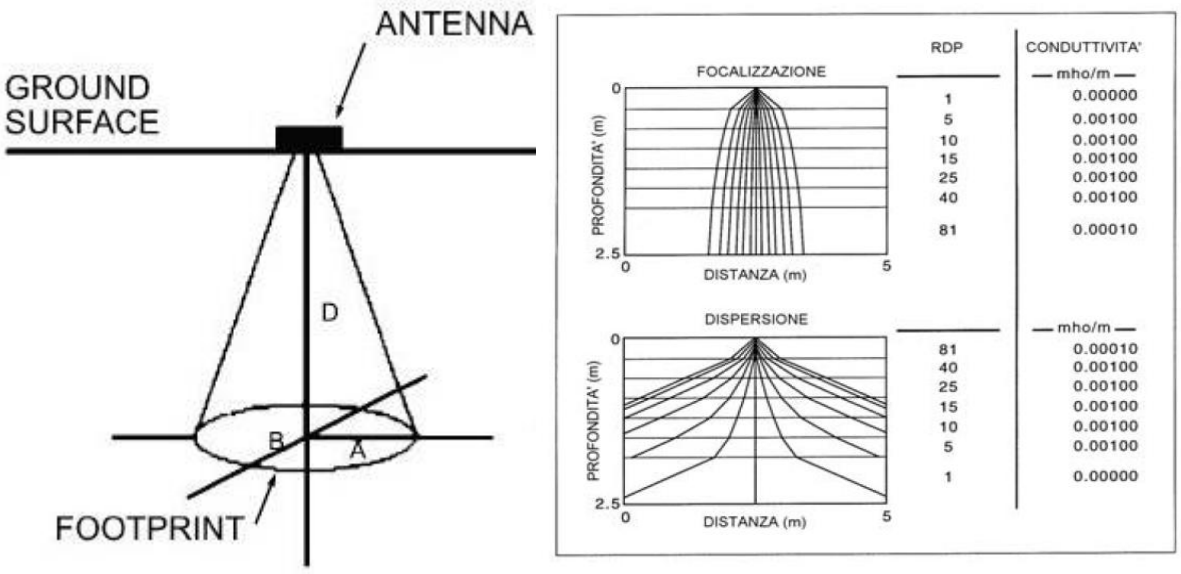

Fig.3.10 (a) Conical spreading of GPR waves, (B) Energy focusing with depth (Conyers & Goodman, 1997)

Fig.3.10 shows that the footprint has an elliptical shape and it increases with depth. According to Annan & Cosway (1992), the footprint dimension can be estimate as follow:

(3.38) $$\mathbf{A} = \frac{\lambda}{4} + \frac{D}{\sqrt{\varepsilon_r - 1}}$$

(3.39) $$\mathbf{B} = \frac{\mathbf{A}}{2}$$

where A is the long axis diameter of the round-shape footprint, B is the short axis diameter, D is the depth and ε_r is the dielectric constant of the subsoil. Conyers & Goodman (1997) report that for higher λ values a bigger footprint which lead lower resolution and vice versa, will be formed. The dimension of transmission cone is also related to value of ε_r; if ε_r increases from the top to the bottom of the subsoil, the energy of the transmission cone will be dispersed and vice versa (Conyers and Goodman 1997; Conyers, 2009, Leucci, 2015). In order to increase resolution, the frequency at which the EM pulse generated must be increased; In fact, as affirmed by Daniels (2004), higher frequency pulses have shorter wavelengths and can be image smaller subsurface features. Thus, in order to increase the depth of investigation, lower frequencies of EM pulses are needed (Daniels, 2004).

3.3 Electrical Resistivity Tomography (ERT)

3.3.1 Introduction

Following the opinion of Loke (2004) "*The purpose of electrical surveys is to determine the subsurface resistivity distribution by making measurements on the ground surface*". Resistivity is related to numerous parameters about the soil like, for example, the mineralogical and fluid contents, the porosity or the saturation degree (e.g. Loke, 2004, Soldovieri, 2006). The resistivity (ρ) of a material is defined in terms of

resistance R between two opposite face of a prism of that material. Each face has an area A and the two faces are separated by a distance I (fig.3.11).

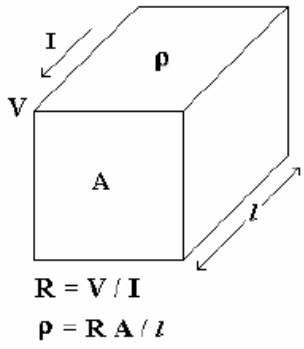

Fig. 3.11 A prism of conductive material (Loke, 2004)

The unit of ρ is Ω∗m.

The ρ value for the most common category of rocks is shown in fig.3.12.

Igneous and metamorphic rocks have often higher resistivity values. The resistivity of these rocks is related to fracturing degree and to water amount in the fractures (Loke, 2004).

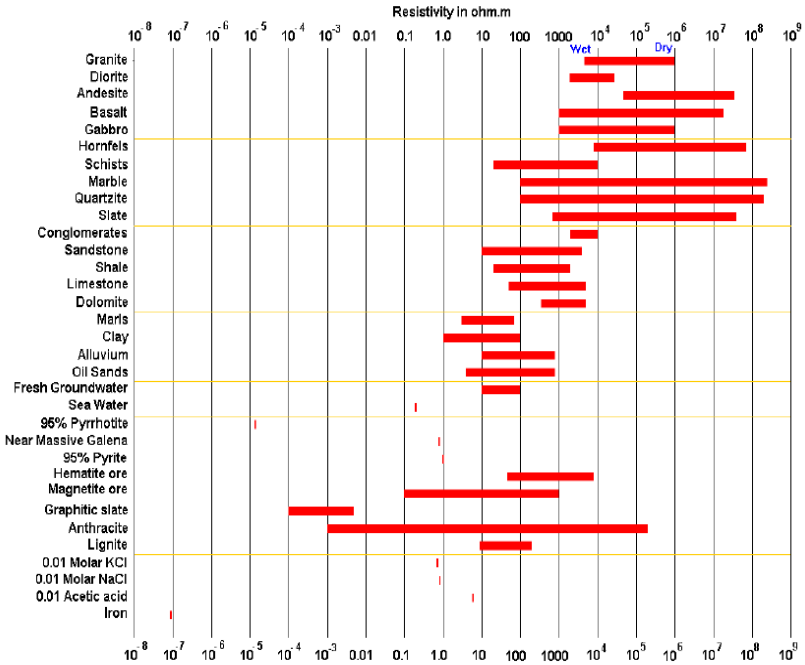

Fig. 3.12 Resistivity values for many natural materials (Loke, 2004)

Referring now to the sedimentary rocks, they have lower resistivity values compared to igneous and metamorphic rocks. Their resistivity values depend on rocks porosity and on the water (Loke, 2004). Clayey soil has a lower resistivity value than sandy soil. The resistivity of groundwater varies from 10 to 100 Ω·m, depending on the concentration of dissolved salts; the low resistivity (about 0.2 Ω·m) of seawater is due to the higher salt content (Loke, 2004).

3.3.2 Potential of homogenous subsoil

Considering now the case of a homogeneous subsurface and a single point power source (A) fixed in to the ground (fig. 3.13)

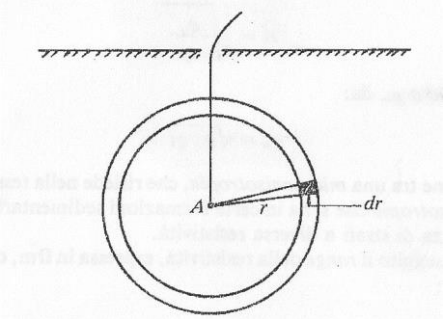

Fig. 3.13 An electrode settled under the ground; the other elements of electric circuit are located far from the system (Norinelli, 1999)

In this case, the power flows are organized radially from the source and equipotential surfaces are concentric respect to the source A. if we consider the equipotential surfaces with radius r and r+dr of fig.3.13 we can write dV as reported by eq.3.40 (Norinelli,1999)

$$dV = -\varrho i dr \tag{3.40}$$

where $i=I/2\pi r^2$ and it is the power intensity related to the soil cylinder; note the minus sign because I decreases from the source A with the distance.

Integrating now from r_1 to ∞, we will obtain the electrical potential in a point called "M" which is expressed by eq.3.41 (Norinelli, 1999):

$$\boldsymbol{V_M} = \frac{\rho I}{2\pi r_1} \tag{3.41}$$

The resistivity measurements are made by injecting power into the ground through the two power electrodes (A and B in fig. 3.14), and measuring the voltage difference at two potential electrodes (M and N): this setting is called quadrupole.

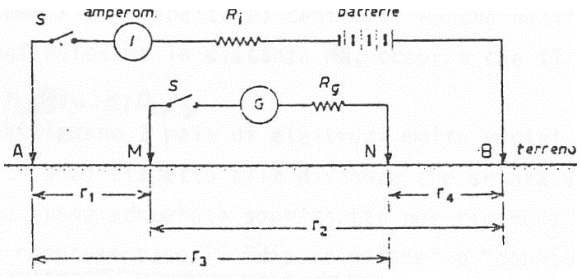

Fig.3.14 a quadruple; A-B are power electrodes pair; M-N are potential electrodes pair (Norinelli, 1999)

Consider now a quadrupole composed by two power electrodes, called A and B, which are located r_1 and r_2 from the point M (fig 3.14). In this frame the V_M will be (eq.3.42):

(3.42) $$\boldsymbol{V_M} = V'_M + V''_M$$

where V'_M+V''_M are potential related to A and B respectively. Thus, considering that I in the A and B flow in opposite direction, V_M is expressed by eq.3.43 (Norinelli, 1999):

(3.43) $$\boldsymbol{V_M} = \frac{\rho I}{2\pi}\left(\frac{1}{r_1} - \frac{1}{r_2}\right)$$

Consider now another potential electrode called "N", V_N is expressed by eq.3.44:

(3.44) $$\boldsymbol{V_N} = \frac{\rho I}{2\pi}\left(\frac{1}{r'_1} - \frac{1}{r'_2}\right)$$

The ΔV between M and N is expressed by eq.3.45:

(3.45) $$\mathbf{\Delta V} = \frac{\rho I}{2\pi}\left(\frac{1}{r_1} - \frac{1}{r_2} - \frac{1}{r'_1} + \frac{1}{r'_2}\right)$$

Now we can write (eq.3.46):

(3.46) $$\mathbf{k} = \frac{2\pi}{\left(\frac{1}{r_1} - \frac{1}{r_2} - \frac{1}{r'_1} + \frac{1}{r'_2}\right)}$$

where *k* is a geometric factor that depends on the arrangement of the four electrodes. Resistivity measurement instruments give a resistance value, $R = \Delta V/I$, so in practice the apparent resistivity value is calculated by eq.3.47:

(3.47) $$\boldsymbol{\rho_{\alpha=}}\ k\frac{\Delta V}{\mathrm{I}}$$

The equation above show and apparent resistivity value which is "*the resistivity of a homogeneous ground that will give the same resistance value for the same electrode arrangement*" (Loke, 2004)

3.3.3 Type of arrays

The most common arrays are the following:

- Wenner
- Pole-dipole
- Schlumberger
- Double dipole (or dipole-dipole)

Each of them have a different *k* equation which is related to the electrode arrangement only (Loke, 2004).

The Wenner array is shown in fig. 3.15 and *k* parameter is reported in eq.3.48

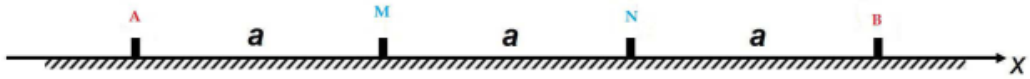

Fig. 3.15 Wenner array (Soldovieri, 2006)

(eq. 3.48)

$$\boldsymbol{k} = 2\pi a$$

The pole-dipole array is shown in fig.3.16 and the *k* parameter is reported in eq.3.49

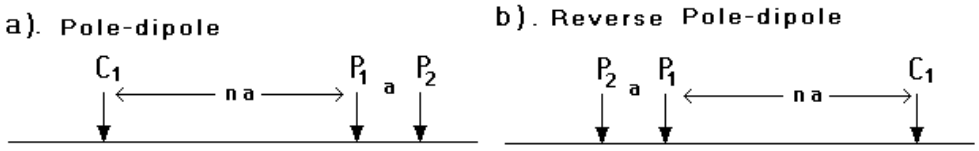

Fig. 3.16 The forward (a) and reverse (b) pole-dipole arrays (Loke, 2004)

(eq. 3.49)

$$\mathbf{k} = \frac{2\pi ab}{(b-a)}$$

The Schlumberger array is shown in fig.3.17 and the *k* parameter is reported in eq.3.50

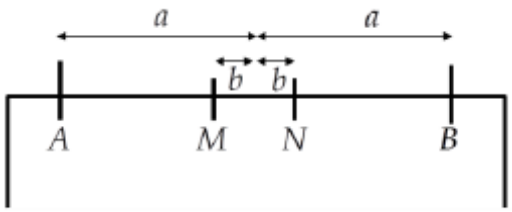

Fig.3.17 Schlumberger array (Piersanti & Della Monica, 2015)

(eq. 3.50)

$$\mathbf{k} = \frac{\pi(a^2 - b^2)}{2b}$$

The double dipole array arrangement is shown in fig.3.18 and the *k* parameter is reported in eq.3.51

Fig. 3.18 Double dipole arrangement (Soldovieri, 2006)

(3.51)

$$\boldsymbol{k} = \pi(n+1)(n+2)na$$

Fig. 3.19 shows the sensitivity sections of double dipole array referring to "**n**" values ranging from 1 to 4. The largest sensitivity values are located between the A-B dipole couple, as well as between the M-N couple (Loke, 2004). When "**n**" parameter increases, the high sensitivity values become located under A-B and M-N dipoles, on the other hand, the sensitivity values under the center of the array between the A-M electrodes drops down (Loke,2004; Soldovieri,2006). Fig.3.19 shows that the sensitivity contour becomes almost vertical for "**n**"> 2 (Loke, 2004). Thus, as reported by Loke, (2001), the dipole-dipole array is very sensitive to horizontal changes in ρ, but relatively insensitive to vertical changes in the ρ; so it is useful to map vertical structures, (e.g. dykes or cavities), but quite unuseful to map horizontal structures (e.g. sills or sedimentary layers).

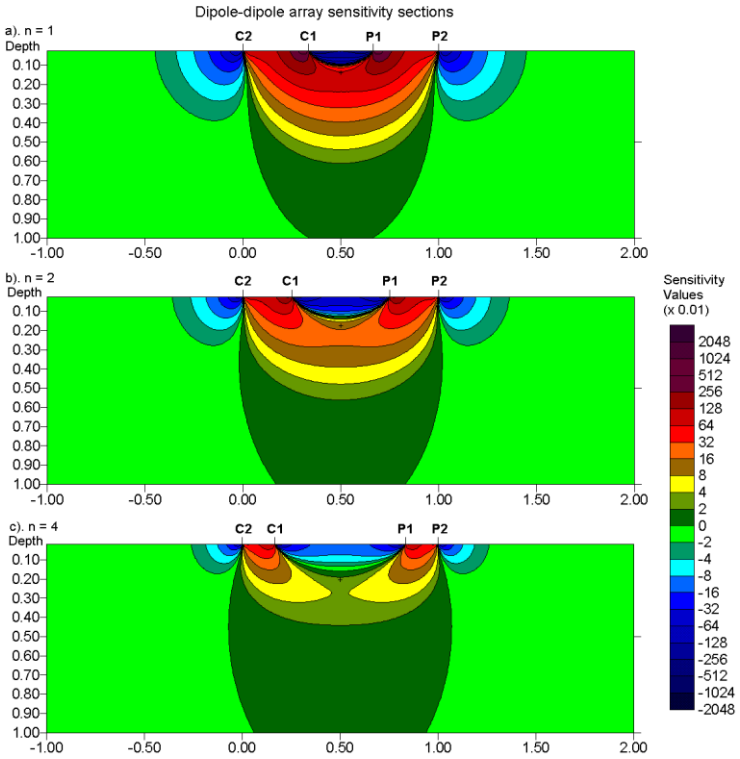

Fig.3.19 Sensitivity sections for the dipole-dipole array (Modified from Loke, 2004)

Chapter IV-Parco della Caffarella test site

4.1 Geological setting of Parco della Caffarella

The *Parco della Caffarella* is located in southern part of Rome; it is enclosed between the Aurelian Walls, the *via Latina*, the *Almone* river and the *Via Appia Antica* (fig 4.1). The "*Valle della Caffarella*" has an extension of about 200 hectares and it represents one of the largest green areas within the city of Rome (Calzolari & Olivieri, 2010).

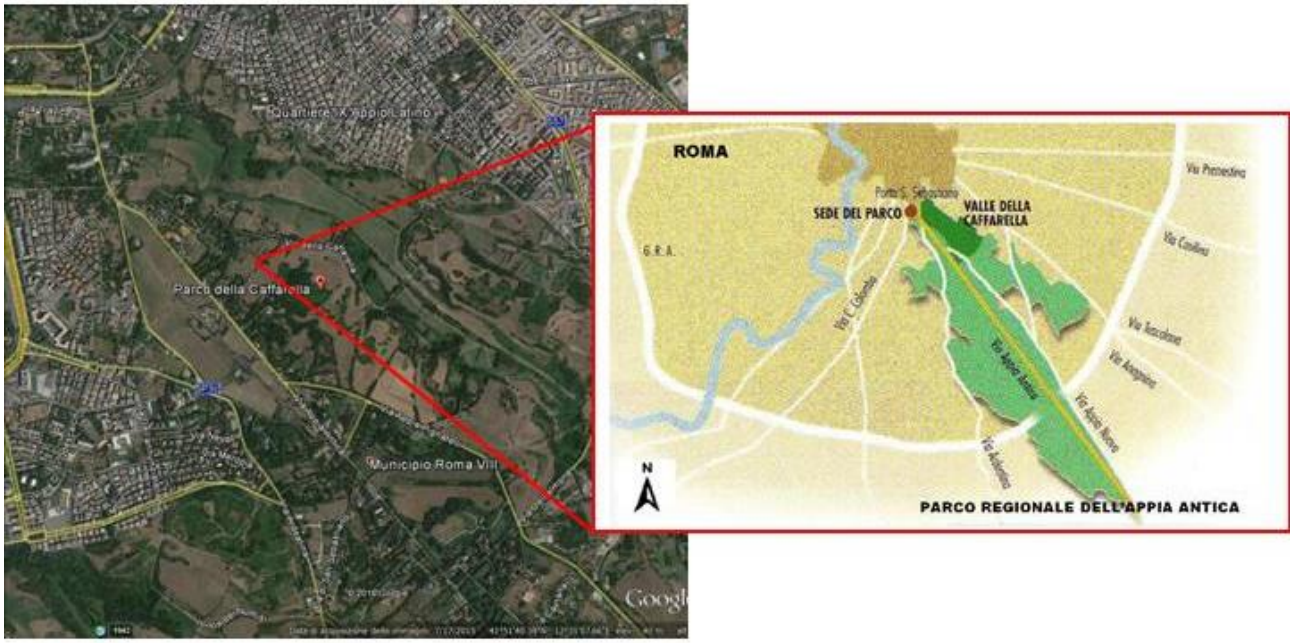

Fig. 4.1 Google earth view and sketch map of *Parco della Caffarella* (modified from www.parcoappiantica.it)

From a geological point of view in "*Valle della Caffarella"* the following lithologies are present (fig. 4.2):

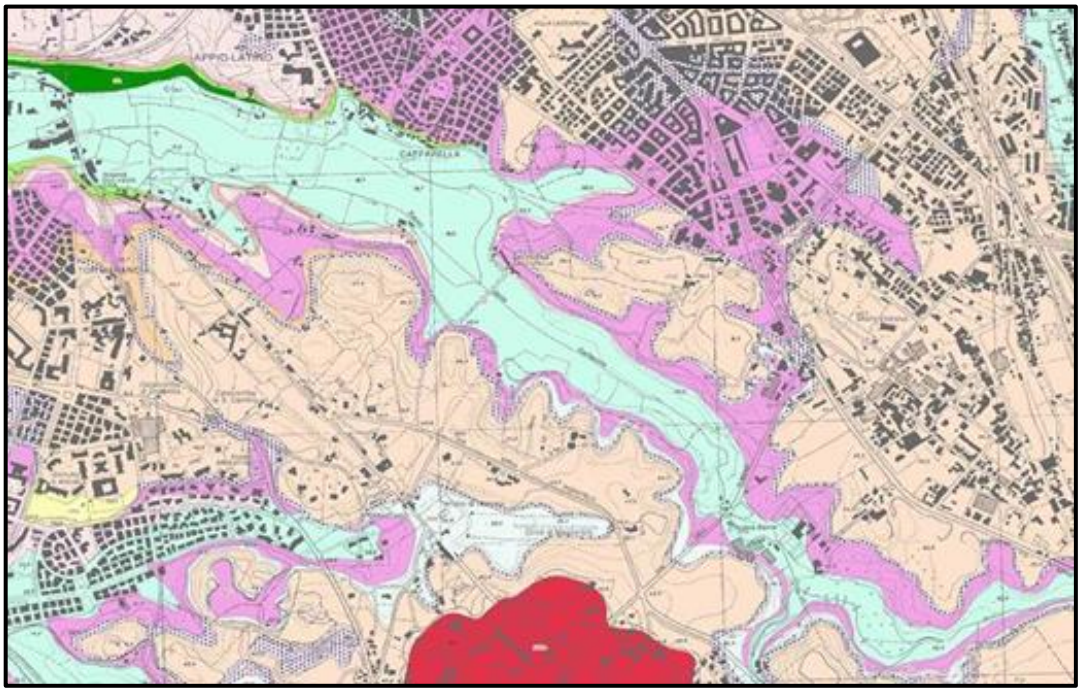

Fig.4.2 Geological map of "*Parco della Caffarella*" (modified from Funiciello & Giordano, 2008); scale 1:10.000

Alluvial deposits (a2)

Deposits composed by sandy clay that derives from the rehashed of volcanic material; it is rich in organic matter. Diffractometer analysis shows that the main mineralogical phases are augite and leucite (Castelluccio, 2012). *(Holocene)*

Pozzolanelle (VNS2)

Massive-litoid deposit having an ash-rich matrix with lithic lava and well-formed crystals (leucite, biotite and clinopyroxene). It is also called "fish-eye tuff" for the high content of leucite crystals (Castelluccio, 2012). *(middle Pleistocene)*

Tufo lionato (VSN1)

Massive-litoid deposit, in has an ash rich matrix, with grayish slag and yellow pumices; lava lithic and crystals are well formed (Trigila *et al*.,1995; Castelluccio, 2012). In the "*Valle della Caffarella*" two different facies are present: *litoid facies* in which slags, analcime, pyroxene augite and biotite are present. *Altered facies* in which the tuff are altered, the slag tend to be much less visible, augite and halloysite are in lesser amounts and analcime is completely removed (Castelluccio, 2012).*(middle Pleistocene)*

Pozzolane Nere (PNR)

It is a layer located between VSN1 and RED. It is composed by loose ash rich material. *(middle Pleistocene)*

Pozzolane Rosse (RED)

It is a massive reddish deposit that has chaotic structure and a scoriaceous matrix. Crystals of leucite and augite are present. *(middle Pleistocene)*

Ventriglia (2002) reports the description of many borehole collected in the *Parco della Caffarella*; their location is reported in fig.4.3a and some of them are shown in fig.4.3b.

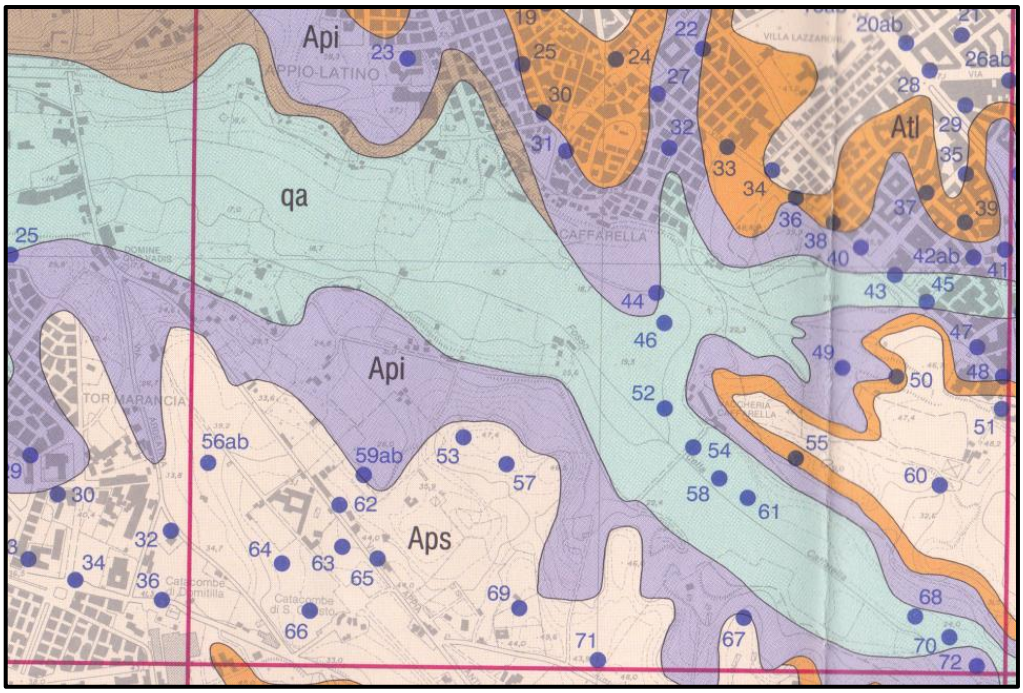

Fig.4.3a Litostratigraphic map of *Parco della caffarella* area; light blue= alluvional material; beige= pozzolanelle; orange= tufo lionato; purple= Pozzolane Nere, Conglomerato Giallo and Pozzolanere Rosse; Gray= Tufi pisolitici; numbers are borehole; (Modified from Ventriglia,2002). Scale 1:25000

Largo Tacchi Venturi (40)

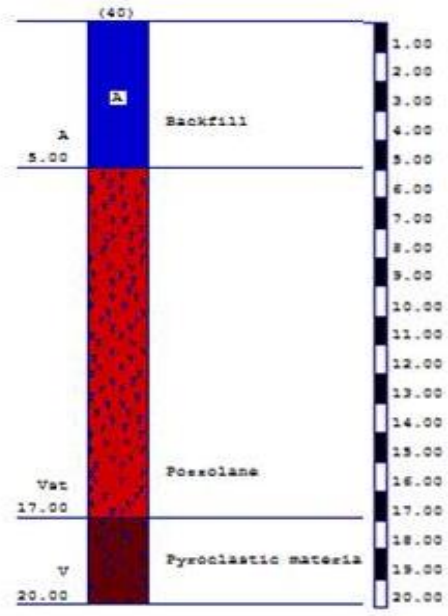

Via della Caffarella (46)

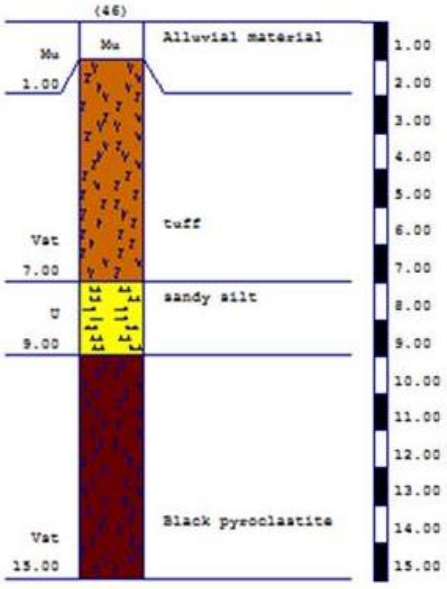

100 m W from Vaccheria Caffarella (40)

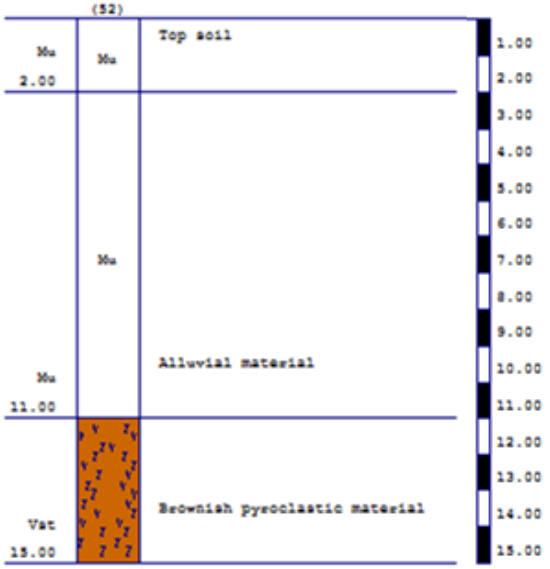

Fosso della Caffarella (68)

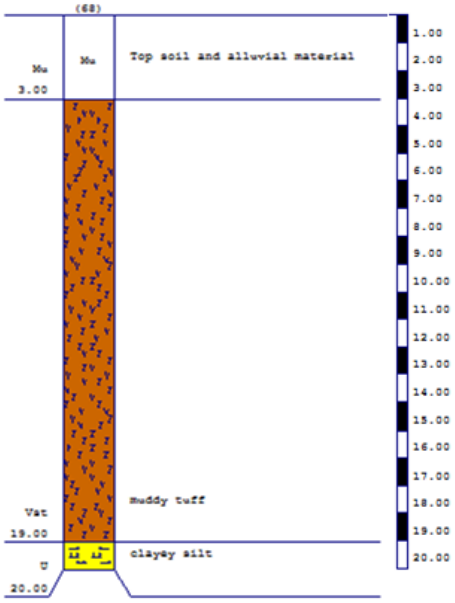

100 m SW from Vaccheria Caffarella (40)

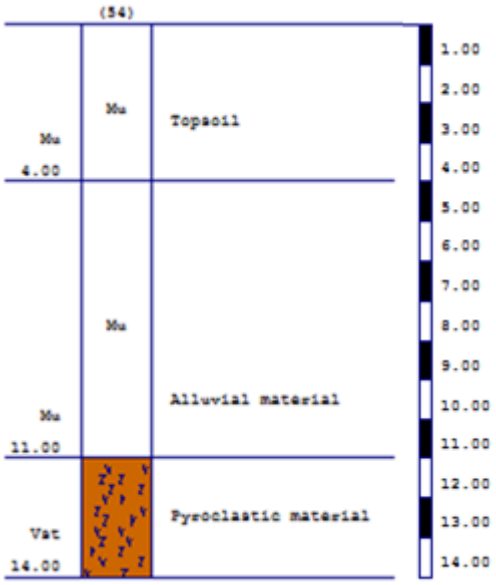

Fig. 4.43b Boroholes close and into *Valle della Caffarella* (data from Ventriglia, 2002).

Bianchi Fasani *et al*., (2012), based on the field work made by Trimarchi (2005), proposed an evolutionary model for underground cavity network formation in Rome area. The process starts from the cavity network developed in *pozzolane nere* formation which has the roof in the paleosoil 1. The first phase of the process starts with the formation of drying structures at the bottom of paleosoil 1. These structures cause the collapses of polygonal blocks and the subsequently upward migration of cavity network (fig.4.4).

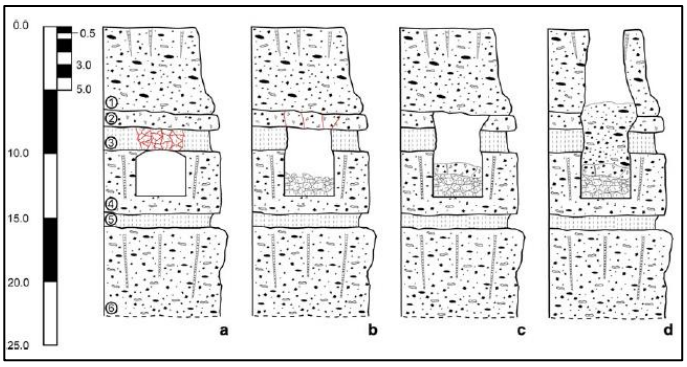

Fig.4.4. Evolutionary model for void migration towards surface a) original cavity within the"Pozzolane Nere" Unit; cracks in the overlying paleosoil 1; b) enlarged cavity with cap migrated into the "Tufo Lionato" Unit; c) collapse of the "Tufo Lionato" plate and cap migration into the "Pozzolanelle" Unit: d) sinkhole formation. Legend: 1) Anthropic deposits and "Pozzolanelle" Unit; 2) "Tufo Lionato" Unit; 3) paleosoil 1; 4) "Pozzolane Nere" Unit; 5) paleosoil 2; 6) "Pozzolane Rosse" Unit (Bianchi Fasani *et al.*, 2012)

4.2 Information about cavity network

Both in the Etruscan period and, subsequently, in the republican and imperial period, following the expansion of the city and the urbanization of the surrounding area, a great work in making groundwater ducts has been done. In addition, an intensive exploitation of the subsoil in order to quarry *pozzolana* and lithoid tuff has been performed (Sciotti, 1999). Some digs have been quarried for worship needs, cemeteries and hypogeums, but for the same reason also abandoned quarry were also reused (Ventriglia, 2002). The underground cavities digged in roman times were then reused, both for mining activities, and both in recent times as emergency shelters, commands and military deposits during the war period, mushroom cultivation on beds or deposits for industrial activities (Crescenzi *et al.*, 1995). Fig. 4.5 shows the different types of cavities located in the southern part of Rome.

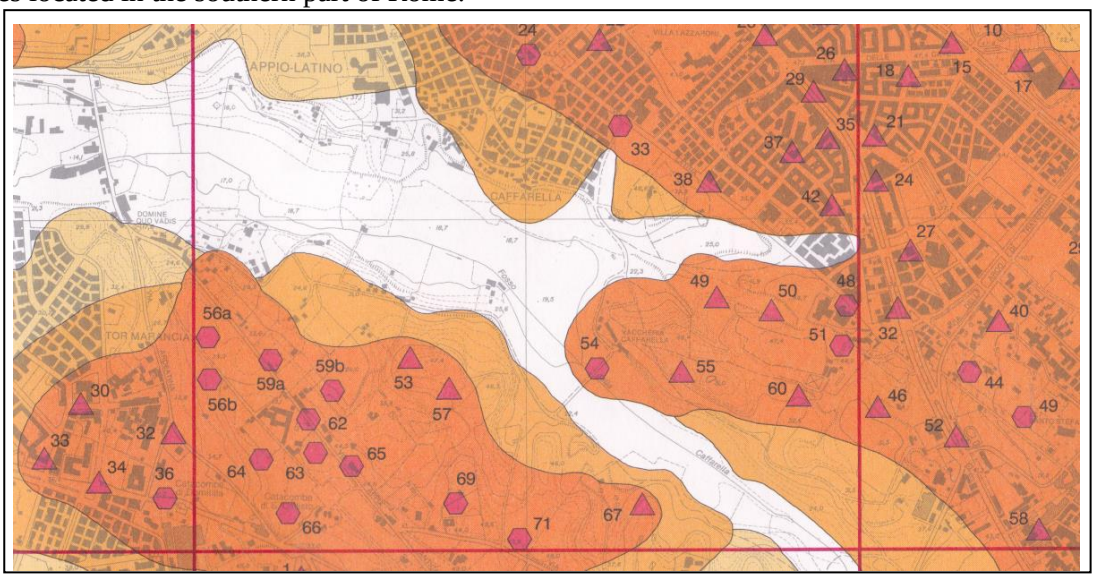

Fig. 4.5 Map of cavities of SE of Rome; area with known cavity; area with geomorphological clues of cavities; area without clues of cavities; old quarries; cavity network; catacombs (modified from Ventriglia, 2002)

In the area of the "*Parco della Caffarella"*, there are numerous underground cavities belonging to different types (fig.4.5); some of them have inlets surface clearly visible (Fig.4.6), others are identifiable on the basis of signs of superficial upheavals. Furthermore, others cavities are cited in the bibliographical sources (e.g. Trimarchi, 2005).

Fig. 4.6 Entrance of an abandoned quarry in *Valle della Caffarella* , it is dug in the eruptive units of "Villa Senni" (from www.parcoappiantica.com).

The caves have developed in the levels of *pozzolana red black* and tuff. They are composed by large rooms communicating each other, whose roof is supported by pillars generally arranged without any rule; in this way dense cavity networks were quarried. Generally, there is not vertically match between pillars of different levels, thus the geological situation is very complex. The size of the galleries depends on the lithology involved: in the case of *pozzolana red/black* galleries there are about 2-3 m width and 3-5 m height. However, the galleries are developed for the most part within 15 meters from the ground level (Ventriglia, 2002). Some years ago, only the entrances of the main galleries were visible, but during the centuries, because of collapse due to the progressive degradation and thinning of the pillars, surface depressions are well visible on some area (fig.4.7)

Fig. 4.7 Surface sinking *in Valle della Caffarella,* due to the presence of underground cavities (from www.parcoappiantica.com)

In the area of "*Parco della Caffarella"* examples of drainage dig are present (Trimarchi, 2005). The digs were built of masonry and their bottom was coated with bricks. The hydraulic tunnels are 2 m high and 1 m width and they are often interrupted ventilation wells. The area delimited by *the Fosso della Caffarella* to Noth ,by the *Fiume Almone* to Est and *Via di Cecilia Metella* to South, from *Fosso di Tor Carbone* at West, it is also concerned, by the Famous Catacombs of *S. Callisto, S. Sebastiano,* etc. and by numerous large caves (fig.4.4). In the area called "*dei Cessati Spiriti*" the presence of extended galleries located between the *Marrana della Caffarella* and the *Via Appia Nuova* are reported (Ventriglia, 2002). In addition, close to the modern *Via Appia Nuova* and the ancient *Via Latina,* a few hypogea quarried in *Pozzolana red* are reported in literature; among them the famous "*Ipogeo anonimo dei Cessati Spiriti*" (e.g. Rendina & Paradisi, 2004).

4.3 Data Collection

We decided to perform our survey in an area of the *Parco della Caffarella* in which the presence of an extended cavity network is only partially known; it is located in the southern part of the park (fig.4.8).

Fig. 4.8 Location of surveyed area employing different methods

The ERT measurements have been acquired in an area with dimension 14m x 48m partially overlapping the area surveyed with GPR. 14 parallel profiles, with a length of 48 m, have been acquired using an Iris Syscal

Junior Switch-72. The Double Dipole configuration has been chosen and the 48 electrodes were arranged with a spacing of 1 m for all profiles (Fig. 4.9)

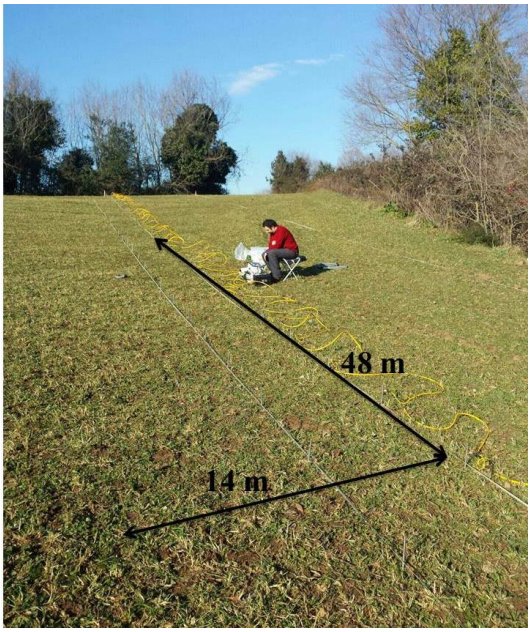

Fig. 4.9 Field arrangement of ERT profiles

GPR measurements have been collected along parallel profiles, employing the SIR3000 (GSSI) system, equipped with a 400 MHz bistatic antenna with constant offset and a 70 MHz monostatic antenna. The horizontal spacing between parallel profiles at the site was 0.50 m and 1 m respectively for the two antennas (fig. 4.10 & fig. 4.11). In the investigated area a total of 90 adjacent profiles across the site have been collected alternatively in forward and reverse directions, employing the GSSI cart system equipped with odometer. All radar reflections within the 105 *n*s (400 MHz) and 230 *n*s (70 MHz) time windows were recorded in the field as 16 bit data and 512 samples per scan as shown in the data collecting tables (table 4.5 & table 4.6).

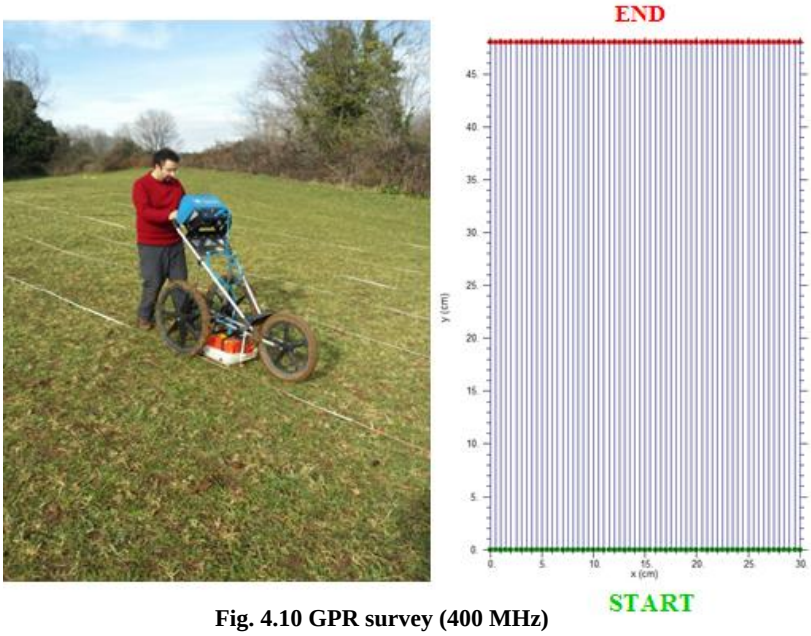

Fig. 4.10 GPR survey (400 MHz)

Antenna	400 MHz	**G1**	-20
Mode	Distance	**G2**	31
GPS	yes	**G3**	40
Samples/trace	512	**G4**	46
Format	16 bit	**G5**	54
Rate	64	**LPF**	700
Time window	105 ns	**HPF**	70
Scan/unit	56	**Stacking**	3

Table 4.5 Acquisition parameters for 400 MHz GPR survey

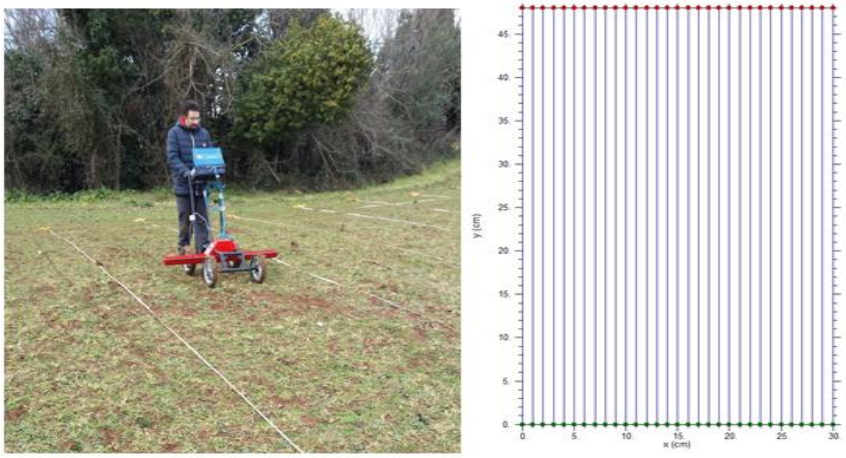

Fig. 4.11 GPR survey (70 MHz)

Antenna	70 MHz	**G1**	-12
Mode	Distance	**G2**	-3
GPS	yes	**G3**	27
Samples/trace	512	**G4**	33
Format	16 bit	**G5**	41
Rate	30	**LPF**	250
Time window	230 ns	**HPF**	30
Scan/unit	20	**Stacking**	3

Table 4.6 Acquisition parameters for 70 MHz GPR survey

4.4 Data processing

4.4.1 ERT Data Processing

The ERT data has been firstly processed using the software Prosys II (Iris instrument) in order to cancel bad datum points (about two bad datum for each profiles were cancelled).Then, the data were exported in formats that are compatible with the processing software. In this work we applied the following specific softwares:

- RES2DINV (Geotomo software) to obtain the 2D pseudosections.
- RES3DINV(Geotomo software) in order to obtain a 3D resistivity model of surveyed area.

Through these software is possible to invert large datasets collected with a multi electrode system and then pass from the apparent resistivity to the "real" resistivity. The two-dimensional model provides for the division of the subsoil in a numbers of rectangular blocks (fig.4.12).

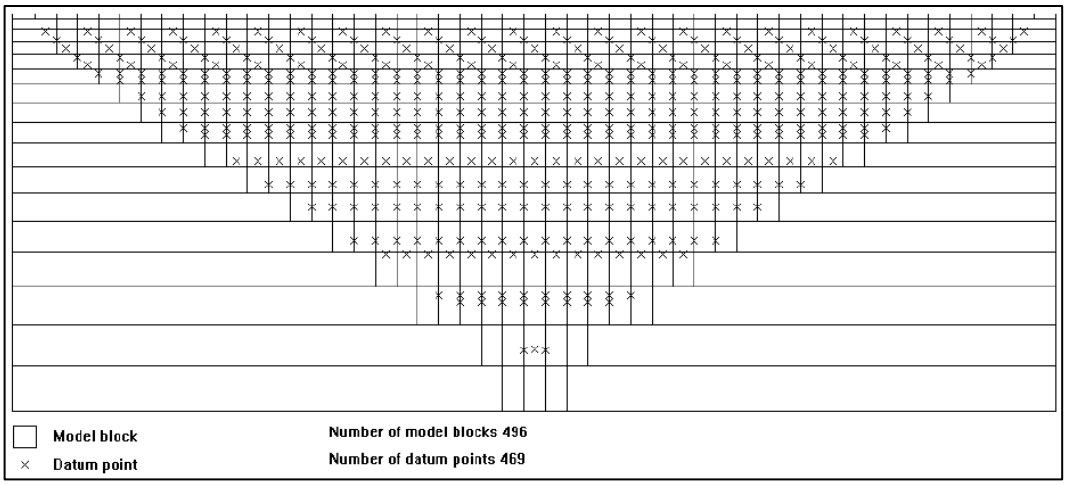

Fig.4.12 Model subdivision of the subsoil in rectangular blocks (modified from Loke, 2004)

The size and arrangement of the blocks is generated automatically using as an input the points measured during the survey. Thus, the blocks of the generated model represent parts of the subsoil to which is

associated automatically by the software a "real" resistivity value. The horizontal position is determined by the midpoint between the electrodes used for measurement, while the vertical position is located at a distance proportional to the spacing between the electrodes. Generally, the first layer of blocks is positioned to a thickness of 0.5 times the distance between the electrodes. This thickness gradually increases of 10% for each successive layer calculated. The last lower row of blocks is set to be roughly equivalent to the average depth of investigation (Edwards, 1977), which will be greater with the increase of the inter-electrode spacing (Loke,2004).

The inversion process used by software is based on iterative method defined method smoothness - constrained least squares (deGroot-Hedlin & Constable 1990; Ellis & Oldenburg 1994a), based on eq. 4.1:

(4.1) $$(J^T J + \lambda F)\Delta q_k = J^T g - \lambda F q_k$$

Where:

F=$a_x C_x^T C_x + a_y C_y^T C_y + a_z C_z^T C_z$

C_x, C_y, C_z= smoothing matrices in the *x*-, *y*- and *z*-directions where a_x, a_y, a_z = the relative weights given to the smoothness filters in the *x*-, *y*- and *z*-directions.

J= Jacobian matrix

λ= Damping factor (we use 0.1 for these survey)

q= The vector of variability of the model, which represents the variations of the model of resistivity

g= The vector of misfit of data that contains the differences between the values measured and calculated of apparent resistivity, generally expressed as root mean square (RMS).

The software uses at the end of each iteration the Gauss-Newton method in order to recalculate the Jacobian matrix (Loke & Dahlin, 2002).

In order to obtain depth slices resistivity map, we joint together the field data and then we inverted the data again using RES3DINV. The damping factor was 0.1 also in this case. The routine inversion of software is equivalent to both the two-dimensional case that three-dimensional. In the latter case, the subsoil will be divided into prisms with a rectangular base and the software determines the values of resistivity of prisms, in order to minimize the difference between the values of apparent resistivity and the "real" resistivity (Loke,2004).

A possible arrangement of the prisms is represented in Fig. 4.13, where the electrodes are positioned on the corners at the top of the model (Loke & Barker, 1996).

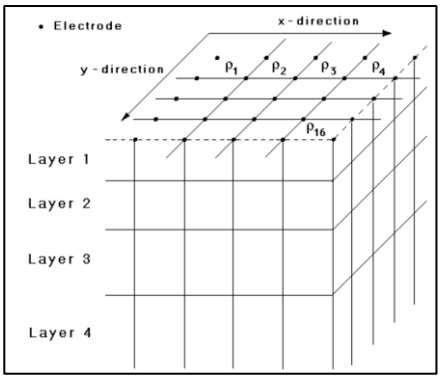

Fig.4.13 Model of discretization of the subsoil used for 3D inversion. The position of the electrodes is indicated by black dots located at the top of the layer (Modified from Loke & Barker, 2006)

At the end of the 3D inversion, we also use Voxler software (Golden software) in order to obtain a 3D isosurfaces resistivity representation (fig.4.17).

4.4.2 GPR Data Processing

We perform the GPR data processing using the software GPR-Slice (v.7.0). The main steps for time-slices representation (Piro *et al*., 2000) will be reported below and briefly described (fig. 4.14)

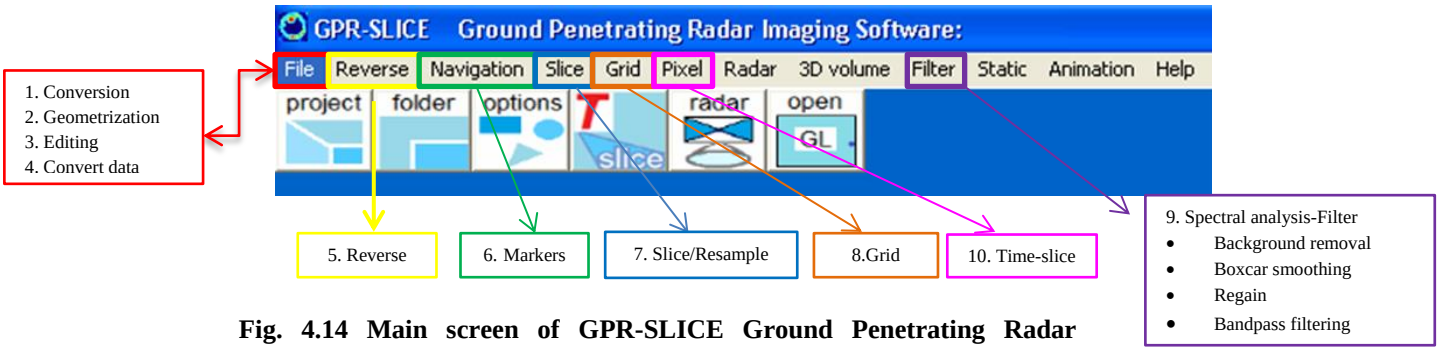

Fig. 4.14 Main screen of GPR-SLICE Ground Penetrating Radar Imaging Software with the principal operation processing (Modified from Goodman, 2017)

1. ***Conversion:*** The first step is to convert the different format into compatible one with the software used for data processing. *GPRSlice* supports many formats like *.dzt* used by SIR 3000 made by GSSI company.
2. ***Geometrization:*** Performing this step, the operator couples the GPR parameters with the geometric localization of profiles. More in details, the parameters that must be insert are listed below:
    - *# of file*: numbers of file collected during the survey.
    - *direction of survey*: The direction along which the data has been collected on the field; in our case the y direction.
    - *x end; y end*: The maximum length (in meters) of the profiles along x and y.
    - *Unit/marker*: It is the distance between a marker and the following one; in our case an odometer that counts the markers automatically has been used.
    - *Sample/Scan*: It is the number of samples that compose a single profile.

- *Time window (ns)*: It is the time range that will record reflections from a single pulse
- *Resample scan/marker:* it is the number of traces that composed one meter of survey.

3. ***Editing***: in this section the grid survey size must be insert as reported in the field spreadsheet.
4. ***Convert data:*** in this step, the user attempts to couple soil-antenna effect doing the so called "batch gain wobble". This process allows taking into account a single track calculating the average in its range and subtracts the average value only in that particular scan (see GPR-Slice manual for further details). The process is repeated for each scan.
5. ***Reverse:*** If profiles has been collected according to a path to "zig-zag" it is necessary to perform an inversion of the coordinates of the acquired profiles in opposite direction (e.g. from 48 m to 0 m)
6. ***Marker:*** it is used to verify if all expected markers have been collected during the survey employing the survey wheel or the manually mode. In the case of manually setting, some markers can be missed during the survey and through this option it is possible to correct the profile.
7. ***Slice & resample:*** The next step in the processing is to prepare the data for the creation of the time-slices. This step in divided in some sub-steps:
   - *Search 0 ns*: using this function, it is possible to assign the real 0 time value to the first stored signal in the time-window. The software allows to perform this operation automatically by examining the variations in the amplitude of the signal. The search 0 ns is important for the following step with which will be calculated the time-slices
   - *Number and depth of slices*: Using this option, it is possible to set the number of slices in which divide the radargrams and thickness (time) of each of them.
8. ***Grid***: Through this process, the software performs a data interpolation along directions x, y, z, in order to create more clear images.
9. ***Filter***: In order to increase the signal/noise ratio some filtering techniques has been used :
   - *Background removal*: The filter is used to remove signals due to environmental noise that are present as a horizontal bands on the radargrams; it consists in calculating the average scan using all profiles and them subtracting it for each single scan that composed the radargrams.
   - *Bandpass filtering*: there are some filters that allow to pass some spectra; the users basing the operation on his experience should choose manually the frequencies to pass.
10. ***Slice & Resample with filtered data***: we made the time-slice using filtered data; they will be used for further data analysis like data integration after the exportation in *.grd* format.

4.5 Data Interpretation

4.5.1 ERT data Interpretation

In fig. 4.15 all the ERT pseudosections are shown.

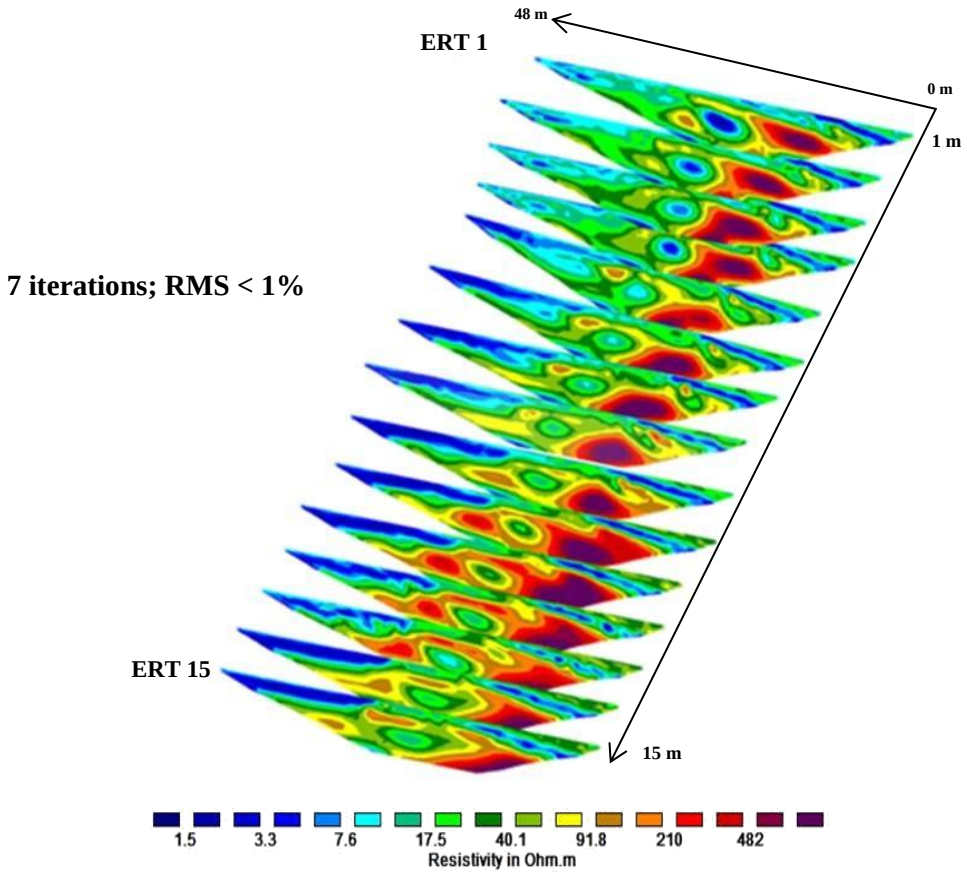

Fig.4.15 ERT Pseudosections collected at *Parco della Caffarella* test site

The ERT inversion results clearly show high resistivity values (~ 800 Ω·m) that deflect towards east; it could be due to a cavity network and a low resistivity anomaly (~10 Ω·m) maybe related to a water-filled small cavity formed by decomposed tuff and topsoil (fig.4.15).

Fig. 4.16a shows the 3D inversion results (2D resistivity map) performed thought RES3DINV and their representation using surfer (fig. 4.16b). Furthermore, in order to obtain a better visualization of high resistivity anomaly, we plotted the most interesting depth-slices on a satellite image (fig.4.16c).

a)

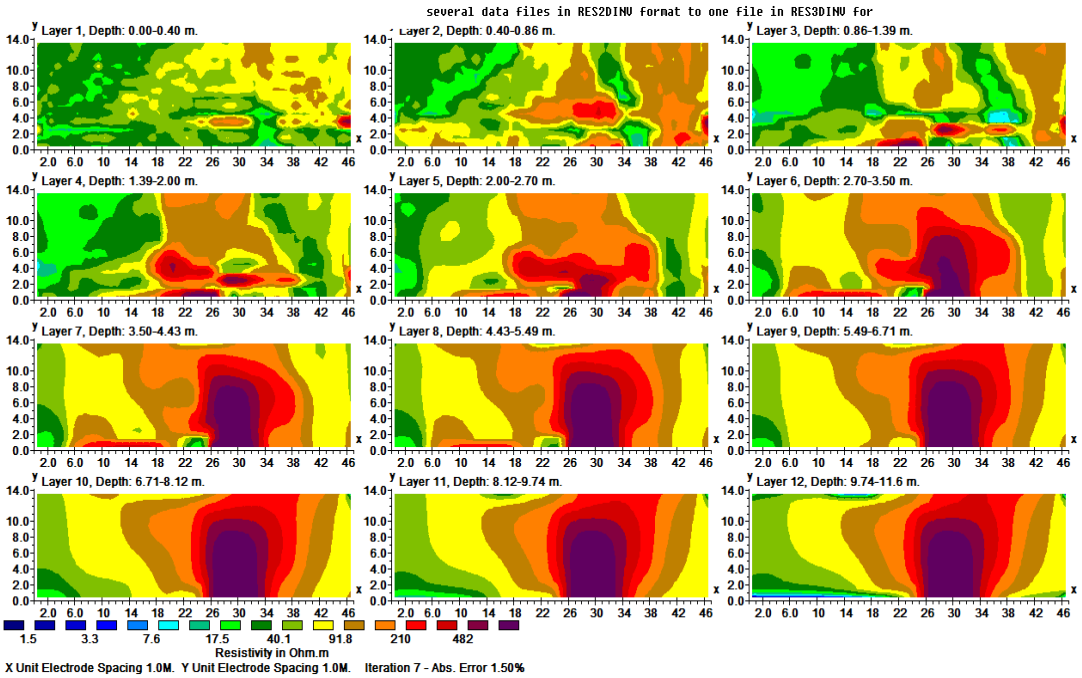

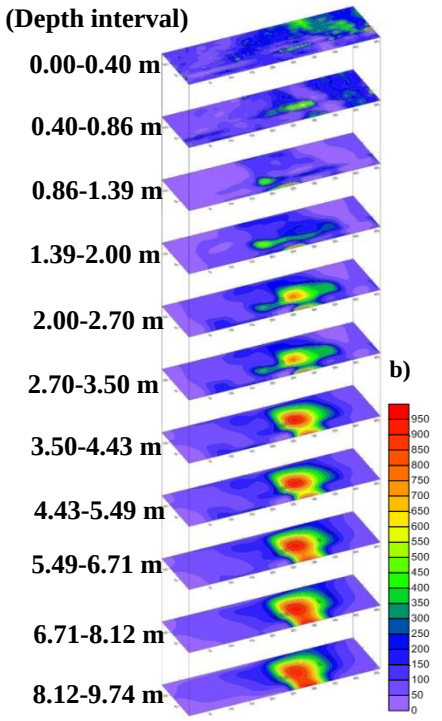

Fig. 4.16a shows that the larger amount of resistivity in the surveyed area drops out starting from 1 m to 2 m below the ground with value comparable with the 2D pseudosections; with the increasing in deep the high resistivity anomaly became globular shape starting from 2.50 m. The same trend is also confirmed by the shape of anomaly and by its resistivity values presented in fig. 4.16b. Referring to fig.4.16c, it shows that the high resistivity anomaly (~ 800 Ω·m) is located close to known cavity inlet; for this reason it was interpreted as a tunnel (compare fig.4.15).

Fig. 4.16 a) Resistivity depth-slices performed using RES3DINV and b) Resistivity depth-slices represented using surfer c) 2.5 and 3.0 m depth-slices plotted on satellite image

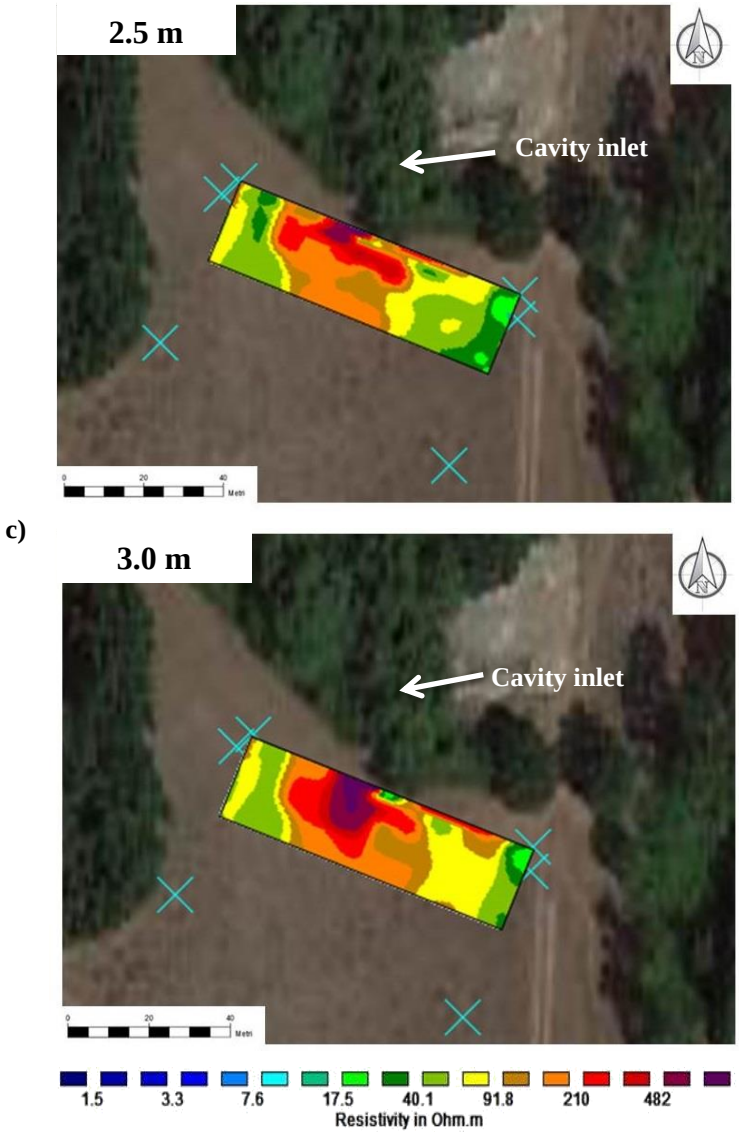

An example of a 3D model was also created using Voxler software (Golden software) which is represented in fig.4.17.

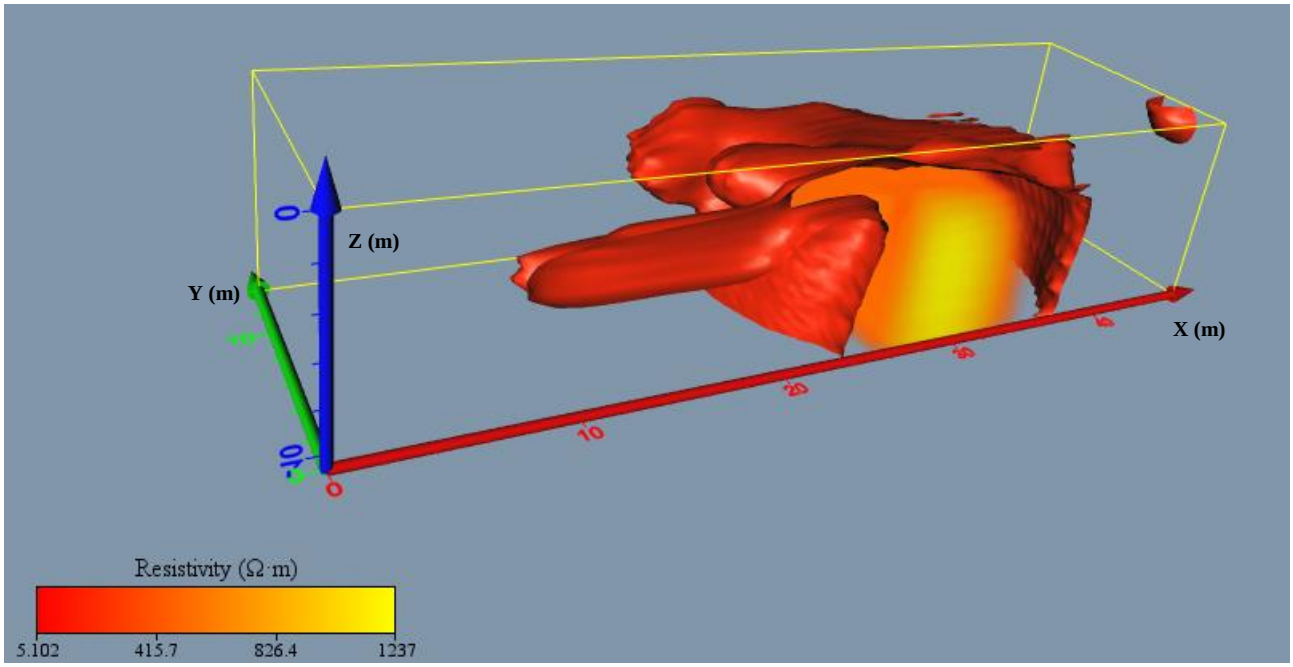

Fig. 4.17 3D resistivity model at *Parco della Caffarella* test site

It should be stressed that the tunnel detected is empty as suggested by the high resistivity values; fig. 4.17 shows resistivity isosurfaces related to different interval of resistivity.

4.5.2 GPR Data Interpretation

In this section only the most interesting time-slices for both antennas will be shown and briefly described; the others are reported in the appendix.

4.5.2.1 GPR 70 MHz Time-Slice

All the time-slices show a scattering phenomenon due to a partially wet soil. Checking the time-slice it is possible to note the presence of a high amplitude anomaly which is clearly visible between 2.5 and 3.0 m below the ground (fig.4.18). It can be considered as the wave reflection between volcanic tuff and partially filled cavity. Since these structures were detected close to a known cavity inlet, it is likely to be correlated with a tunnel.

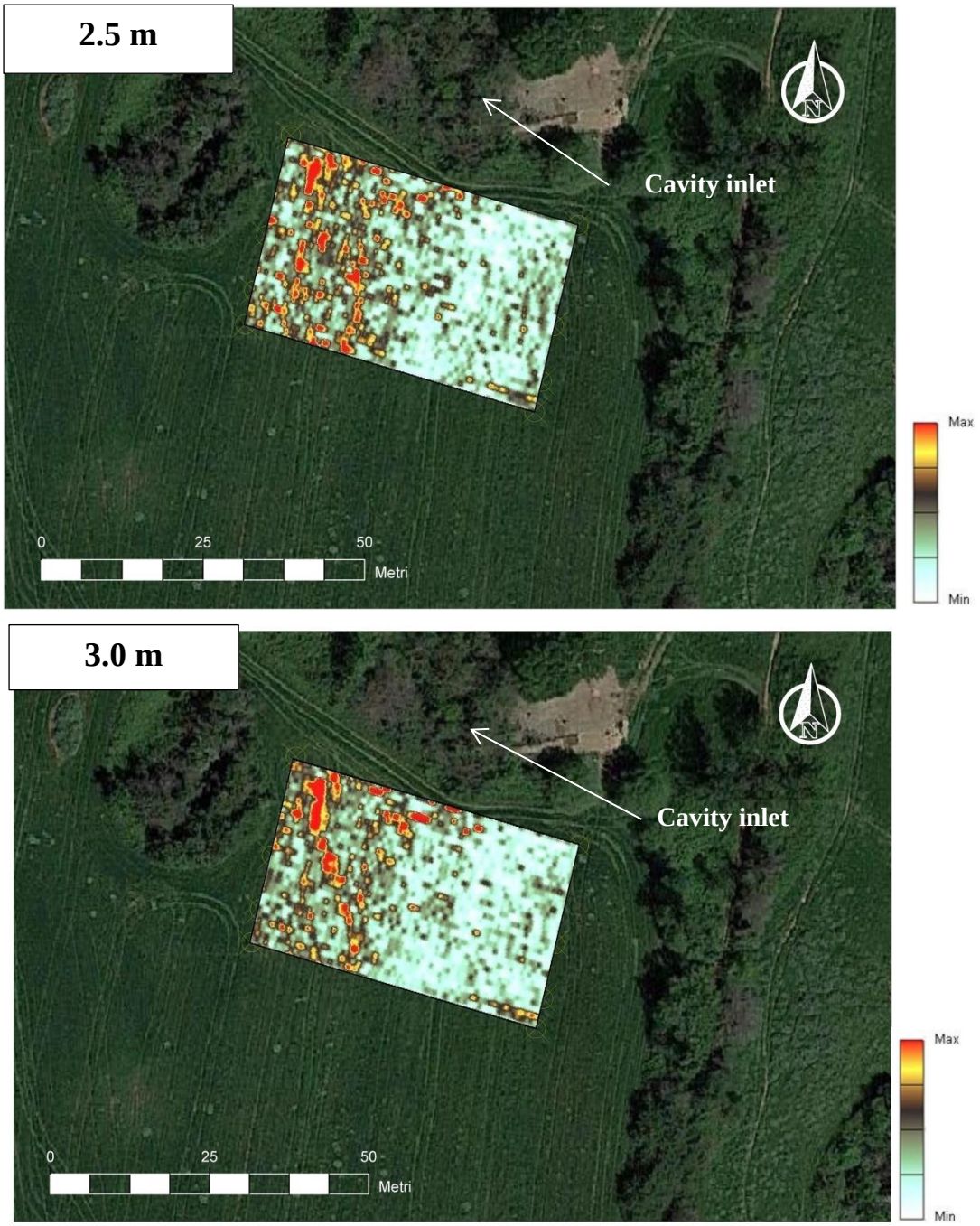

Fig. 4.18 Time-Slice (70 MHz) collected at *Parco della Caffarella* test site plotted using Autocad 3D map

4.5.2.2 GPR 400 MHz Time-Slice

Also the time-slices taken from the survey with GPR 400 MHz show a scattering phenomenon due a partially wet soil. Checking the time-slices it is possible to note the presence of a high amplitude anomaly which is clearly visible between 1.0 m and 1.5 m below the ground (fig.4.19). It can be interpreted as the top of tunnel show in fig 4.18.

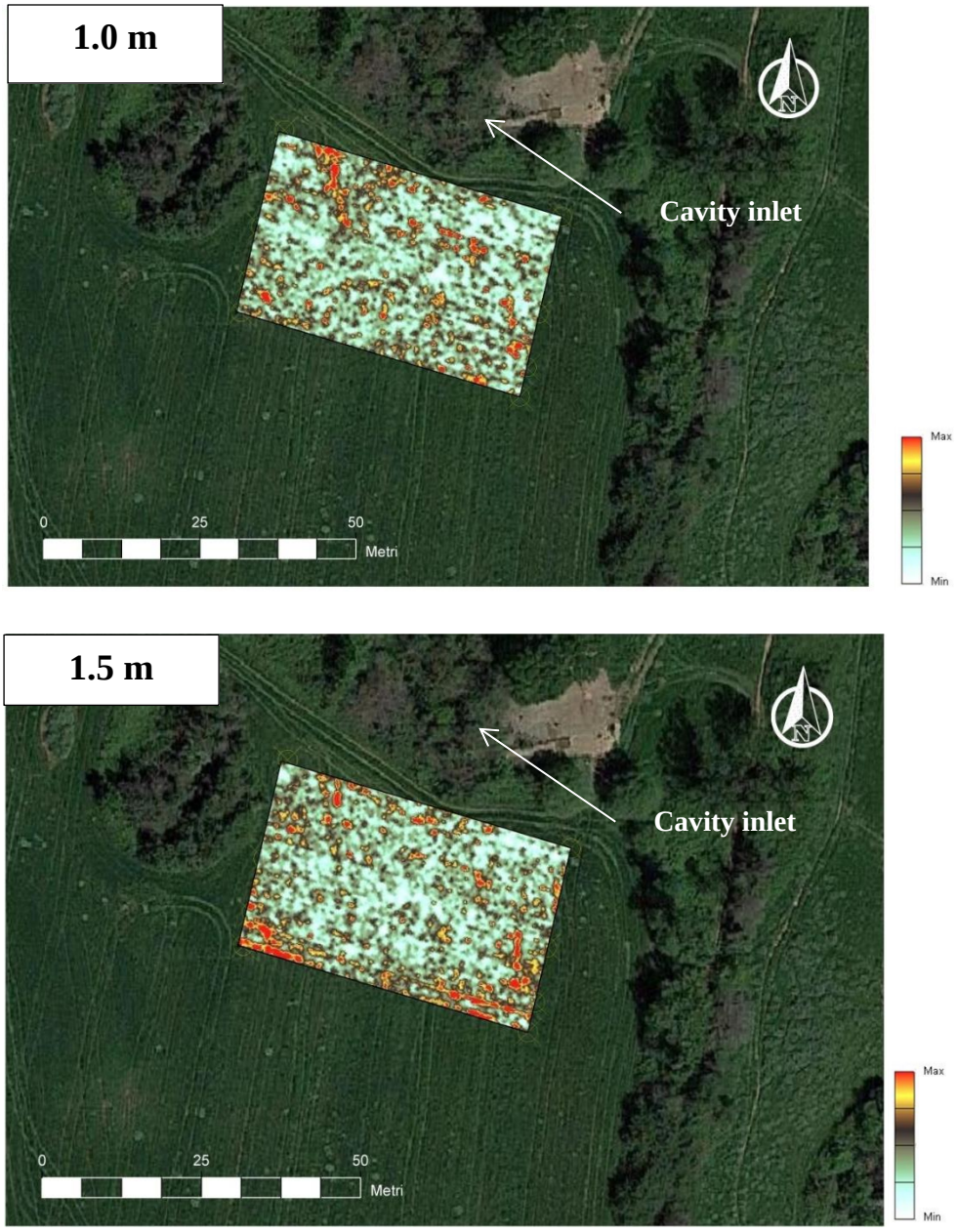

Fig. 4.19 Time-Slice (400 MHz) collected at *Parco della Caffarella* test site plotted using Autocad 3D map

4.6 Results of data integration

In this section the most interesting results for each types of integration are shown and described; the others are reported in the appendix.

4.6.1 Graphical integration

Fig.4.20 shows the results for contour map overlay integration for 70 MHz GPR survey and ERT depth-slice.

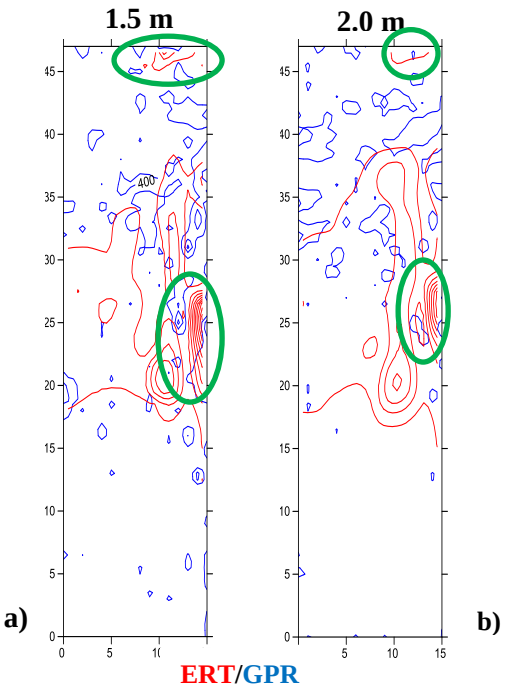

It shows the partial correspondence between the contours of anomalies given by the two methods. This correspondence should be noted at x-coordinate 12.5 m and y-coordinate at 25 m and also at the end surveyed area at x-coordinates 12.5 m and y-coordinates 47 m for both depth-slices. These are underlined by green circles in fig. 4.20. It should be stressed that, as shown by contours maps overlay reported in the appendix, this match is lost with the increase in depth.

Fig. 4.20 Contour map overlay at 1.5 m (a) and 2.0 m (b) below the ground; ERT contour is reported in RED, GPR contour is reported in DARK BLU. All axes are in m.

Fig. 4.21 shows RGB colour composite referred to GPR 70 MHz and ERT depth–slice.

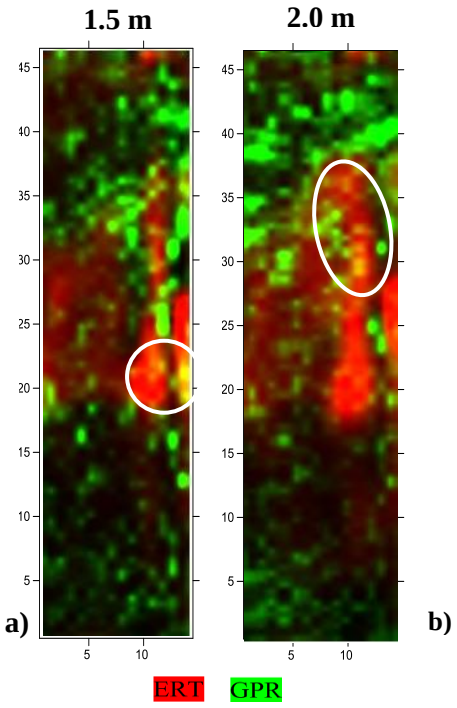

Even if the e.m. waves had difficulty in penetrating into the moist soil, some match between two methods can be noted. For example, checking fig 4.21a at y-coordinate =20 m and x-coordinate= 15 m there is a match represented by the yellow part of the figure (white circle in fig.4.21a). On the other hands, checking fig. 4.21b the match can be noted at x-coordinate =10 m and y-coordinate = 30 m (white circle in fig.4.21b). It should be stressed that, as shown by RGB maps reported in the appendix, this matching is lost with the increase in depth.

Fig. 4.21 RGB Colour composite at 1.5 m (a) and 2.0 m (b) below the ground; ERT anomalies are reported in RED, GPR anomalies are reported in GREEN ; White circles area matching points. All axes are in m.

4.6.2 Mathematical integration

Before performing mathematical and statistical integration methods, the data taken from both methods were normalized using the min-max scaling technique in order to remove the physical meaning of each method and in order to obtain datasets with values between 0 and 1. The min-max scaling formula (e.g. Patru & Sahu, 2015) is the following (eq. 4.2):

(4.2)

$$Z_i = \frac{x_i - \min(x)}{\max(x) - \min(x)}$$

where $\mathbf{x=(x_1,\ldots,x_n)}$ and $\mathbf{Z_i}$ is the $\mathbf{i^{th}}$ normalized data.

Fig. 4.22 shows the **binary representation** method referred to GPR 70 MHz and ERT depth–slice.

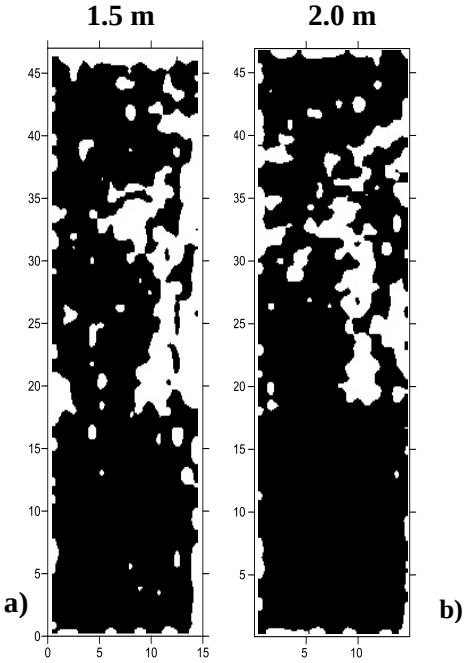

Fig. 4.22 Binary representation at 1.5 m (a) and 2.0 m (b) below the ground; white is the presence of anomaly and black is lack of anomaly; All axes are in m.

Even if the e.m. waves had difficulty in penetrating into the moist soil, binary representation give us the knowledge about where, in the surveyed area, is the main part of anomaly concertation in terms of presence/absence of anomalies. Thus, fig.4.22 shows the lack of anomalies for about half of the surveyed area and the presence of anomalies manly concentrated from y-coordinate=20 m and x-coordinate=5 m for both of depth-slice. Fig.4.22b shows that the "s" shape of anomalies detected is comparable with a quarried tunnel located at about 2 m below the ground. It should be stressed that, as shown by binary representation maps reported in the appendix, this trend is lost with the increase in depth and only a globular shape anomaly given by ERT method is shown.

Fig. 4.23 shows the **data sum** method referred to GPR 70 MHz and ERT depth–slice.

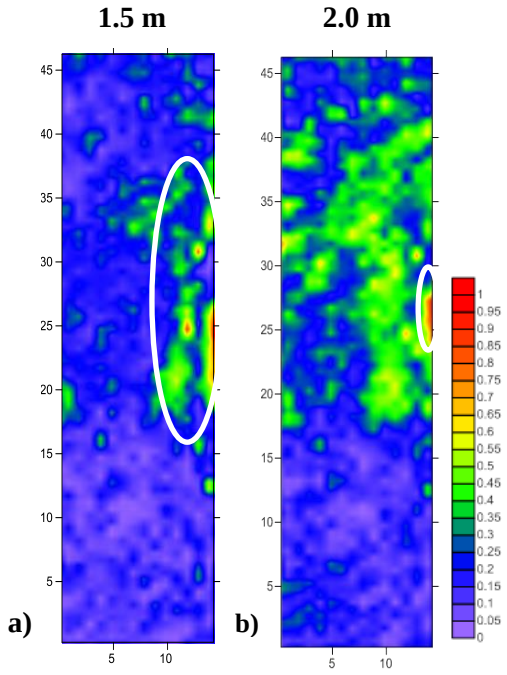

Fig. 4.23 give us a general overview of anomalies detected in the surveyed area just adding two normalized datasets; more in details, green areas in fig.4.23 are places in which only one of the two applied methods detected an anomaly (values are < 1); the areas in orange or red indicated that both methods detected the same anomalies at the same time. Thus, fig.4.23a (white circles) confirms that both methods detected partially a tunnel even in a complicated geological setting. Fig.4.23b shows that both methods detected the same anomalies only at y-coordinate =25 m and x-coordinate=15 m. It should be stressed that, as shown by data sum maps reported in the appendix, this trend is lost with the increase in depth and only a globular shape anomaly given by ERT method is shown.

Fig. 4.23 data sum at 1.5 m (a) and 2.0 m (b) below the ground; white circles are zone of surveyed area in which at least one method detected some anomalies. All axes are in m.

Fig.4.24 shows the data multiplication results given by GPR 70 MHz and ERT depth-slices; the other results are reported in the appendix.

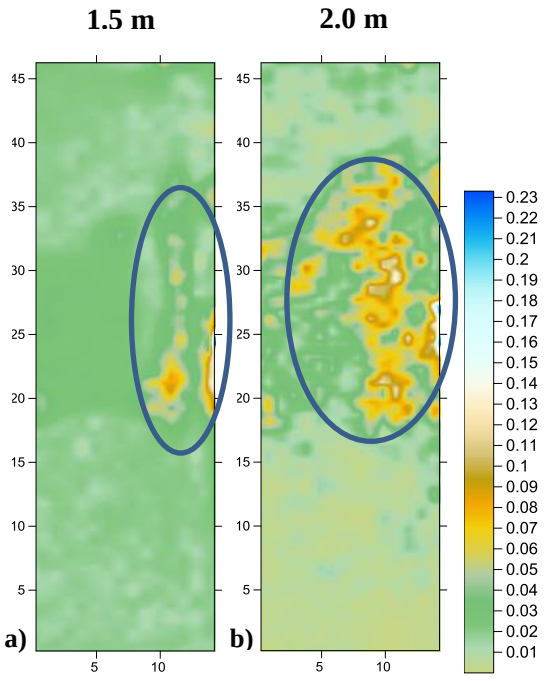

Fig.4.24 gives us a detailed view in which place of the surveyed area both methods detected the same anomalies at same time. Thus, for this reason the area where it occurs is smaller than the area highlighted by data sum method. Fig.4.24a (blue circle) suggest us that the area in which anomalies were detected by both methods at same time are at y-coordinate from 20 m to 35 m and at x-coordinate from about 7.5 m to 15 m. fig.4.24b (blue circle) shows a more extended area in fact this area is located at y-coordinates from 20 m to 38 m and at x-coordinate from 5 m to 15 m. It should be stressed that, as shown by data product maps reported in the appendix, this trend is lost with the increase in depth and only a globular shape anomaly given by ERT method is shown.

Fig. 4.24 data product at 1.5 m (a) and 2.0 m (b) below the ground; dark blue circles are zone of surveyed area in which both methods detected the same anomalies at same time. All axes are in m.

4.6.3 Statistical integration

Fig. 4.25 shows K-means cluster analysis given by GPR 70 MHz and ERT depth-slices

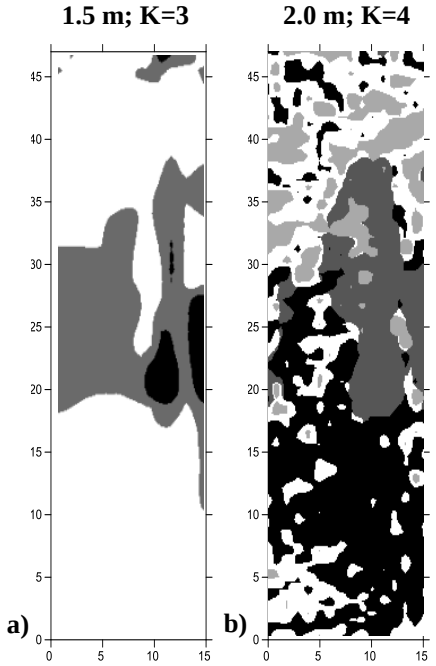

Fig.4.25 shows an attempt to divide the anomalies detected by both methods in categories, which is the main goal of cluster analysis. In this type of analysis, the investigator must choose how many clusters divide the anomalies detected (e.g.Wilks,2011); Sometimes different numbers of clusters can be chosen between two different depth-slice as in the presented case in which we choose K=3 (fig.4.25a) and K=4 (fig.4.25b). More in details, fig.4.25a shows anomalies having shape similar to the others integration methods; the cluster represented in black suggests us a possible separation of this two anomalies that could be related to two different cavities that ERT method joint together as shown, for example, in fig.4.25b.

Fig.4.25 K-means cluster analysis at 1.5 m and K=3 (a) and 2.0 m and K=4 (b) below the ground. All axes are in m.

Fig. 4.26 and fig.4.28 show the results PCA given by GPR 70 MHz and ERT depth-slices.

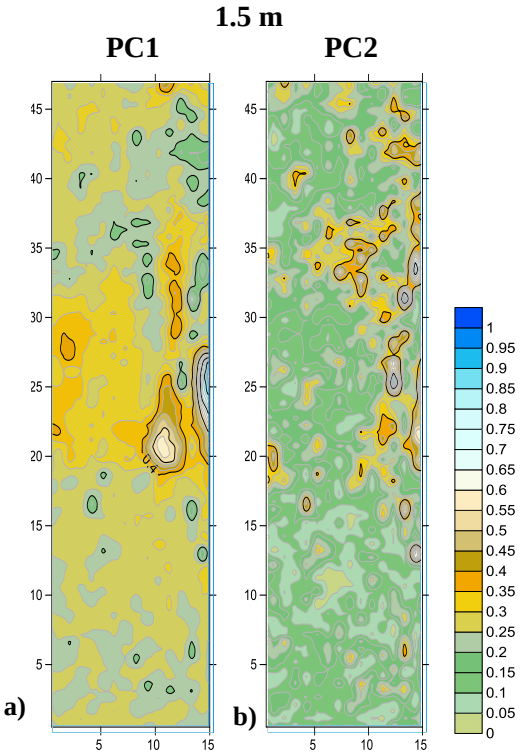

Fig. 4.26 shows, just at a first glance, that the collected data are well correlated because in the aforementioned figure, the contribution of both methods are clearly identifiable even if mainly PC1. This information is clearly expressed in the fig. 4.27a in which it is presented that the data are correlated for up to 70 %. As PCA theory suggests, the PC1 contains the main part of variance thus, just from a statistical point of view, the main part of information which is expressed in term of eigenvalues (fig.4.27b); anyway, it should be stressed that the PC2 give us the 39% of information. In addition, PCA methods support our hypothesis that the high resistivity area detected by ERT methods was properly related to two close cavities that the ERT method approximates to an only one high resistivity anomaly.

Fig. 4.26 Principal Component Analysis at 1.5 m below the ground; the first principal component (PC1) is reported in a) and the second Principal Component (PC2) is reported in b); All axes are in m.

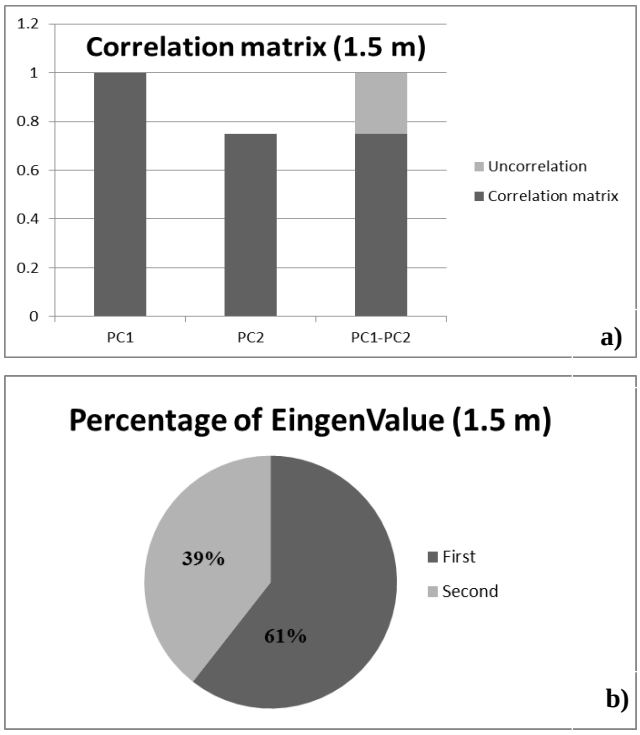

Fig. 4.27 a) Correlation matrix referred to PCA at 1.5 m b) Percentage of information expressed in terms of Eigenvalues.

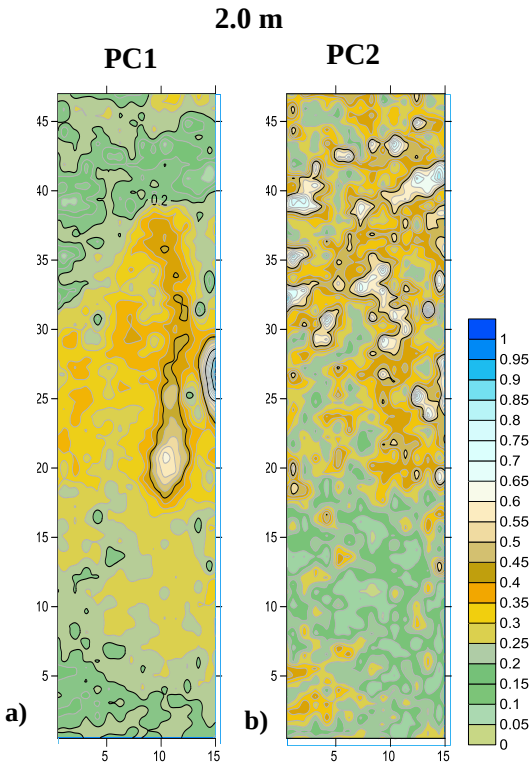

Also fig.4.28 shows a very good correlation between data and also in this case the contribution of both methods are well identifiable even if manly in PC1. This information is clearly expressed in the fig. 4.29a in which shows that the data are correlated for up to 95%. Fig.4.29b shows that the PC1 provides the 93 % of information (expressed in terms of eigenvalues) so in this case PC2 less important in terms of information. Fig.4.28a supports out hypothesis that two small cavities close each other have been detected.

Fig. 4.28 Principal Component Analysis at 2.0 m below the ground; the first principal component (PC1) is reported in a) and the second Principal Component (PC2) is reported in b); All axes are in m.

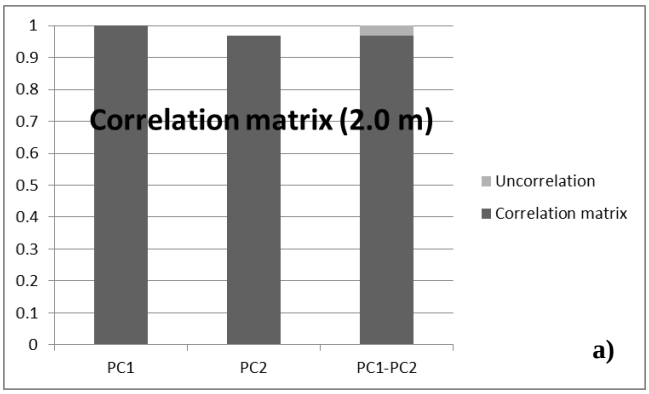

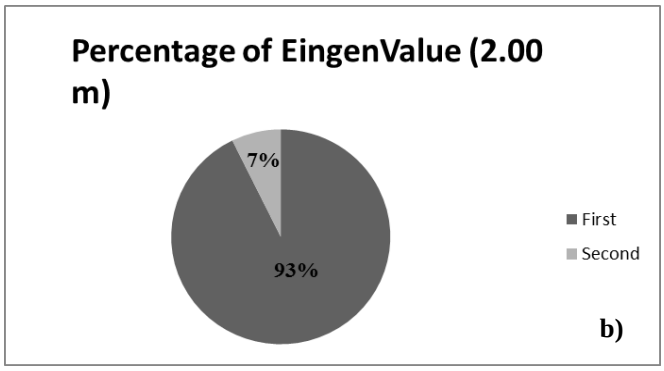

Fig. 4.29 a) Correlation matrix referred to PCA at 2.0 m b) Percentage of information expressed in terms of Eigenvalues.

Fig. 4.30 shows the results of the Bayesian Maximum Entropy (BME) (see section 3.5) given by GPR 70 MHz and ERT depth-slices.

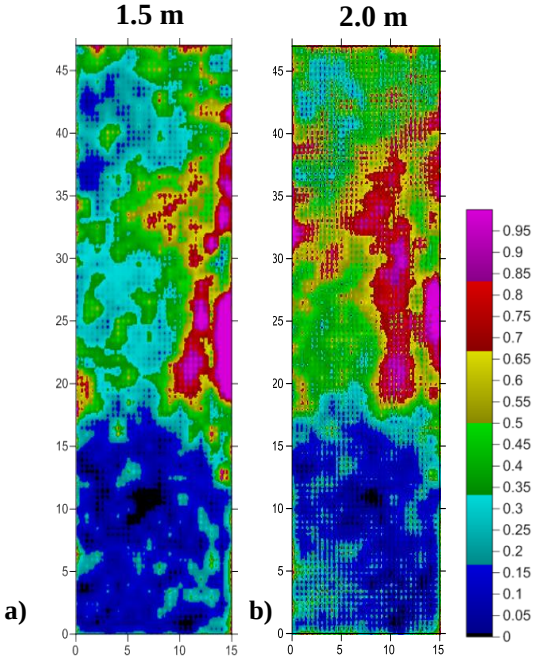

Fig.4.30 BME at 1.5 m (a) and at 2.0 m (b) below the ground. Table 4.7 Comparison between BME and Ordinary Kriging (OK); All axes are in m.

Fig. 4.30 shows that the results of The BME results are quite similar to the data sum (see fig.4.23) but their meaning are very different; in fact purple area in fig.4.30 shows where the results anomalies has the maximum probability to be "true" (0 = minimum probability 1= maximum probability) (see for example Christakos, 2001 p.95). We also compare the results of BME with an Ordinary Kriging (OK) in terms of RMSE, Variance and Standard deviation; the results are reported in table 4.7. They show only a small difference among the two interpolation methods (about 10^{-3}). This result is supported by statistical literature (e.g. Liedtke Tesar, 2011) in which is reported that when we have 50% of hard data end 50 % of soft data different integration methods could produce more or less the same results.

Error BME	1.39 m	2.00 m
RMSE	0.1364	0.1774
VARIANCE	0.0026	0.0042
STD. DEV	0.0513	0.0653
Error Kriging	**1.39 m**	**2.00 m**
RMSE	0.1402	0.2072
VARIANCE	0.0030	0.0065
STD. DEV	0.0555	0.0809

4.7 Concluding remarks

We employed eight different integration methods to merge GPR and ERT data collected in a suburban area in which an extended cavity network is only partially known. Among the qualitative techniques, the RGB Colour composite shows the most interesting results because it allows to know quickly in which part of the surveyed area both methods detected the same anomalies at the same time without any modification on the original data. Among the quantitative techniques, it should be stressed that the data sum integration method is the one that clearly gives the contribution of all the anomalies detected by all methods and is therefore the one that contains the most information and helps interpretation. Referring to statistical integration methods all proposed techniques help the interpretation because, for example, PCA method allows to go deeper in data interpretation giving information in terms of data correlation and amount of information provided by each method employ. The K-means clusters is useful to reasoning from the general to the specific because it allows to view specific clusters of anomalies, suggesting, as confirmed by PCA results, that the high resistivity anomalies detected by ERT method is probably related to two small cavities close to each other. BME method instead shows a result similar to that of the Sum integration, but it should be stressed that it also gives us information in terms of probability of find results.

Chapter V- Magliano Sabina Test site

5.1 Geological and archeological setting

The area of *Magliano Sabina* (Rieti, Latium, central Italy) is located in the so called Middle Valley of the Tiber River (M.V.T.). It is bordered to the West by the River Tiber, to the South by the "*Campana*" creek, to the East by the chain of *Monti Sabini* and to the North by the so-called "*Fosso dell'Aia*", not so far from *Otricoli* (fig.5.1).

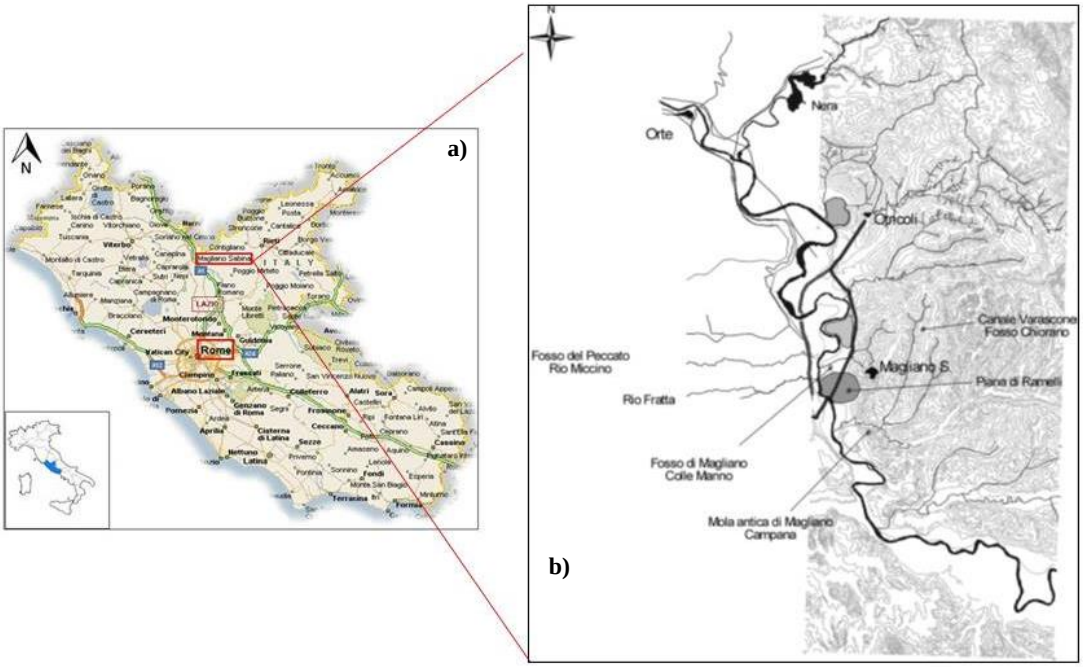

Fig.5.1 Location of *Magliano Sabina* (a); (b) the ancient and the modern *Via Flaminia*, the main rivers and topographic relief through contour lines close to *Magliano Sabina* town (modified from Colosi *et al.*, 2000)

From a tectonic point of view (fig. 5.2), the MVT is bordered to the East by the Mount *Peglia–Amerini–Narni–Sabini–Lucretil*i Mountains (central Apennines), and to the West by the quaternary volcanic hills of the *Vulsini* Mountains, Mount *Cimino*, *Sabatini* Mountains Volcanic Districts. The Mesozoic–Cenozoic calcareous and siliciclastic successions lie underneath the Plio-Quaternary basin and they are laterally continuous with successions exposed on the Mount *Peglia–Lucretili* Mountains ridge (Mancini & Cavinato, 2005). The MVT (fig.5.2) is filled with almost 1 km of Plio-Pleistocene continental and shallow marine siliciclastic deposits (Girotti & Mancini, 2003), beneath which Mesozoic–Cenozoic marine calcareous and terrigenous successions are arranged into a thrust pile trending NW–SE to N–S (e.g. Giustini *et al*., 2018). The Plio-Pleistocene sedimentary fill is overlain by a wide Early–Middle Pleistocene volcanic cover that is up to 1 km thick (Mancini *et al*.,2004; Mancini & Cavinato, 2005).

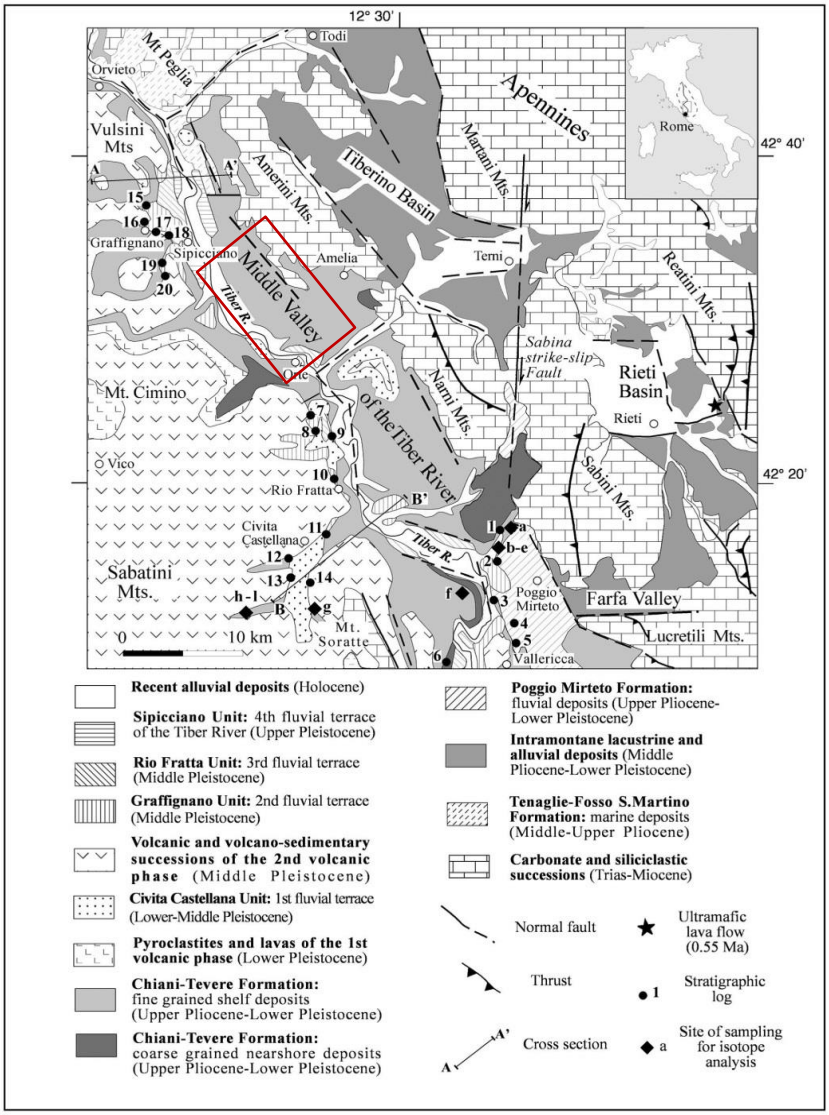

Fig. 5.2 Simplified geological map of M.V.T. (Modified from Mancini & Cavinato, 2005)

Moving from the general to the specific, in the area of *Magliano Sabina*, the following lithology outcrop (fig. 5.3; Mancini *et al*., 2004)

Alluvial deposits composed by gravel with calcareous, arenaceous and siliceous clasts, alternated with lime sands and levels of peat. *(Holocene)*

Silty sand and silt of marine environment that have an horizontal stratification or cross stratification; structures hummocky-type are present. Maximum thickness: 200 m *(Pliocene)*

Sandy loams of marine environment composed by clays and sandy silt poorly layered with cross stratification. maximum thickness: 50 m *(Lower Pleistocene)*

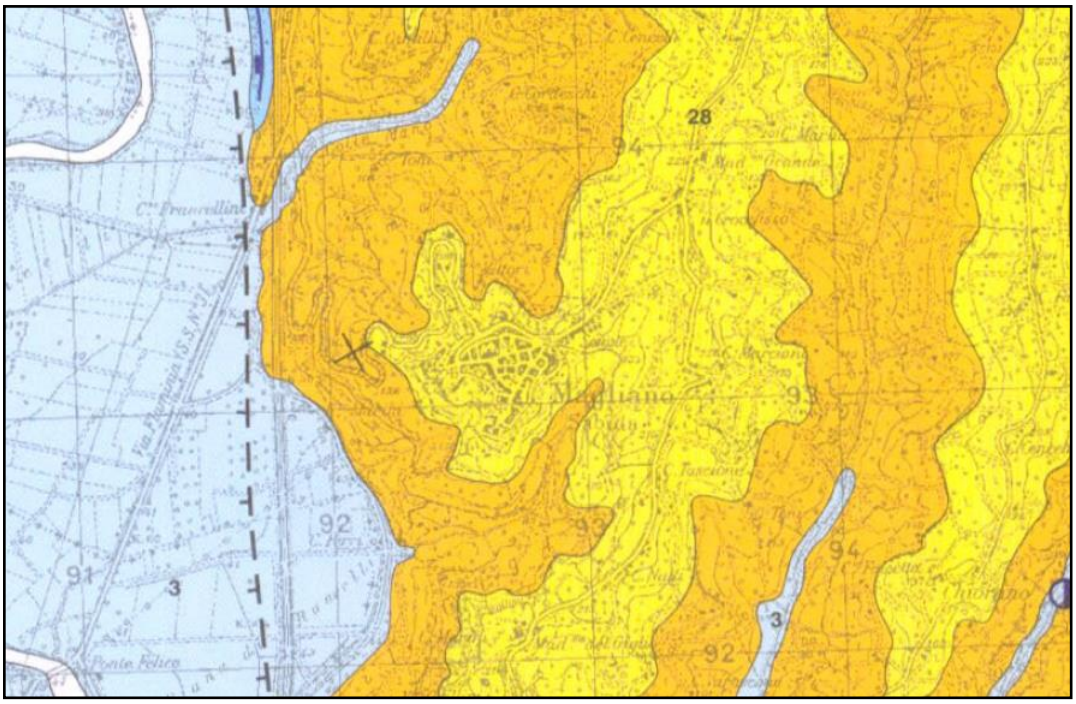

Fig. 5.3 Sketch of Geological map of M.V.T. scale 1:40000 (modified from Mancini *et al.*, 2003)

From archeological point of view, in the area around the town of *Magliano Sabina* the presence of necropolis (VII-VI century B.C.) is already known. In fact, as reported by Santoro (1996a), during the VII century B.C. there was a generalized occupation of the plateaus located at the top of the hills that constitute the *Magliano Sabina* Hill. The necropolis that occupy the hills are called with the toponyms "*Madonna Grande*", "*San Biagio*" and "*Colle del Giglio*" (fig.5.4). The typology of tomb provides ditch tombs with pillar made in tuff that supported a perishable coverage. More in details, in the *Colle del Giglio* area, the tombs extend on the flat plateau along an axis 400 m, while would not seem to occupy the area to the east (Santoro, 1996a). In the aforementioned area of *Colle del Giglio*, we made our geophysical survey (blue square in fig. 5.4).

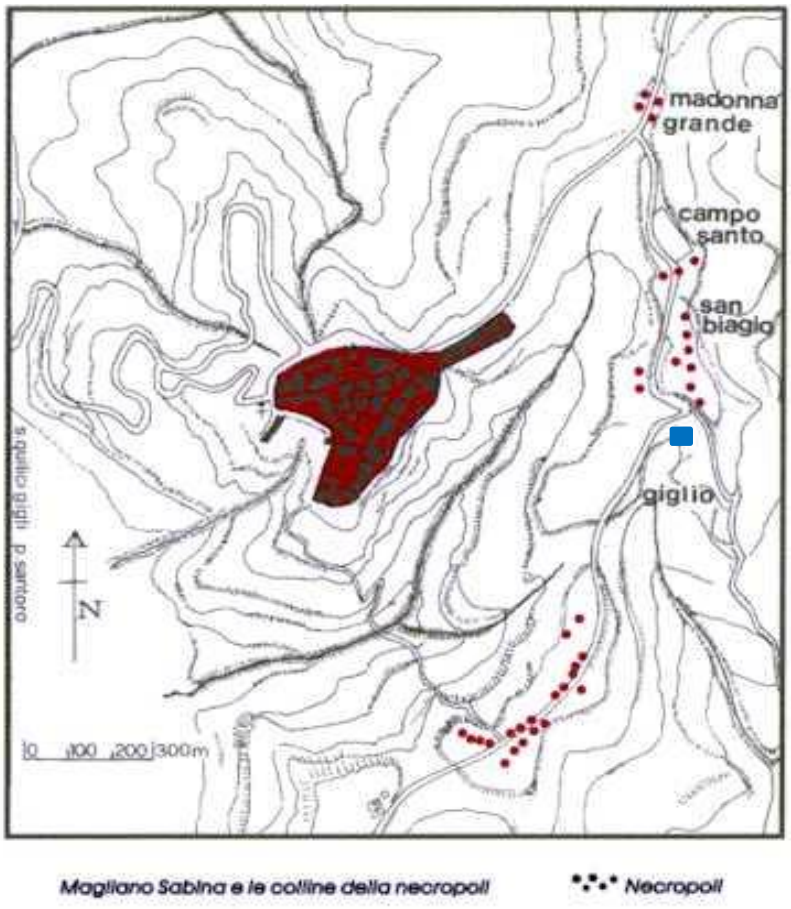

Fig. 5.4 Location of known necropolis around the town of *Magliano Sabina*; in the blue square area geophysical survey has been done (modified from Santoro, 1996a)

5.2 Data Collection

The selected area was 30 m x 80 m in size plus two squares 10 m x 10 m in size (fig. 5.5). The whole area has been investigated with the GPR method and partially with the Fluxgate Gradiometer in spring 2017.

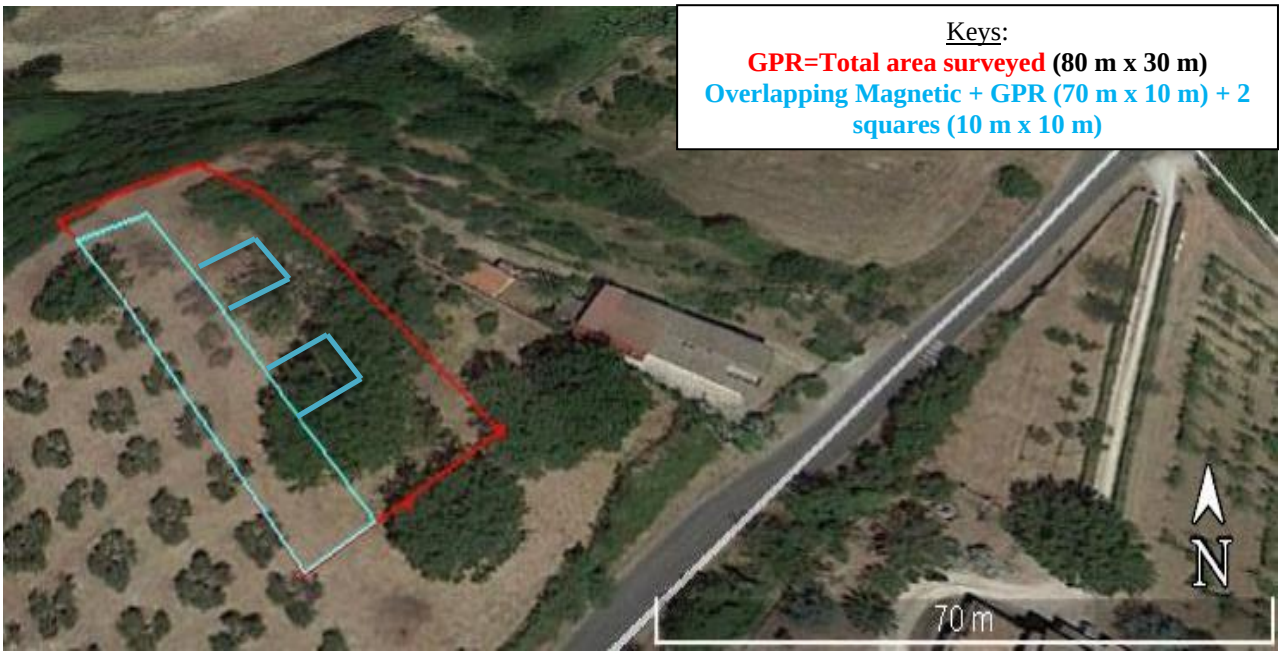

Fig. 5.5 Details of geophysical survey; red area= GPR, Light blue area= magnetic method

GPR measurements have been collected, along parallel profiles, employing the SIR3000 (GSSI) system, equipped with a 400 MHz bistatic antenna. The horizontal spacing between parallel profiles at the site was 0.50 m. In the investigated area a total of 63 adjacent profiles across the site have been collected alternatively in forward and reverse directions, employing the GSSI cart system equipped with odometer (fig.5.6); all radar reflections within the 85 *n*s time windows (twt) were recorded in the field as 16 bit data and 512 samples per scan. The acquisition parameters are reported in table 5.1.

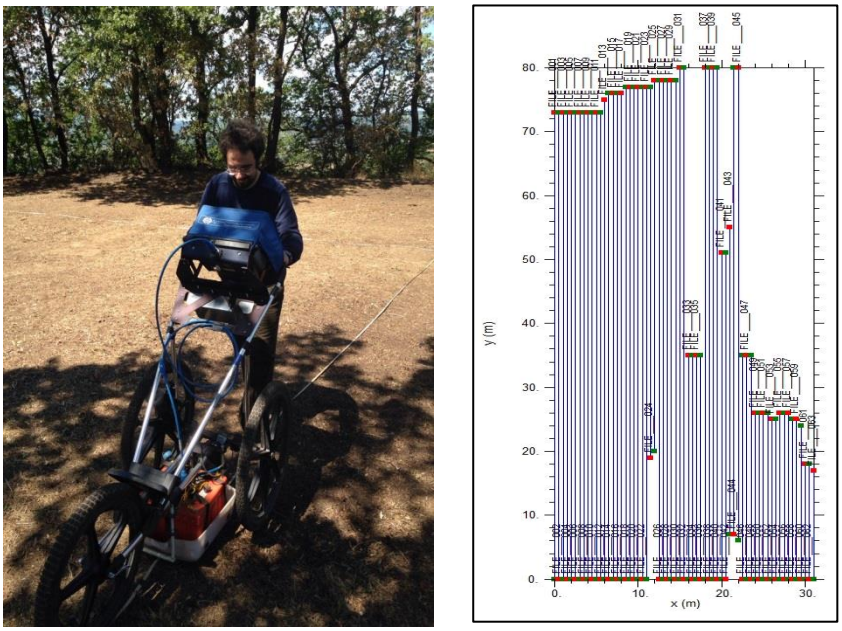

Fig.5.6 Scheme of GPR data collection at *Magliano Sabina* test site

Antenna	400 MHz	**G1**	-20
Mode	Distance	**G2**	21
GPS	no	**G3**	42
Samples/trace	512	**G4**	49
Format	16 bit	**G5**	54
Rate	64	**LPF**	700
Time window	85 ns	**HPF**	70
Scan/unit	52	**Stacking**	3

Table 5.1 Acquisition parameters for GPR survey at *Magliano Sabina*

The FDM data have been acquired in an area with dimension 10 m x 70 m (plus two squares 10 m x 10 m in size as shown in fig. 5.5), overlapping the same area investigated with GPR. In particular, the area was divided into 10 squares 10 m x 10 m in size, where the vertical gradient of total magnetic field has been measured using a Fluxgate Gradiometer FM256 (Geoscan Research, UK) along parallel profiles with horizontal spacing 1 m and with a sampling interval of 0.5 m along the profile. Fig. 5.7 shows an example of data acquisition in a square 10 m by 10 m in size.

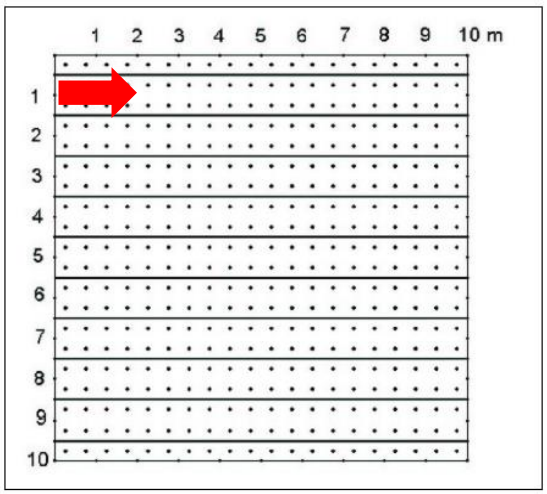

Fig. 5.7 Example of magnetic data survey; red arrow shows the acquisition direction (modified from Geoscan research manual, 2002)

5.3 Data processing

5.3.1 GPR data processing

GPR data have been processed using GPR-Slice v7.0 (Goodman, 2017). The radargrams signal processing has been performed through the following steps: (*1*) Post processing pulse regaining, (*2*) DC drift removal, (*3*) Data resampling, (*4*) Band pass filtering, (*5*) Background filtering. With the aim to obtain a planimetric view of anomalous bodies, the time-slice representation technique was applied (Goodman & Piro, 2013). Furthers information are reported in section 4.3.2.

5.3.2 Magnetic data processing

A first processing has been performed using the Geoplot 3.0 software. We employ the following steps (Geoscan Research Geoplot v.3.0 instruction manual, 2003):

- Despike: this process removes spikes caused by metal objects on the ground and it remove instrumental errors.
- Rearranging: it joints together the single squares allowing a general overview of surveyed area
- Zero mean grid: it is performed to eliminate the discontinuity at the joining edges of the individual squares.
- Low Pass filter: it is a low pass filter that removes high frequency and surface noise, allowing the passage of low frequencies that often correspond to the deeper anomalies.
- Interpolation along X and Y: It is applied a Sin (x)/(x) function in order to improve the graphic resolution of the recorded data.

The final result of the aforementioned processing is represented as contour map of the gradient of the vertical component Z of the TMF (fig.5.8).

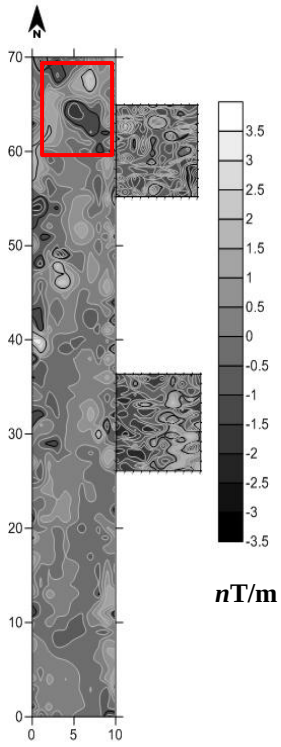

Fig. 5.8 Z contour map of TMF at *Magliano Sabina*; in the red square is presented the only anomaly detectable through the described process.

Fig. 5.8 shows the gradient of the vertical component Z of TMF detected in the *Magliano Sabina* test site; it also shows that sometimes, as in this case, a contour map doesn't show well the geometry and the position of the targets that caused dipolar anomalies. For example, in fig. 5.8 only a dipolar anomaly is visible even if the aforementioned processing has been performed.

In order to overcome this problem the so called "2D normalized cross-correlation" (Piro *et al*., 1998; 2000; 2009) was applied. This technique is based on a comparison in shape between theoretical anomalies, calculated using different contrasts of susceptibility ($\Delta\chi$) and different depths, and the anomalies detected during the survey (Piro *et al*., 1998). For the calculation of the theoretical anomalies relating to a one-dimensional portion 1×1×1 (unit of grid) of the hypothesized body, a specific software written in ITABC, based on algorithms proposed by Talwani (1965) has been used. The theoretical magnetic anomalies were calculated with the following geomagnetic parameters: F=45000 nT, I=55°, D=0° and assuming a uniform magnetization (M) and a constant contrast of susceptibility. The results of the cross-correlation 2D were normalized, in relation to the models used to obtain a variation between -1 and +1. As far as the value of the cross-correlation approximates 1, the more the model employed confirms the experimental data (Piro *et al*., 1998).

We calculated the theoretical anomalies for 0.5 m, 1 m and 2 m below the ground and for different $\Delta\chi$ both positive and negative. They are reported in the table 5.2.

a)

D=0.5 m	$\Delta\chi$ (>0)	2D crosscorrelation result	D=0.5 m	$\Delta\chi$ (< 0)	2D crosscorrelation result
Square Q1	0.0002	1.03	Q1	-0.0002	1.12
Q2	0.00025	1.15	Q2	-0.00025	1.17
Q3	0.0007	1.14	Q3	-0.00025	0.94
Q4	0.0002	1.15	Q4	-0.0007	1.17
Q5	0.0002	0.9	Q5	-0.002	1.11
Q6	0.0002	1.02	Q6	-0.0005	1.12
Q7	0.0002	0.96	Q7	-0.0004	1.12

b)

D=1.0 m	$\Delta\chi$ (>0)	2D crosscorrelation result	D=1.0 m	$\Delta\chi$ (< 0)	2D crosscorrelation result
Square Q1	0.0004	0.90	Q1	-0.0004	0.88
Q2	0.0004	1.05	Q2	-0.0004	1.05
Q3	0.0009	0.89	Q3	-0.0004	0.82
Q4	0.002	0.92	Q4	-0.001	1.15
Q5	0.0009	1.13	Q5	-0.003	0.96
Q6	0.0009	1.15	Q6	-0.001	0.85
Q7	0.00075	0.98	Q7	-0.0007	0.95

c)

D=2.0 m	$\Delta\chi$ (>0)	2D crosscorrelation result	D=2.0 m	$\Delta\chi$ (< 0)	2D crosscorrelation result
Square Q1	0.0006	1.09	Q1	-0.001	1.14
Q2	0.0007	1.02	Q2	-0.001	1.09
Q3	0.00075	1.02	Q3	-0.001	0.9
Q4	0.0009	0.98	Q4	-0.003	0.85
Q5	0.003	0.97	Q5	-0.006	1.1
Q6	0.002	0.93	Q6	-0.003	0.84
Q7	0.003	0.95	Q7	-0.002	0.95

Table 5.2 Value of normalized 2D crosscorrelation for positive and negative $\Delta\chi$; a) D=0.5 m; b) D=1.0 m; c) D=2.0 m

5.4 Data interpretation

5.4.1 GPR data interpretation

Fig. 5.9 shows the most interesting time-slices (400 MHz) for the *Magliano Sabina* test site, the others are reported in the appendix. More in details, for both presented time-slices some low amplitude anomalies are clearly visible among some high amplitude anomalies (fig.5.9). These suggests us that the difference in term of dielectric proprieties between the top and the bottom material is very small (thus $e_0/e_1 \sim 1$). The aforementioned situation could be compatible with buried tomb that during the centuries collapses, and consequently they were filled with the same material of the surrounding area giving as results small amplitude of e.m. waves.

Low amplitude anomalies underlined by red arrows in fig. 5.9 have an round shape and dimensions compatible with tombs typical of Sabine necropolis (Verga, F., ITABC, Personal communication, 2018). In addition, the depth below the ground could be compatible with buried tombs. These anomalies are clearly visible between 0.5 m and 2.0 below the ground (see appendix).

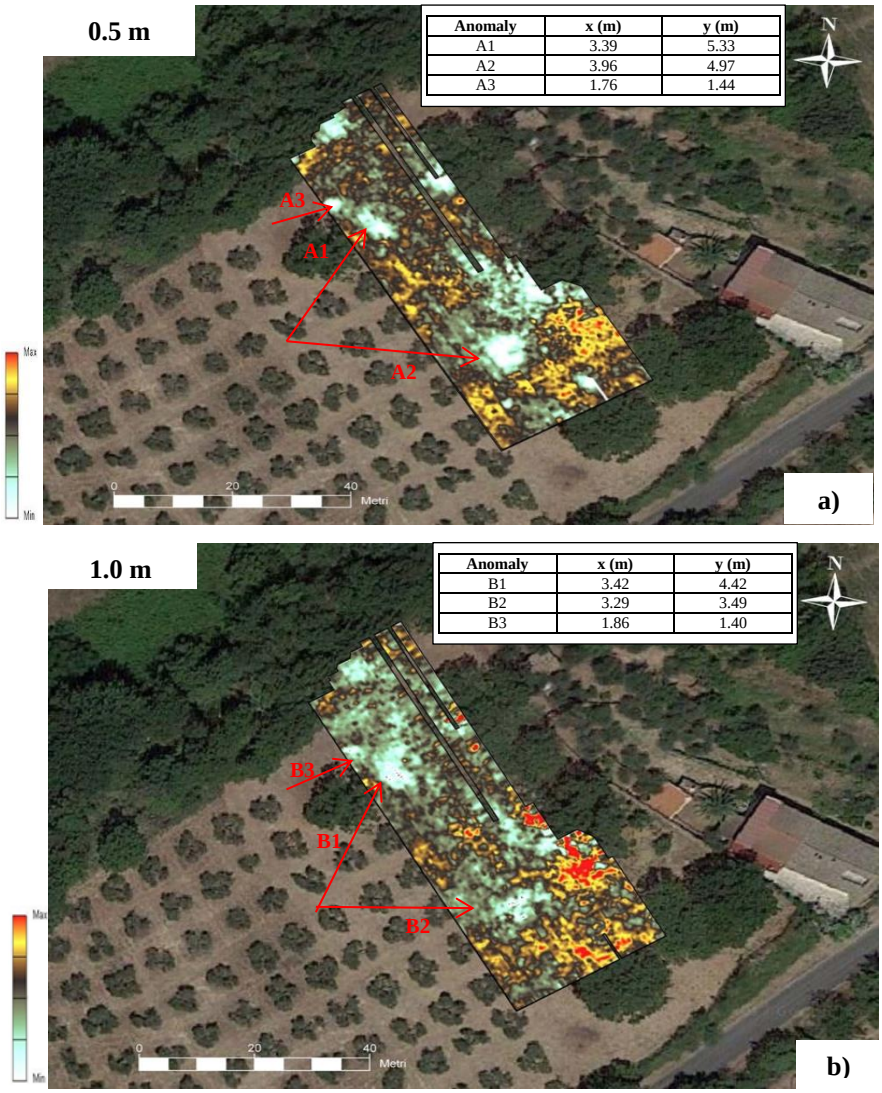

Fig. 5.9 Time-Slices for *Magliano Sabina* test site plotted using AutoCAD3Dmap a) depth about 0.5 m (2.7-5.6 *ns*); in the table the dimensions of the most interesting anomalies are reported b) depth about 1.0 m (7.8-10.8 *ns*); in the tables the dimensions of the most interesting anomalies are reported

5.4.2 Magnetic data interpretation

Fig. 5.10 shows the anomalies detected thought the 2D normalized crosscorrelation for $\Delta\chi$ both positive and negative and for D= 0.5 m and 1.0 m. The other results are presented in the appendix.

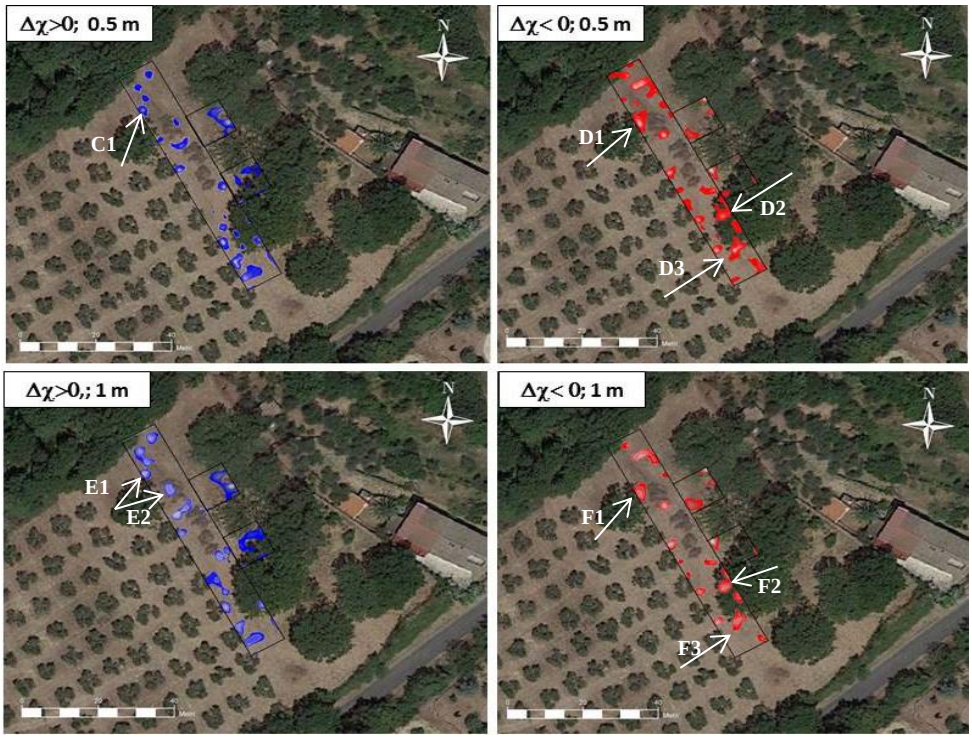

Fig.5.10 Results of 2D normalized crosscorrelation plotted using AutoCAD3Dmap for D =0.5 m and D=1.0 m; in table 5.3 the dimensions of labeled anomalies are reported.

Fig. 5.10 shows a lot of anomalies but some of them (white arrows), are comparable in terms of position with those detected by GPR. Their dimensions (table 5.3) were calculated using a specific function in AutoCAD3D map as previously done for the GPR results.

Anomaly	x (m)	y (m)
C1	1.92	2.60
D1	2.67	5.72
D2	4.54	2.88
D3	3.36	2.59
E1	2.42	3.10
E2	2.56	3.94
F1	2.32	4.78
F2	3.41	3.00
F3	3.62	2.74

Table 5.3 dimensions of anomalies indicated by white arrows of the fig. 5.10; x is the width (in m) and y is the height (in m).

5.5 Results of Data integration

5.5.1 Graphical integration

Fig. 5.11 shows the results of contour map overlay for D= 1.0 m and Δχ both positive and negative. The integrations for other depths are reported in the appendix.

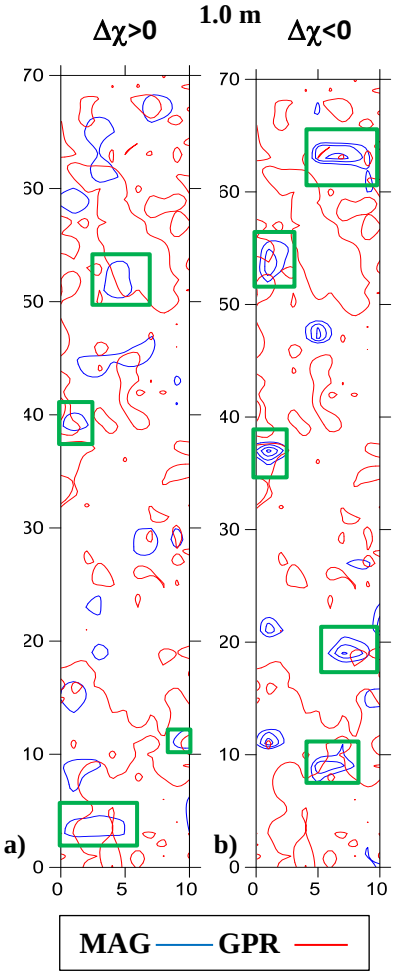

As shown by a simple visual comparison between fluxgate methods and GPR results, there is a good match between the anomalies detected by the two methods. This situation is confirmed by the results of contour map overlay in which the match between the anomalies detected by the employed methods is highlighted by green squares in fig 5.11. As it possible to observe, the main part of match is concentrated in fig.5.11b (Δχ<0).

Fig. 5.11 Contour map overlay at 1.0 m below the ground for Δχ both positive (a) and negative (b); GPR contours are reported in RED, Magnetic contour are reported in DARK BLUE; GREEN squares are matching points. All axes are in m.

Fig. 5.12 shows the results of RGB Colour Composite at D=1.0 m and Δχ both positive and negative. The integrations for other depth are reported in the appendix.

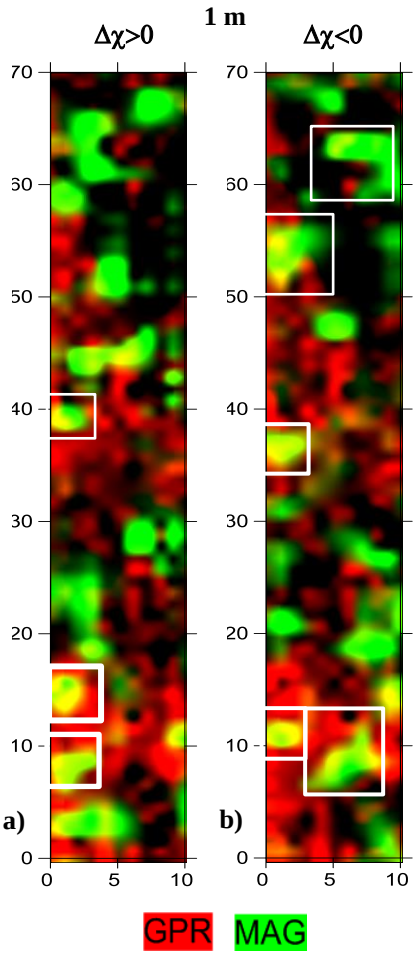

Fig.5.12 shows a good match between the anomalies detected by both methods. In particular, this match is clearly evident where the graphical fusion between red anomalies (**GPR**) and green anomalies (**MAG**) gives "yellow" anomalies as results (white squares in fig.5.12). As it possible to see, the main part of match is concentrated in fig.5.12b (Δχ<0).

Fig. 5.12 RGB Colour composite at 1.0 m below the ground for Δχ both positive (a) and negative (b); GPR anomalies are reported in RED, Magnetic anomalies are reported in GREEN; White squares area matching points. All axes are in m.

5.5.2 Mathematical integration

Before performing mathematical and statistical integration methods, the data collected on the field were normalized using the min-max scaling technique in order to remove the physical meaning of each method and to obtain datasets with values between 0 and 1.

Fig. 5.13 shows the results of Binary integration at D=1.0 m and Δχ both positive and negative. The integrations for other depth are reported in the appendix

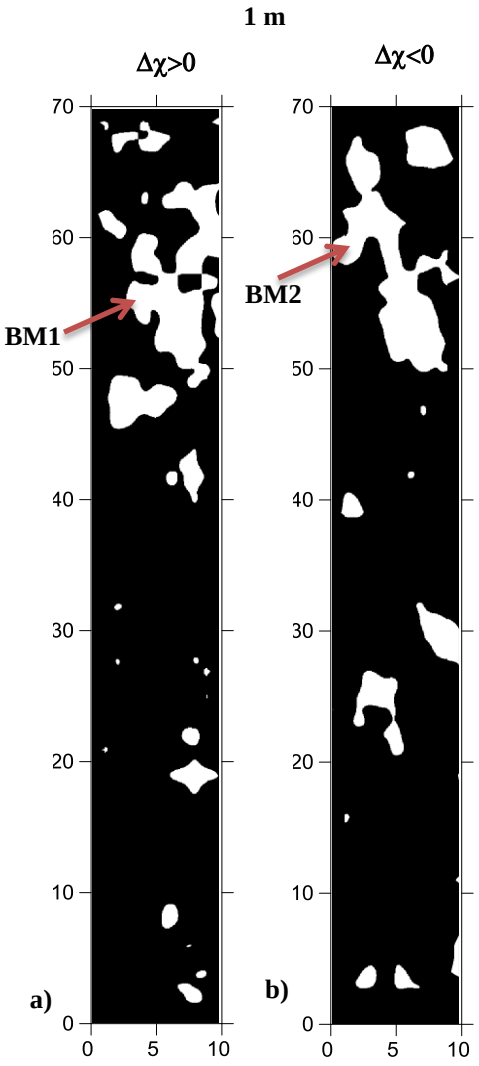

Fig. 5.13 Binary representation at 1.0 below the ground for Δχ both positive (a) and negative (b); All axes are m.

Fig. 5.13 shows that the main parts of the anomalies are concentrated in the upper part of surveyed area; furthermore for both Δχ a huge anomaly oriented NE-SW is present. Anyway it should be stressed that it could not be interpreted as a buried tomb because its dimensions are not comparable with other tombs already known in *Madonna grande* and *Camposanto* area (Verga F.,2018, ITABC personal communication).

Anomaly	x (m)	y (m)
BM1	5,2	9,7
BM2	5.1	14,9

Table 5.4 dimensions of anomalies labeled in fig.5.13; x is the width (in m) and y is the height (in m)

Fig. 5.14 shows the results of Data sum integration at D=1.0 m and Δχ both positive and negative. The integrations for other depths are reported in the appendix.

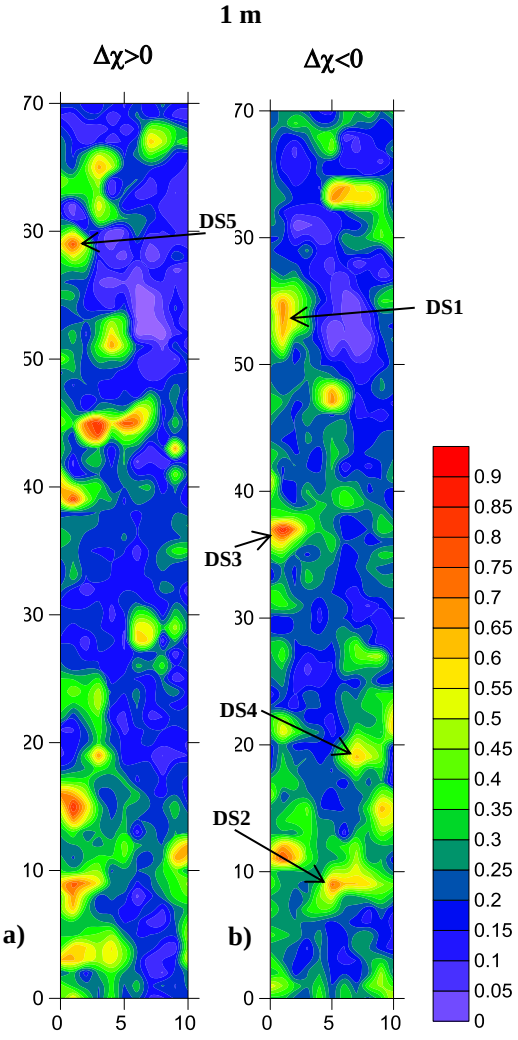

Fig. 5.14 Data sum at 1.0 below the ground for Δχ both positive (a) and negative (b): All axes are in m.

Fig. 5.14 give us a general overview of anomalies detected in the surveyed area just adding two normalized datasets; more in details, blue, green or yellow areas in fig.5.14 are places in which only one of the two applied methods detected an anomaly (values are <<1); areas in orange-red indicated that both methods detected the same anomalies at the same time (values are close to 1). Fig.5.14 confirms again the match zones already detected by graphical integration method but giving us close up view of which are the matching zone; it should be stressed that the orange-red zones labeled in fig.5.14b has dimensions (table 5.4) comparable to them for buried tombs already known in the surrounding area (Verga F.,2018,personal communication). In addition the aforementioned zones has similar location to the low amplitude anomalies detected by GPR methods (fig. 5.9b)

Anomaly (D=1.0 m)	x (m)	y (m)
DS1	2.60	3.72
DS2	3.55	2.30
DS3	2.00	1.34
DS4	2.01	1.91
DS5	1.86	1.85

Table 5.4 dimensions of anomalies labeled in fig.5.14; x is the width (in m) and y is the height (in m)

Fig. 5.15 shows the results of Data product integration at D=1.0 m and Δχ both positive and negative. The integrations for other depths are reported in the appendix.

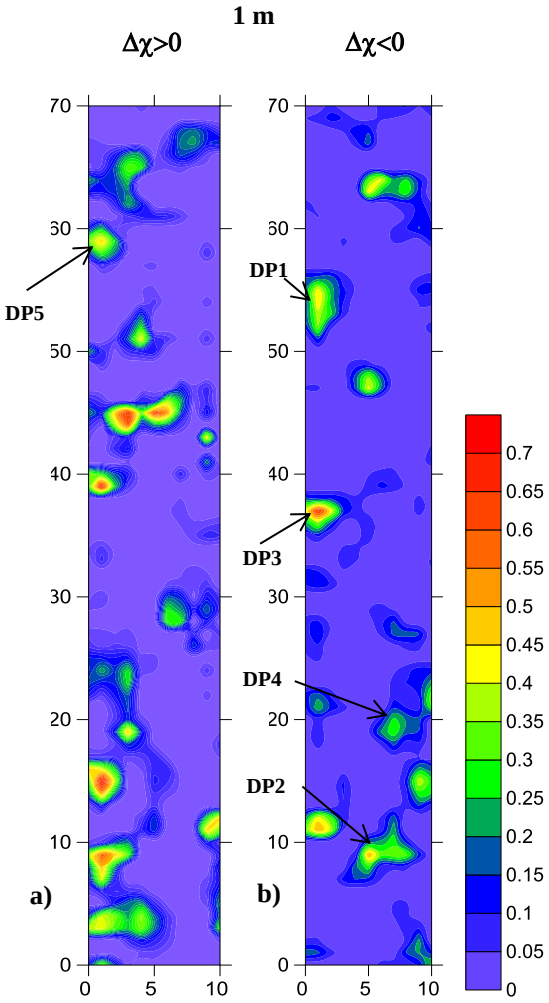

Fig. 5.15 Data sum at 1.0 below the ground for Δχ both positive (a) and negative (b). All axes are in m.

Fig.5.15 gives an accurate view in which place of the surveyed area both methods detected the same anomalies at same time. Thus, for this reason, the area where it occurs is smaller than the area underlined by data sum integration method. The data product method confirms again the match zones previously detected through graphical integration method and data sum. The dimensions of anomalies match with the information referred to Sabine necropolis in the *Magliano Sabina* area (Verga F., ITABC 2018, personal communication). In table 5.5 the dimensions of labeled anomalies in fig. 5.15 are reported. In addition it should be stressed that the aforementioned zones has a similar location to the low amplitude anomalies detected by GPR methods (fig. 5.9b).

Anomaly (D=1.0 m)	**x (m)**	**y (m)**
DP1	1.06	3.04
DP2	1.33	3.17
DP3	1.96	1.31
DP4	1.97	1.90
DP5	1.94	1.80

Table 5.5 dimensions of anomalies labeled in fig.5.15; x is the width (in m) and y is the height (in m).

5.5.3 Statistical integration

Fig. 5.16 shows K-means cluster analysis (see section 3.5) given by GPR 400 MHz time-slices and 2D normalized crosscorrelation results of magnetic data at D=1.0 m and Δχ both positive and negative.

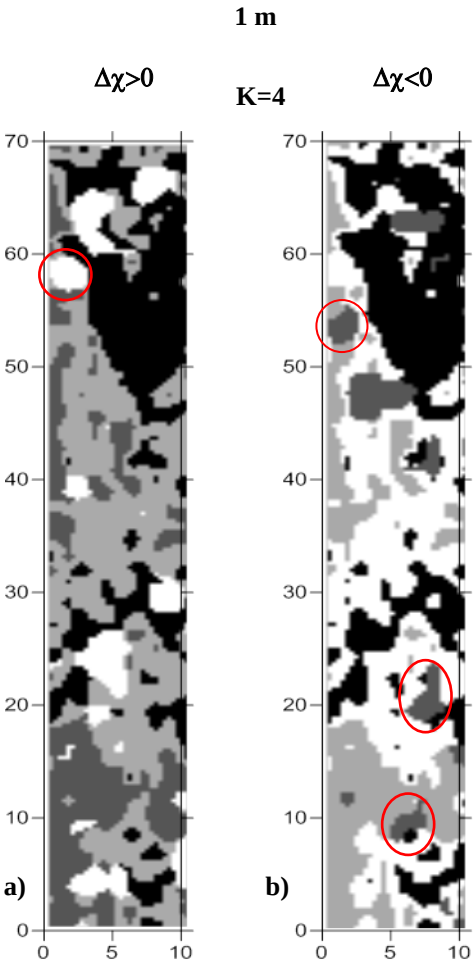

Fig. 5.16 shows an attempt to divide the anomalies detected by both methods in categories, which is the main goal of cluster analysis. In this type of analysis, the operator must choose in how many clusters divide the anomalies detected (e.g. Ray & Turi, 1999). The results are shown by fig.5.16 in which red circles underline anomalies previously detected thought other integration methods: they are assigned to different clusters and they have the same position and size as determined by, the data sum and the data product. It should be stressed that, in this frame, it wasn't possible to assign a class to each cluster.

Fig.5.16 K-means cluster analysis at 1.0 below the ground for Δχ both positive (a) and negative (b). All axes are in m.

Fig. 5.17 shows the results of PCA at D=1.0 m and Δχ both positive and negative.

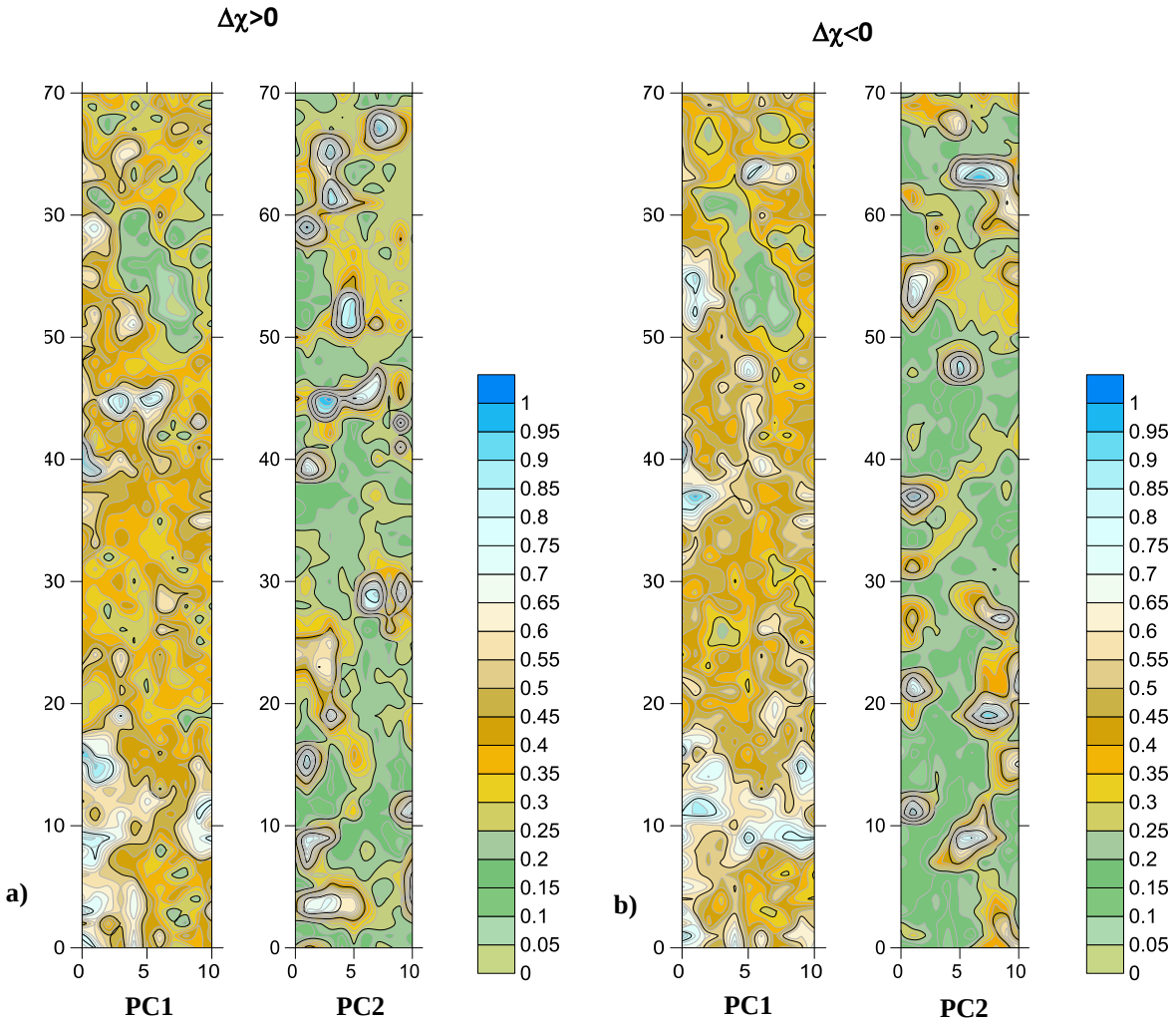

Fig. 5.17 Principal Component Analysis at 1.0 m below the ground for Δχ both positive (a) and negative (b); PC1 and PC2 are first and second component. All axes are in m.

Fig. 5.17 shows that the collected data are generally well correlated because in the aforementioned figure the contribution of both methods is clearly identifiable in both principal components (Abdi & Williams, 2010). The aforementioned information is reported in fig. 5.18; it shows that the data at are correlated up to 92 %. As PCA theory suggests, the PC1 contains the main part of variance thus, just from a statistical point of view, the main part of information which is expressed in terms of Eingenvalues (fig.5.19). In this frame the 97% of information is statistically contained in the PC1 for both Δχ. Generally speaking, PCA method confirms the position of the main anomalies detected by the employed methods; it can be noted comparing just visually the results obtained through the colour map overlay (fig.5.11) and PCA (fig.5.17).

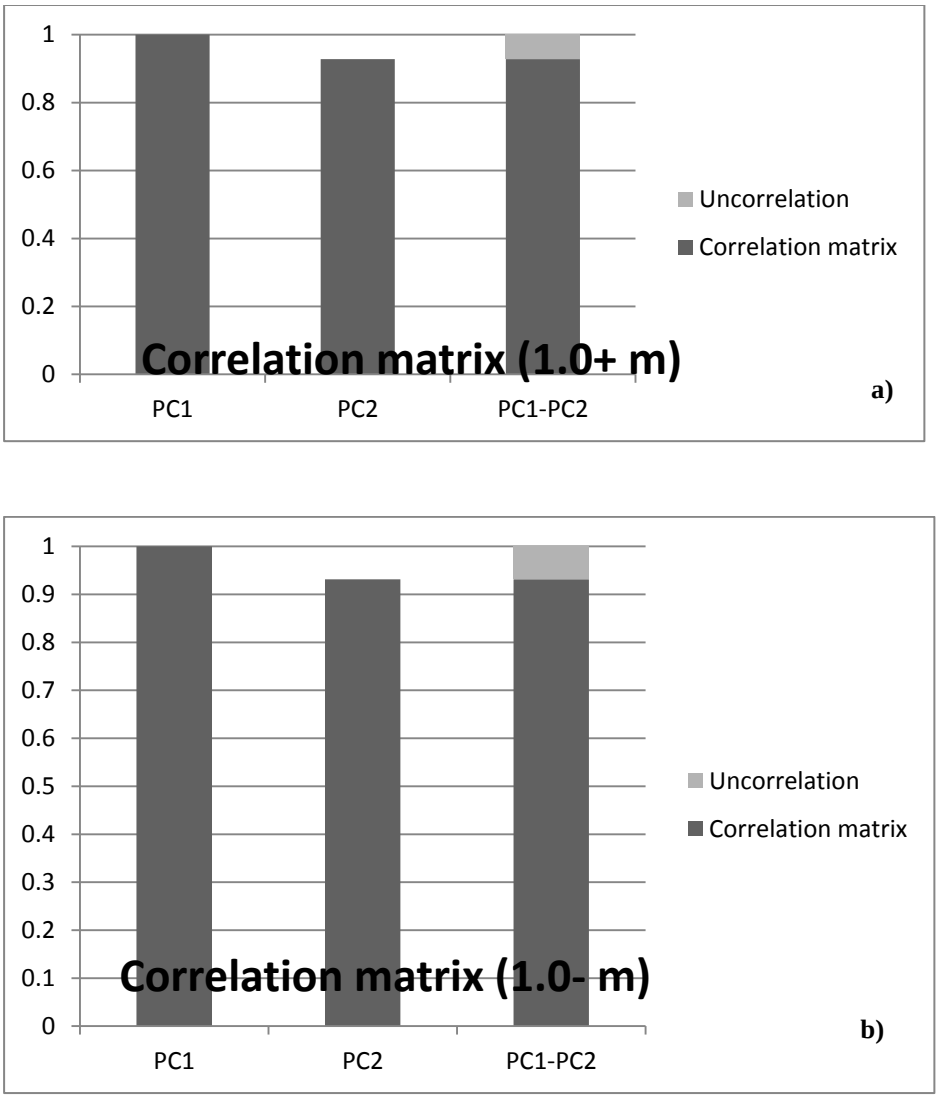

Fig. 5.18 Histogram of correlation matrix for D = 1.0 m and $\Delta\chi$ both (a) positive and (b) negative.

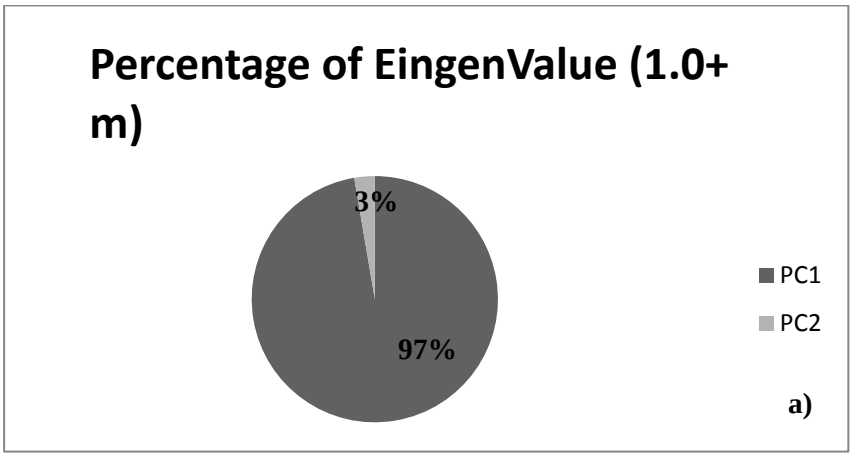

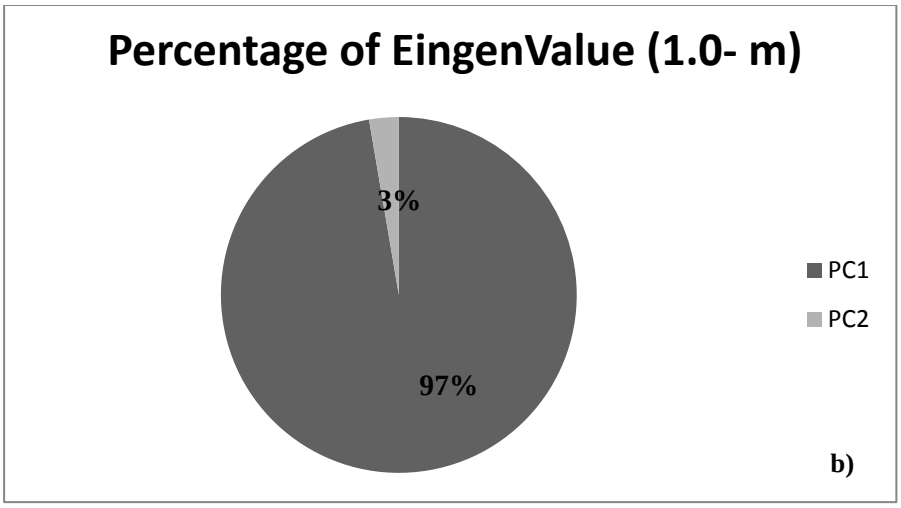

Fig.5.19 Percentage of information expressed in terms of Eigenvalues for D= 1.0 m and Δχ both (a) positive and (b) negative.

Fig. 5.20 shows the results of BME at D=1.0 m and Δχ both positive and negative. The integrations for other depth are reported in the appendix.

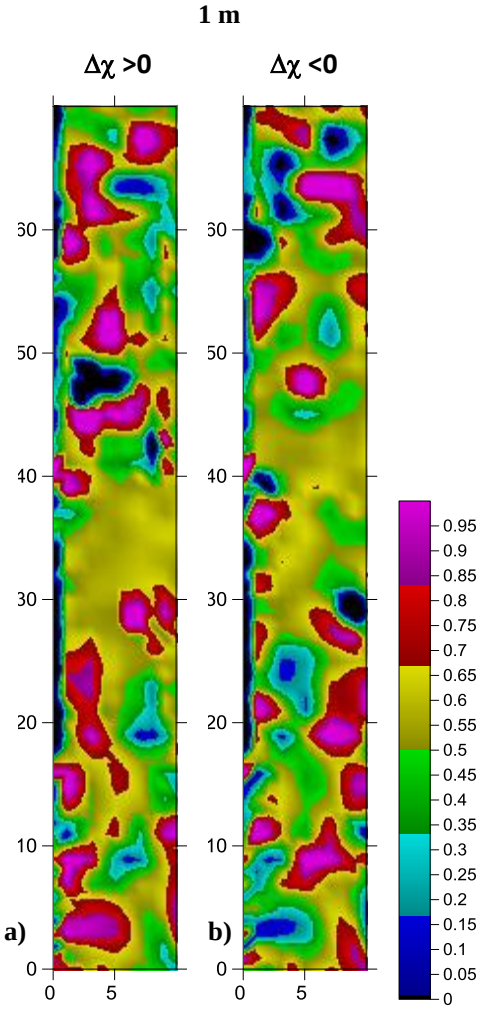

Fig. 5.20 shows that the results of the BME results are quite similar to the data sum (see fig.5.14) but their meaning are very different; in fact purple area in fig.5.20 shows where the results anomalies has the maximum probability to be "true" (0 = minimum probability 1= maximum probability) (Christakos, 2001 p. 95). We also compare the results of BME with an Ordinary Kriging (OK) interpolation in terms of RMSE, Variance and Standard deviation; the results are reported in table 5.7. They show only a small difference among the two interpolation methods (about 10^{-3}) as occurred with *Parco della Caffarella* test site. This result is supported by statistical literature (e.g. Liedtke Tesar, 2011) in which is reported that when we have 50% of hard data end 50 % of soft data different integration methods could produce more or less the same results.

Error (1m) BME	Δχ>0	Δχ<0
RMSE	0.5560	0.5391
VARIANCE	0.0033	0.0031
STD. DEV	0.0578	0.0559
Error (1m) Kriging	**Δχ >0**	**Δχ<0**
RMSE	0.5577	0.5448
VARIANCE	0.0035	0.0066
STD. DEV	0.0592	0.0812

Fig. 5.20 BME for D= 1.0 m and Δχ both (a) positive and (b) negative. Table 5.7 Comparison between BME and Ordinary Kriging (OK): All axes are in m.

5.6 Concluding remarks

We employed different integration methods to merge GPR data and Magnetic fluxgate data with aim to find buried tombs in the *Colle del Giglio* area. In this frame, we can conclude that, in this case, the contour map overlay gives a quickly overview to the match zone between both methods more accurate than the RGB. The data sum gives information in terms of a general overview of anomalies detected by at least one methods and it allows to make a more accurate estimation of the anomalies' dimensions. Referring to statistical integration methods all proposed techniques help the interpretation because, for example, PCA method allows to go deeper in data interpretation giving information in terms of data correlation and amount of information provided by each employ method. The K-means-cluster confirms the shape and position of the more evident anomalies and it assigns them to the same cluster. The BME confirms the results through the data sum method but it should be stressed that it gives also us information in terms of probability of finding results. In addition, it should be emphasized that, in this test site, a careful observation of the data obtained by the single geophysical methods and the study of archaeological literature is extremely important to interpret successfully the results arising from the different integration methods mainly in terms of the position and size of the detected anomalies.

Chapter VI - Final remarks and conclusions

In the present work an attempt to find a quick way to detect buried cavities in suburban environments through integrated geophysical methods has been done. In this frame, we tested eight different integration methods both qualitative and quantitative in two different test sites. Referring to the open questions that addressed these work, we can conclude that:

- The first way to provide a "quick" integration method is to use geophysical instruments that are able to survey large areas into short time like for example GPR and MDF; anyway it should be stressed, as shown by the *Parco della Caffarella* example, that the ERT method is extremely useful as a "control" tool that can be performed before using GPR or MDF in a survey aimed at cavity location.

- The integration methods presented in this work could be useful in the field of engineering geology because they allow to find the location of the cavity network; in fact by performing the data sum and the data product, we can know where the anomalies have been detected at least by one method and by both employed method respectively. However, in order to be able to interpret effectively the results of the integration methods, they must be observed in the light of the results obtained through the single methods as shown by the emblematic case of *Magliano Sabina*. Finally, we cannot avoid taking into account the geoarchaeological framework for a correct interpretation of the results.

- The hypothesis on conservation state of the cavity network can be done satisfactorily by a visual comparison between the single employed methods without the need to perform the integration methods presented in this work: it confirms what is presented in Cammarano *et al*.,(1998)

- The presented results show that it is not possible to identify which is the" best" integration method; in fact, each of them provide a kind of contribution in terms of interpretation but some of them are now useful for engineering geology problems (e.g. Contour map overlay, Data sum and Data product) while others are still on "research state" (K-means cluster analysis, PCA and BME). More in detail, using a metaphor, we could affirm that using different integration techniques is how to use an elevator to reach the different floors of a building; by visual comparison of various methods (first floor) up to the roof (the BME). As you climb one floor, the knowledge about the collected datasets tends to rise also to the detriment of a full applicability of them in engineering geology field.

References

Abdi, H., & Williams, L. J. (2010). Principal component analysis. *Wiley interdisciplinary reviews: computational statistics*, *2*(4), 433-459.

Annan, A. P., & Cosway, S. W. (1992). Simplified GPR beam model for survey design. In *SEG Technical Program Expanded Abstracts 1992* (pp. 356-359). Society of Exploration Geophysicists.

Annan, A.P. and Cosway, S.W., (1994), GPR Frequency Selection. *Proceedings of the Fifth International Conference on Ground-Penetrating Radar*, Kitchener, Ontario, Canada, June 12-16, 1994, pp. 747-760.

Annan, A. P. (2005). Ground-penetrating radar. In *Near-surface geophysics* (pp. 357-438). Society of Exploration Geophysicists.

Aspinall, A., Gaffney, Ch., Schmidt, A. Magnetometry for Archaeologists (2008) ISBN-10: 978-0- 7591-1106-6 Altamira Press. Plymouth

Balia R, Gavaudo E, Ardau F, Ghiglieri G (2003) Case history: geophysical approach to the environmental study of a coastal plain. *Geophysics* 68(5):1446–1459.

Balkaya, Ç., Göktürkler, G., Erhan, Z., & Levent Ekinci, Y. (2012). Exploration for a cave by magnetic and electrical resistivity surveys: Ayvacık Sinkhole example, Bozdağ, İzmir (western Turkey). *Geophysics*, *77*(3), B135-B146.

Barone, P.M., Carlucci G., Smriglio F., Basile F., Della Monica G. (2015) Can Integrated Geophysical Investigations Solve an Archaeological Problem? The Case of the So-Called Domus septem Parthorum in Rome (Italy). *International Journal of Archaeology.* Special Issue: Archaeological Sciences. Vol. 3, No. 1-1, 2015, pp. 21-25. doi: 10.11648/j.ija.s.2015030101.1

Batayneh, A. T., Abueladas, A. A., & Moumani, K. A. (2002). Use of ground-penetrating radar for assessment of potential sinkhole conditions: an example from Ghor al Haditha area, Jordan. *Environmental Geology*, *41*(8), 977-983.

Benson, A.K., (1995) . Applications of ground penetrating radar in assessing some geological hazards: examples of groundwater contamination, faults, cavities. *J. Appl. Geophys*. 33, 177 – 193

Bevington, P. R., & Robinson, D. K. (1992). Estimates of mean and errors. *Data Reduction and Error Analysis for the Physical Sciences*, *3*, 53-54.

Bianchi Fasani G, Bozzano F, Cercato M (2012). The underground cavity network of south-eastern Rome (Italy): an evolutionary geological model oriented to hazard assessment. *Bulletin of Engineering Geology and the Environment*, 70(4):533–542. doi: 10.1007/ s10064-011-0360-0

Bianchi Fasani G., Bozzano F., Cardarelli E., Cercato M., (2013) Underground cavity investigation within the city of Rome (Italy): a multi-disciplinary approach combining geological and geophysical data. *Engineering Geology* vol.159 p.109-121.

Bitri, A., Samyn, K., & Filippi, C. (2016). Can We Really Detect Cavities Using Seismic Surface Wave?. In *Near Surface Geoscience 2016-22nd European Meeting of Environmental and Engineering Geophysics*.

Bogaert, P., & D'Or, D. (2002). Estimating soil properties from thematic soil maps. *Soil Science Society of America Journal*, *66*(5), 1492-1500.

Boubaki, N., Saintenoy, A., & Tucholka, P. (2011). GPR profiling and electrical resistivity tomography for buried cavity detection: A test site at the abbaye de l'Ouye (France). In *Advanced Ground Penetrating Radar (IWAGPR), 2011 6th International Workshop on* (pp. 1-5). IEEE.

Brizzolari, E., Ermolli, F., Orlando, L., Piro, S., & Versino, L. (1992). Integrated geophysical methods in archaeological surveys. *Journal of Applied Geophysics*, *29*, 47-55.

Calzolari, V., & Olivieri, M. (2010). Piano per il Parco dell'Appia antica . Italia nostra (Association). Sezione romana.

Cammarano, F., Mauriello, P., Patella, D., & Piro, S. (1997). Integrated geophysical methods for archaeological prospecting. *Volcanism and Archaeology in Mediterranean Area*.

Campana, S., & Piro, S. (Eds.). (2008). *Seeing the unseen. Geophysics and landscape archaeology*. CRC Press.

Cardarelli E., Di Filippo G., Tuccinardi D., (2006). Electrical Resistivity Tomography to detect buried cavity in Rome (A case Study), *Near Surface Geophysics* V. 5 N° 1 387-3

Cardarelli, E., Fischanger, F., & Piro, S. (2008). Integrated geophysical survey to detect buried structures for archaeological prospecting. A case-history at Sabine Necropolis (Rome, Italy). *Near Surface Geophysics*, *6*(1), 15-20.

Cardarelli, E., Cercato, M., Cerreto, A., & Di Filippo, G. (2010). Electrical resistivity and seismic refraction tomography to detect buried cavities. *Geophysical Prospecting*, *58*(5), 685-695.

Castelluccio, C., (2012). Studio del soil radon nel test-site della valle della Caffarella (Roma) [Ph.D Thesis, in Italian]. Università Roma Tre.

Chen, L., Gao, S., Zhang, H., Sun, Y., Ma, Z., Vedal, S., ... & Bai, Z. (2018). Spatiotemporal modeling of PM 2.5 concentrations at the national scale combining land use regression and Bayesian maximum entropy in China. *Environment international*, *116*, 300-307.

Choi, K. M., Christakos, G., & Wilson, M. L. (2006). El Niño effects on influenza mortality risks in the state of California. *Public health*, *120*(6), 505-516.

Christakos, G. (1990). A Bayesian/maximum-entropy view to the spatial estimation problem. *Mathematical Geology*, *22*(7), 763-777.

Christakos, G. (2000). *Modern spatiotemporal geostatistics* (Vol. 6). Oxford University Press.

Christakos, G., Bogaert, P., & Serre, M. (2001). *Temporal GIS: advanced functions for field-based applications*. Springer Science & Business Media.

Coléou, T., Poupon, M., & Azbel, K. (2003). Unsupervised seismic facies classification: A review and comparison of techniques and implementation. *The Leading Edge*, *22*(10), 942-953.

Colosi, F., Costantini, A., Gabrielli, R., Piro, S., & Santoro, P. (2000). Lo studio del territorio impiegando diverse metodologie d'indagine: il caso della valle del Tevere. *Archeologia e Calcolatori, 11*, 171-189.

Conolly, J. and Lake, M., (2006). *Geographical Information Systems in Archaoelogy: Cambridge Manuals In Archaeology*. Cambridge, UK: Cambridge University Press.

Conyers, L. B. & Goodman, D. (1997). Ground Penetrating Radar. An Introduction for Archaeologists. Walnut Creek: Altamira Press

Conyers, L. B. (2009). Ground-penetrating radar for landscape archaeology: method and applications. *Seeing the Unseen. Geophysics and Landscape Archaeology*, 245-255.

Cormack, R., (1971). A review of classification, *Journal of the Royal Statistical Society A*, 134, 321-367

Crescenzi, R., Piro M. & Vallesi L., (1995) Le cavità sotterranee a Roma. In: "La geologia di Roma: il centro storico", *Mem. Descr. Carta Geol. d'It*., 50: 249-278.

Daniels, D. J. (Ed.). (2004). *Ground penetrating radar* (Vol. 1). Iet.

Davis, J.L. and Annan, A.P. (1989) Ground Penetrating Radar for High Resolution Mapping of Soil and Rock Stratigraphy. *Geophysical Prospecting*, 37, 531-551. https://doi.org/10.1111/j.1365-2478.1989.tb02221.x

Davis, L. (2000). Handbook of genetic algorithms. Nostrand, New York, N.Y.

deGroot-Hedlin, C., & Constable, S. (1990). Occam's inversion to generate smooth, two-dimensional models from magnetotelluric data. *Geophysics*, *55*(12), 1613-1624.

Di Filippo M., Toro B., (1999) Individuazione di aree urbane soggette a rischio di crollo per la presenza di cavità ipogee. ATTI del Convegno "*Le cavità sotterranee nell'area urbana e della Provincia. Problemi di pericolosità e gestione*"-Roma, Servizio Geologico e Difesa del Suolo- 165,Provincia di Roma/Società Italiana di Geologia Ambientale- Sezione Lazio, Sistema Informativo Provinciale. pp.73-82.

Di Filippo M., Nolasco F., Rizzo S. & Toro B. (2004) - Indagini geolfisiche per l'individuazione di aree a rischio sinkhole nella Piana di S. Vittorino (RI). Atti Conv: "Stato dell'arte sullo studio dei fenomeni di sinkholes e ruolo delle amministrazioni statali e locali nel governo del territorio di Roma". 20-21 maggio 2004, 389-398.

Dobecki, T.L. and Upchurch, S.B., (2006). Geophysical applications to detect sinkholes and ground subsidence: *The Leading Edge*, 25, 336-341, doi:10.1190/1.2184102

Doneus, M., & Neubauer, W. (1998). 2D combination of prospection data. *Archaeological Prospection*, *5*(1), 29-56.

D'Or, D., Bogaert, P., & Christakos, G. (2001). Application of the BME approach to soil texture mapping. *Stochastic Environmental Research and Risk Assessment*, *15*(1), 87-100.

Douaik, A., Van Meirvenne, M., & Tóth, T. (2005). Soil salinity mapping using spatio-temporal kriging and Bayesian maximum entropy with interval soft data. *Geoderma*, *128*(3-4), 234-248.

Edwards L.S., (1977). A modified pseudosection for resistivity and induced-polarization. Geophysics, 42, 1020-1036.

Ellis, R. G., & Oldenburg, D. W. (1994a). Applied geophysical inversion. *Geophysical Journal International*, *116*(1), 5-11.

El-Qady, G., Hafez, M., Abdalla, M. A., & Ushijima, K. (2005). Imaging subsurface cavities using geoelectric tomography and ground-penetrating radar. *Journal of Cave and Karst studies*, *67*(3), 174-181.

Ernenwein, E. G. (2009). Integration of multidimensional archaeogeophysical data using supervised and unsupervised classification. *Near Surface Geophysics*, *7*(3), 147-158.

Funiciello, R., & Giordano, G. (2008). Carta Geologica di Roma alla scala 1: 10000. *Dipartimento Scienze Geologiche Università Roma TRE-Comune di Roma-APAT. DVD insert to Mem. Descr. Carta Geol. d'It.*, *80*.

Garcia-Garcia, F., Valls-Ayuso, A., Benlloch-Marco, J., & Valcuende-Paya, M. (2017). An optimization of the work disruption by 3D cavity mapping using GPR: A new sewerage project in Torrente (Valencia, Spain). *Construction and Building Materials*, *154*, 1226-1233.

Gazley, M. F., Collins, K. S., Roberston, J., Hines, B. R., Fisher, L. A., & McFarlane, A. (2015). Application of principal component analysis and cluster analysis to mineral exploration and mine geology. In AusIMM New Zealand Branch Annual Conference. the origin and geochemical behavior of potentially hazardous elements in sediment around the Sarcheshmeh copper mine, SE Iran." *Environmental Earth Sciences* (Vol. 66, No. 2, pp. 589-605).

Geoscan Research (2003). Geoplot 3.00 for Windows: Instruction Manual Version 3.00. *Bradford, United Kingdom*.

Gibson, P.J. P. Lyle, and George D.M.,(2004). Application of resistivity and magnetometry geophysical techniques for near-surface investigations in karstic terranes in Ireland. *Journal of Cave and Karst Studies*, v. 66, no. 2, p. 35-38.

Girotti, O., & Mancini, M. (2003). Plio-Pleistocene stratigraphy and relations between marine and non-marine successions in the Middle Valley of the Tiber River (Latium, Umbria). *Il Quaternario*, *16*(1), 89-106.

Giustini, F., Brilli, M., & Mancini, M. (2018). Geochemical study of travertines along middle-lower Tiber valley (central Italy): genesis, palaeo-environmental and tectonic implications. *International Journal of Earth Sciences*, *107*(4), 1321-1342.

Goodman, D., & Piro, S. (2013). *GPR remote sensing in archaeology* (Vol. 9). New York: Springer.

Goodman, D. (2017). GPR-SLICE v7.0 Manual. *www.gpr-survey.com*.

Hargrave, M. L. (2006). Ground truthing the results of geophysical surveys. *Remote Sensing in Archaeology: An Explicitly North American Perspective*, 269-304.

Heath, P., Gouthas, G., Irvine, J. A., Dutch, R. A., & Krapf, C. B. E. (2017). *Microgravity surveys to identify potential hidden cavities on the Nullarbor*. Department of the Premier and Cabinet.

Hill, I., (2008). Resolution and quality assurance in near-surface geophysical surveys: A multimethod field trail and results. *The Leading Edge*, 27 (11), 1516–1524.

Jain, A. K. (2010). Data clustering: 50 years beyond K-means. *Pattern recognition letters*, *31*(8), 651-666.

Jat, P., & Serre, M. L. (2016). Bayesian Maximum Entropy space/time estimation of surface water chloride in Maryland using river distances. *Environmental pollution*, *219*, 1148-1155.

Jol, H. M. (Ed.). (2008). *Ground penetrating radar theory and applications*. elsevier.

Jolliffe, I. T., & Cadima, J. (2016). Principal component analysis: a review and recent developments. *Phil. Trans. R. Soc. A*, *374*(2065), 20150202.

Jongmans, D., Garambois, S., (2007). Geophysical investigation of landslides: a review. *Bulletin de la Société Géologique de France*, 178 (2), 101–112.

Kalayci, T., (2013). Data Integration in Archaeological Prospection, *Best Practices of GeoInformatic Technologies for the Mapping of Archaeolandscapes*.Edited by Apostolos Sarris, Archaeopress Archaeology, 71-84.

Kearey, P., Brooks, M., & Hill, I. (2013). *An introduction to geophysical exploration*. John Wiley & Sons.

Keay, S., Earl, G., Hay, S., Kay, S., Ogden, J., & Strutt, K. D. (2009). The role of integrated geophysical survey methods in the assessment of archaeological landscapes: the case of Portus. *Archaeological Prospection*, *16*(3), 154-166.

Kucukdemirci,M., Piro.S.,Baydemir,N.,Ozer.,E. Zamuner.,D. (2015). Mathematical and Statistical Integration approach on archaeological prospection data,case studies from Aizanoi-Turkey. *43rd Computer Applications and Quantitative Methods in Archaeology*, Siena.

Küçükdemirci, M., Özer, E., Piro, S., Baydemir, N., & Zamuner, D. (2018). An application of integration approaches for archaeo-geophysical data: Case study from Aizanoi. *Archaeological Prospection*, *25*(1), 33-44.

Kvamme, K. L. (2007). Integrating multidimensional geophysical data. *Archaeological Prospection*, *13*(1), 57-72.

Lanzini M., (1999). Indagine sulle cavità di via Borsa (V Circoscrizione, Roma). Atti del Convegno "*Le cavità sotterranee nell'area urbana e della Provincia. Problemi di pericolosità e gestione*"- Roma, Servizio Geologico e Difesa del Suolo- Provincia di Roma/Società Italiana di Geologia Ambientale- Sezione Lazio, Sistema Informativo Provinciale. pp.151-159.

Law, D. C. G., Bernstein, K. T., Serre, M. L., Schumacher, C. M., Leone, P. A., Zenilman, J. M., ... & Rompalo, A. M. (2006). Modeling a syphilis outbreak through space and time using the Bayesian maximum entropy approach. *Annals of Epidemiology*, *16*(11), 797-804.

Leparoux, D., Grandjean, G., & Bitri, A. (1999). Underground cavities detection using seismic Rayleigh waves. In *5th EEGS-ES Meeting*.

Leucci, G., (2015) Geofisica applicata all'archeologia e ai beni monumentali. Dario Flaccovio ed. ISBN 978-88-579-0506-8.

Liedtke Tesar, M. L. (2011). A comparison of spatial prediction techniques using both hard and soft data [Ph.D Thesis]. *University of Nebraska-Lincoln*,USA

Lillesand, T., Kiefer, R. W., & Chipman, J. (2008). *Remote sensing and image interpretation*. John Wiley & Sons.

Loke, M. H., & Barker, R. D. (1996). Rapid least-squares inversion of apparent resistivity pseudosections by a quasi-Newton method 1. *Geophysical prospecting*, *44*(1), 131-152.

Loke, M. H. (2001). Res2DMod ver. 3.02 a. Geotomo Software.

Loke, M. H., & Dahlin, T. (2002). A comparison of the Gauss–Newton and quasi-Newton methods in resistivity imaging inversion. *Journal of applied geophysics*, *49*(3), 149-162.

Loke, M. H. (2004). Tutorial: 2-D and 3-D electrical imaging surveys.

MacQueen, J., (1967). Some methods for classification and analysis of multivariate observations. In: Fifth Berkeley Symposium on Mathematics. *Statistics and Probability*. University of California Press, pp. 281–297.

Mancini, M., Girotti, O., & Cavinato, G. P. (2004). Il Pliocene e il Quaternario della media valle del Tevere (Appennino Centrale). *Geologica Romana*, *37*(2003-2004), 175-236.

Mancini, M., & Cavinato, G. P., (2005). The Middle Valley of the Tiber River, Central Italy: Plio-Pleistocene Fluvial and Coastal Sedimentation, Extensional Tectonics and Volcanism. *Fluvial sedimentology VII*, 373-396.

Marrs, A., Leighly, K., Wagner, C., & Macinnis, F. (2017). EMPCA and Cluster Analysis of Quasar Spectra: Construction and Application to Simulated Spectra. In *American Astronomical Society Meeting Abstracts* (Vol. 229).

Martinez-Moreno, F. J., J. Galindo-Zaldívar, A. Pedrera, T. Teixido, P. Ruano, J. A. Peña, L. González-Castillo, A. Ruiz-Constán, M. López-Chicano, and W. Martín-Rosales, (2014), Integrated geophysical methods for studying the karst system of Gruta de las Maravillas (Aracena, Southwest Spain): *Journal of Applied Geophysics*, 107, 149–162, doi: 10.1016/j.jappgeo.2014.05.021.

McElhinny, M. W., & McFadden, P. L. (1998*). The magnetic field of the earth: paleomagnetism, the core, and the deep mantle* (Vol. 63). Academic Press.

McMechan, G.A., Gaynor, G.C. and Szerbiak, R.B. (1997), Use of ground-penetrating radar for 3-D sedimentological characterization of clastic reservoir analogs. *Geophysics*, 62, 786–796.

McNeill, J. D. (1980). Electrical conductivity of soils and rocks, Technical Note TN-5, Geonics Ltd. *Mississauga, Ontario*, 22.

Metwaly, M., & AlFouzan, F. (2013). Application of 2-D geoelectrical resistivity tomography for subsurface cavity detection in the eastern part of Saudi Arabia. *Geoscience Frontiers*, 4(2013), 469-476.

Mochales, T., Casas, A. M., Pueyo, E. L., Pueyo, O., Román, M. T., Pocoví, A., ... & Ansón, D. (2008). Detection of underground cavities by combining gravity, magnetic and ground penetrating radar surveys: a case study from the Zaragoza area, NE Spain. *Environmental Geology*, *53*(5), 1067-1077.

Moghaddam, S., Dejpasand, S., Rohani, A.K., Parnow, S. & Ebrahimi, M. (2017). Detection and determination of groundwater contamination plume using time-lapse electrical resistivity tomography (ERT) method. *Journal of Mining and Environment* 8(1): 103-110

Morey, R. M. (1974). Continuous subsurface profiling by impulse radar. In *Proc. Engineering Foundation Conf.* (pp. 213-232).

Neal, A. (2004). Ground-penetrating radar and its use in sedimentology: principles, problems and progress. *Earth-science reviews*, *66*(3-4), 261-330.

Neubauer, W., & Eder-Hinterleitner, A. (1997). Resistivity and magnetics of the Roman town Carnuntum, Austria: an example of combined interpretation of prospection data. *Archaeological Prospection*, *4*(4), 179-189.

Norinelli, A. (1996). *Elementi di geofisica applicata*. ISBN-10: 8855523945, Patron ed.

Ogden, J., Strutt, K., Keay, S., Earl, G., & Kay, S. (2010). Geophysical prospection at Portus: an evaluation of an integrated approach to interpreting subsurface archaeological features.

Orlando, L. (2013). GPR to constrain ERT data inversion in cavity searching: Theoretical and practical applications in archeology. *Journal of Applied Geophysics*, *89*, 35-47.

Patro, S., & Sahu, K. K. (2015). Normalization: A preprocessing stage. *arXiv preprint arXiv:1503.06462*.

Piersanti, M., & Della Monica, G.(2015) Metodi Geofisici per l'esplorazione del sottosuolo. Univ. Roma Tre, p.184.

Piro S., (1996). Integrated geophysical prospecting in Ripa Tetta neolithic site (Lucera - Foggia, Italy). *Archaeological Prospection*, Vol. 3, 81-88.

Piro S., (1998). Multimethodological approach using GPR, Magnetic and Geoelectric methods to detect archaeological structures. *Special Issue "Filtering, optimisation and modelling of geophysical data in archaeological prospecting*", Prospezioni Archeologiche (Fondazione Lerici), 135-148.

Piro, S., Samir, S., & Versino, L. (1998). Position and spatial orientation of magnetic bodies from archaeological magnetic surveys. *Annals of Geophysics, 41(3).*

Piro S., Cammarano F., Mauriello P., (2000). Quantitative integration of geophysical methods for archaeological prospection. *Archaeological Prospection*, Vol. 7, n.4, pp 203-213.

Piro S., Tsourlos P. and Tsokas G.N. (2001). Cavity detection employing advanced geophysical techniques: a case study. *European Journal of Environmental and Engineering Geophysics* 6, 3–31.

Piro S, Sambuelli L, Godio A, Taormina R. (2007). Beyond image analysis in processing archaeomagnetic geophysical data: case studies of chamber tombs with dromos. *Near Surface Geophysics* 5: 405–414.

Piro, S., & Gabrielli, R. (2009). Multimethodological approach to investigate chamber tombs in the Sabine Necropolis at Colle del Forno (CNR, Rome, Italy). *Archaeological Prospection*, *16*(2), 111-124.

Piro, S., (2012) Dispense del Corso di Geofisica Applicata. Univ. La Sapienza.

Piro, S., Papale, E., & Zamuner, D. (2016). Different integrated geophysical approaches to investigate archaeological sites in urban and suburban area. In *EGU General Assembly Conference Abstracts* (Vol. 18, p. 2128).

Piro, S., Papale, E., Kucukdemirci, M., & Zamuner, D. (2017). Analysis and interpretation of geophysical surveys in archaeological sites employing different integrated approach. In *EGU General Assembly Conference Abstracts* (Vol. 19, p. 3355).

Raper, J. (Ed.). (1989). *Three dimensional applications in GIS*. CRC Press.

Ray, S., & Turi, R. H. (1999). Determination of number of clusters in k-means clustering and application in colour image segmentation. In *Proceedings of the 4th international conference on advances in pattern recognition and digital techniques* (pp. 137-143).

Rendina C., Paradisi D., (2004). *Le strade di Roma*, volume primo A-D, Roma, Newton & Compton editori, ISBN 88-541-0208-3.

Reynolds, J. M. (2011). *An introduction to applied and environmental geophysics*. John Wiley & Sons.

Roberts, R.L., and J.J. Daniels, 1996, Analysis of GPR Polarization Phenomena: Journal of Environmental and Engineering Geophysics, vol. 1, No.2, p. 139-157.

Rubio-Melendi, D., Gonzalez-Quirós, A., Roberts, D., García, M. D. C. G., Domínguez, A. C., Pringle, J. K., & Fernández-Álvarez, J. P. (2018). GPR and ERT detection and characterization of a mass burial, Spanish Civil War, Northern Spain. *Forensic science international*, *287*, e1-e9.

Santoro W.M.,& Federici V., (1999) Studi e indagini di un sistema di cavità sul colle Aventino: valutazione del rischio nell'area urbana di via San Giosafat e proposte di intervento per il ripristino della viabilità. Atti del Convegno "*Le cavità sotterranee nell'area urbana e della Provincia. Problemi di pericolosità e gestione*"- Roma, Servizio Geologico e Difesa del Suolo- Provincia di Roma/Società Italiana di Geologia Ambientale- Sezione Lazio, Sistema Informativo Provinciale. pp.59-72

Santoro,P.,(1996a). Il museo di Magliano Sabina nella prospettiva delle ricerche sulla cultura sabina, in identità e civiltà dei Sabini. *Atti del XVIII Convegno di Studi Etruschi e Italici*, (Rieti-Magliano Sabina 30 maggio-3giugno 1993) Firenze,pp.275-285.

Sayar, A., Pierce, M., & Fox, G. (2005). Developing GIS visualization web services for geophysical applications. In *ISPRS 2005 spatial data mining workshop, Ankara, Turkey*.

Schowengardt, R. A., 1997. Remote Sensing: Models and Methods for Image Processing. San Diego: Academic Press.

Sciotti.M., (1999). Il sottosuolo delle aree urbane: risorsa o minaccia?. Atti del Convegno "*Le cavità sotterranee nell'area urbana e della Provincia. Problemi di pericolosità e gestione"*-Roma, Servizio Geologico e Difesa del Suolo- Provincia di Roma/Società Italiana di Geologia Ampientale- Sezione Lazio, Sistema Informativo Provinciale. pp.16-19.

Scotto di Santolo, A., Evangelista, L., Silvestri, F., Cavuoto, G., Di Fiore, V., Punzo, M., ... & Evangelista, A. (2015). Investigations on the stability conditions of a tuff cavity: the Cimitero delle Fontanelle in Naples. *Rivista Italiana di Geotecnica XLIX (3)*, 28-46.

Serre M. L. (1999). Environmental Spatiotemporal Mapping and Groundwater Flow Modeling Using the BME and ST Methods [Ph.D Thesis]. Chapel Hill: University of North Carolina.

Serre ML, Christakos G (1999). Modern geostatistics: computational BME in the light of uncertain physical knowledge – TheEquus Beds study. *Stochastic Environ Res Risk Assessment* 13(1/2): 1–26.

Sheffield, T. M., Harvey, E. L., Lees, J., Meyer, D., Payne, B., and Zeitlin, M., (2000). Geovolume visualization interpretation: A lexicon of basic techniques. *The Leading Edge*, 19 (5), 518–522.

Sheriff, R. E., & Geldart, L. P. (1982). Exploration seismology: history, theory, and data acquisition, vol. 1.

Smith, L. I. (2002). A Tutorial on Principal Component Analysis. Available at: http://csnet.otago.ac.nz/cosc453/student_tutorials/principal_components. pdf. Accessed July 18, 2018.

Soldovieri MG, (2006). Prospezioni geoelettriche: ottimizzazione in acquisizione e ricostruzione 3D per problematiche ambientali e archeologiche. PhD thesis, University of Naples ''Federico II''. [Available Online at: http://www.fedoa.unina.it/1039/].

Styles, P., Toon, S., Thomas, E., and Skittrall, M., (2006). Microgravity as a tool for the detection, characterization and prediction of geohazard posed by abandoned mining cavities, *First Break*, 24, 51–60.

Talwani, M. (1965). Computation with the help of a digital computer of magnetic anomalies caused by bodies of arbitrary shape. *Geophysics*, *30*(5), 797-817.

Todeschini, R. (1998). Introduzione alla chemiometria. *EdiSES, Napoli*, pp.321.

Tomassen, P., Vandeplas, G., Van Zele, T., Cardell, L. O., Arebro, J., Olze, H., ... & De Ruyck, N. (2016). Inflammatory endotypes of chronic rhinosinusitis based on cluster analysis of biomarkers. *Journal of Allergy and Clinical Immunology*, *137*(5), 1449-1456.

Trigila R, Agosta E, Currado C, De Benedetti AA, Freda C, Gaeta M, Palladino DM, Rosa C (1995) Petrology. In: Trigila R (ed) The volcano of the Alban Hills. Universit degli Studi di Roma "La Sapienza", Rome, pp 95–165

Trimarchi,S., (2005). La problematica geologico tecnica delle cavità sotterrannee del sottosuolo sud-orientale della città di Roma [MSc. Thesis, in Italian] Università degli studi di Roma "La Sapienza".

Ungureanu C., Priceputu A., Bugea A.L., Chirică A., (2017). Use of electric resistivity tomography (ERT) for detecting underground voids on highly anthropized urban construction sites. *Procedia Engineering*, 209 202–209.

Van Schoor, M., (2002). Detection of sinkholes using 2D electrical resistivity imaging. *Journal of Applied Geophysics* 50, 393 – 399.

Ventriglia, U. (2002). Geologia del territorio del Comune di Roma. Amministrazione provinciale di Roma.

Viola, K. L., Sbarboro, J., Sureka, R., De, M., Bicca, M. A., Wang, J., ... & Velasco, P. T. (2015). Towards non-invasive diagnostic imaging of early-stage Alzheimer's disease. *Nature nanotechnology*, *10*(1), 91.

Von Hippel, A. R. (1954). *Dielectric materials and applications*(Vol. 2). Artech House on Demand.

Wilks, D. S. (2011). Cluster analysis. In *International geophysics* (Vol. 100, pp. 603-616). Academic press.

Witten, A. (2006) Handbook Of Geophysics In Archaeology. ISBN-10: 1904768601. Equinox Publishing

Witten, A. J., & Calvert, G., (1999). Characterizing the distribution of near-surface solution channels using electromagnetic induction and ground penetrating radar. *Journal of Environmental and Engineering Geophysics*, *4*(1), 35-43.

Wold, S., Esbensen, K., & Geladi, P. (1987). Principal component analysis. *Chemometrics and intelligent laboratory systems*, *2*(1-3), 37-52.

Young, R. A., & Sun, J. (1998). Noise attenuation using 3-D GPR methods. In *Proceedings of the seventh International Conference on Ground Penetrating Radar, Lawrence, Kansas*(Vol. 1, pp. 239-244).

Yu, H. L., Chen, J. C., Christakos, G., & Jerrett, M. (2009). BME estimation of residential exposure to ambient PM10 and ozone at multiple time scales. *Environmental Health Perspectives*, *117*(4), 537.

Zheng, W., Li, X., Lam, N., Wang, X., Liu, S., Yu, X., ... & Yao, J. (2013). Applications of integrated geophysical method in archaeological surveys of the ancient Shu ruins. *Journal of Archaeological Science*, *40*(1), 166-175.

Zhu,T. Zhou,J. Wang,H., (2017). Localization and characterization of the Zhangdian-Renhe fault zone in Zibo city, Shandong province, China, using electrical resistivity tomography (ERT). *Journal of Applied Geophysics*, Volume 136, 343-352

Acknowledgement

Firstly, I would like to express my sincere gratitude to my two advisors Prof. Salvatore Piro (ITABC-CNR) and Prof. Francesca Bozzano (La Sapienza University of Rome) for their continuous support to my Ph.D. study and related research.

My sincere thanks also go to Dr. Flamina Verga (ITABC-CNR) for the fruitful discussions about the *Magliano Sabina* data, Daniele Verrecchia (ITABC-CNR) for the technical support during the surveys.

Furthermore, I'm also indebted with the "*Parco Appia Antica istitution*" for the help before and after the surveys made at *Parco della Caffarella* and with the "Magliano Sabina Municipality" for the help during the data collection in their small (but beautiful) town.

I thank Enrico Papale (ITABC-CNR) both for friendship and his support during this three-year-long work.

I would thank my reviewers Prof. Nikos Papadopoulos (Institutes for Mediterrean studies, Greece) and Prof. Michele Di Filippo (IGAG-CNR) for their fruitful suggestions. They greatly improve my work!.

Last but not least, I would like to thank my mother, Fiorella, without her continuous support and encouragement I never would have been able to achieve my goals.

Appendix A- Parco della Caffarella

A1) ERT pseudosections 1-15

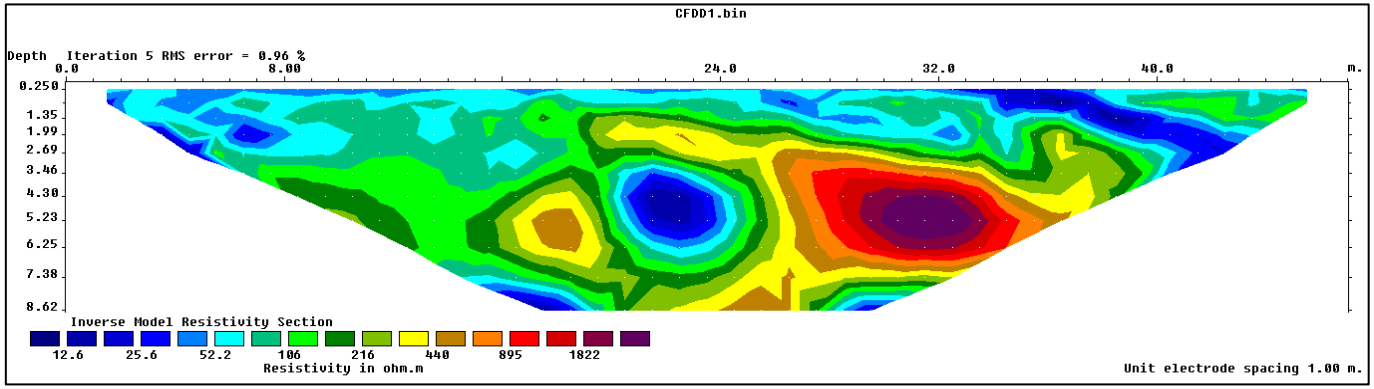

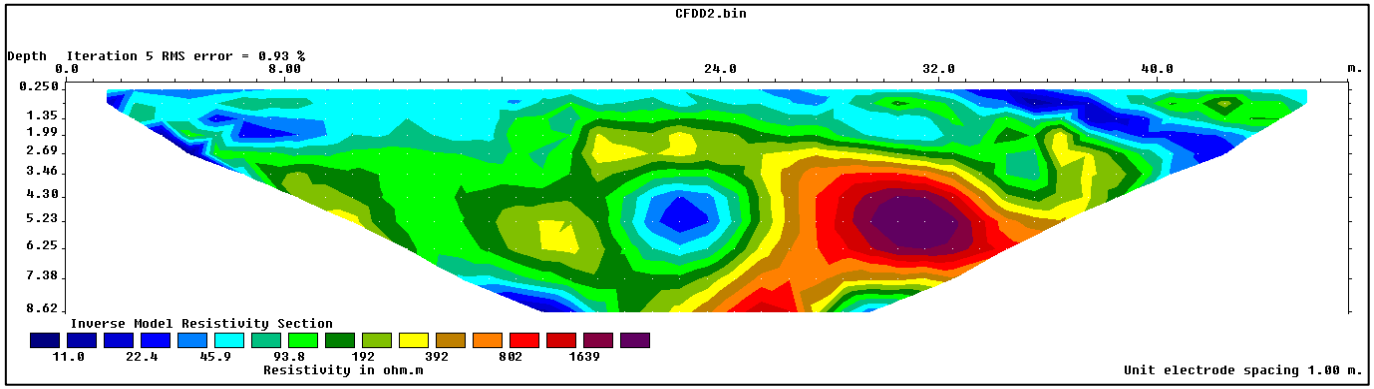

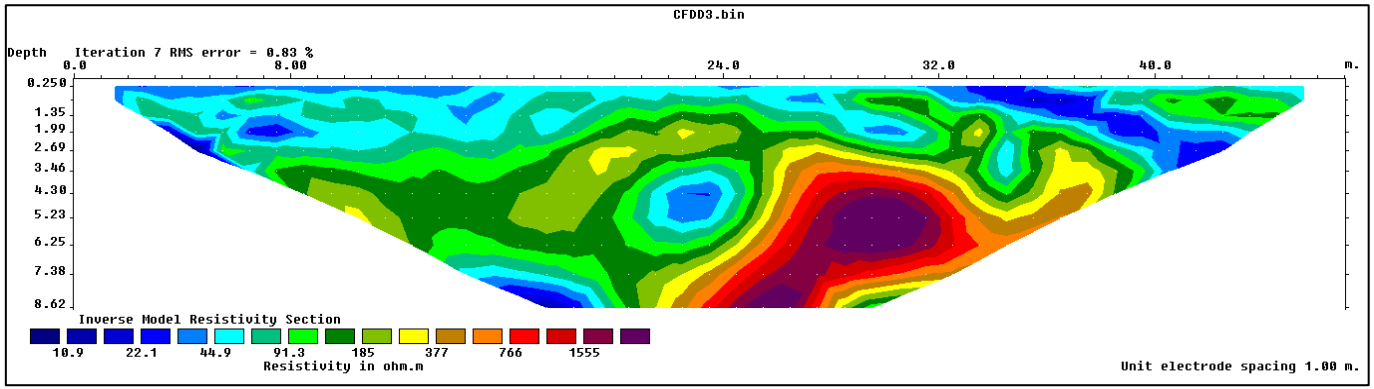
CFDD3.bin
Depth
Iteration 7 RMS error = 0.83 %
0.0
8.00
24.0
32.0
40.0
m.
0.250
1.35
1.99
2.69
3.46
4.30
5.23
6.25
7.38
8.62
Inverse Model Resistivity Section
10.9
22.1
44.9
91.3
185
377
766
1555
Resistivity in ohm.m
Unit electrode spacing 1.00 m.

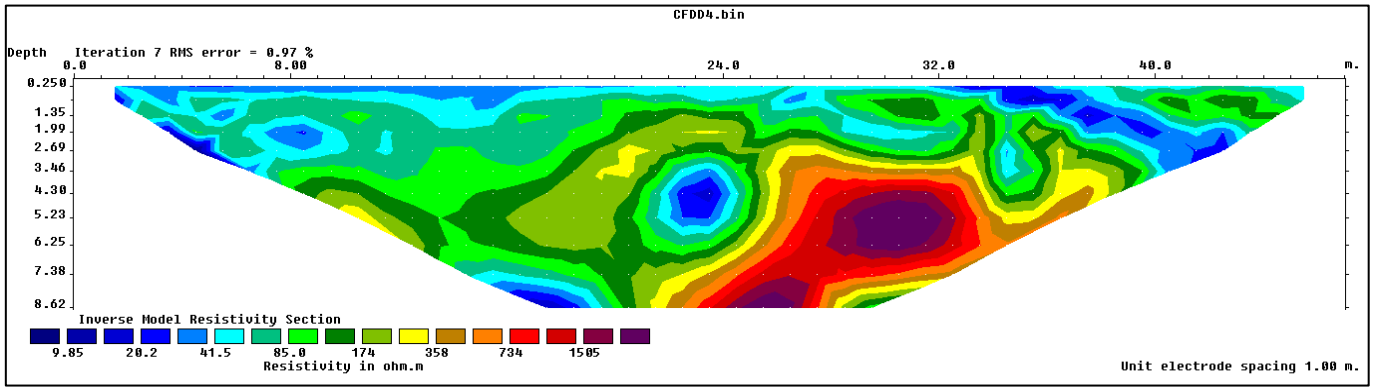
CFDD4.bin
Depth
Iteration 7 RMS error = 0.97 %
0.0
8.00
24.0
32.0
40.0
m.
0.250
1.35
1.99
2.69
3.46
4.30
5.23
6.25
7.38
8.62
Inverse Model Resistivity Section
9.85
20.2
41.5
85.0
174
358
734
1505
Resistivity in ohm.m
Unit electrode spacing 1.00 m.

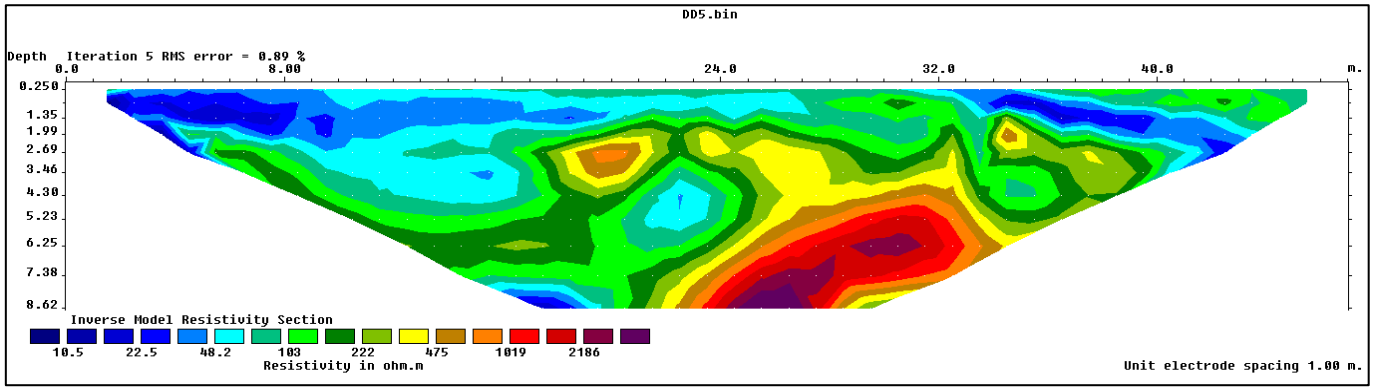
DD5.bin
Depth
Iteration 5 RMS error = 0.89 %
0.0
8.00
24.0
32.0
40.0
m.
0.250
1.35
1.99
2.69
3.46
4.30
5.23
6.25
7.38
8.62
Inverse Model Resistivity Section
10.5
22.5
48.2
103
222
475
1019
2186
Resistivity in ohm.m
Unit electrode spacing 1.00 m.

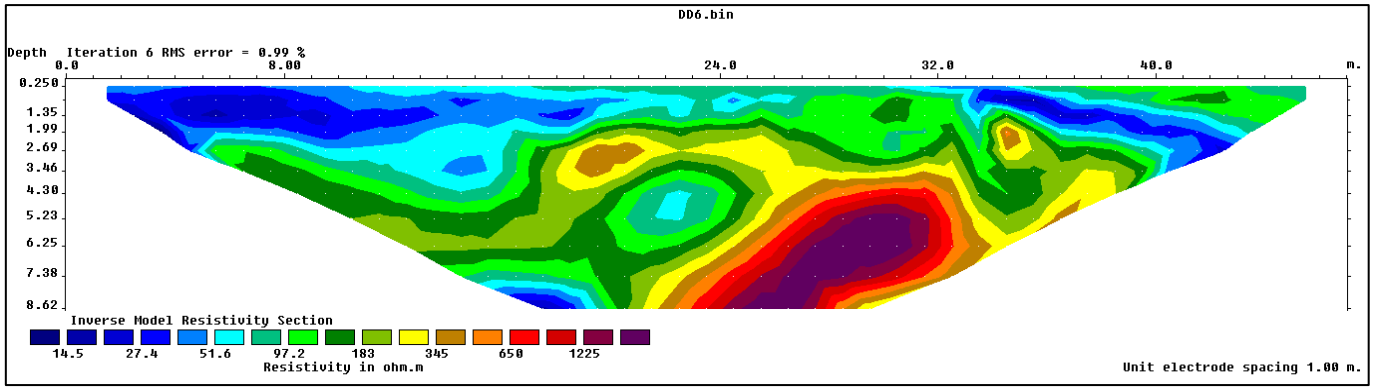
DD6.bin
Depth
Iteration 6 RMS error = 0.99 %
0.0
8.00
24.0
32.0
40.0
m.
0.250
1.35
1.99
2.69
3.46
4.30
5.23
6.25
7.38
8.62
Inverse Model Resistivity Section
14.5
27.4
51.6
97.2
183
345
650
1225
Resistivity in ohm.m
Unit electrode spacing 1.00 m.

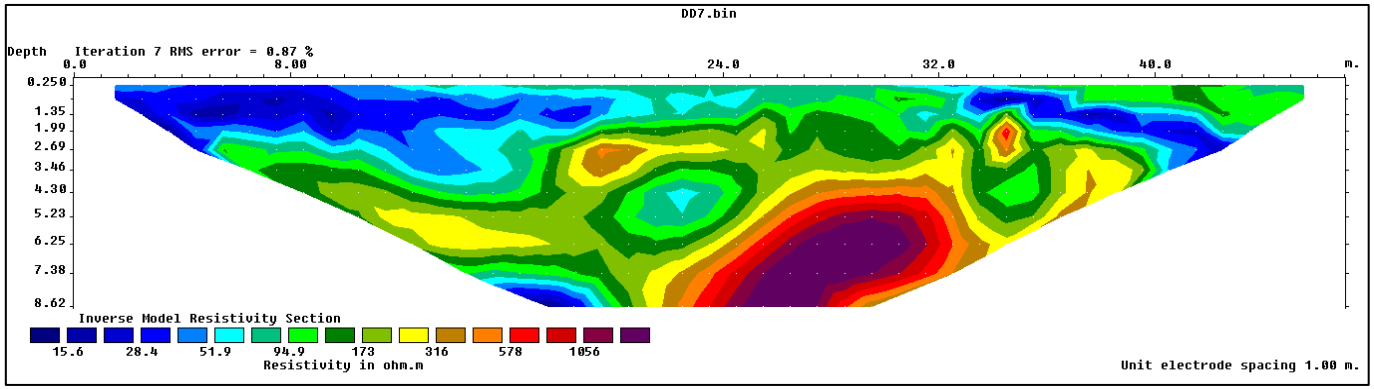
DD7.bin
Depth
Iteration 7 RMS error = 0.87 %
0.0
8.00
24.0
32.0
40.0
m.
0.250
1.35
1.99
2.69
3.46
4.30
5.23
6.25
7.38
8.62
Inverse Model Resistivity Section
15.6
28.4
51.9
94.9
173
316
578
1056
Resistivity in ohm.m
Unit electrode spacing 1.00 m.

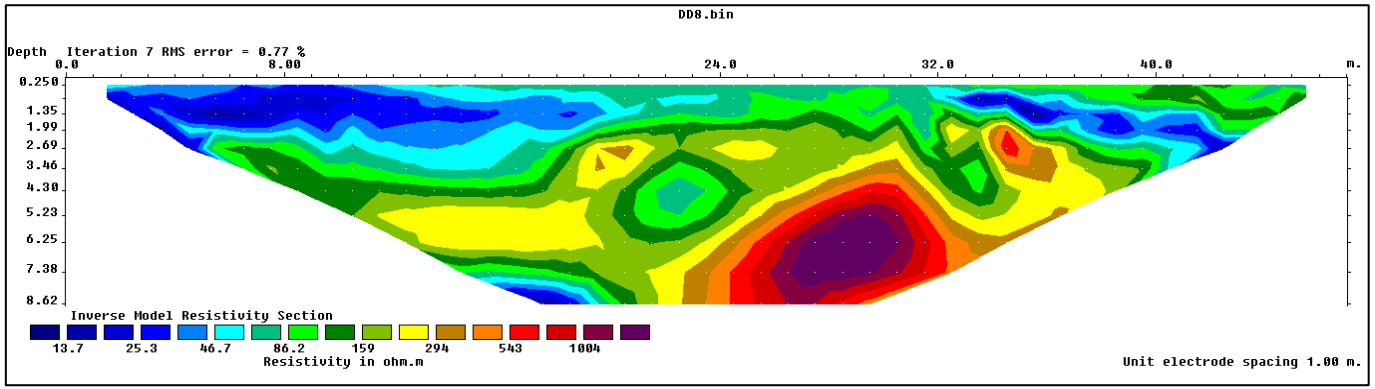
DD8.bin
Depth
Iteration 7 RMS error = 0.77 %
0.0
8.00
24.0
32.0
40.0
m.
0.250
1.35
1.99
2.69
3.46
4.30
5.23
6.25
7.38
8.62
Inverse Model Resistivity Section
13.7
25.3
46.7
86.2
159
294
543
1004
Resistivity in ohm.m
Unit electrode spacing 1.00 m.

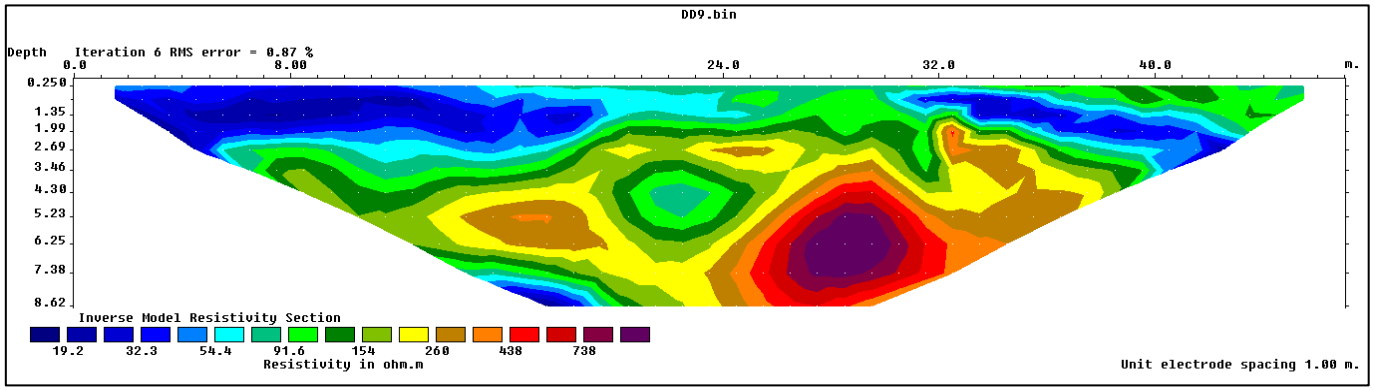
DD9.bin
Depth
Iteration 6 RMS error = 0.87 %
0.0
8.00
24.0
32.0
40.0
m.
0.250
1.35
1.99
2.69
3.46
4.30
5.23
6.25
7.38
8.62
Inverse Model Resistivity Section
19.2
32.3
54.4
91.6
154
260
438
738
Resistivity in ohm.m
Unit electrode spacing 1.00 m.

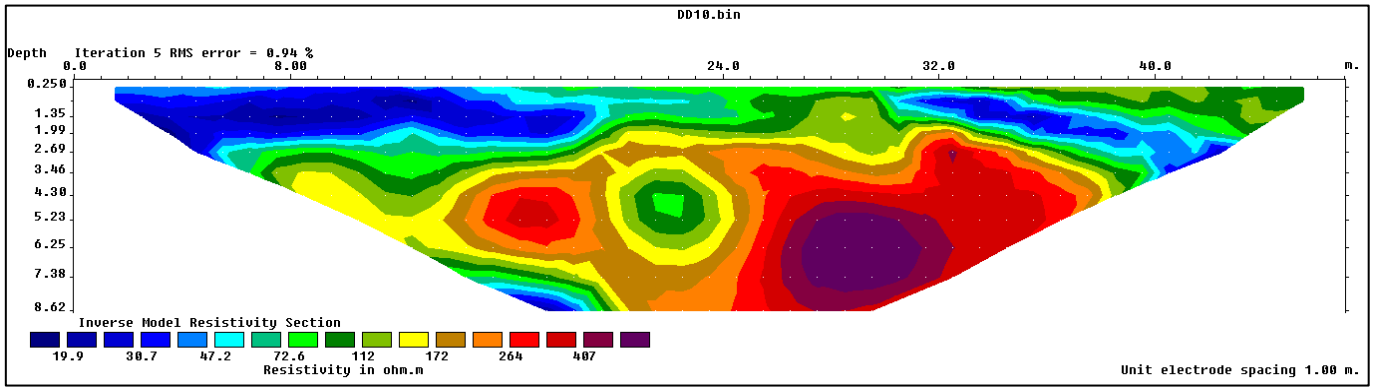
DD10.bin
Depth
Iteration 5 RMS error = 0.94 %
0.0
8.00
24.0
32.0
40.0
m.
0.250
1.35
1.99
2.69
3.46
4.30
5.23
6.25
7.38
8.62
Inverse Model Resistivity Section
19.9
30.7
47.2
72.6
112
172
264
407
Resistivity in ohm.m
Unit electrode spacing 1.00 m.

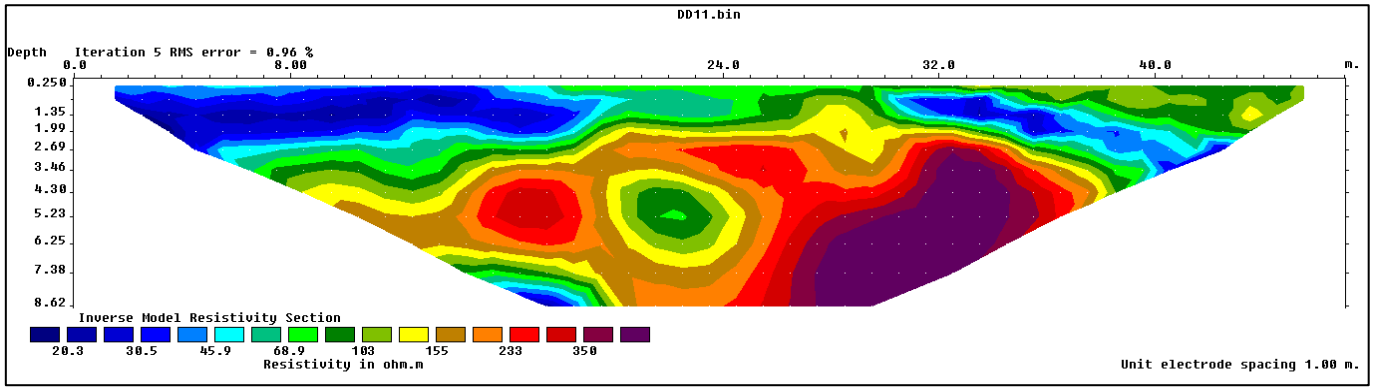
DD11.bin
Depth
Iteration 5 RMS error = 0.96 %
0.0
8.00
24.0
32.0
40.0
m.
0.250
1.35
1.99
2.69
3.46
4.30
5.23
6.25
7.38
8.62
Inverse Model Resistivity Section
20.3
30.5
45.9
68.9
103
155
233
350
Resistivity in ohm.m
Unit electrode spacing 1.00 m.

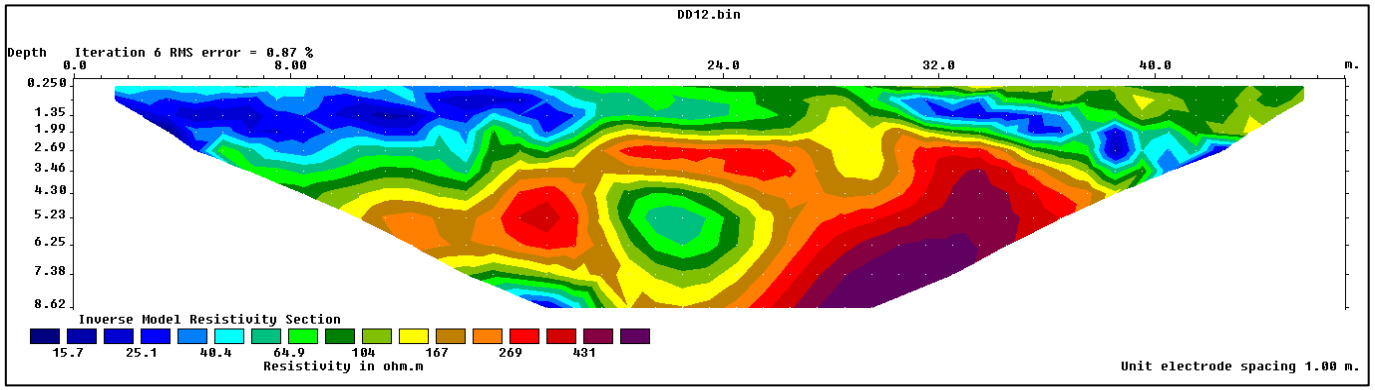
DD12.bin
Depth
Iteration 6 RMS error = 0.87 %
0.0
8.00
24.0
32.0
40.0
m.
0.250
1.35
1.99
2.69
3.46
4.30
5.23
6.25
7.38
8.62
Inverse Model Resistivity Section
15.7
25.1
40.4
64.9
104
167
269
431
Resistivity in ohm.m
Unit electrode spacing 1.00 m.

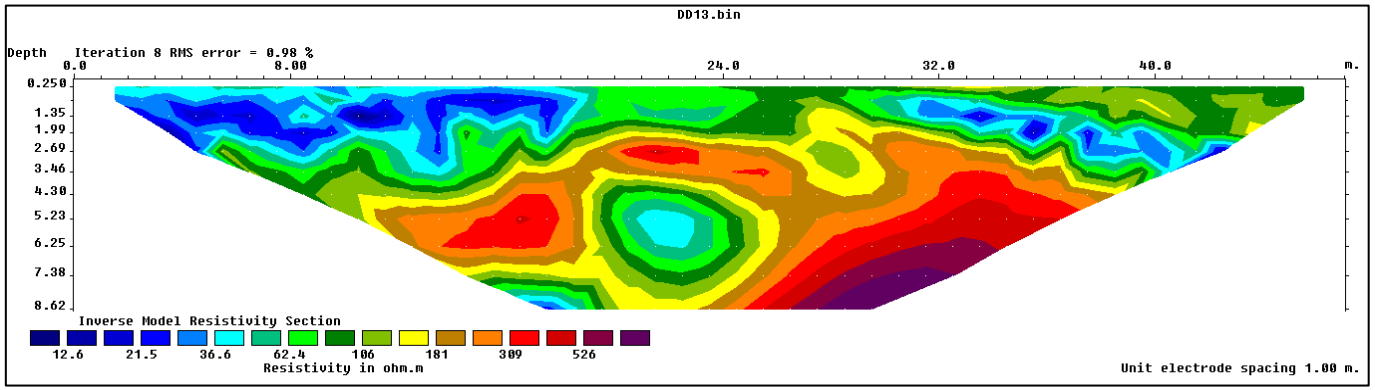
DD13.bin
Depth
Iteration 8 RMS error = 0.98 %
0.0
8.00
24.0
32.0
40.0
m.
0.250
1.35
1.99
2.69
3.46
4.30
5.23
6.25
7.38
8.62
Inverse Model Resistivity Section
12.6
21.5
36.6
62.4
106
181
309
526
Resistivity in ohm.m
Unit electrode spacing 1.00 m.

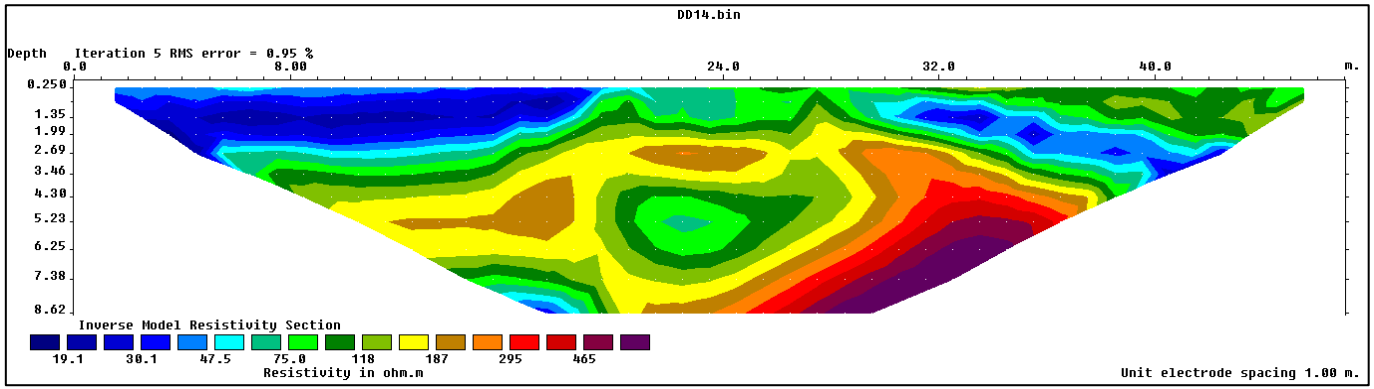
DD14.bin
Depth
Iteration 5 RMS error = 0.95 %
0.0
8.00
24.0
32.0
40.0
m.
0.250
1.35
1.99
2.69
3.46
4.30
5.23
6.25
7.38
8.62
Inverse Model Resistivity Section
19.1
30.1
47.5
75.0
118
187
295
465
Resistivity in ohm.m
Unit electrode spacing 1.00 m.

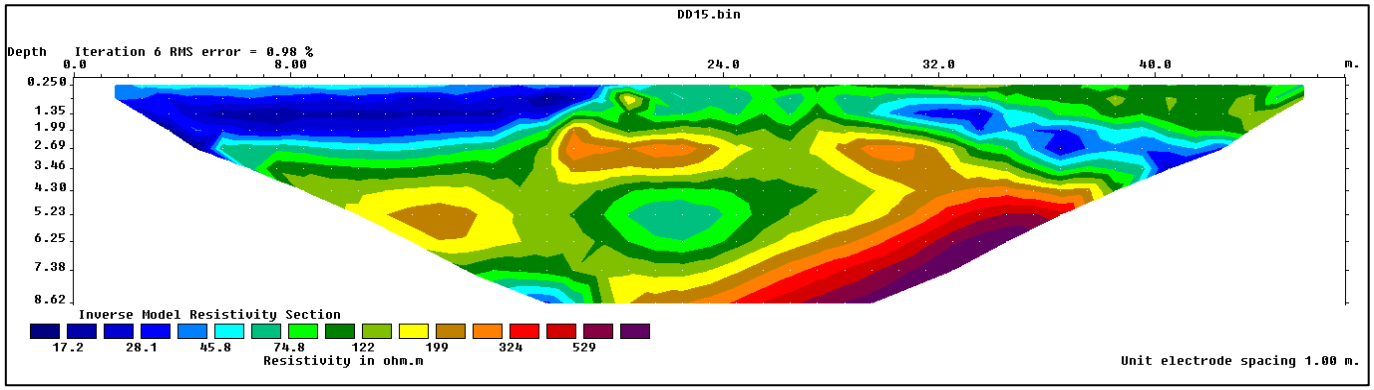
DD15.bin
Depth
Iteration 6 RMS error = 0.98 %
0.0
8.00
24.0
32.0
40.0
m.
0.250
1.35
1.99
2.69
3.46
4.30
5.23
6.25
7.38
8.62
Inverse Model Resistivity Section
17.2
28.1
45.8
74.8
122
199
324
529
Resistivity in ohm.m
Unit electrode spacing 1.00 m.

A2) GPR time-slice 70 MHz Time window 105 ns; slices 1-6 (all axes are in m)

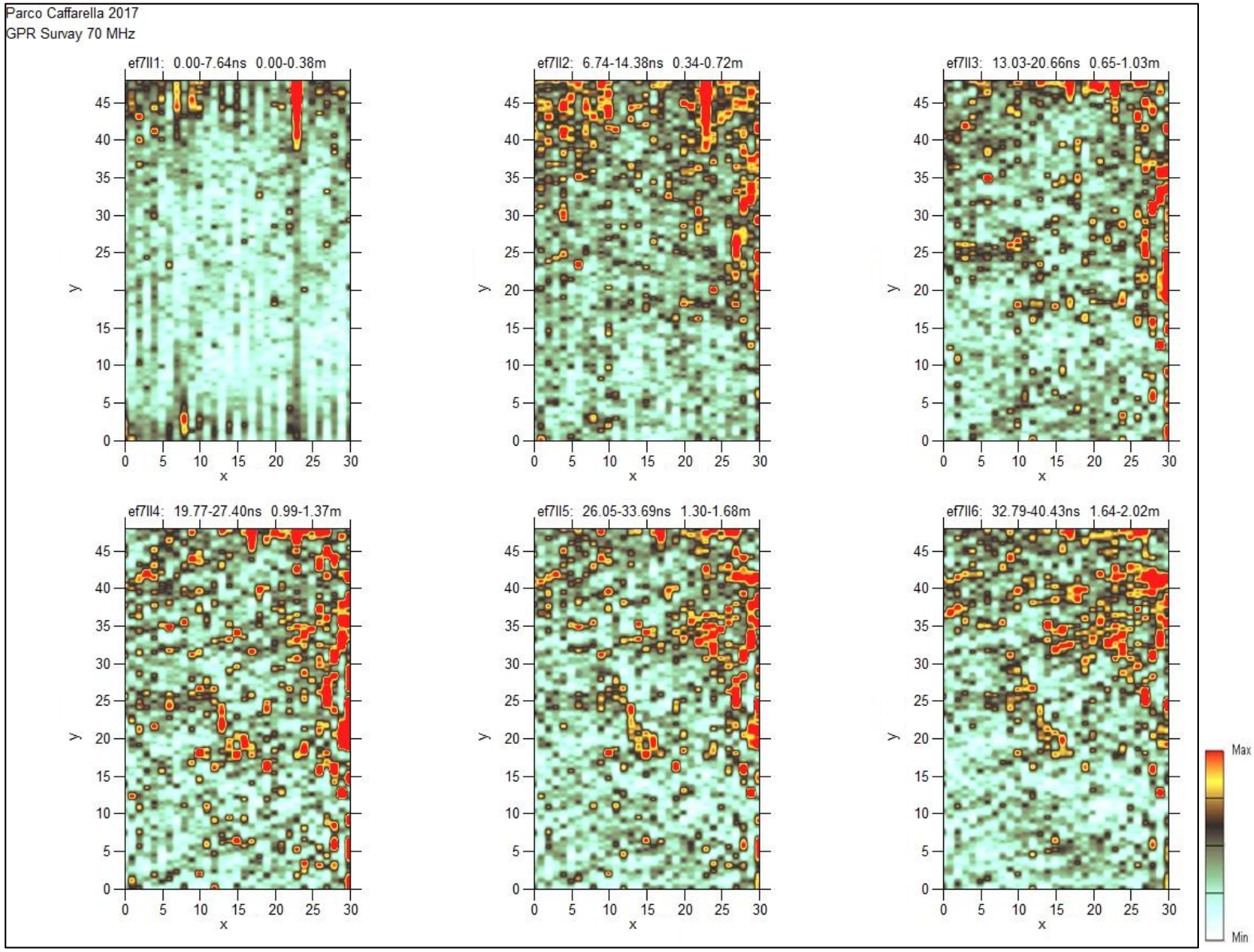

GPR time-slice 70 MHz Time window 105 ns; slices 7-13 (All axes are in m)

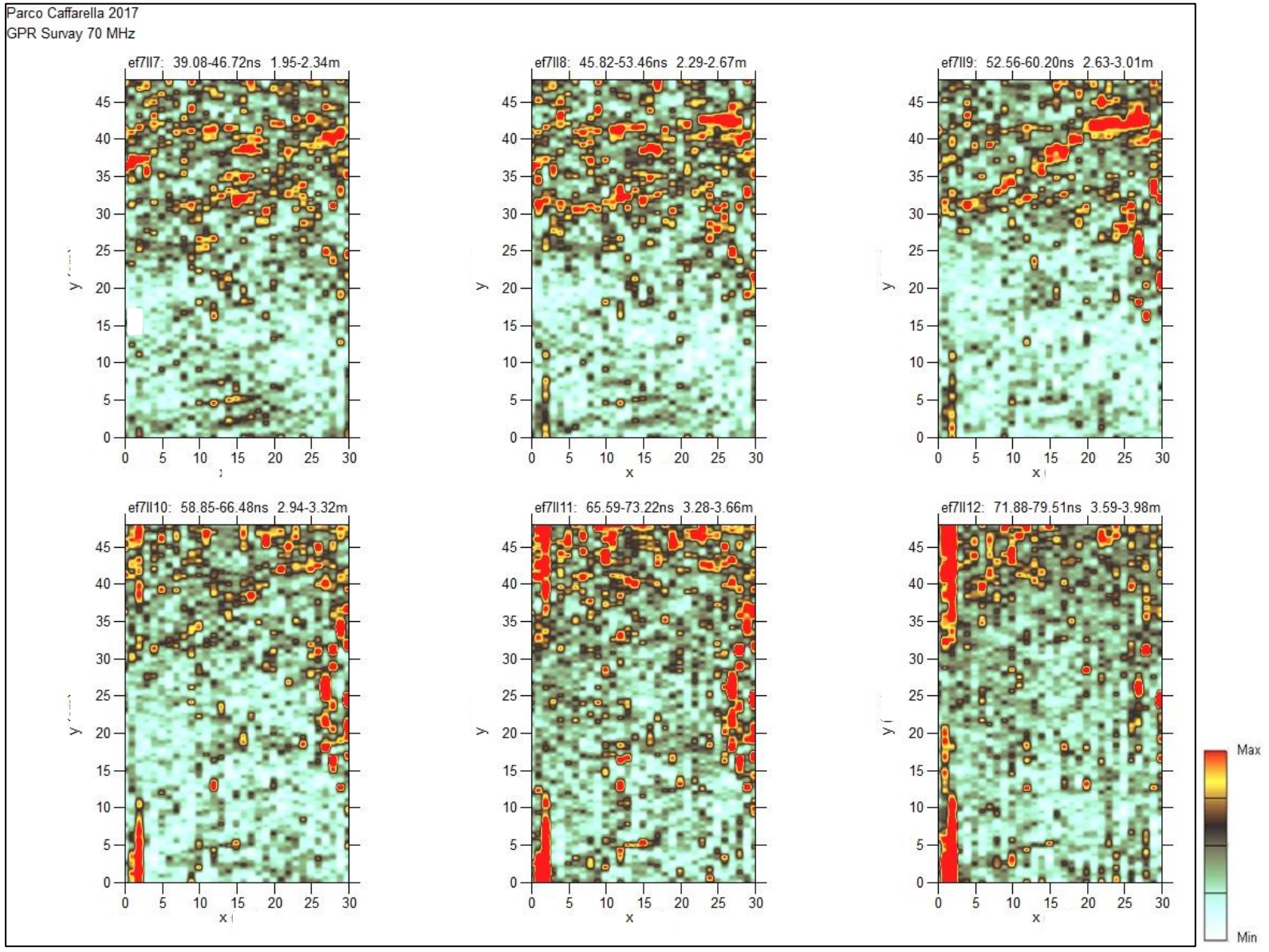

GPR time-slice 70 MHz Time window 105 ns; slices 13-18 (All axes are in m)

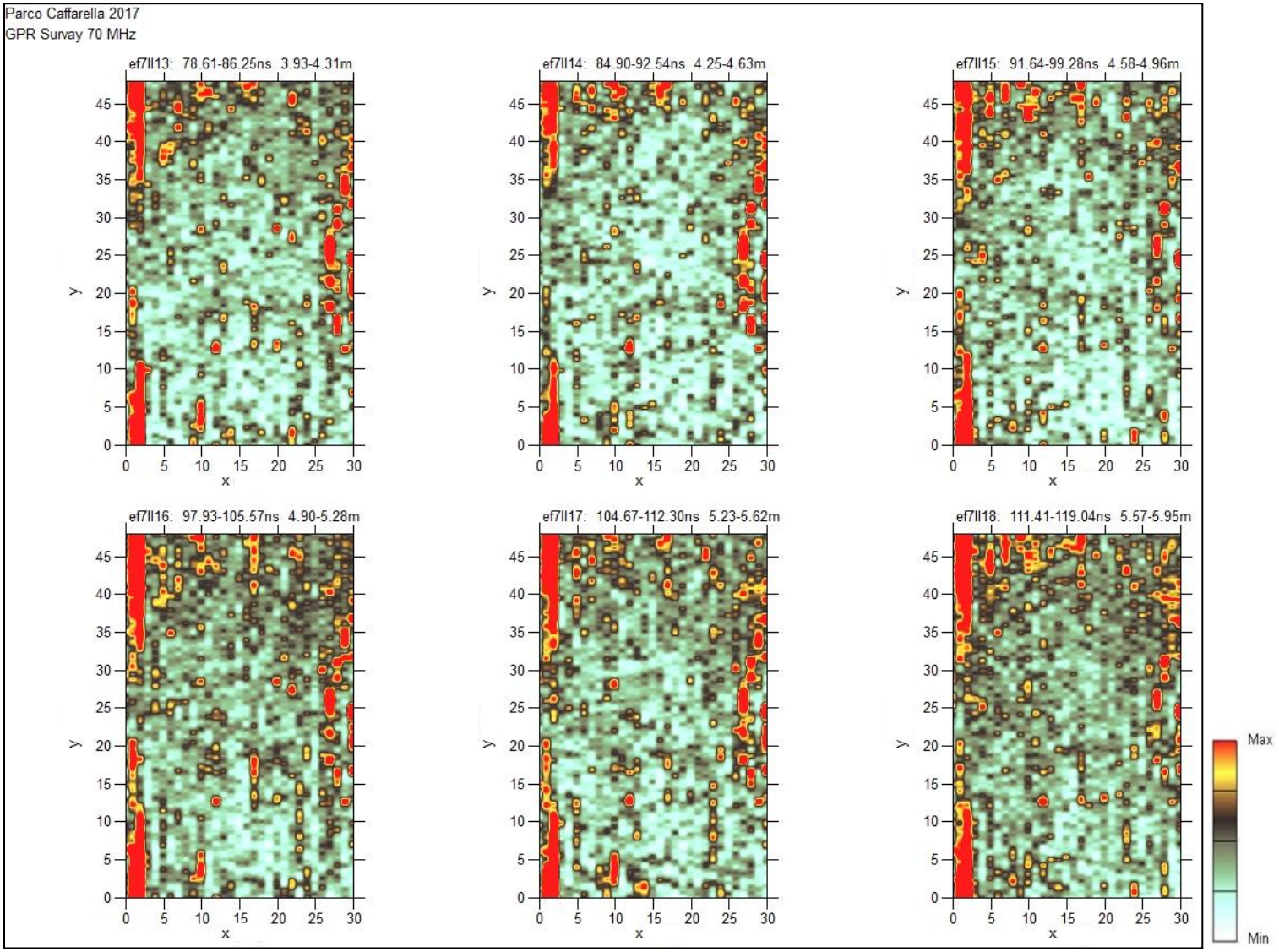

GPR time-slice 70 MHz Time window 105 ns; slice 19-24

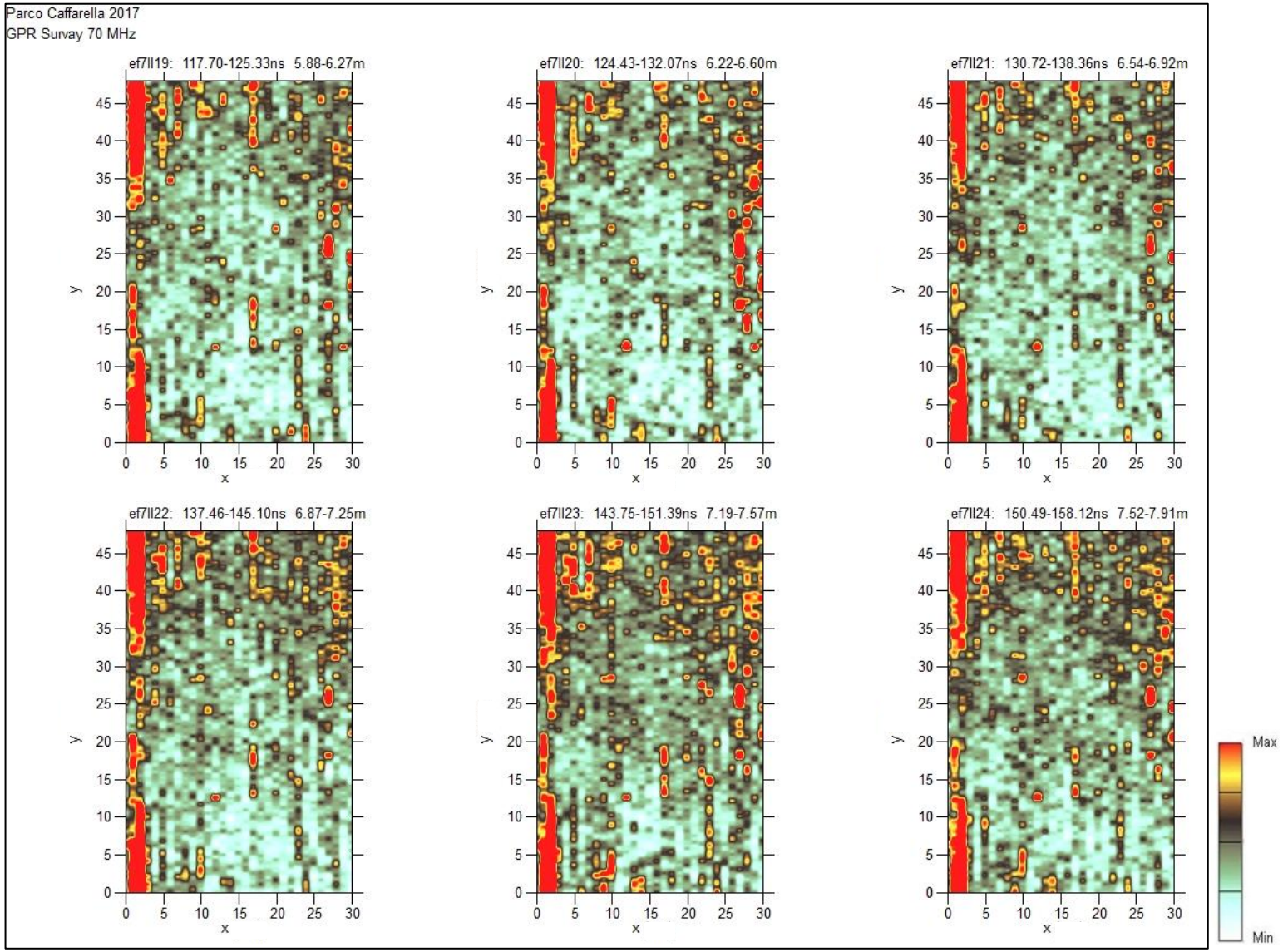

GPR time-slice 70 MHz Time window 105 ns; slices 24-30

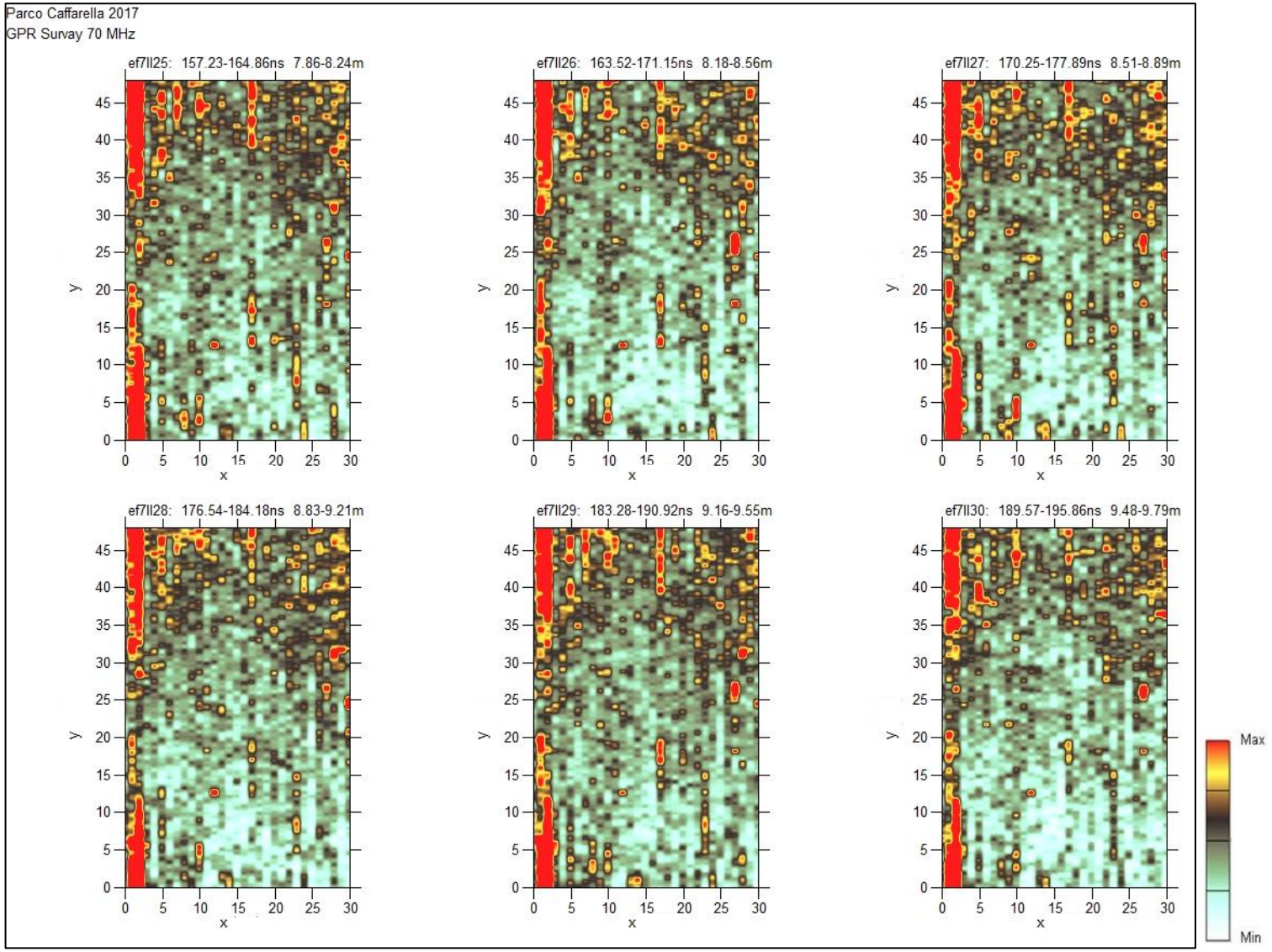

A3) Contour map overlay GPR 70 MHz time-slice and ERT depth-slice

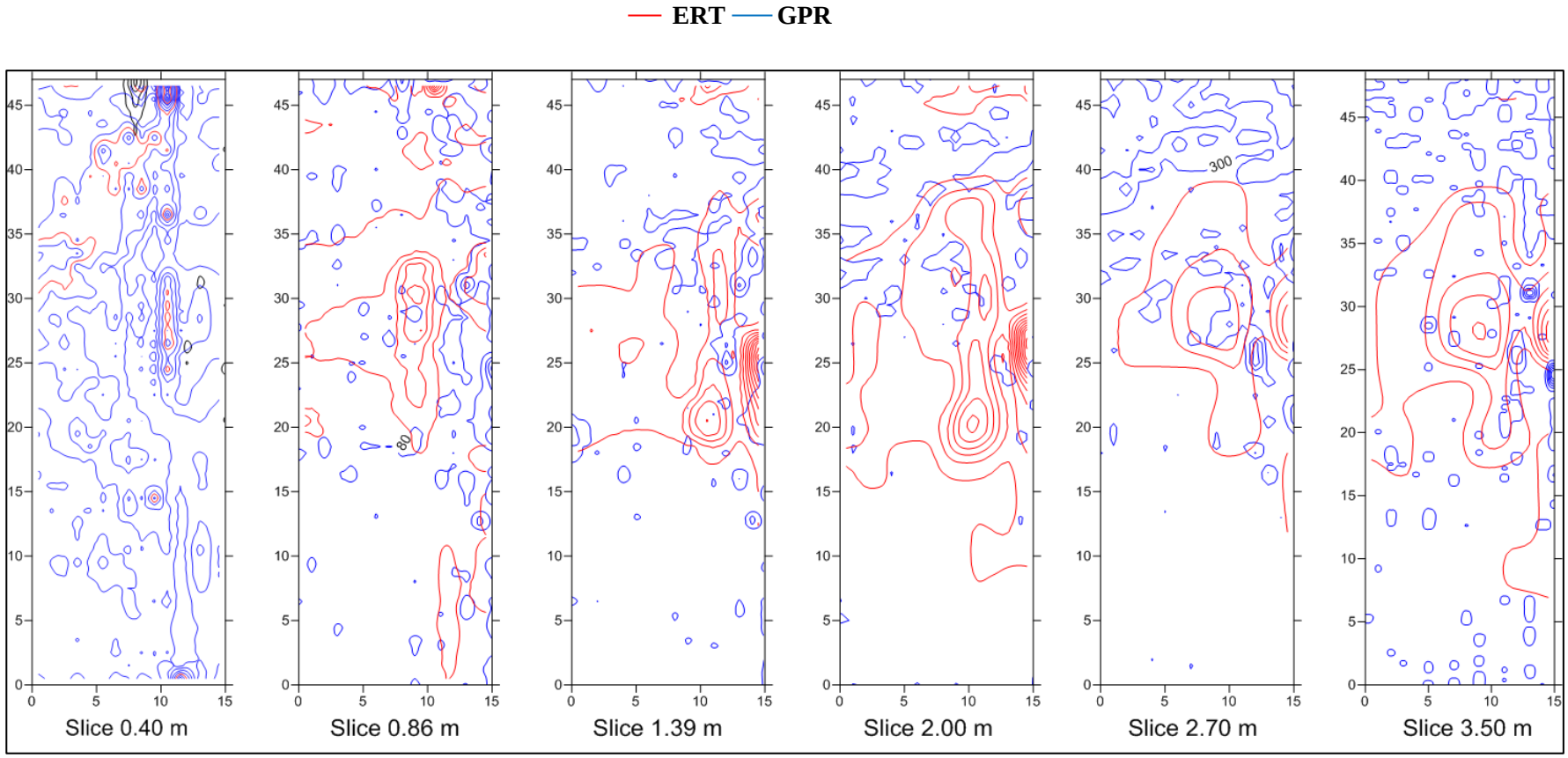

(All axes are in m)

Contour map overlay GPR 70 MHz time-slice and ERT depth-slice

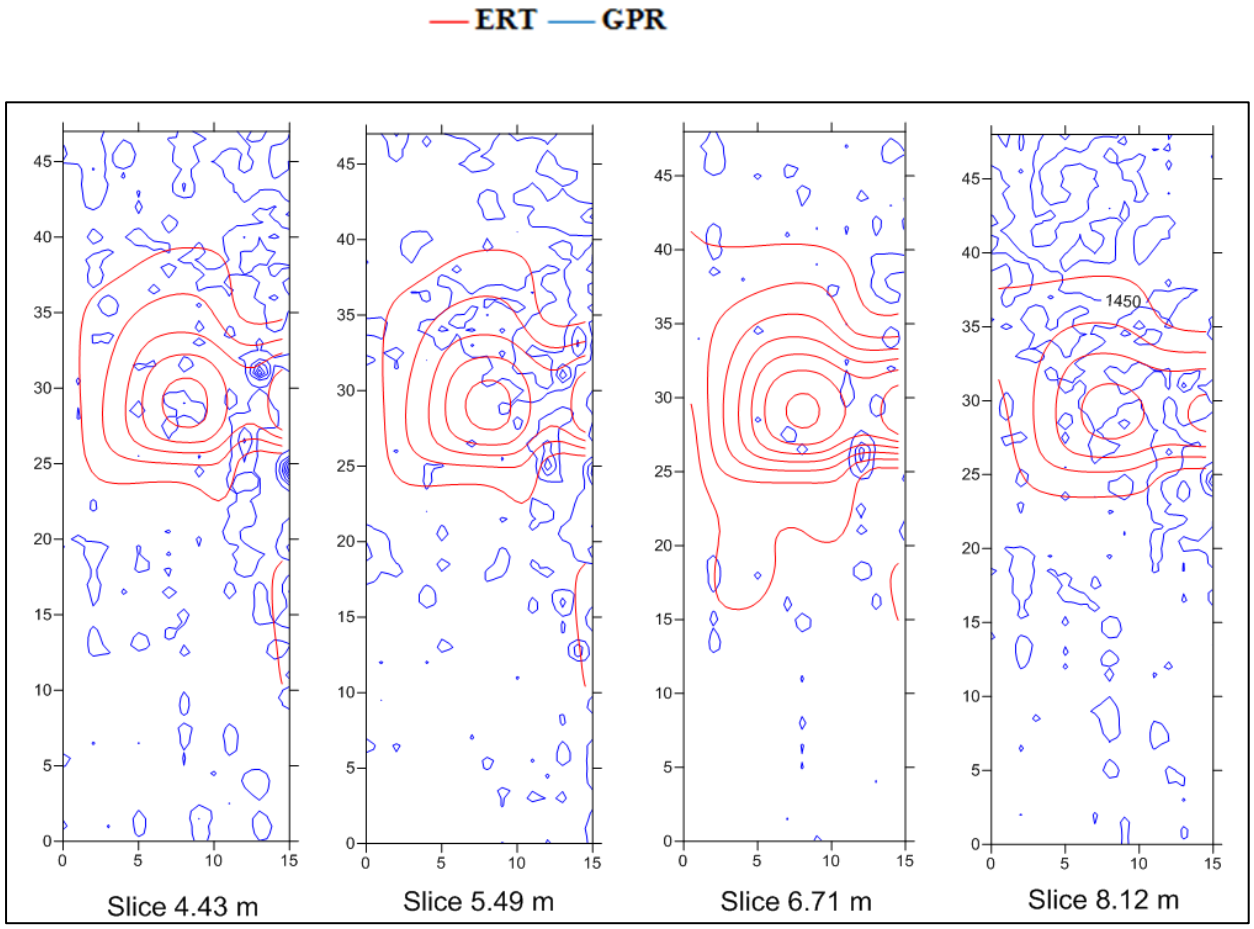

(All axes are in m)

A4) RGB Color Composite GPR 70 MHz time-slice and ERT depth-slice

ERT GPR

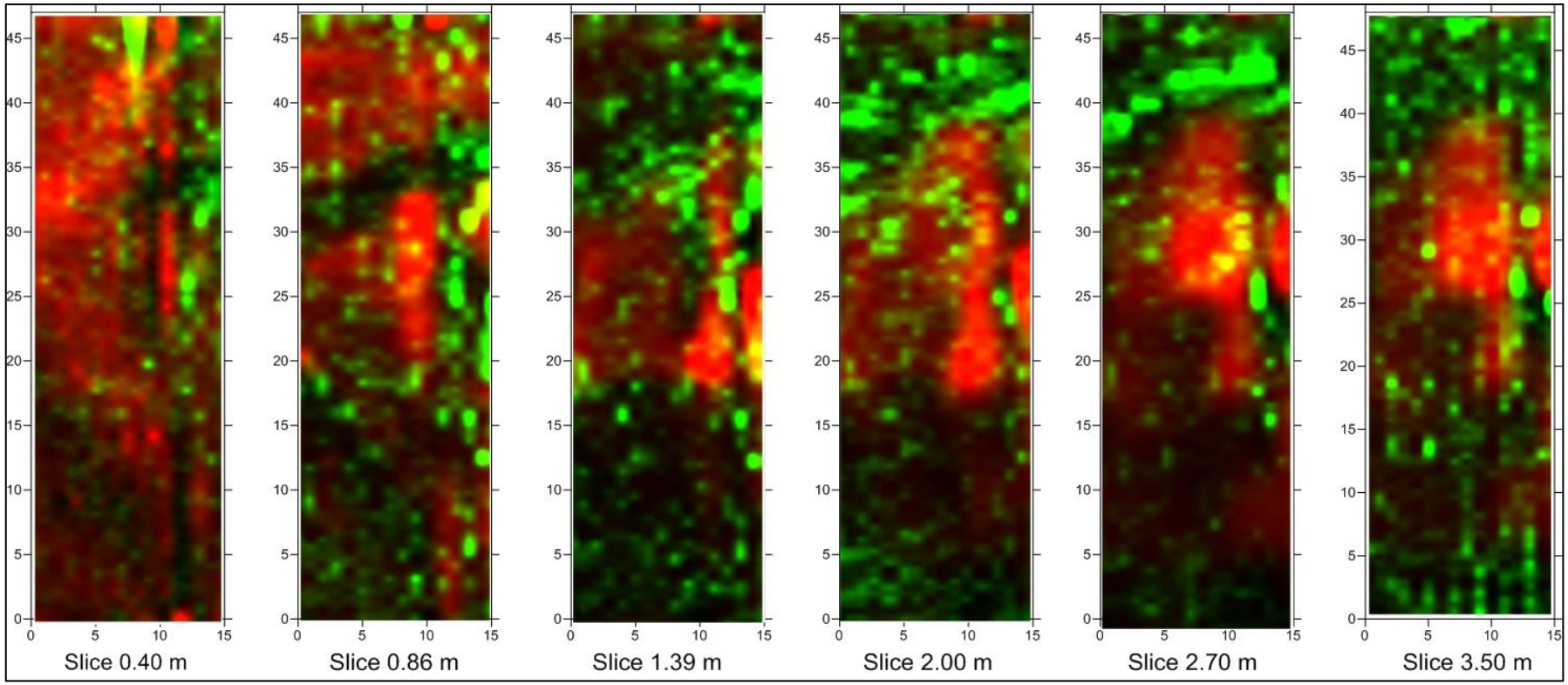

(All axes are in m)

RGB Color Composite GPR 70 MHz time-slice and ERT depth-slice

ERT GPR

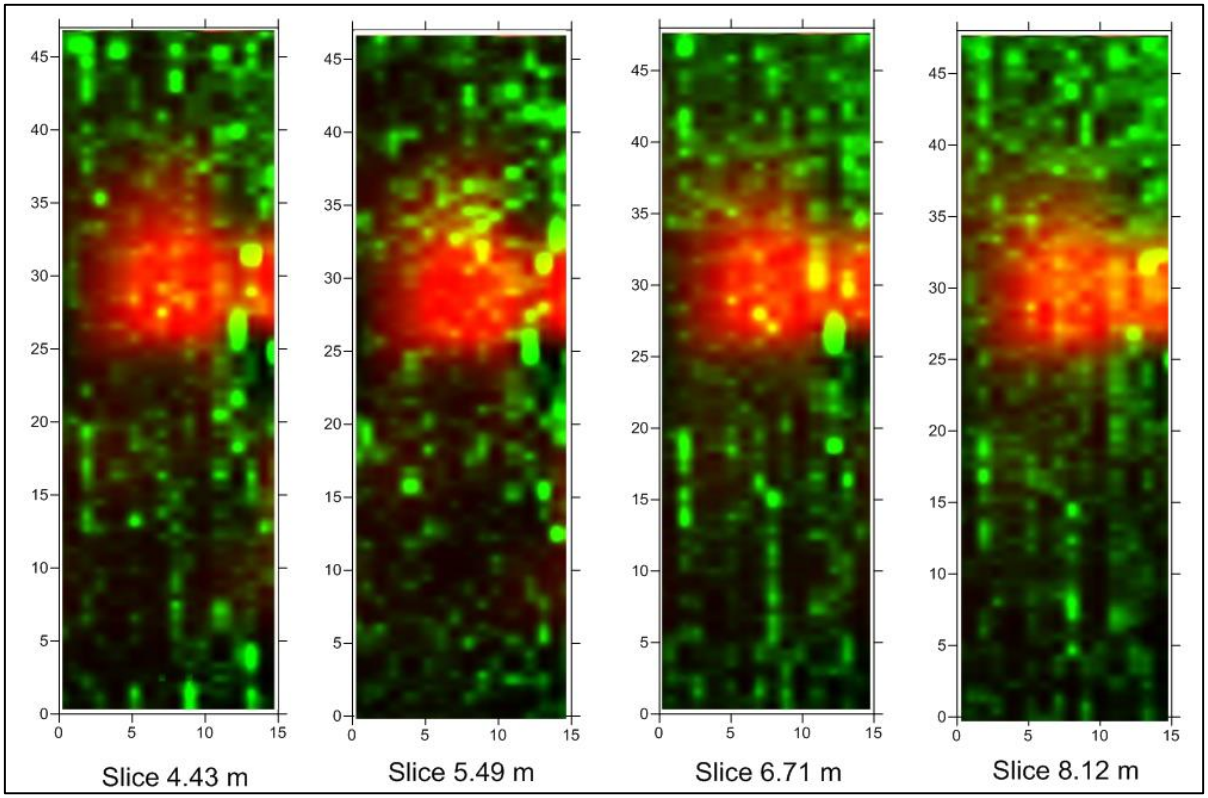

(All axes are in m)

A5) Binary representation GPR 70 MHz and ERT depth slice

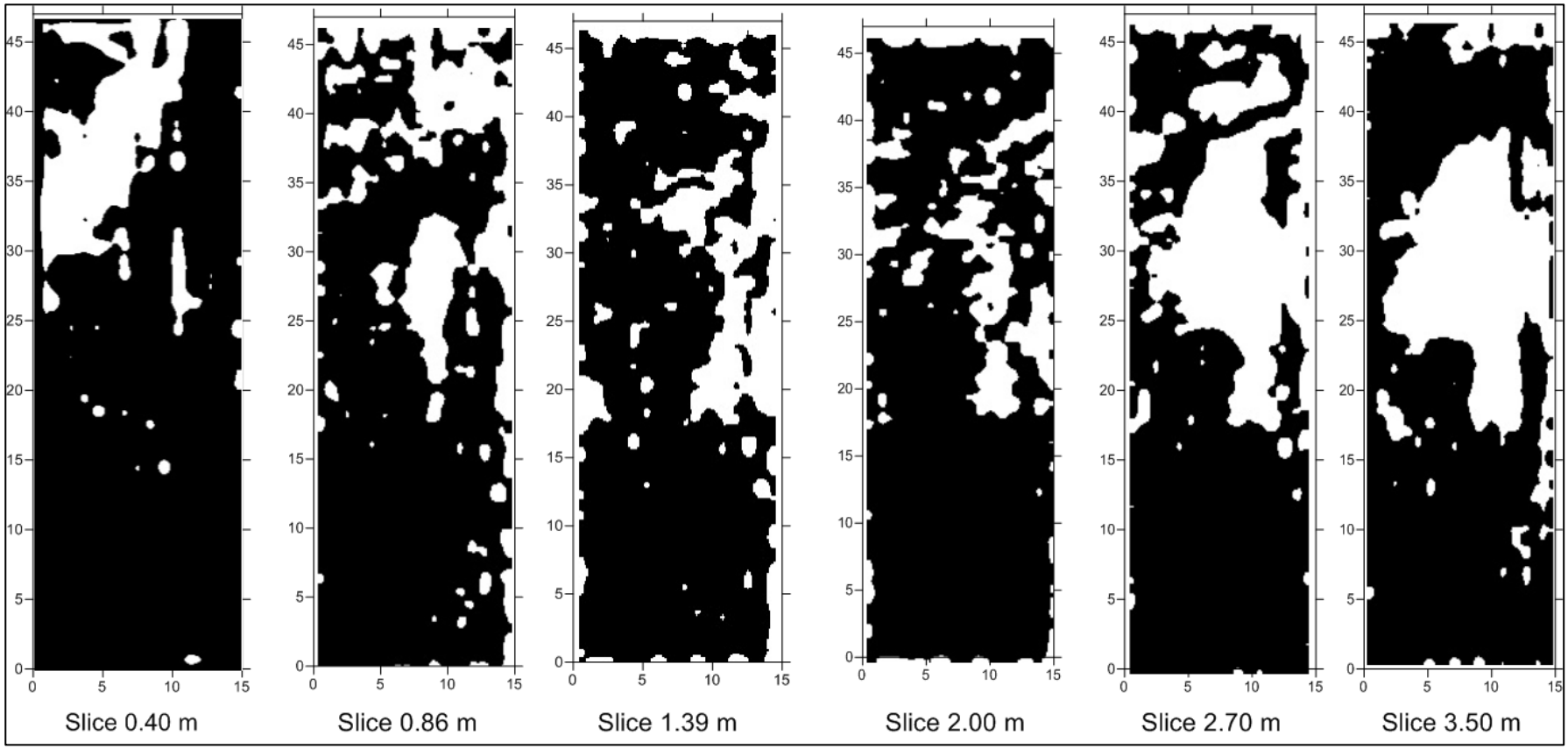

(All axes are in m)

Binary representation GPR 70 MHz and ERT depth slice

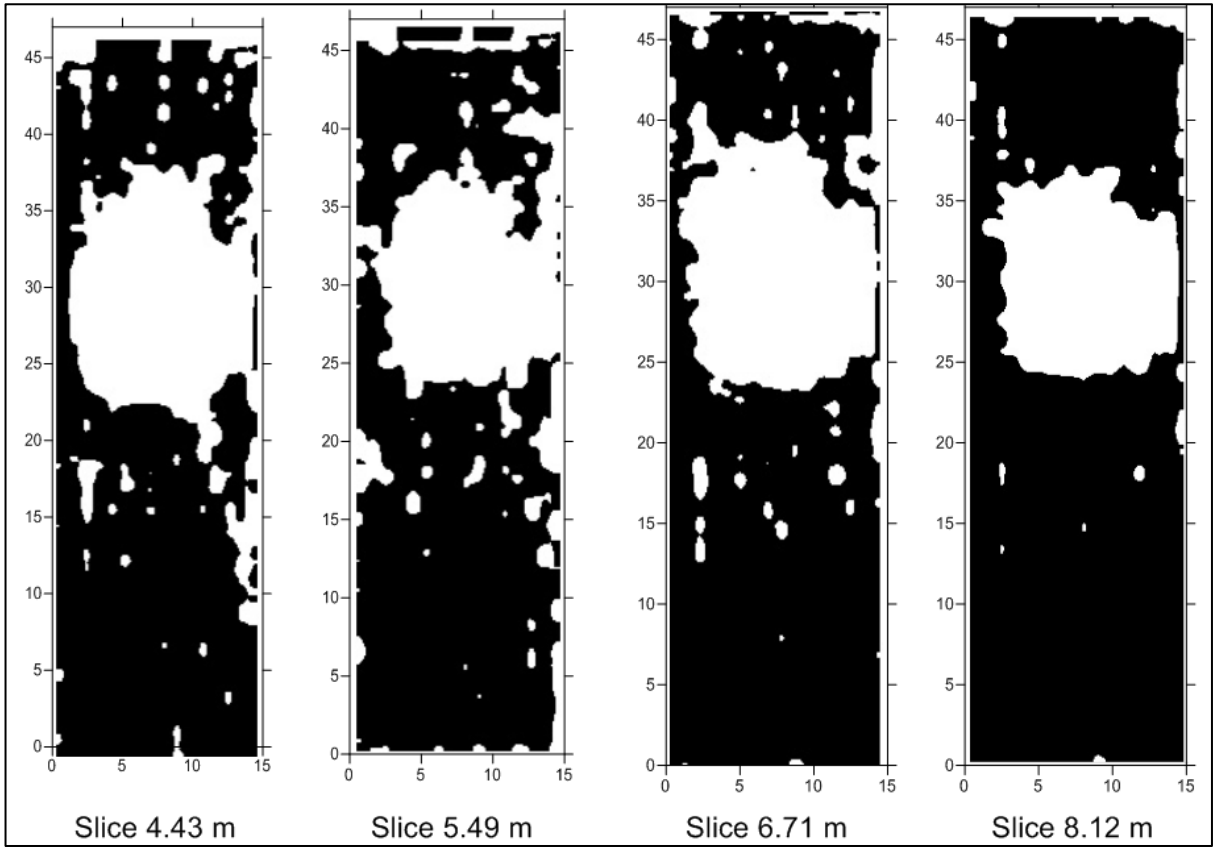

(All axes are in m)

A6) Data Sum (GPR 70 MHz + ERT depth slice)

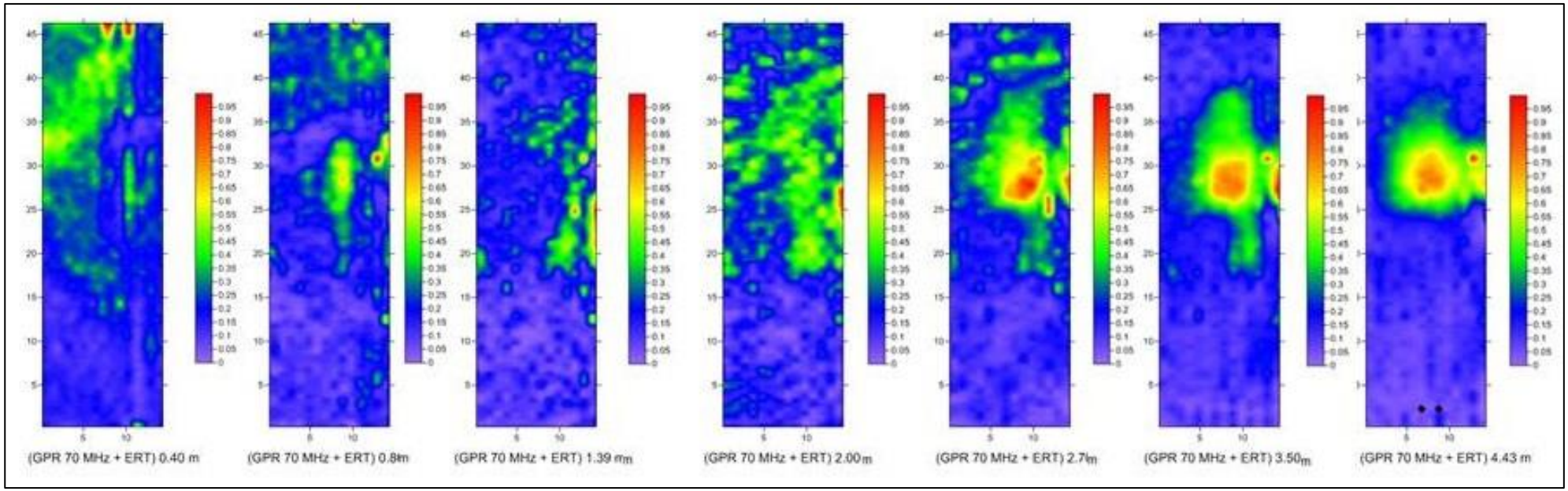

(All axes are in m)

Data Sum (GPR 70 MHz + ERT depth slice)

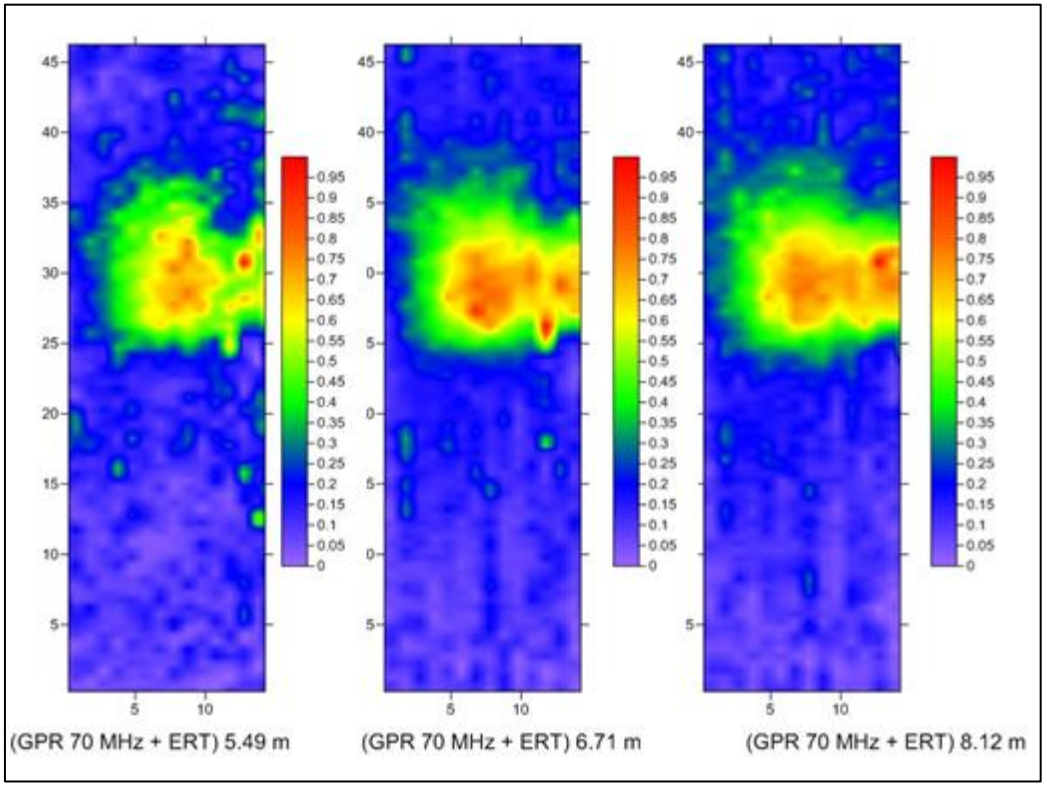

(All axes are in m)

A7) Data Product (GPR 70 MHz ·ERT depth slice)

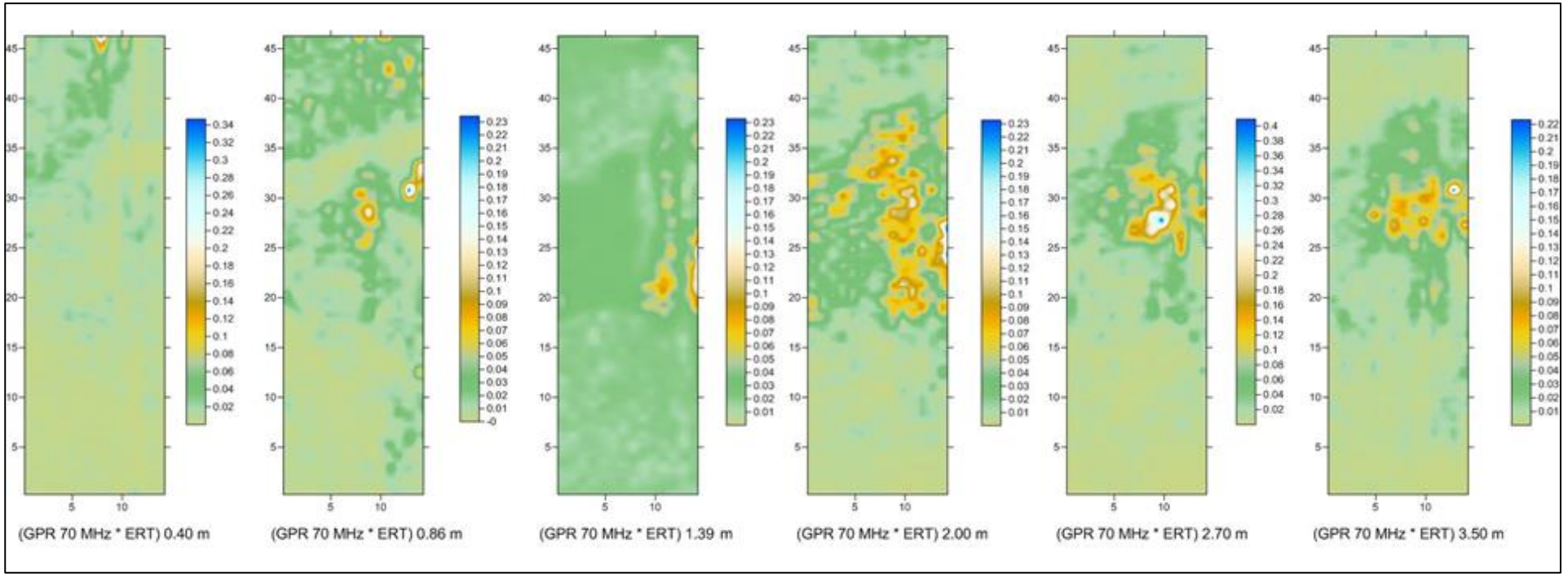

(All axes are in m)

Data Product (GPR 70 MHz ·ERT depth slice)

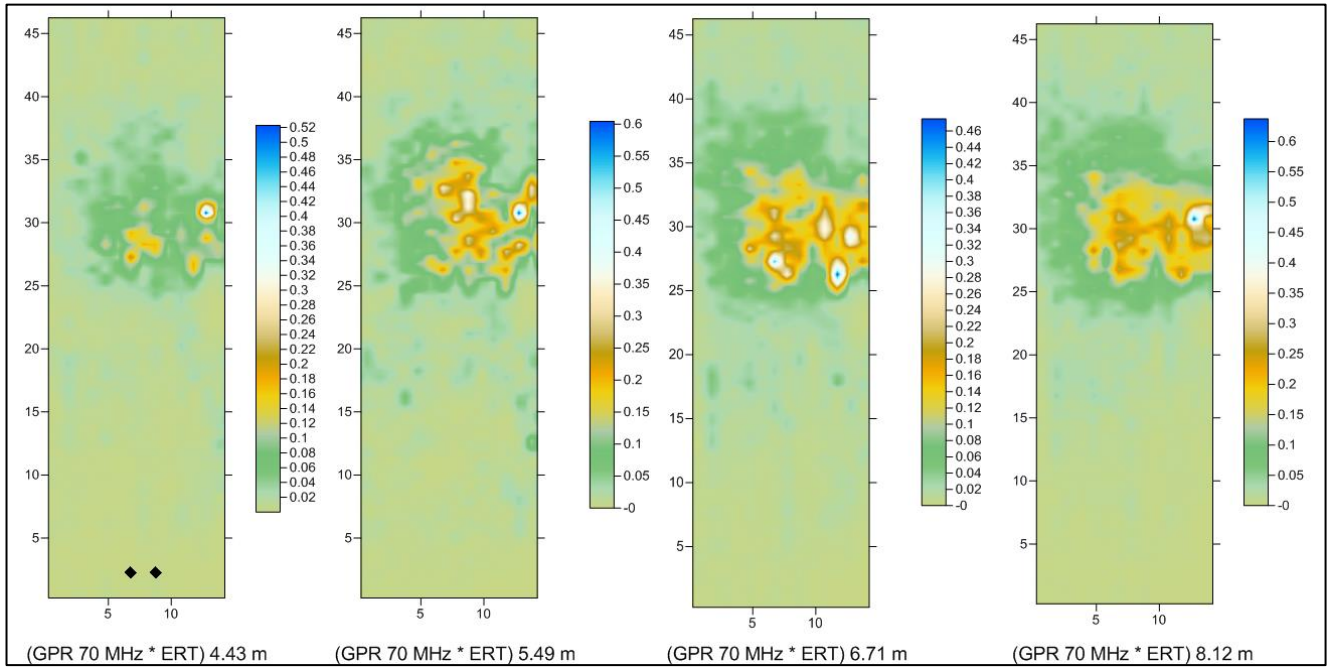

(All axes are in m)

A8) Principal Component analysis (GPR 70 MHz Time-slice and ERT depth slice)

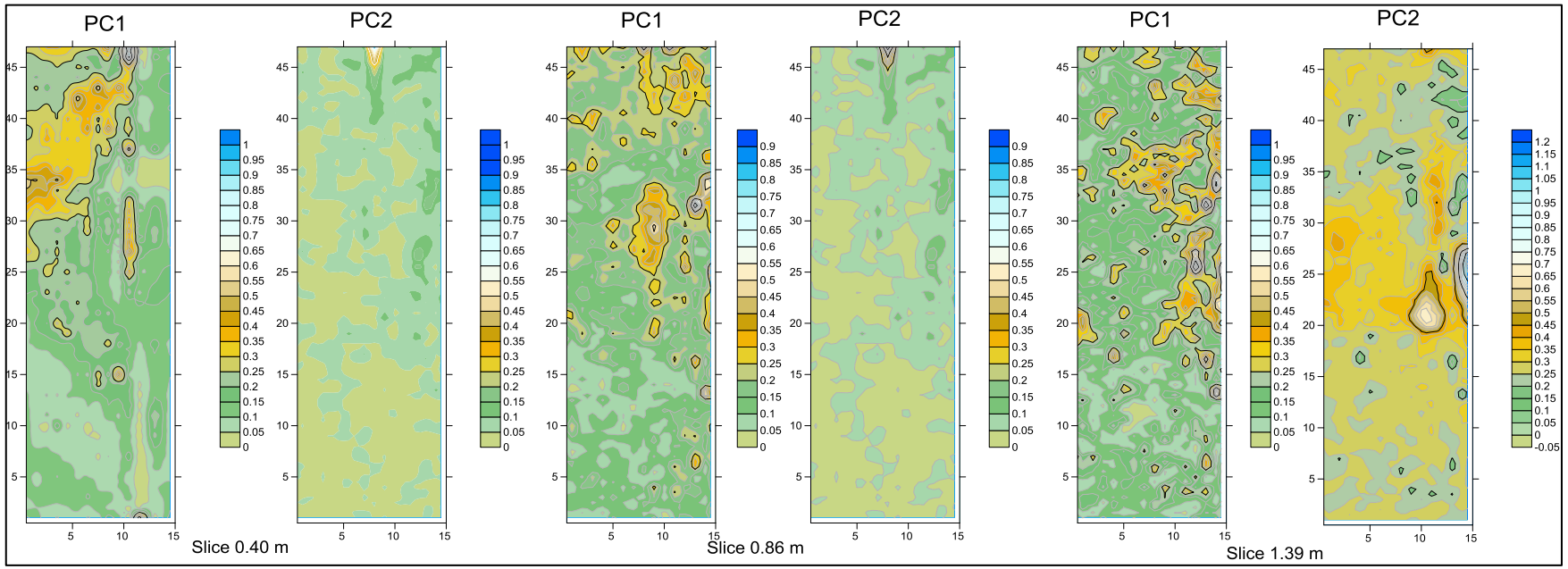

(All axes are in m)

Principal Component analysis (GPR 70 MHz Time-slice and ERT depth slice)

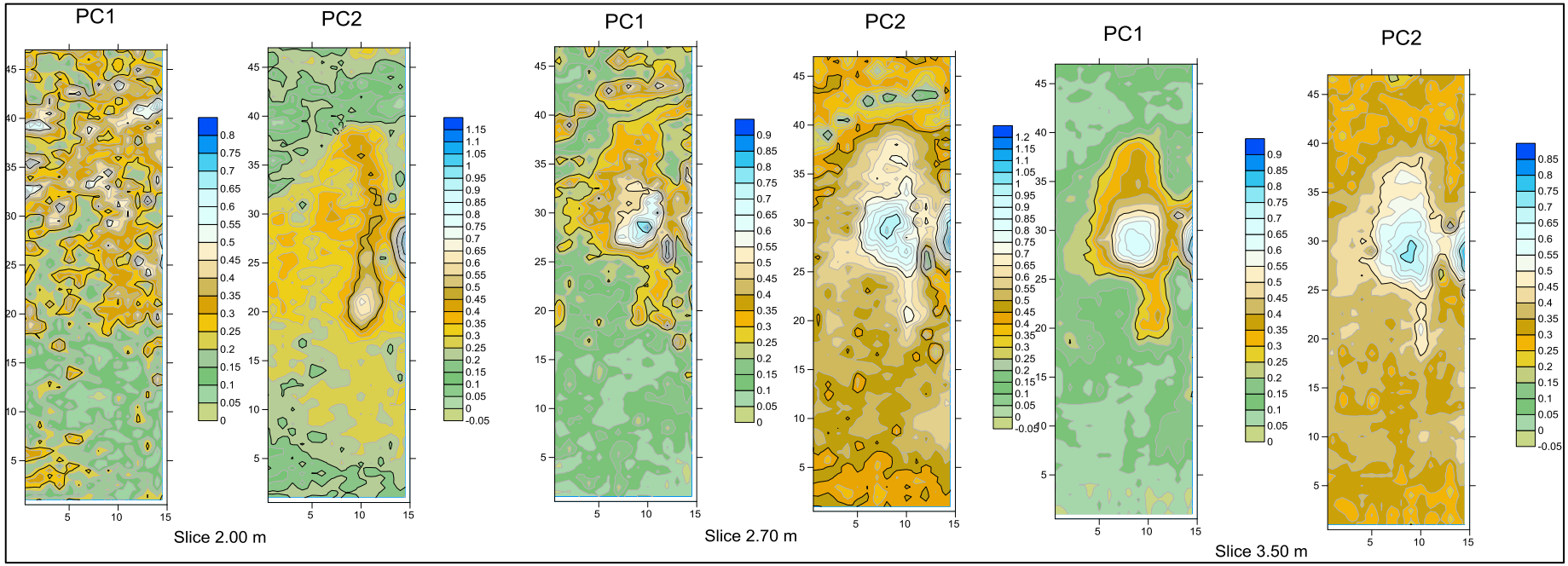

(All axes are in m)

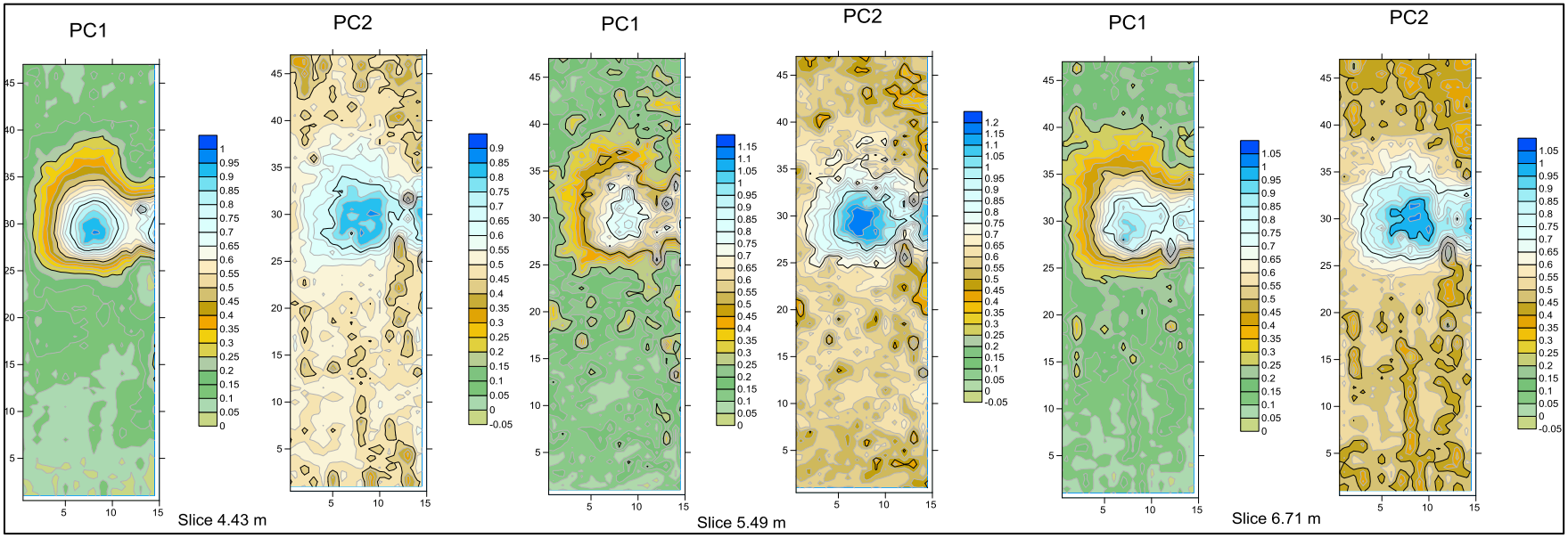

(All axes are in m)

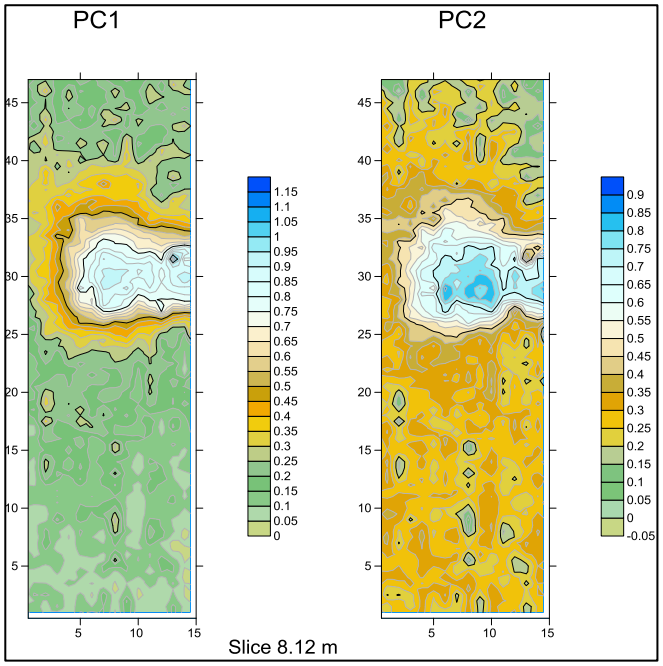

(All axes are in m)

A9) Bayesian Maximum Entropy (GPR 70 MHz Time-slice and ERT depth slice)

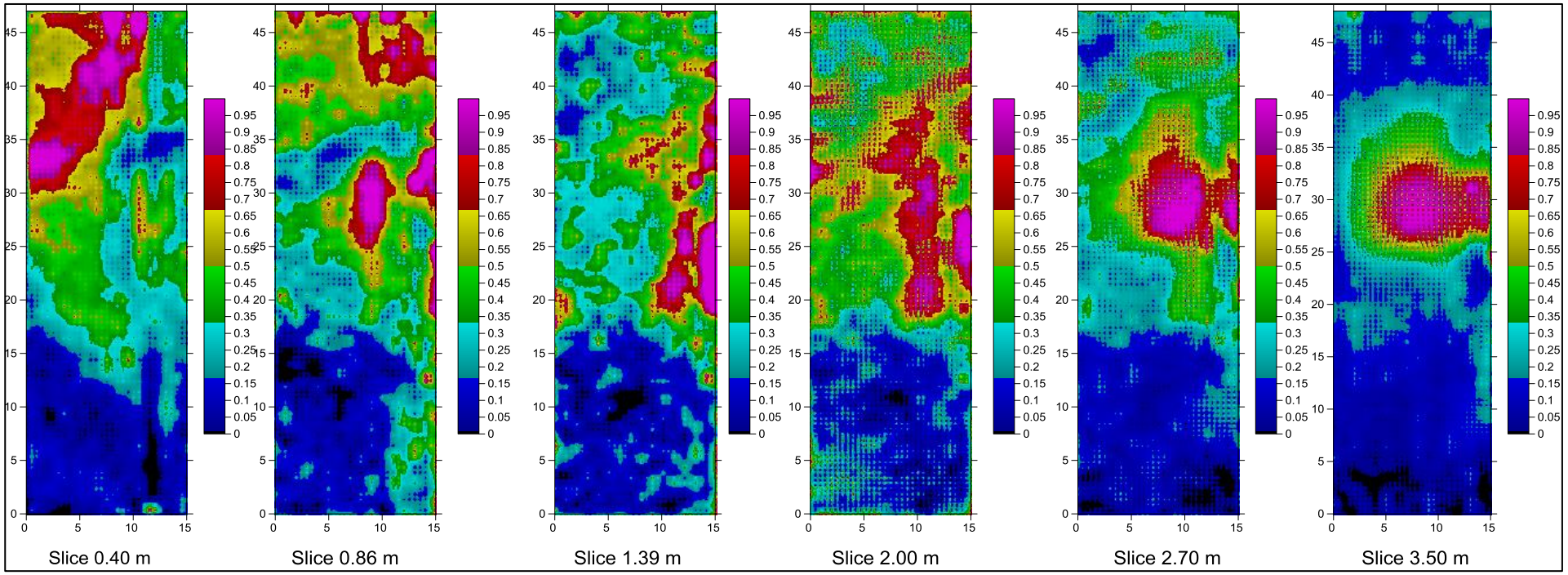

(All axes are in m)

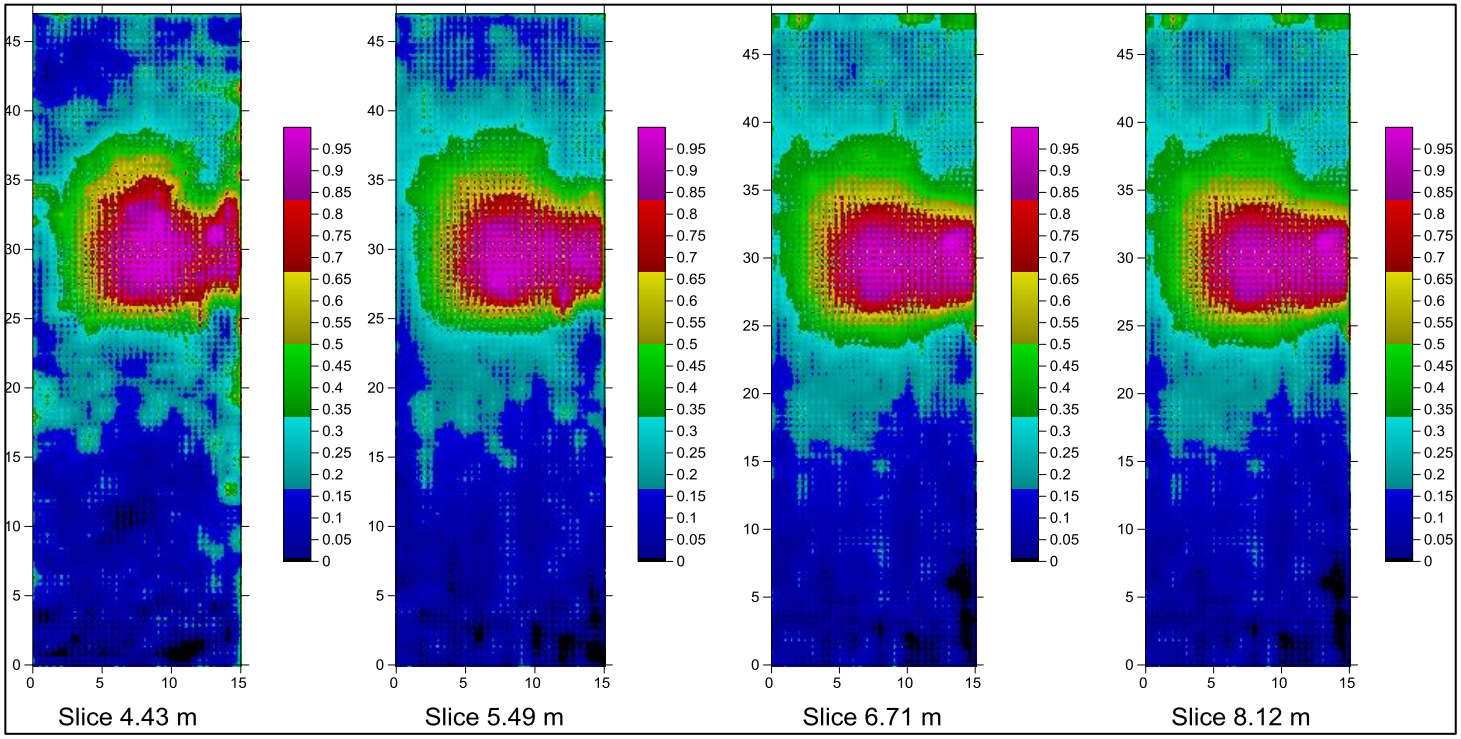

(All axes are in m)

A9) K-Means cluster analysis (GPR 70 MHz Time-slice and ERT depth slice)

(K=4)

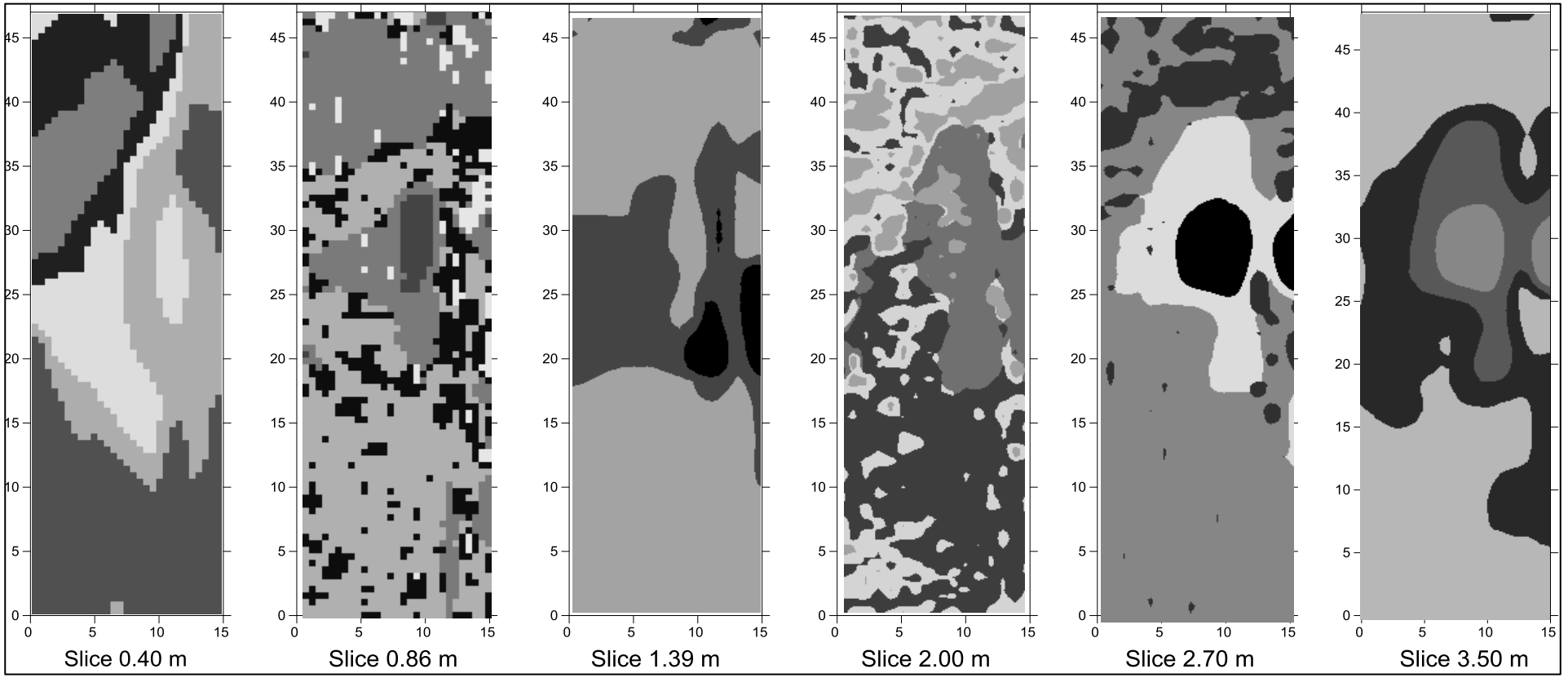

(All axes are in m)

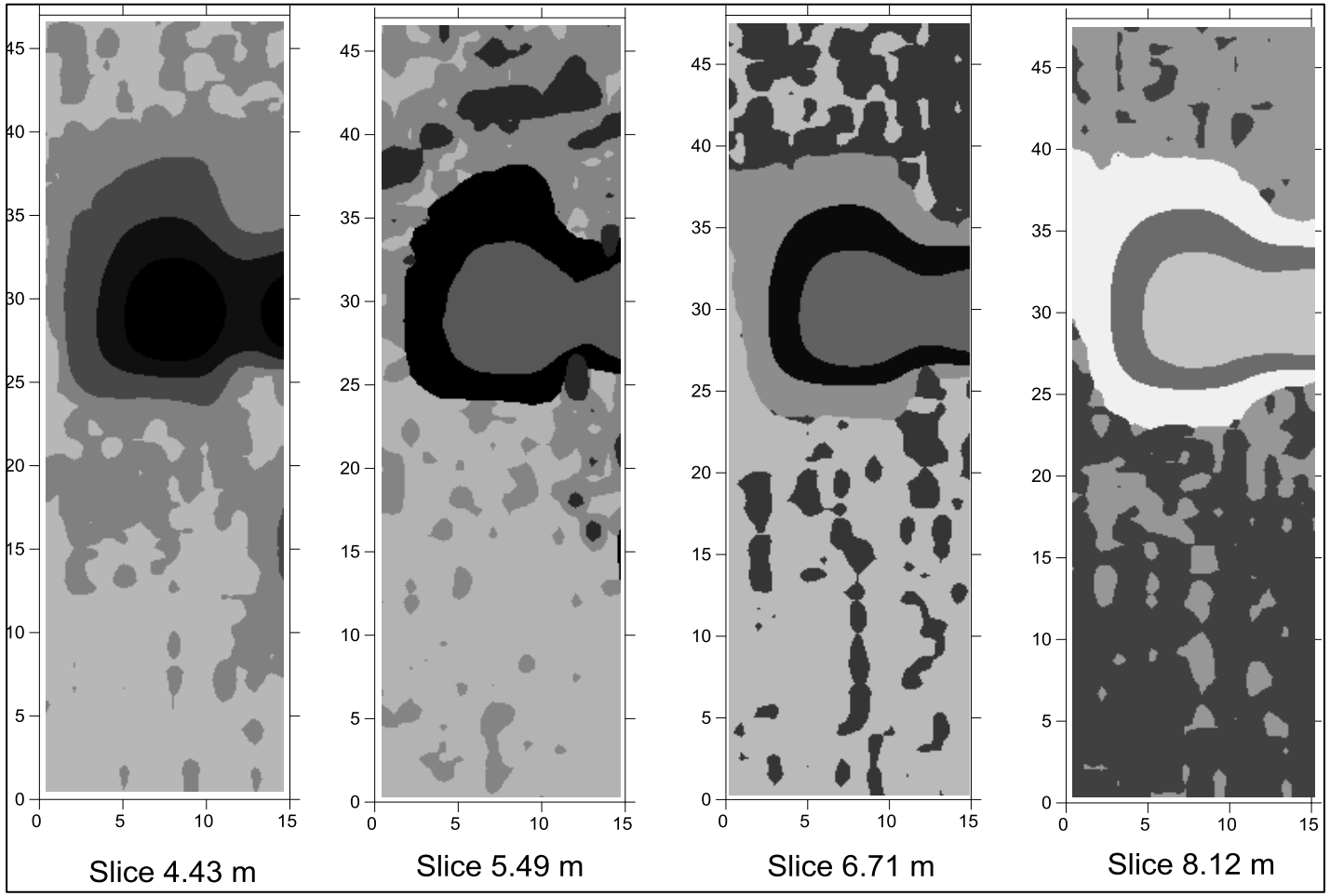

(All axes are in m)

A10) GPR time-slice 400 MHz Time window 85 ns; slices 1-6

(All axes are in m)

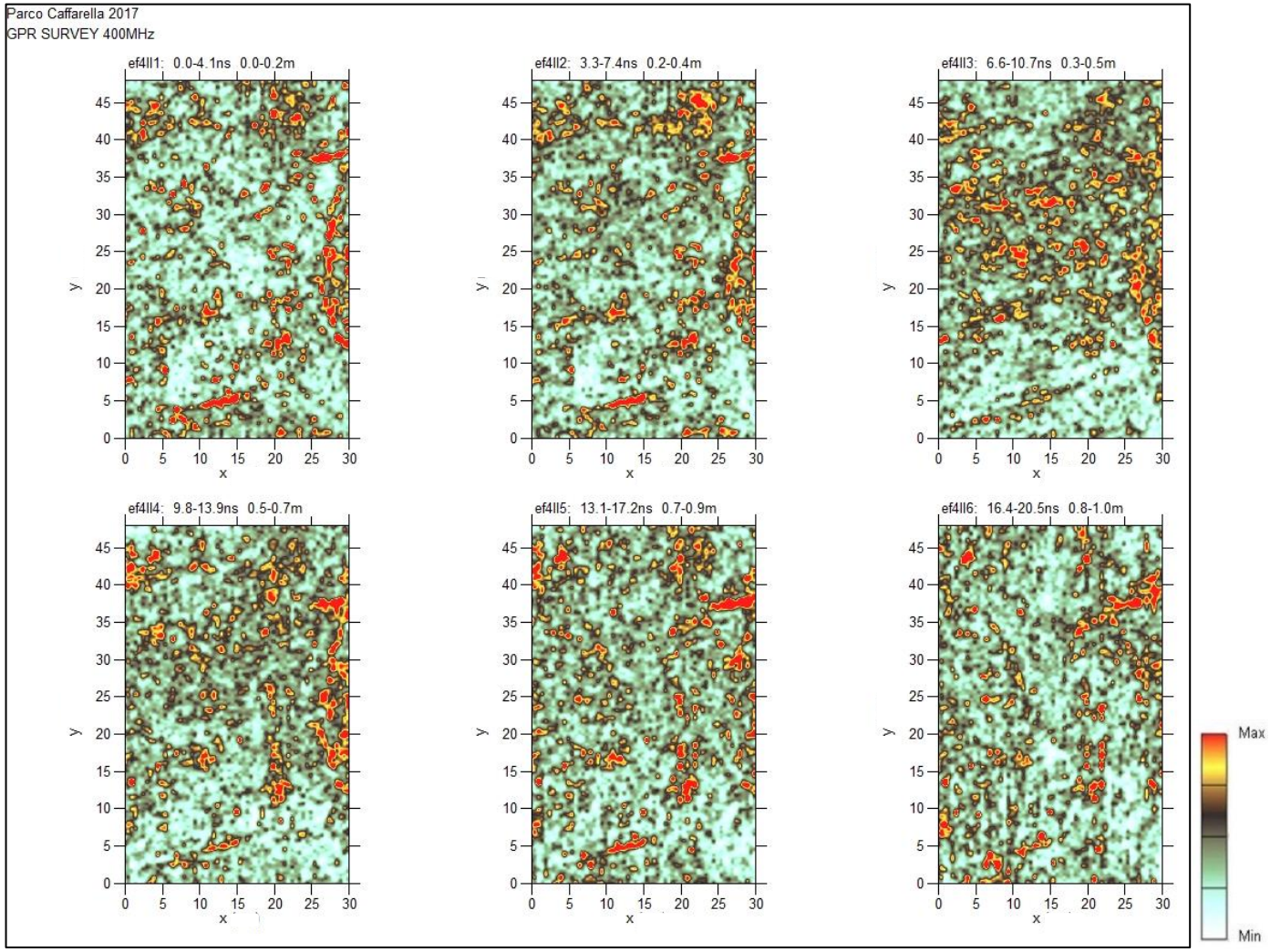

GPR time-slice 400 MHz Time window 85 ns slices 7-12 (All axes are in m)

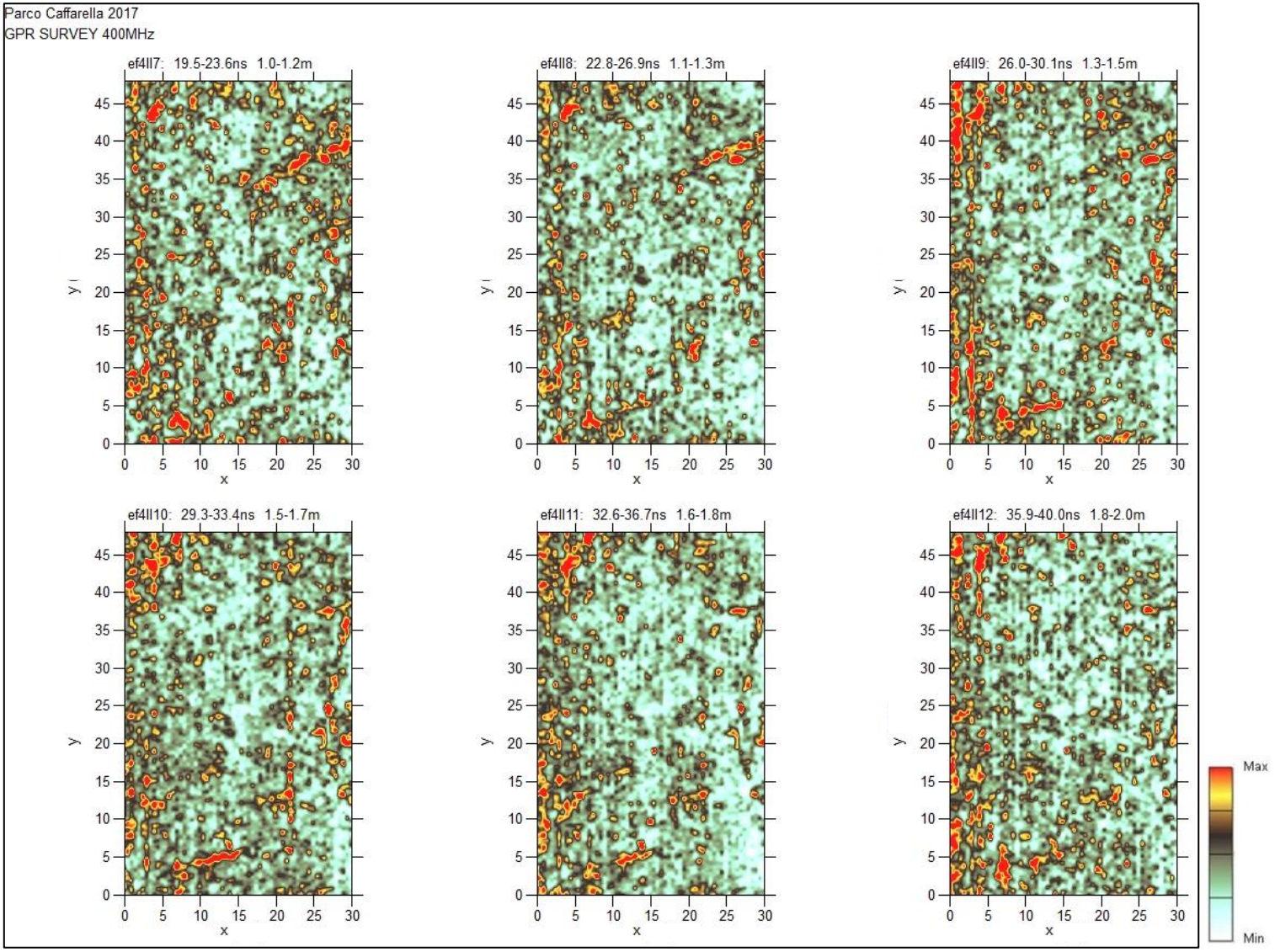

GPR time-slice 400 MHz Time window 85 ns Slices 13-18 (All axes are in m)

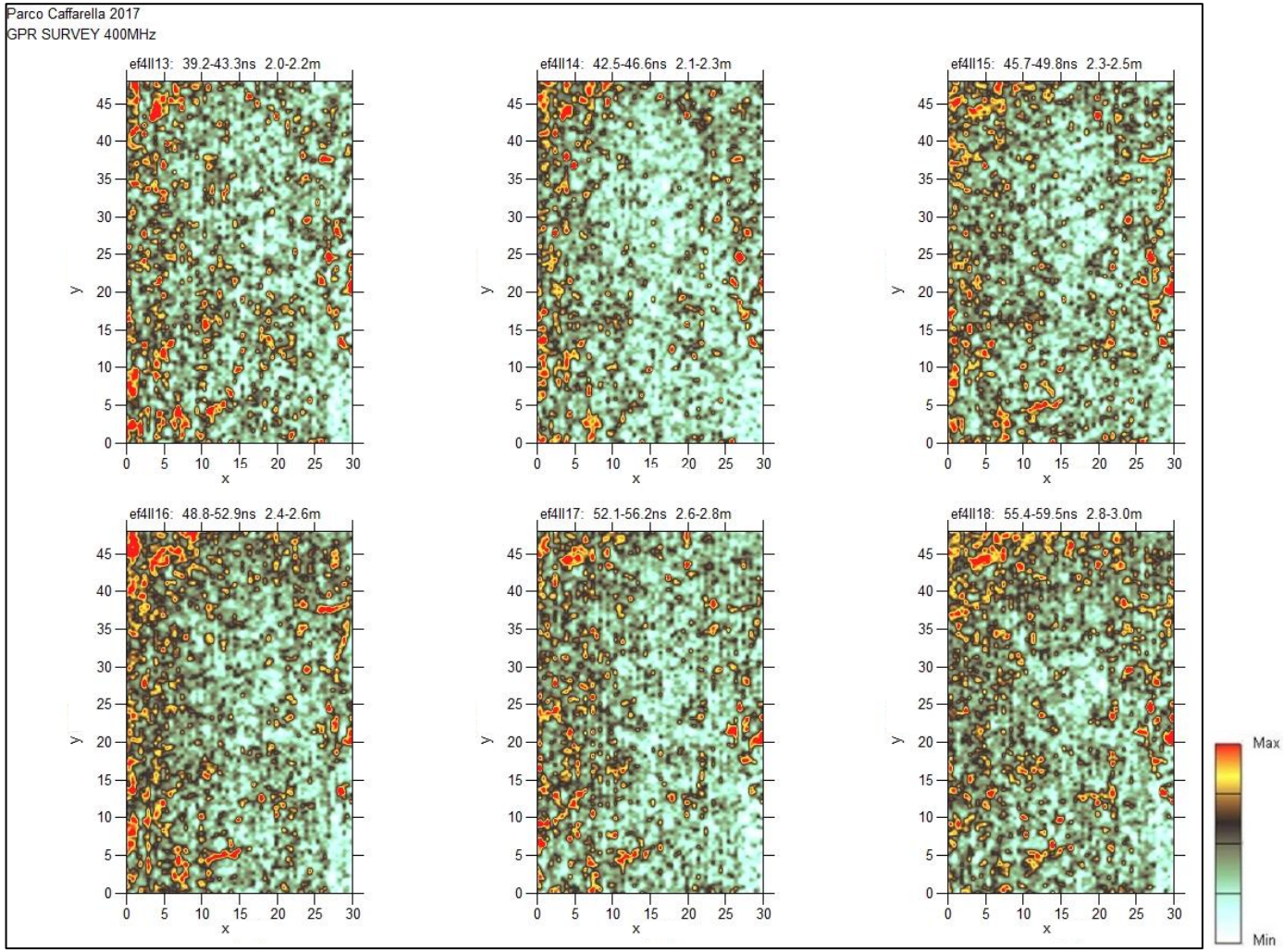

GPR time-slice 400 MHz Time window 85 ns Slices 19-24 (All axes are in m)

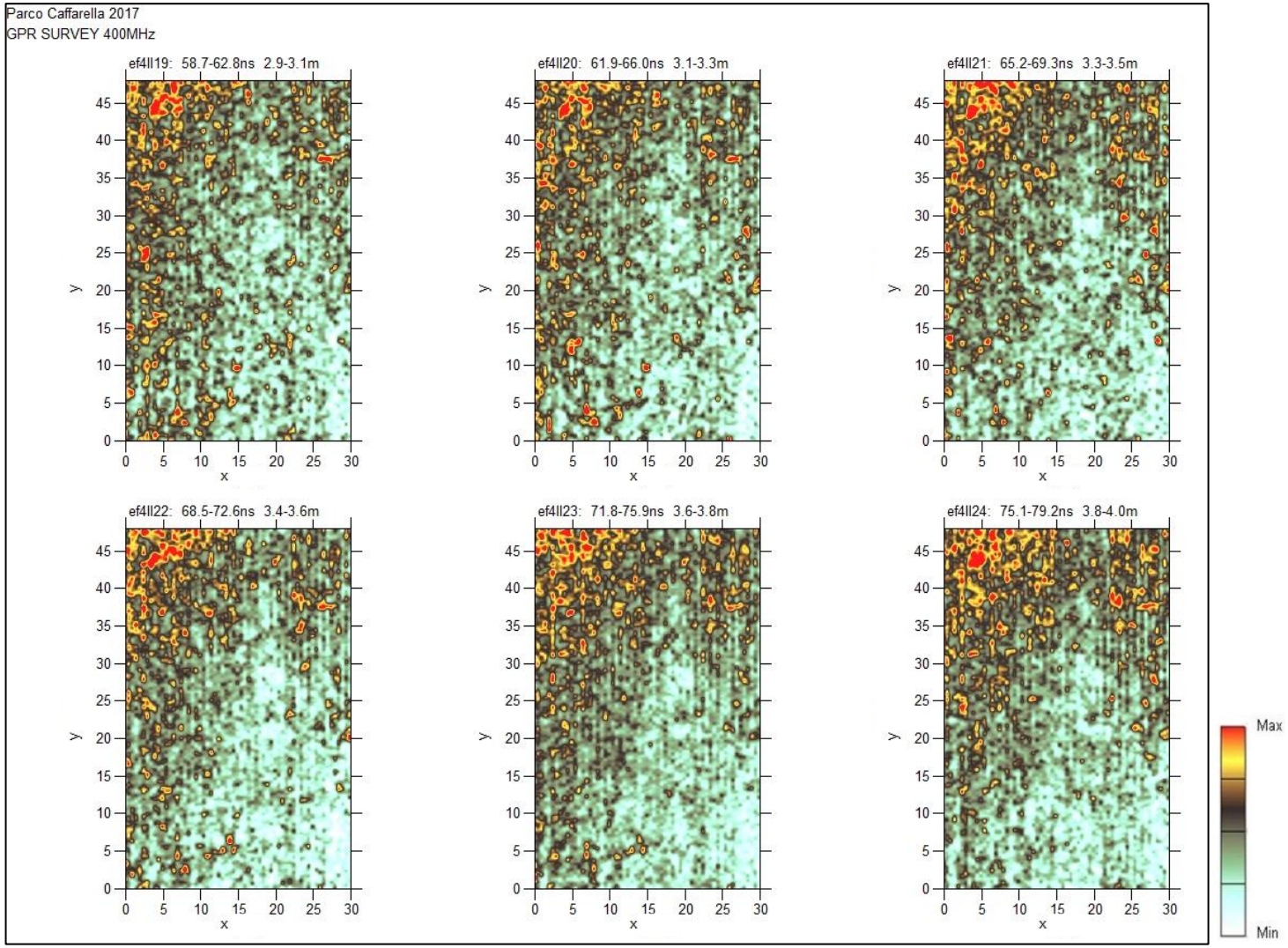

GPR time-slice 400 MHz Time window 85 ns Slices 25-30 (All axes are in m)

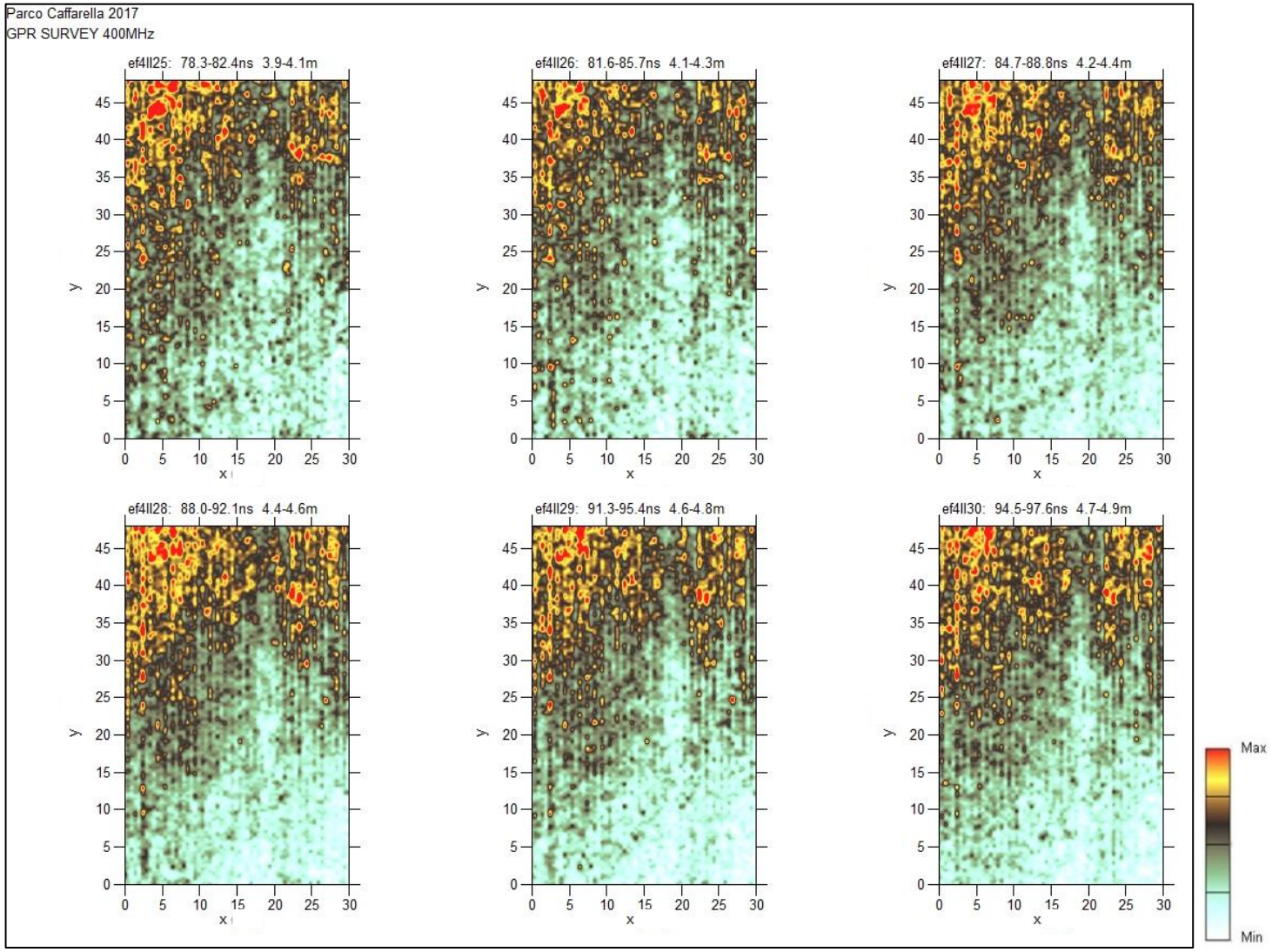

A11) Contour map overlay GPR 400 MHz time-slice and ERT depth-slice

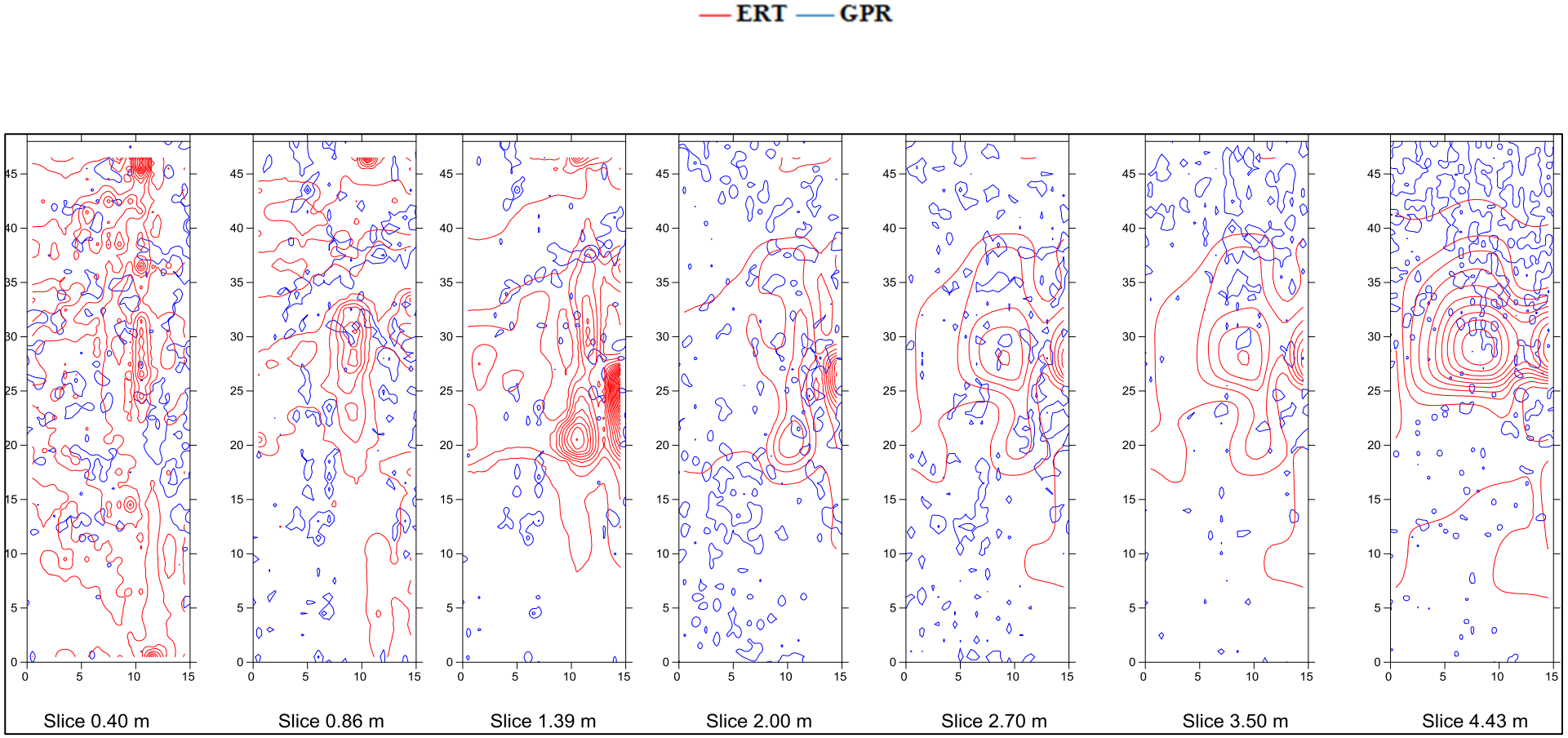

(All axes are in m)

A12) RGB Color Composite GPR 400 MHz time-slice and ERT depth-slice

ERT GPR

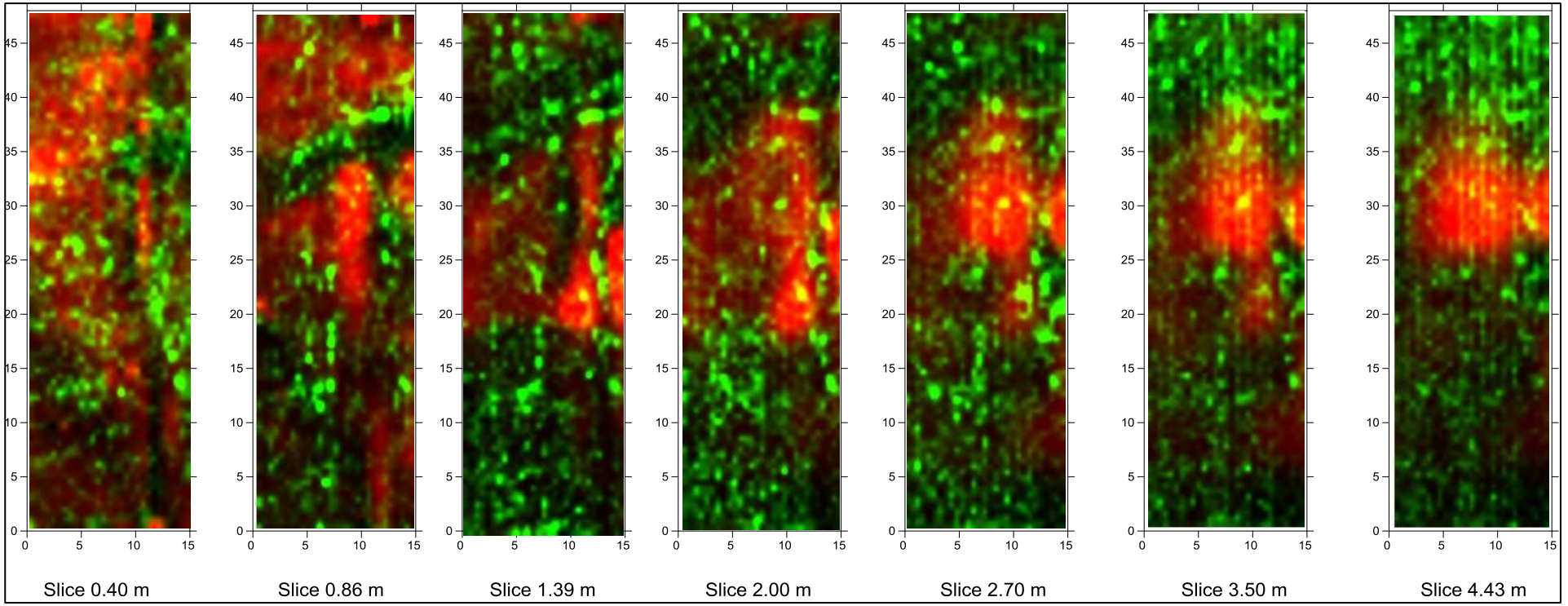

(All axes are in m)

A13) Binary representation GPR 400 MHz and ERT depth slice

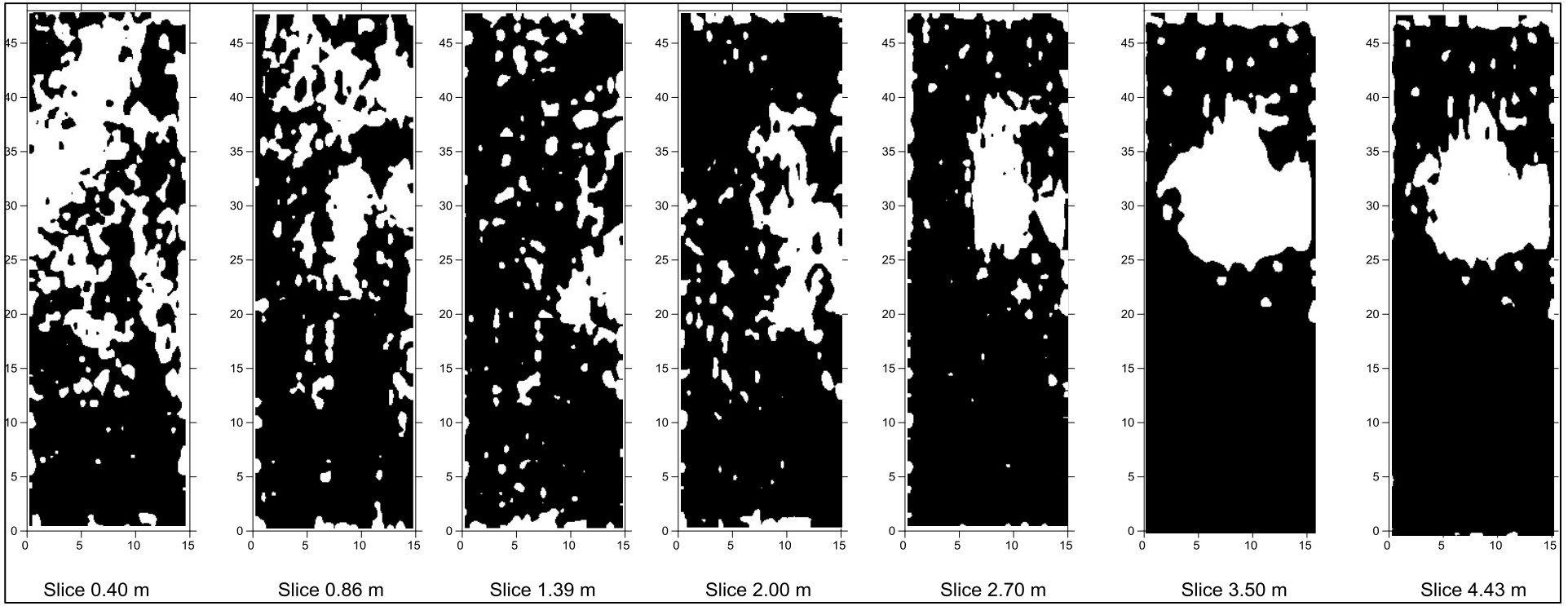

(All axes are in m)

A14) Data Sum (GPR 400 MHz + ERT depth slice)

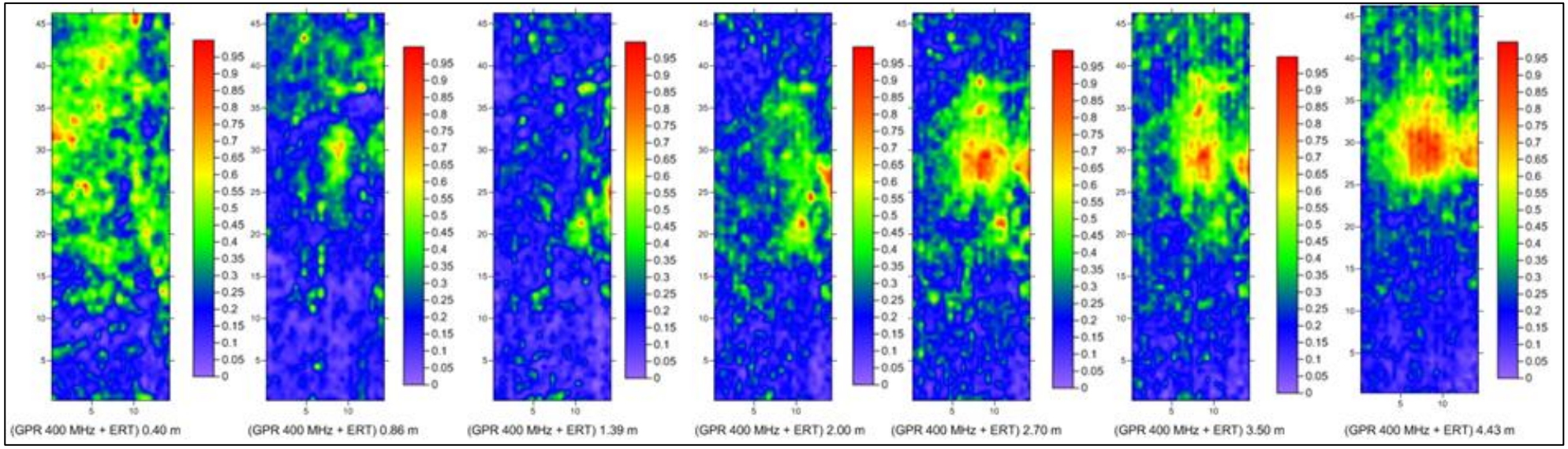

(All axes are in m)

A15) Data Product (GPR 400 MHz ·ERT depth slice)

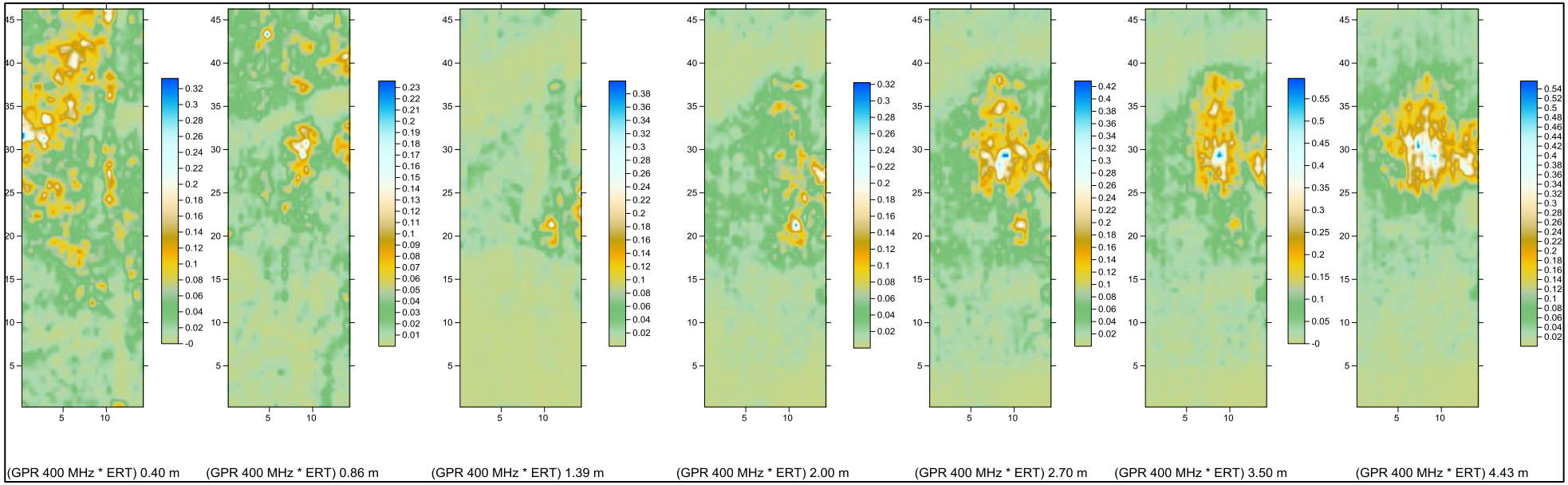

(All axes are in m)

A16) Principal Component analysis (GPR 400 MHz Time-slice and ERT depth slice)

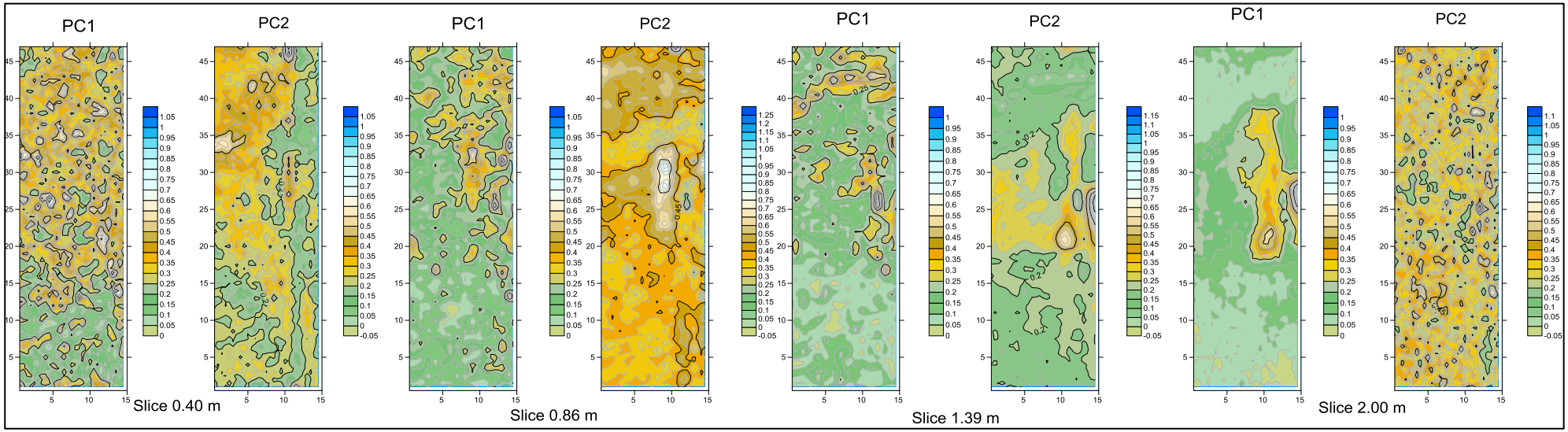

(All axes are in m)

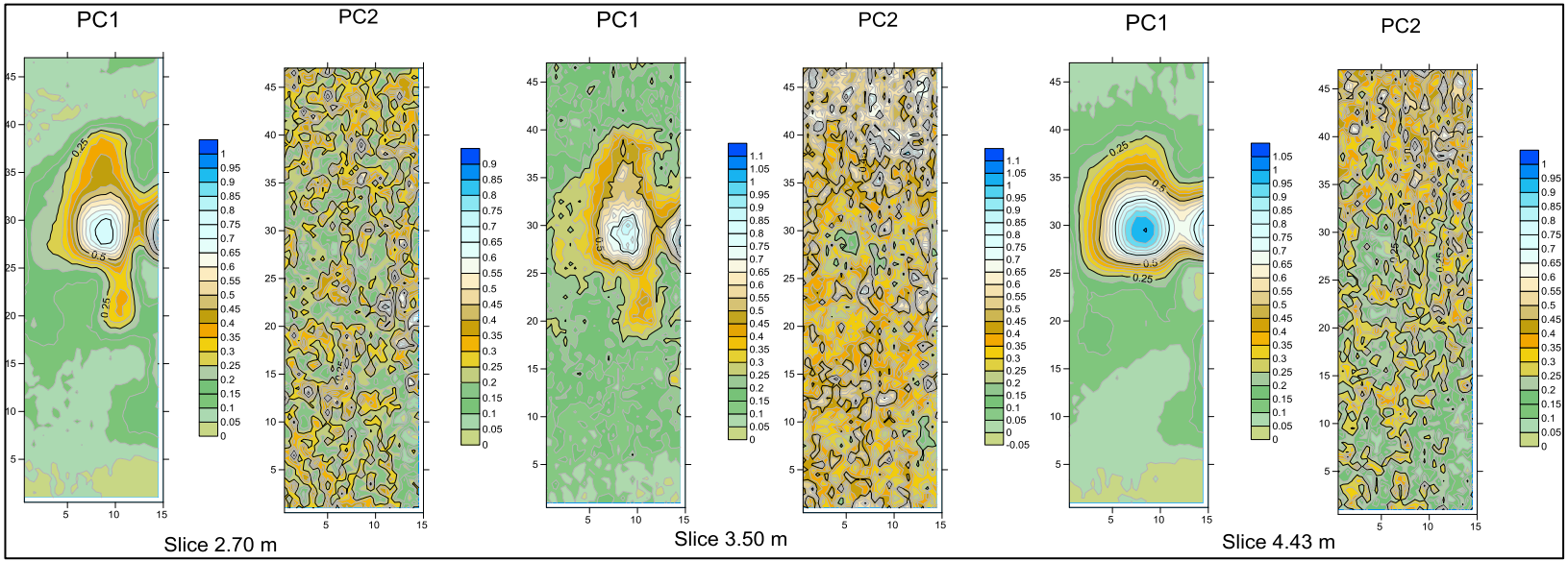

(All axes are in m)

A17) Bayesian Maximum Entropy (GPR 400 MHz Time-slice and ERT depth slice)

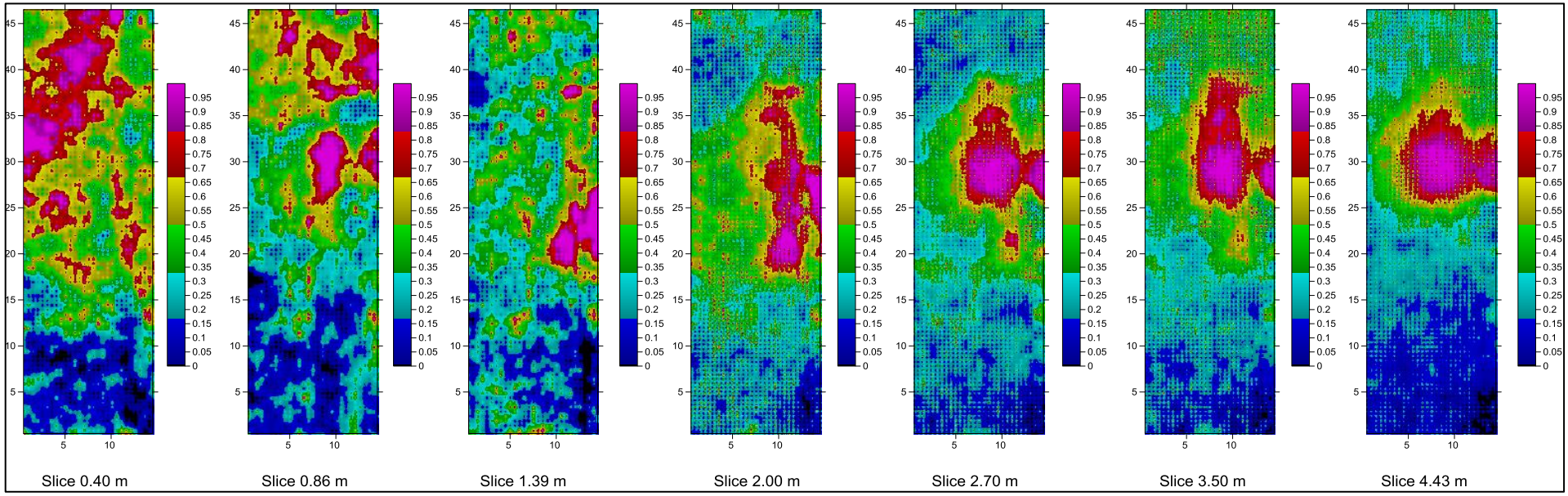

(All axes are in m)

A18) K-Means cluster analysis (GPR 400 MHz Time-slice and ERT depth slice)

(K=4)

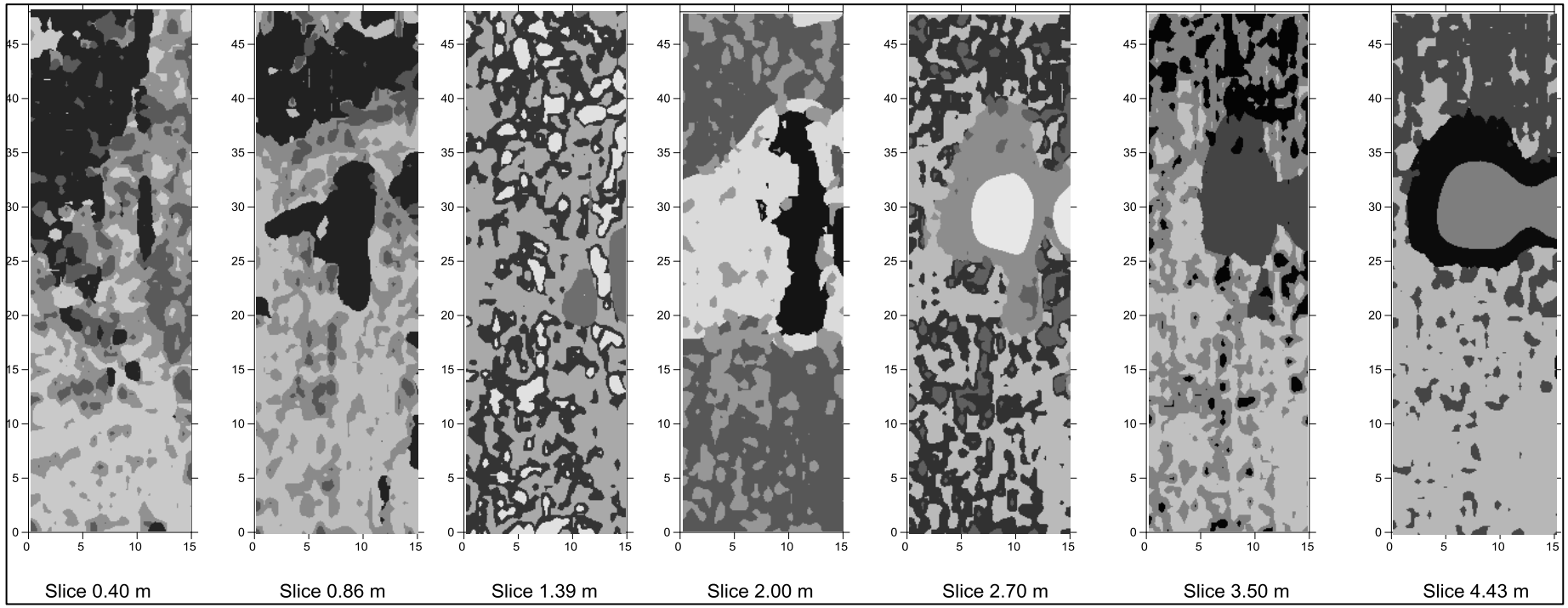

(All axes are in m)

Appendix B-Magliano Sabina

B1) GPR time-slice 400 MHz Time window 85 ns; slices 1-5

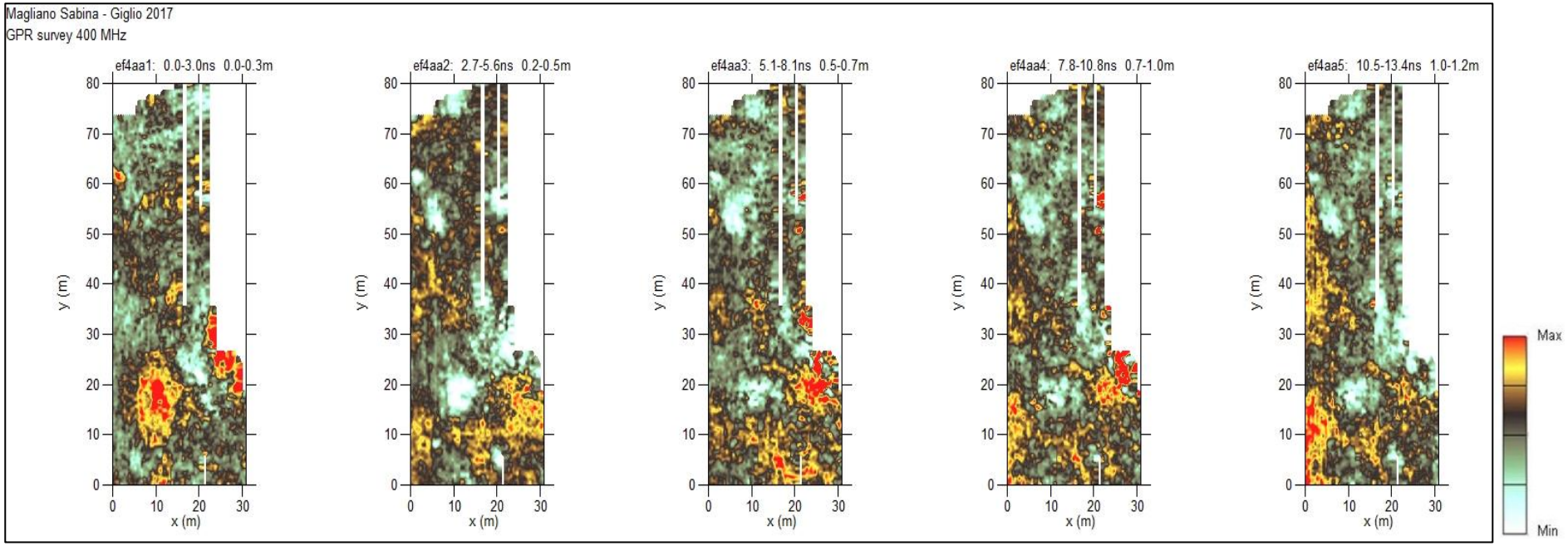

GPR time-slice 400 MHz Time window 85 ns; slices 6-10

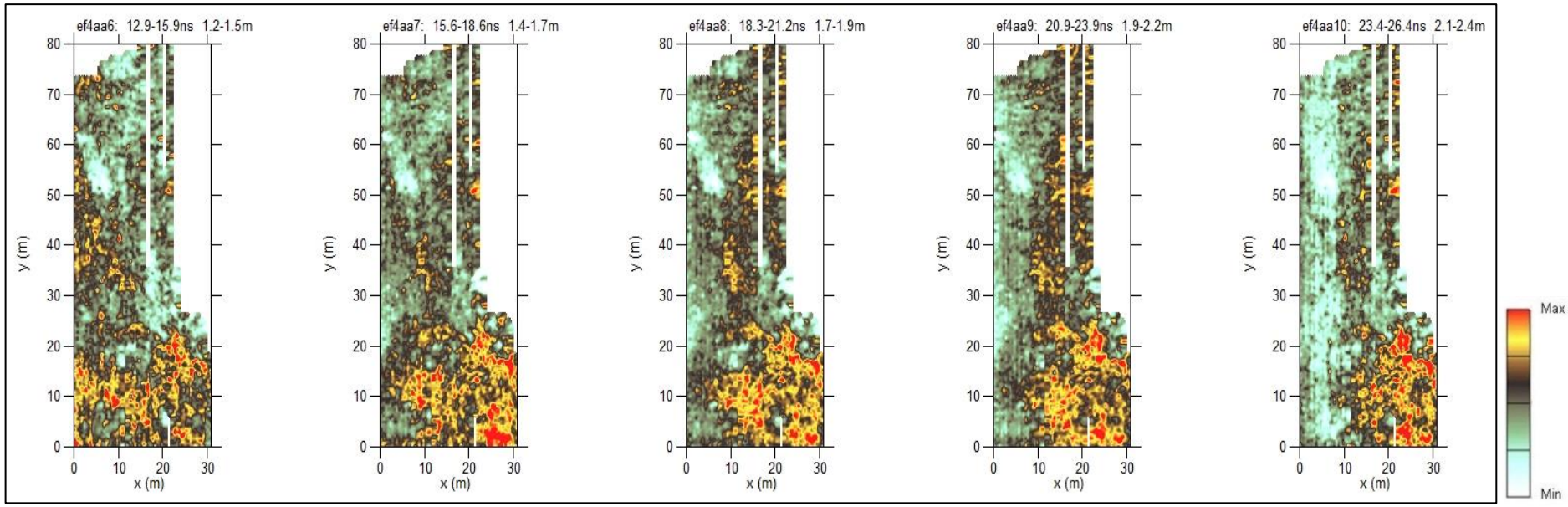

GPR time-slice 400 MHz Time window 85 ns; slices 11-15

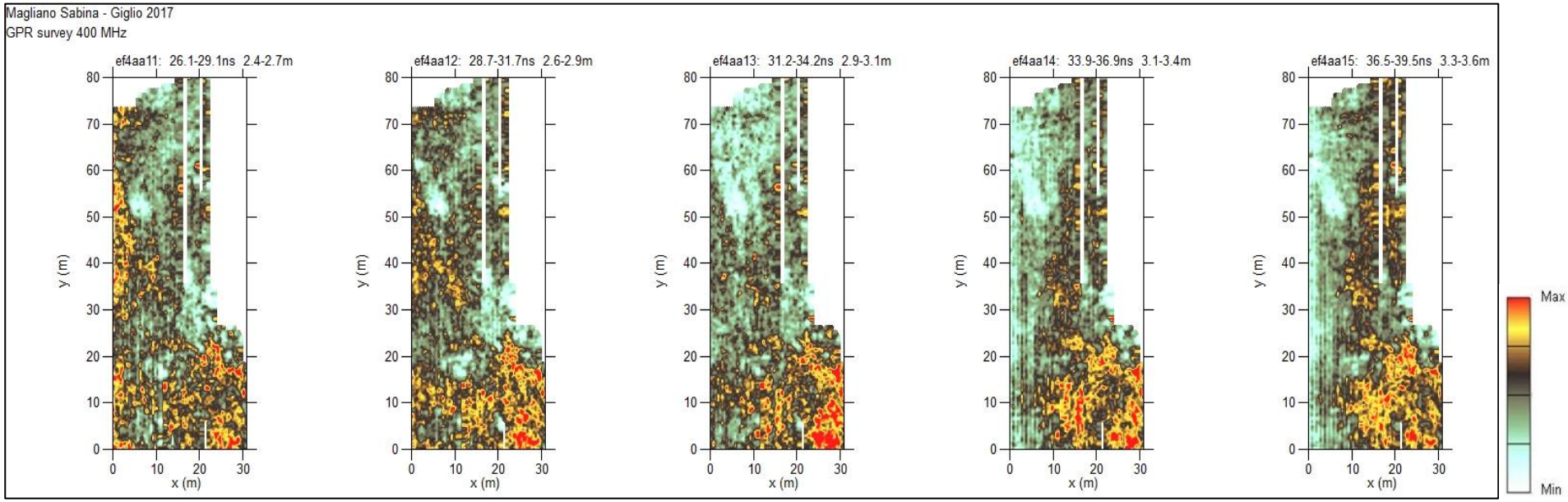

GPR time-slice 400 MHz Time window 85 ns; slices 16-20

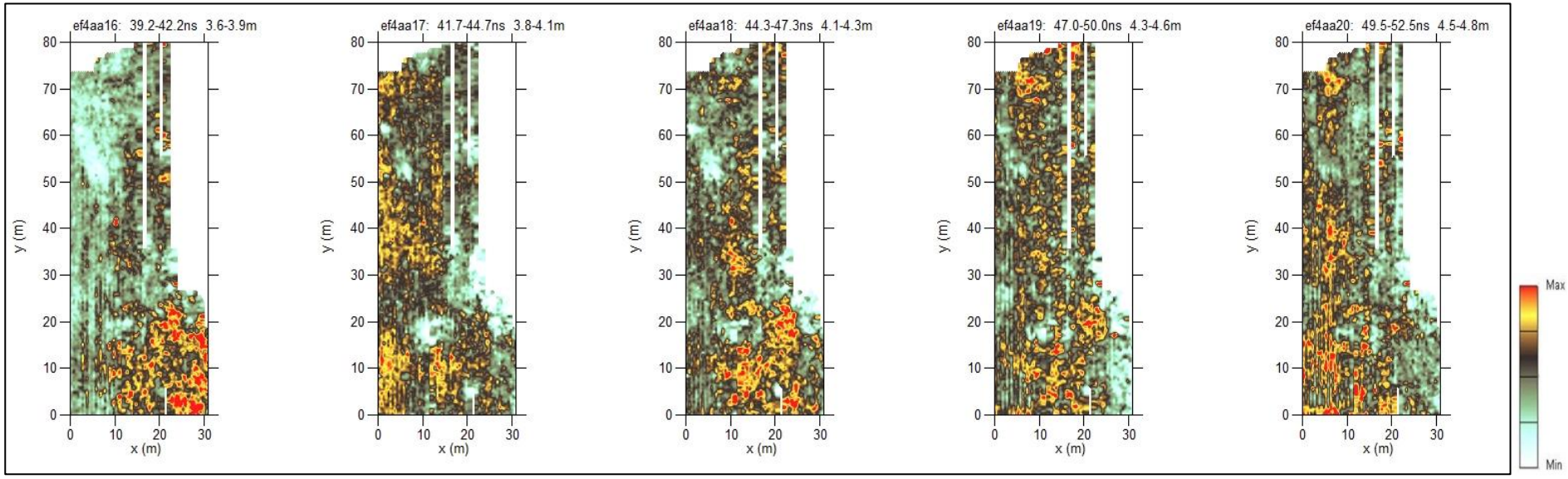

GPR time-slice 400 MHz Time window 85 ns; slices 21-25

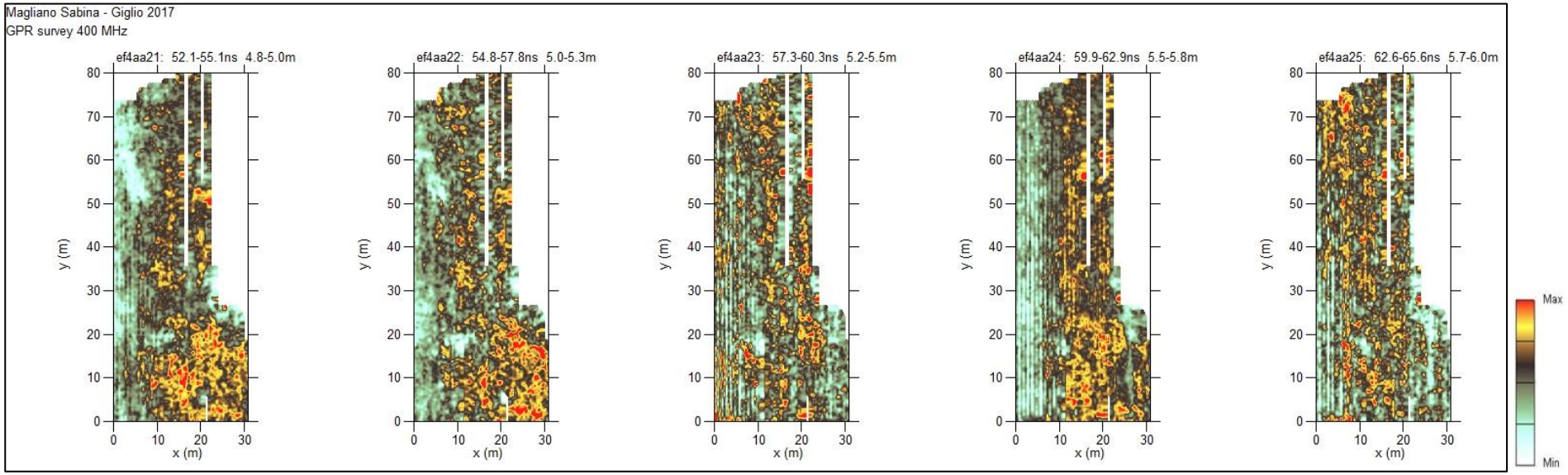

GPR time-slice 400 MHz Time window 85 ns; slices 26-30

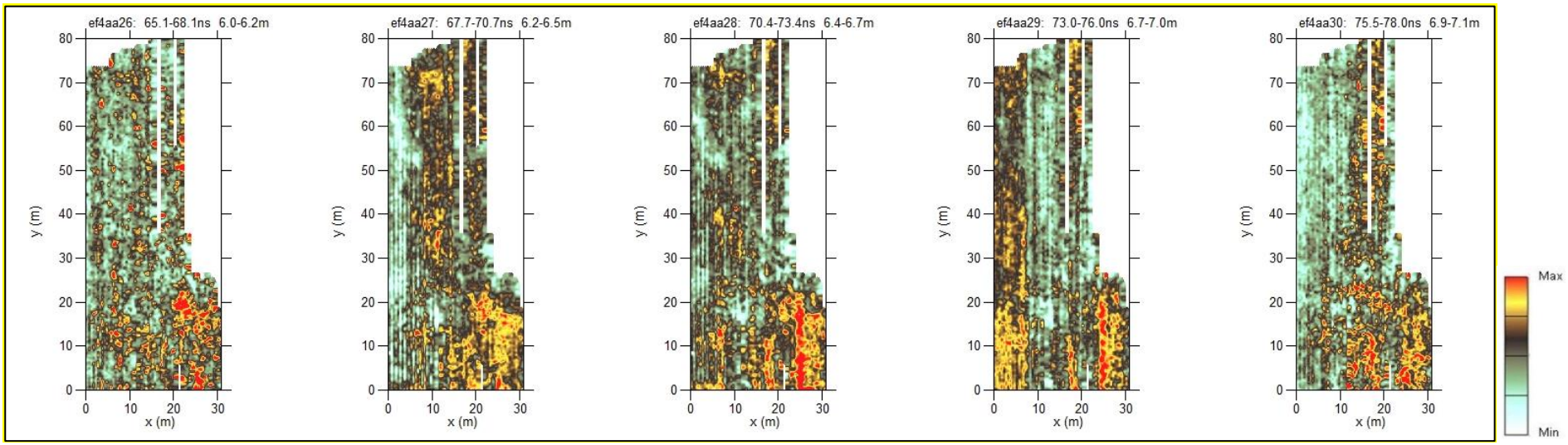

B2) 2D normalized Crosscorrelation for different depth (All axes are in m)

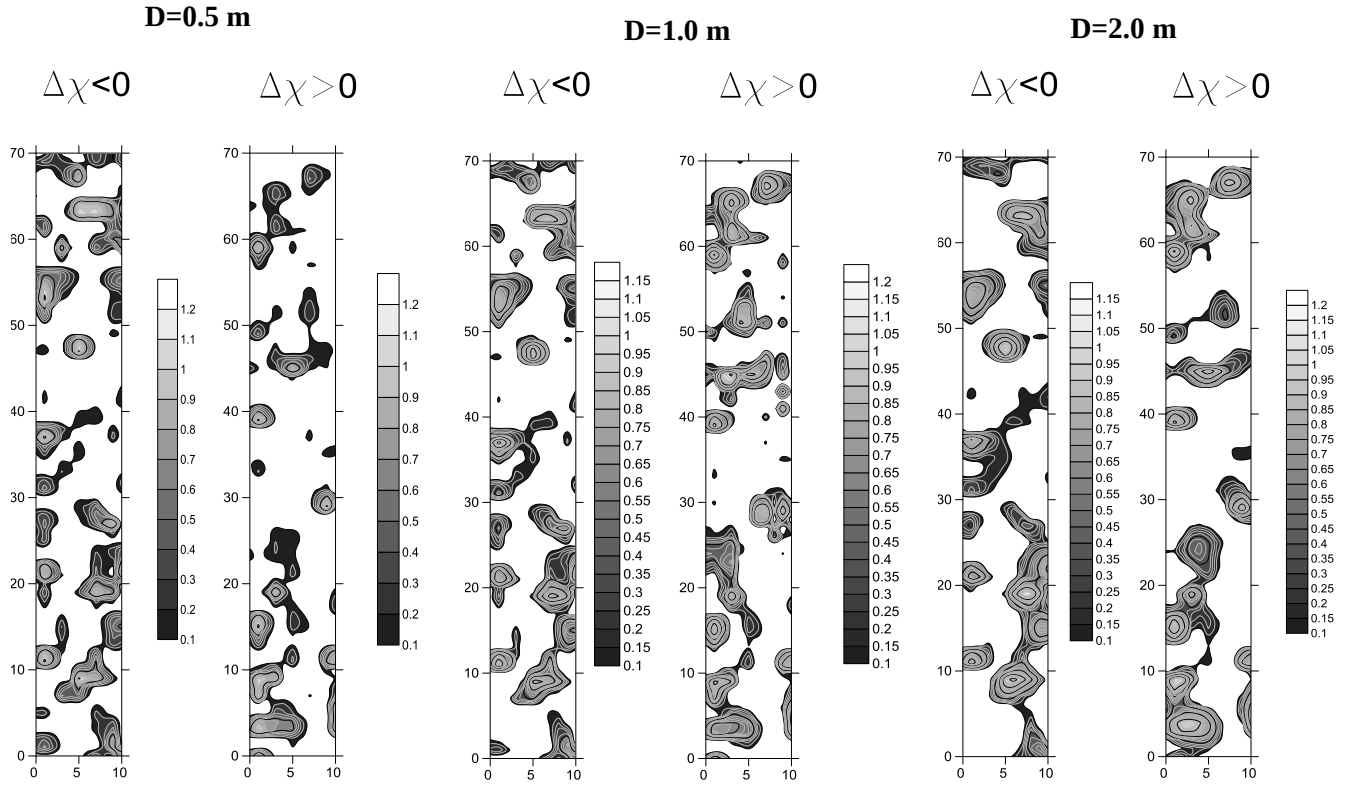

B3) Different integration methods between GPR 400 MHz time-slices and 2D Crosscorrelation results at D=0.5 m.

(All axes are in m)

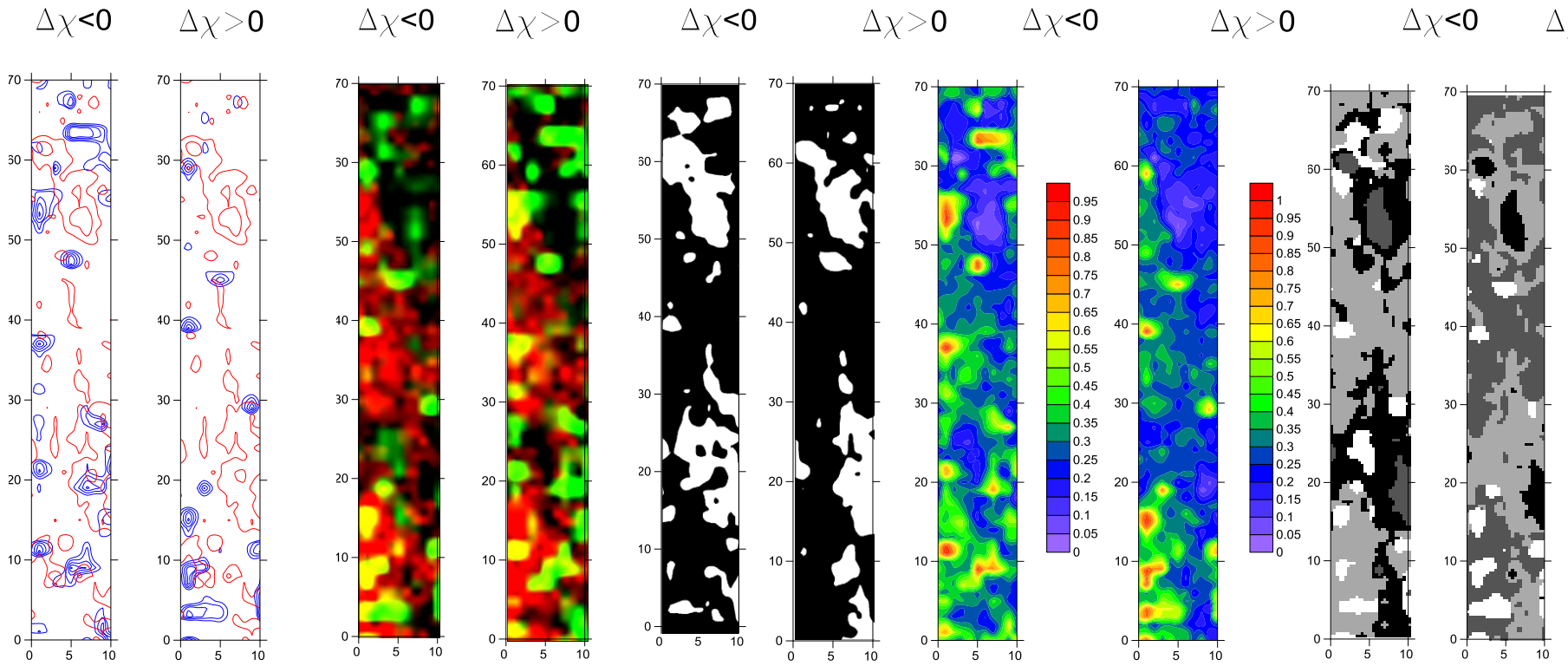

Contour map overlay

(MAG;GPR)

RGB Colour composite

(MAG;GPR)

Binary representation

Data Sum

K-means cluster analysis (K=4)

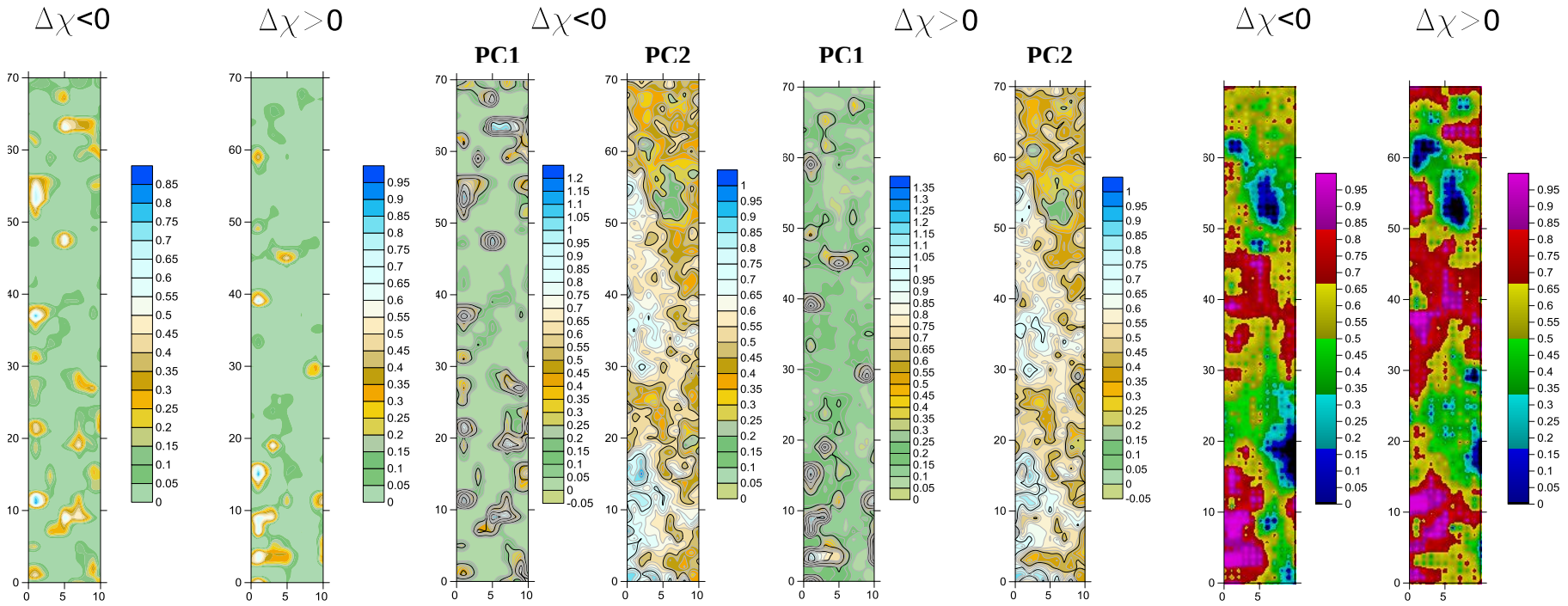
$\Delta\chi$<0
$\Delta\chi$>0
$\Delta\chi$<0
$\Delta\chi$>0
$\Delta\chi$<0
$\Delta\chi$>0
PC1
PC2
PC1
PC2
Data Product
Principal Component Analysis
Bayesian Maximum Entropy

B4) Different integration methods between GPR 400 MHz time-slices and 2D Crosscorrelation results at D=1.0 m.

(All axes are in m)

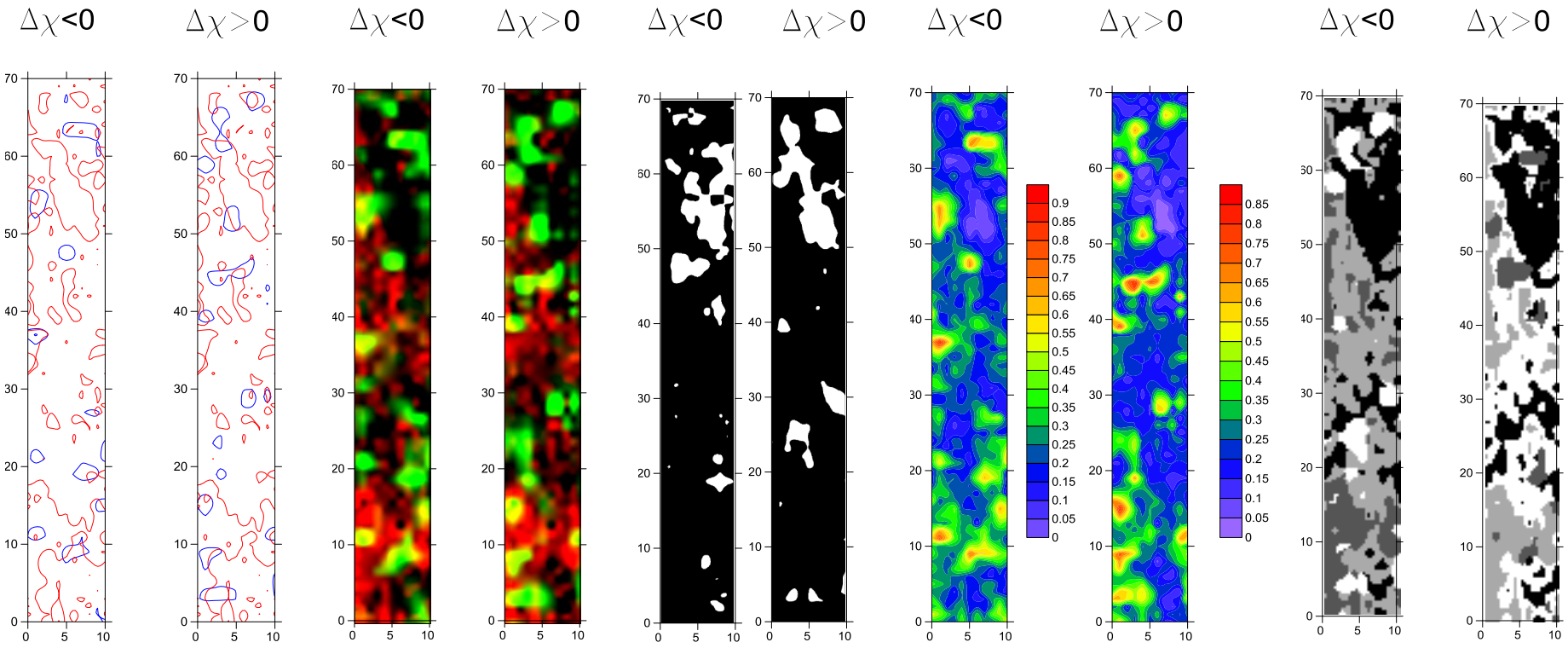

Contour map overlay

(MAG;GPR)

RGB Colour composite

(MAG;GPR)

Binary representation

Data Sum

K-means cluster analysis (K=4)

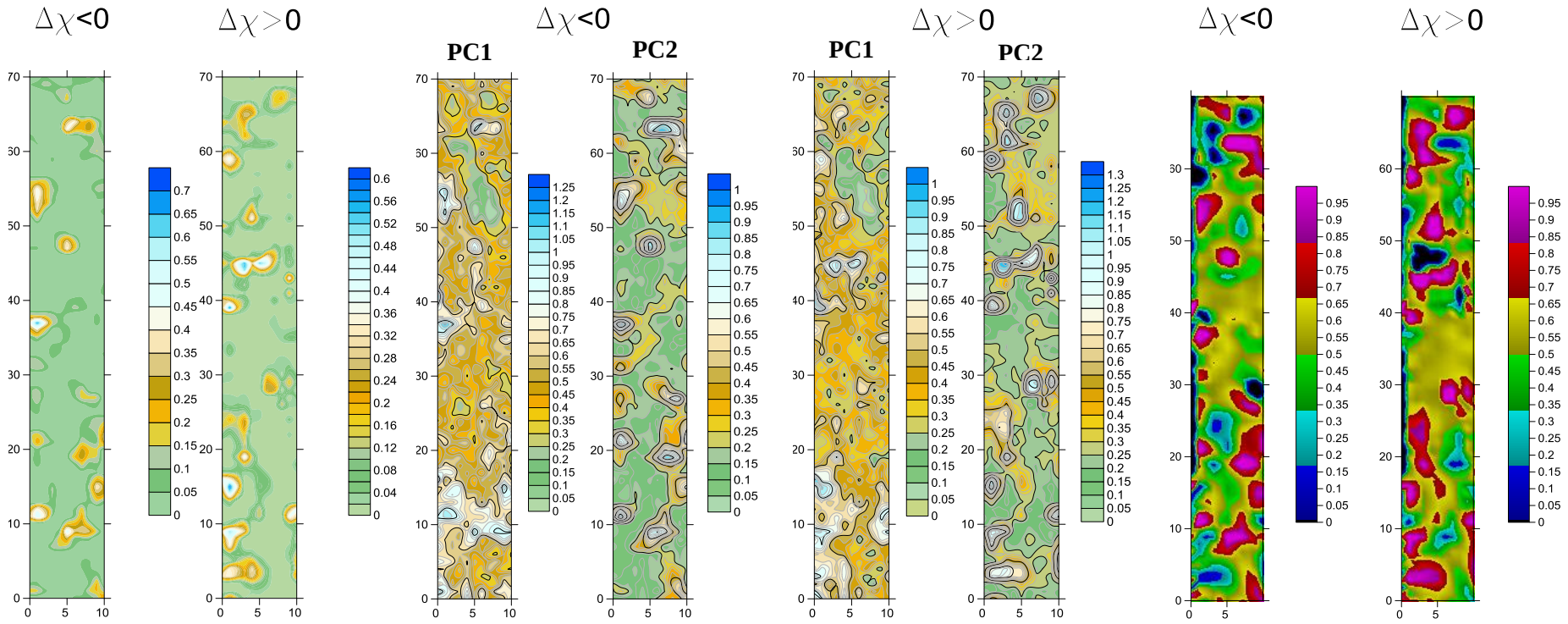
$\Delta\chi$<0
$\Delta\chi$>0
PC1
PC2
$\Delta\chi$<0
$\Delta\chi$>0
PC1
PC2
$\Delta\chi$<0
$\Delta\chi$>0
Data Product
Principal Component analysis
Bayesian Maximum Entropy

B5) Different integration methods between GPR 400 MHz time-slices and 2D Crosscorrelation results at D=2.0 m.

(All axes are in m)

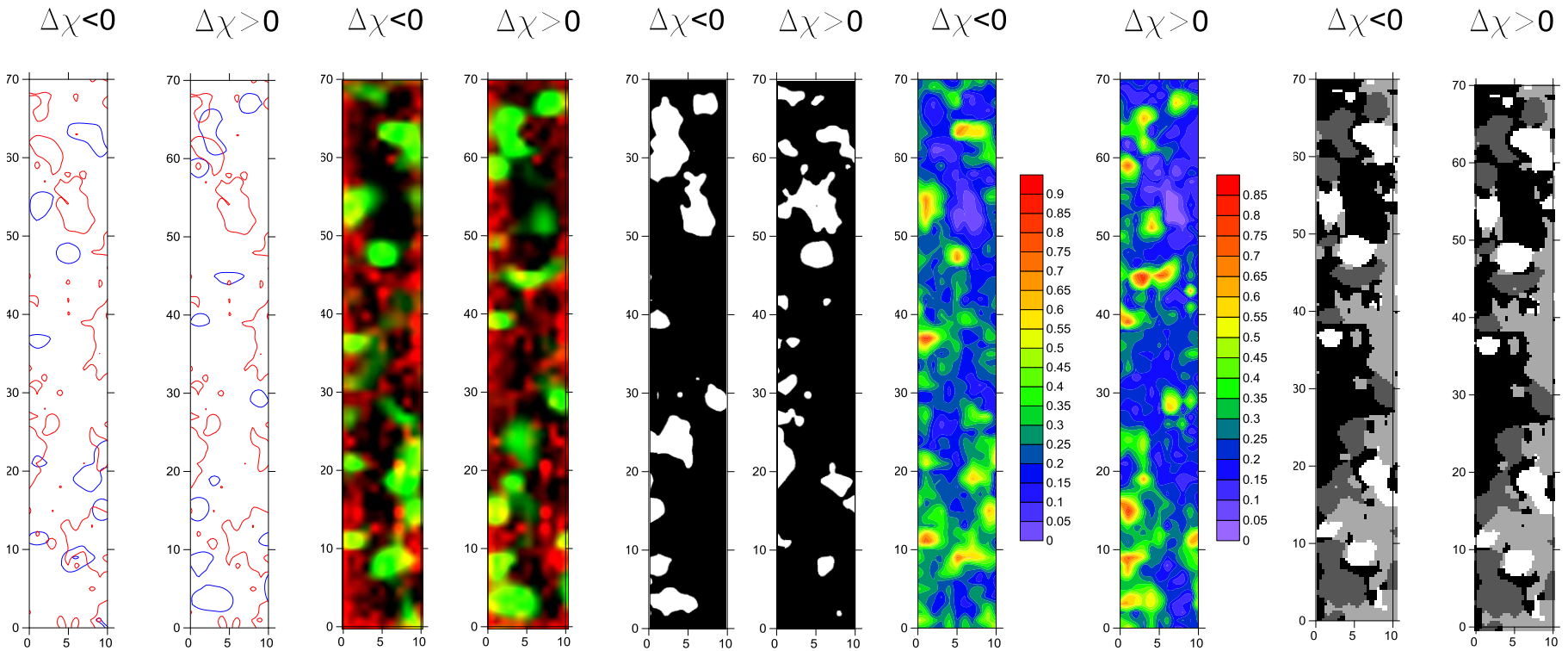

Contour map overlay

(MAG;GPR)

RGB Colour composite

(MAG;GPR)

Binary representation

Data Sum

K-means cluster analysis (K=4)

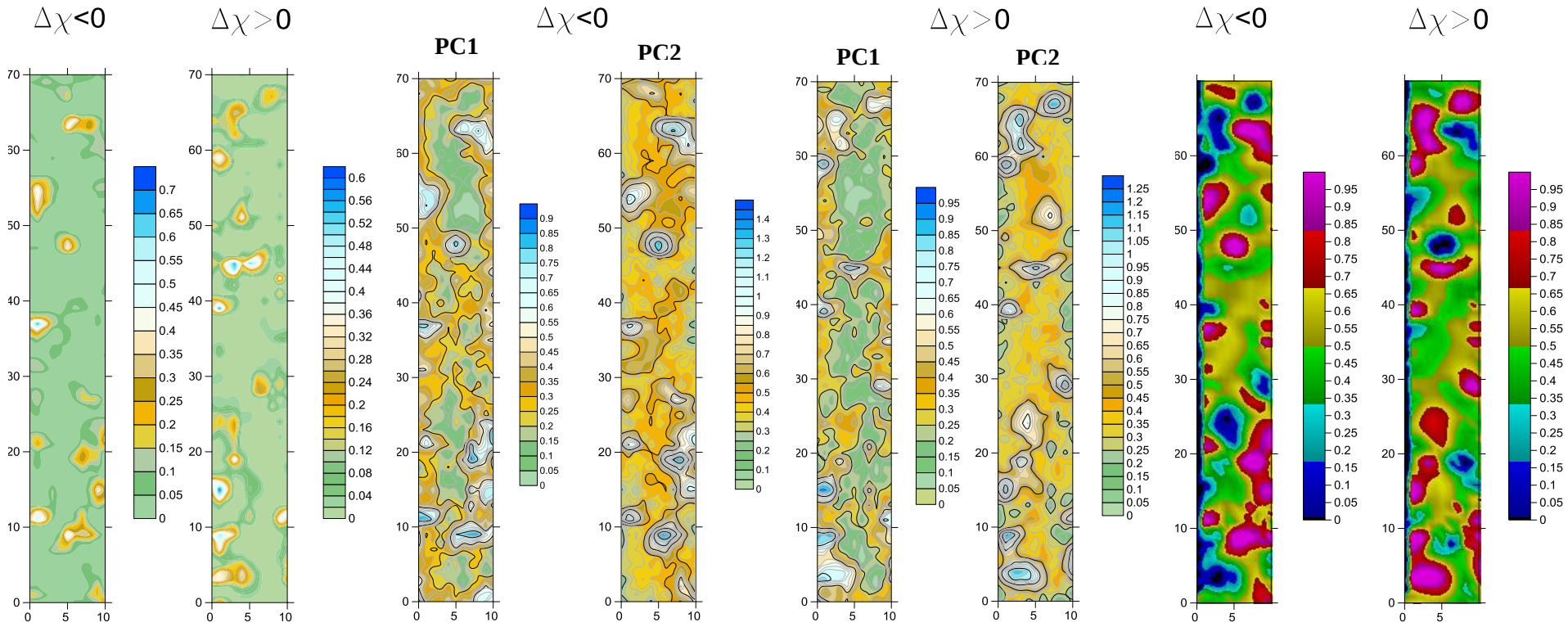
Δχ<0
Δχ>0
PC1
PC2
Δχ<0
Δχ>0
PC1
PC2
Δχ<0
Δχ>0
Data Product
Principal Component analysis
Bayesian Maximum Entropy